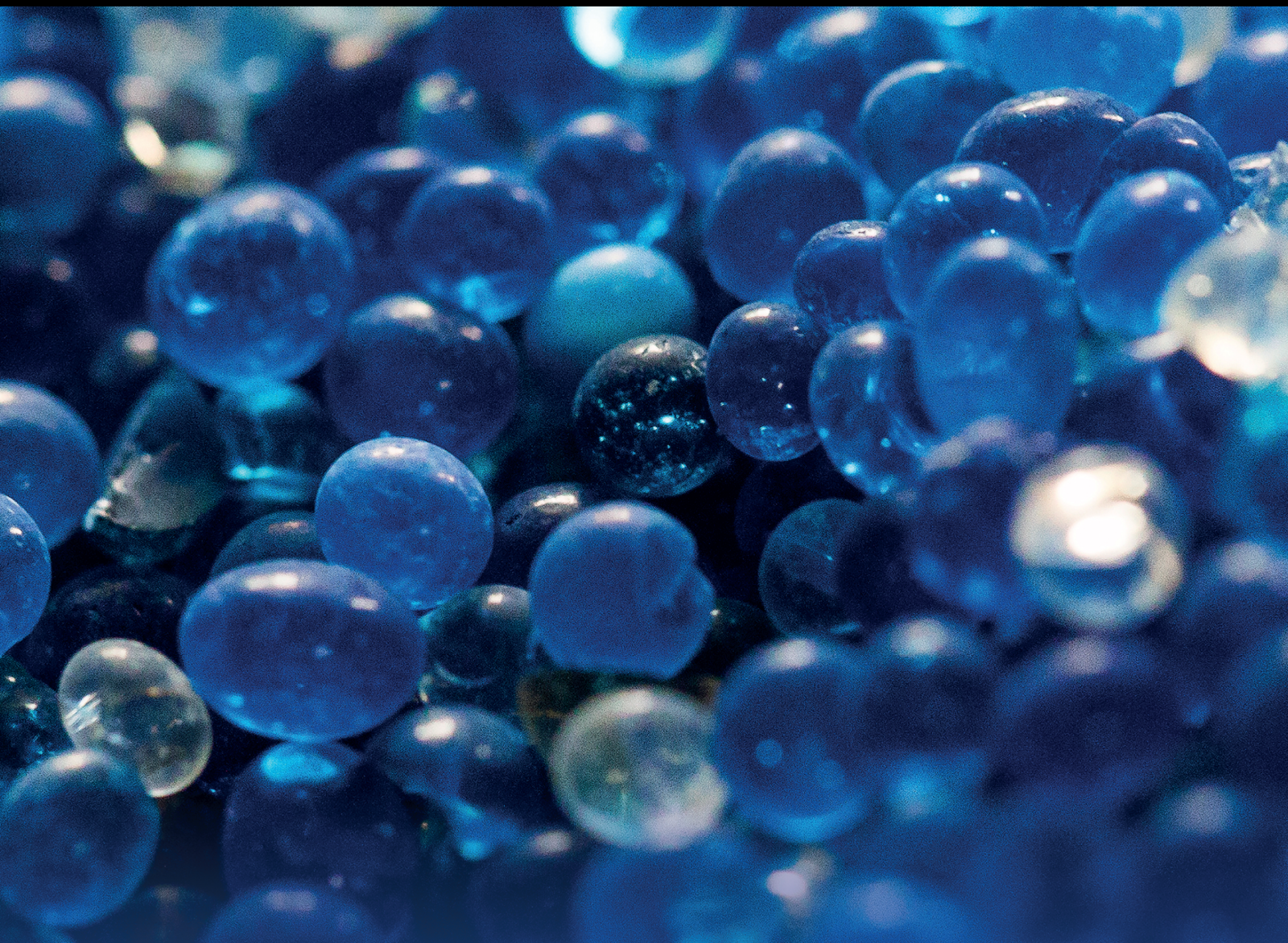


# Synthesis, Characteristics, and Applications of Novel Nanomaterials in Adsorption and Catalysis

Lead Guest Editor: Tien Duc Pham

Guest Editors: Thi Ngoc Mai Pham, Thanh Son Le, and Ngo Nghia Pham





---

**Synthesis, Characteristics, and Applications  
of Novel Nanomaterials in Adsorption and  
Catalysis**

Adsorption Science & Technology

---

**Synthesis, Characteristics, and  
Applications of Novel Nanomaterials in  
Adsorption and Catalysis**

Lead Guest Editor: Tien Duc Pham

Guest Editors: Thi Ngoc Mai Pham, Thanh Son Le,  
and Ngo Nghia Pham



---

Copyright © 2022 Hindawi Limited. All rights reserved.

This is a special issue published in "Adsorption Science & Technology" All articles are open access articles distributed under the Creative Commons Attribution License, which permits unrestricted use, distribution, and reproduction in any medium, provided the original work is properly cited.

# Chief Editor

Ashleigh J. Fletcher , United Kingdom

## Academic Editors

Chinenye Adaobi Igwegbe , Nigeria  
Adrián Bonilla-Petriciolet, Brazil  
Mohammad Hadi Dehghani, Iran  
Tony Hadibarata, Malaysia  
Ming Hua, China  
Muhammad Raziq Rahimi Kooh, Brunei  
Darussalam  
Monoj Kumar Mondal , India  
George Kyzas, Greece  
MU NAUSHAD, Saudi Arabia  
Hai Nguyen Tran , Vietnam  
Walid Oueslati , Tunisia  
Szabolcs Pap , United Kingdom  
Sami-Ullah Rather , Saudi Arabia  
Anjani Ravi Kiran Gollakota , Taiwan  
Eloy S. Sanz P rez , Spain  
Stefano Salvestrini , Italy  
N. Selvaraju , India  
Rangabhashiyam Selvasembian , India  
P. Senthil Kumar , India  
Lingzhi Yang , China

## Advisory Board Member(s)

## Contents

### **N-TiO<sub>2</sub>/g-C<sub>3</sub>N<sub>4</sub> Dual Photocatalysts for Efficient Oxytetracycline Hydrochloride Photodegradation and CO<sub>2</sub> Photoreduction**

Thanh-Binh Nguyen , Thuy Hang Dinh Thi, Kim Hue Dinh Thi, Hien Bui Minh, Ngoc Quynh Nguyen Thi, Duy Vu Ngoc, and Bang Nguyen Dinh  
Research Article (14 pages), Article ID 3057189, Volume 2022 (2022)

### **Adsorption Characteristics of Antibiotic Meropenem on Magnetic CoFe<sub>2</sub>O<sub>4</sub>@Au Nanoparticles**

Thi Ngoc Mai Pham , Thi Hieu Hoang, Thu Phuong Nguyen, Quang Khanh Nguyen, Bach Pham , Quoc Anh Hoang, Tien Duc Pham , Thi Anh Huong Nguyen , Anh Tuan Le , and Duc Thang Pham   
Research Article (10 pages), Article ID 9759759, Volume 2022 (2022)

### **Synthesis of CeO<sub>2</sub>-Fe<sub>2</sub>O<sub>3</sub> Mixed Oxides for Low-Temperature Carbon Monoxide Oxidation**

Chuc Ngoc Pham, Quyen Van Trinh, Dang Van Thai , Nhiem Ngoc Dao , Bac Quang Nguyen , Dung Trung Doan, Hung Bao Le, Vinh Van Nguyen, Lim Thi Duong, and Lam Dai Tran  
Research Article (12 pages), Article ID 5945169, Volume 2022 (2022)

### **Graphene Oxide/Fe<sub>3</sub>O<sub>4</sub>/Chitosan-Coated Nonwoven Polyester Fabric Extracted from Disposable Face Mask for Enhanced Efficiency of Organic Dye Adsorption**

Hoang V. Tran , Nhan T. Hoang, Thu D. Le , Luyen T. Tran , and Hue T. M. Dang  
Research Article (13 pages), Article ID 8055615, Volume 2022 (2022)

### **Characterization of Co<sup>2+</sup>- and Fe<sup>3+</sup>-Codoped TiO<sub>2</sub> Nanomaterials for Photocatalytic Degradation of Organic Pollutants under Visible Light Irradiation**

Nguyen Thi Tuyet Mai, Nguyen Kim Nga , Dang Thi Minh Hue, Ta Ngoc Dung, Huynh Dang Chinh, and Tran Quang Huy   
Research Article (12 pages), Article ID 9193052, Volume 2021 (2021)

### **Preparation and Characterization of Biochar Derived from Agricultural By-Products for Dye Removal**

Phuong Thu Le , Huyen Thuong Bui, Duy Ngoc Le, Thi Hue Nguyen, Le Anh Pham, Hong Nam Nguyen, Quoc Son Nguyen, Thu Phuong Nguyen, Ng#c Trinh Bich, Thi Thuy Duong, Marine Herrmann, Sylvain Ouillon , and Thi Phuong Quynh Le  
Research Article (14 pages), Article ID 9161904, Volume 2021 (2021)

### **Crosslinking, Mechanical Properties, and Antimicrobial Activity of Photocurable Diacrylate Urethane/ZnO-Ag Nanocomposite Coating**

Truc Vy Do , Minh Nguyet Ha , Tuan Anh Nguyen , Hoang Thu Ha , and Thien Vuong Nguyen   
Research Article (8 pages), Article ID 7387160, Volume 2021 (2021)

**Improving SERS Sensing Efficiency and Catalytic Reduction Activity in Multifunctional Ternary Ag-TiO<sub>2</sub>-GO Nanostructures: Roles of Electron Transfer Process on Performance Enhancement**

Mai Quan Doan , Nguyen Ha Anh , Hoang Van Tuan , Nguyen Cong Tu , Nguyen Huu Lam ,  
Nguyen Tien Khi , Vu Ngoc Phan , Pham Duc Thang, and Anh-Tuan Le 

Research Article (13 pages), Article ID 1169599, Volume 2021 (2021)

**Electrochemical Determination of Diclofenac by Using ZIF-67/g-C<sub>3</sub>N<sub>4</sub> Modified Electrode**

Dang Thi Ngoc Hoa, Nguyen Thi Thanh Tu , Le Van Thanh Son, Le Vu Truong Son, Tran Thanh Tam Toan,  
Pham Le Minh Thong, Dao Ngoc Nhiem, Pham Khac Lieu, and Dinh Quang Khieu 

Research Article (14 pages), Article ID 7896286, Volume 2021 (2021)

## Research Article

# N-TiO<sub>2-δ</sub>/g-C<sub>3</sub>N<sub>4</sub> Dual Photocatalysts for Efficient Oxytetracycline Hydrochloride Photodegradation and CO<sub>2</sub> Photoreduction

Thanh-Binh Nguyen <sup>1</sup>, Thuy Hang Dinh Thi,<sup>1,2</sup> Kim Hue Dinh Thi,<sup>1</sup> Hien Bui Minh,<sup>1</sup> Ngoc Quynh Nguyen Thi,<sup>3</sup> Duy Vu Ngoc,<sup>1</sup> and Bang Nguyen Dinh<sup>1</sup>

<sup>1</sup>VNU University of Science, 19 Le Thanh Tong, Hanoi, Vietnam

<sup>2</sup>Vietnam Maritime University, 484 Lach Tray, Hai Phong, Vietnam

<sup>3</sup>Vietri University of Industry, Tien Kien, Phu Tho, Vietnam

Correspondence should be addressed to Thanh-Binh Nguyen; [nguyenthanhbinh@hus.edu.vn](mailto:nguyenthanhbinh@hus.edu.vn)

Received 13 November 2021; Revised 30 March 2022; Accepted 26 April 2022; Published 11 May 2022

Academic Editor: Adrián Bonilla-Petriciolet

Copyright © 2022 Thanh-Binh Nguyen et al. This is an open access article distributed under the Creative Commons Attribution License, which permits unrestricted use, distribution, and reproduction in any medium, provided the original work is properly cited.

A series of  $x\%$  (wt) N-TiO<sub>2-δ</sub>/g-C<sub>3</sub>N<sub>4</sub> composites was synthesized by calcination and hydrothermal methods (labeled  $x$ TiCN,  $x$ : 5, 10, and 15). All composites were characterized by X-ray diffraction, Fourier transform infrared spectroscopy, UV-vis diffuse reflectance spectroscopy, transmission electron microscopy, and X-ray photoelectron spectroscopy. The photocatalytic activity of these composites was evaluated through oxytetracycline hydrochloride (denoted as OTC) photodegradation and CO<sub>2</sub> photoreduction. The  $x$ TiCN composites exhibited higher OTC photodegradation than bulk g-C<sub>3</sub>N<sub>4</sub>. 10TiCN was slightly more active than 5TiCN and 15TiCN, with a photodegradation yield of 97% after 5 h of light irradiation and constant rate of 0.647 h<sup>-1</sup>. For CO<sub>2</sub> photoreduction, it was observed that 5TiCN exhibited the highest activity among the synthesized composites, with 7.0 ppm CH<sub>4</sub> formed. This CH<sub>4</sub> concentration was 7.8 times higher than the concentration formed by bulk g-C<sub>3</sub>N<sub>4</sub> (0.9 ppm). A Z-scheme mechanism was proposed to explain the enhanced photocatalysis by  $x\%$  (wt) N-TiO<sub>2-δ</sub>/g-C<sub>3</sub>N<sub>4</sub> composites. The Z-scheme structure increased redox ability, caused better separation of photogenerated electron-hole pairs, and broadened the light absorption zone of the photocatalysts.

## 1. Introduction

Antibiotics are widely used to control bacterial infections in medical, agricultural, and veterinary sectors [1]. Oxytetracycline hydrochloride (OTC) is a commonly used tetracycline antibiotic. Large amounts of OTC have been released into the environment due to its extensive use [2, 3]. It has a long half-life due to its naphthacene core, persisting in the environment for long periods of time. Its environmental residue, especially in water sources, being carcinogenic, and causing antibiotic resistance in bacteria, is dangerous for human health and the ecosystem [3, 4]. Along with antibiotic water pollution, air pollution has also increased in recent times. With rapid worldwide industrial development, large amounts of CO<sub>2</sub> are released into the atmosphere, causing the greenhouse effect and global warming [5, 6]. Climate change, due to pollution, has caused severe meteorological phenomena, such as typhoons and floods. Thus, CO<sub>2</sub> emission reduction and its environmental remediation are an urgent necessity.

Among different ways to solve these above pollution problems, photocatalysis is an attracted one in recent times [7–12]. The photocatalysis can oxidize OTC to nontoxic compounds [13] and reduce CO<sub>2</sub> to useful chemical compounds, such as CH<sub>4</sub> and CH<sub>3</sub>OH [14], reducing water and air pollution. It is a simple and green process, requiring only light irradiation for catalyst activation. The TiO<sub>2</sub> photocatalyst is commonly used because of its high photocatalytic efficiency, good stability, and nontoxicity [15, 16]. However, it is only activated under 380 nm light irradiation. UV light intensity in the sunlight spectrum is approximately 5%; therefore, the TiO<sub>2</sub> photocatalyst requires a UV light source, increasing the process cost. To overcome this drawback, numerous studies report reducing

the TiO<sub>2</sub> bandgap, activating TiO<sub>2</sub> at longer wavelengths (such as visible light), or combining TiO<sub>2</sub> with narrow bandgap semiconductors. In the first strategy, the TiO<sub>2</sub> oxide is doped with nonmetallic elements (N, F) or transition metals (Fe, Co) [17–22]. In the second method, TiO<sub>2</sub> is combined with other semiconductors, such as CuO, BiOBr, metal Au, Pt, or both [23–29]. When combining with an oxide-owned narrower bandgap energy, the new composite will be activated by a longer light wavelength, such visible light, and prevent electron-hole pair recombination. With metal deposition, the metallic phase conduction band attracts free electrons, reducing the recombination of electron-hole pairs.

Recently, graphitic carbon nitride (g-C<sub>3</sub>N<sub>4</sub>), a nonmetallic photocatalyst, has attracted immense interest [30–36]. Synthesized by facile and cost-effective methods, it exhibits high chemical and thermal stability. In particular, it exhibits potential for antibiotic-photocatalytic degradation in aqueous solutions and CO<sub>2</sub> photoreduction [37, 38]. A low bandgap of 2.7 eV enables their visible-light activation. However, rapid recombination of photogenerated electron-hole pairs is a limitation of the g-C<sub>3</sub>N<sub>4</sub> photocatalyst. The combining of g-C<sub>3</sub>N<sub>4</sub> with other semiconductors to prevent this recombination is an interesting strategy [39].

Among the aforementioned photocatalyst improvement strategies, the construction of a heterojunction between two semiconductors is a promising method. In this structure, the photogenerated electron-hole pairs are separated into different zones, thus preventing recombination and enhancing photocatalytic activity. Further, the carrier transfer behavior has been altered by several photocatalytic mechanisms such as type-I, type-II, and, quite recently, the Z-scheme [40]. Among these mechanisms, the Z-scheme has garnered considerable attention as it not only exhibits electron-hole pair separation in two different zones but also enhances the redox properties. For instance, Guan et al. demonstrated that the activity of 20% LaFeO<sub>3</sub>/BiOBr was ~21.0 and ~1.3 times that of bare LaFeO<sub>3</sub> and BiOBr, respectively [41]. Additionally, in 2022, Cheng's group also revealed that the optimal photocatalyst 20% Bi<sub>4</sub>Ti<sub>3</sub>O<sub>12</sub>/CdS exhibited an activity 1.6 and 3.3 times that of bare CdS and Bi<sub>4</sub>Ti<sub>3</sub>O<sub>12</sub>, respectively [42]. An improved photocatalytic activity was also observed on the Bi<sub>2</sub>O<sub>2</sub>CO<sub>3</sub> photocatalyst [43]. The enhanced composite photoactivity was explained by improved photoexcited carrier separation in the composite. Therefore, with a similar targeted photocatalyst structure, TiO<sub>2</sub>- and g-C<sub>3</sub>N<sub>4</sub>-based composites were also developed, which exhibited positive results. Wang et al. demonstrated that the tetracycline (TCL) photodegradation on TiO<sub>2</sub>@g-C<sub>3</sub>N<sub>4</sub> was 75% and 12% greater than that on TiO<sub>2</sub> and g-C<sub>3</sub>N<sub>4</sub>, respectively [44]. Similarly, for CO<sub>2</sub> photoreduction, Reli et al. showed a twofold increase in CH<sub>4</sub> formation on TiO<sub>2</sub>/g-C<sub>3</sub>N<sub>4</sub> (0.3/1) as compared to g-C<sub>3</sub>N<sub>4</sub> [45]. These studies indicate that along with the nature of coupled semiconductors, the morphology and interface interaction between two semiconductors play an important role in photocatalytic improvement.

In view of the above, this study demonstrates the coupling of TiO<sub>2</sub> and g-C<sub>3</sub>N<sub>4</sub> to obtain heterojunction photocatalysts, x% TiO<sub>2</sub>/g-C<sub>3</sub>N<sub>4</sub>. On the one hand, TiO<sub>2</sub> has the disadvantage

of a large bandgap energy,  $E_g = 3.2$  eV; on the other hand, g-C<sub>3</sub>N<sub>4</sub>, despite having a lower bandgap energy,  $E_g = 2.7$  eV, demonstrates a fast recombination of electron-hole pairs. Therefore, the formation of a heterojunction composite through semiconductor coupling could allow overcoming the disadvantages of each constituent. Additionally, the CB/VB potential position of TiO<sub>2</sub> (-0.17 V/+3.0 V) and g-C<sub>3</sub>N<sub>4</sub> (-1.15 V/+1.5 V) [44] would allow the establishment of a staggered band structure and the formation of a Z-scheme photocatalyst. The hydrothermal method, prevalently employed for tuning the morphology of synthesized compounds, was used to prepare the composite. Subsequently, calcination was conducted to enhance the interaction between TiO<sub>2</sub> and g-C<sub>3</sub>N<sub>4</sub> such as an in situ nitrogen doping into TiO<sub>2</sub>. The photocatalytic activity was estimated through OTC oxidation in the liquid phase. OTC is the most stable compound in the TCL group, and as per our knowledge, no studies on OTC oxidation were reported using this composite type. To further evaluate the synthesized photocatalyst composites, CO<sub>2</sub> photoreduction was also investigated in the gas phase.

## 2. Materials and Methods

**2.1. Materials.** Chemical compounds, melamine (C<sub>6</sub>H<sub>6</sub>N<sub>6</sub>) (Sigma-Aldrich), C<sub>16</sub>H<sub>36</sub>O<sub>4</sub>Ti (Sigma-Aldrich), CH<sub>3</sub>COOH (China), C<sub>2</sub>H<sub>5</sub>OH (China), TiO<sub>2</sub> (Evonik P25), and oxytetracycline hydrochloride (OTC) (Sigma-Aldrich), of analytical purity were used as obtained.

### 2.2. Synthesis of g-C<sub>3</sub>N<sub>4</sub> and N-TiO<sub>2-δ</sub>/g-C<sub>3</sub>N<sub>4</sub> Composites

**2.2.1. Synthesis of g-C<sub>3</sub>N<sub>4</sub> and N-TiO<sub>2</sub>.** Melamine calcination at 550°C, for 3 h, in nitrogen gas medium, was used to synthesize g-C<sub>3</sub>N<sub>4</sub>.

The nitrogen-doped TiO<sub>2</sub> (N-TiO<sub>2</sub>) synthesis was inspired by the work of Viswanath et al. [46]. In this typical procedure, titanium (IV) butoxide in ethanol solution and melamine in hot water-ethanol (1:3 volume ratio) solution were mixed, then stirred for 24 hours and aged for 5 days. The obtained gel was dried and calcined at 400°C for 3 hours.

**2.2.2. Synthesis of N-TiO<sub>2-δ</sub>/g-C<sub>3</sub>N<sub>4</sub>.** Calculated amounts of g-C<sub>3</sub>N<sub>4</sub>, titanium (IV) butoxide, and acetic acid (1:30 in volume) were mixed in a 250 ml beaker, with 15 min magnetic stirring, and autoclaved at 140°C for 12 h. The resulting solution was centrifuged and rinsed several times with ethanol. The solid obtained was oven dried at 60°C for 24 h and calcined at 400°C for 3 h, under nitrogen gas. The x% (wt) N-TiO<sub>2-δ</sub>/g-C<sub>3</sub>N<sub>4</sub> composites were denoted as xTiCN (x: 5, 10, and 15).

### 2.3. Photocatalytic Procedure

**2.3.1. OTC Photodegradation.** Into a beaker containing 100 ml 10 ppm OTC solution (C<sub>0</sub>), g-C<sub>3</sub>N<sub>4</sub> or xTiCN composite (0.1 g) was added with stirring (Figure 1(a)) and left in the dark for 1 h to attain adsorption equilibrium. The mixture was then illuminated with a 200 W LED lamp. Every 1 hour, 5 ml sample was taken, filtered, and analyzed by a

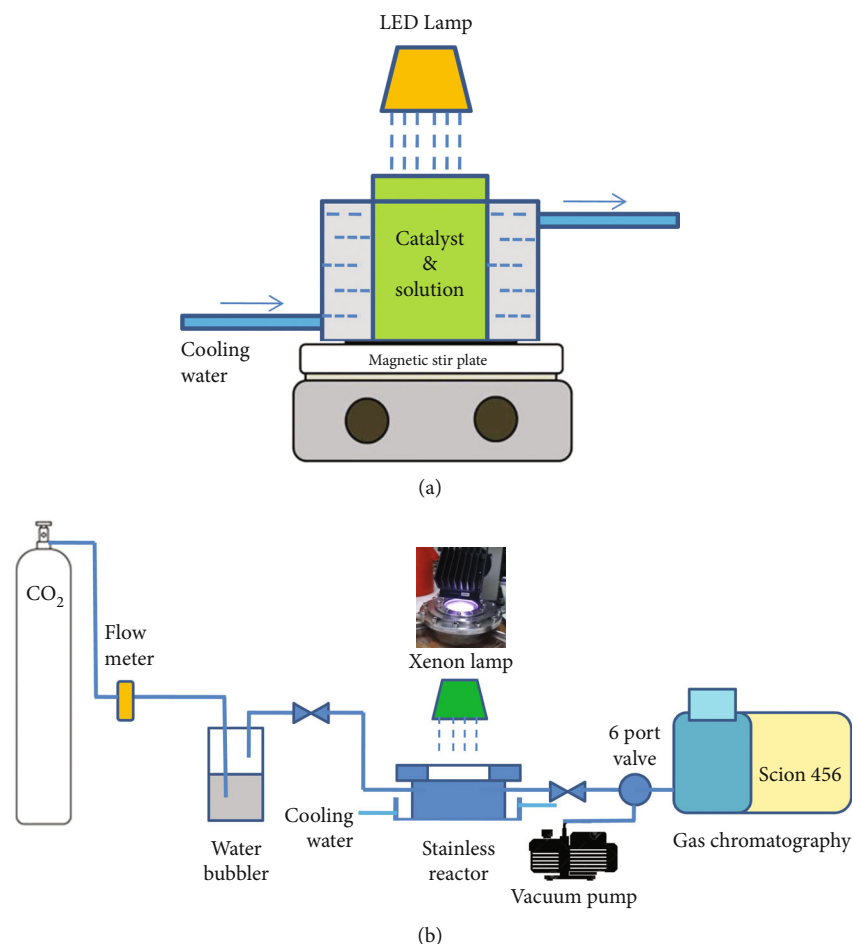


FIGURE 1: Scheme of the photocatalytic reactor used for OTC oxidation (a) and  $\text{CO}_2$  reduction (b).

UV-vis spectrophotometer to detect OTC content ( $C_t$ ) of the reaction mixture. The photostability test was performed 5 times. The separation of the catalyst and the reaction solution was carried out by centrifugation (6000 rpm).

**2.3.2.  $\text{CO}_2$  Photoreduction.** Into a glass beaker (5 cm diameter) containing 15 ml deionized water,  $\text{g-C}_3\text{N}_4$  or  $x\text{TiCN}$  composite (0.1 g) was added. After 15 min stirring, the mixture was evaporated in an oven, at  $70^\circ\text{C}$ , to obtain a well-dried, homogeneously dispersed powder. The catalyst-containing beaker was placed in a handmade closed stainless steel reactor ( $169\text{ cm}^3$  volume), equipped with a 6 cm diameter quartz window, and purged with high-purity (99.999%) 500 ml/min  $\text{CO}_2$  flow for 30 min. The reactor was illuminated with a 150 W Xenon lamp (Newport model 67005) for 18 h. Gaseous products were analyzed using a gas valve system connected to a gas chromatograph, equipped with a thermal conductivity detector and flame ionization detector (TCD-FID) (Scion 456) (Figure 1(b)).

**2.4. Characterizations.** X-ray diffraction (XRD) (Bruker D8), Fourier-transform infrared spectroscopy (FTIR) (8101M Shimadzu),  $\text{N}_2$  adsorption-desorption (TriStar 3000-Micromeritics), UV differential reflectance spectroscopy (UV-DRS) (Jaco V-530), transmission electronic microscopy (TEM, JEM 1400

Plus Jeon), and X-ray photoelectron spectroscopy (XPS) (Thermo Scientific MultiLab 2000) were used to characterize  $\text{g-C}_3\text{N}_4$  and  $x\text{TiCN}$  composites.

### 3. Results and Discussion

**3.1. Structural Characterization.** XRD patterns of  $x\text{TiCN}$  composites are shown in Figure 2(a). The formation of the  $\text{g-C}_3\text{N}_4$  crystalline phase, with a characteristic peak at  $27.8^\circ$ , was observed in all XRD patterns, confirming the  $\text{g-C}_3\text{N}_4$  structure after composite synthesis. Characteristic peaks at  $25.5^\circ$ ,  $38.0^\circ$ ,  $48.1^\circ$ ,  $54.2^\circ$ , and  $62.8^\circ$ , corresponding to the  $\text{TiO}_2$  anatase phase, were observed in the XRD patterns of all composites. In the  $\text{N-TiO}_2$  XRD patterns, a small quantity of the rutile phase was recognized at 2 theta of  $27.5$  and  $36.1^\circ$ . To identify different components, FTIR characterization was carried out, and the spectra are shown in Figure 2(b). In the  $\text{g-C}_3\text{N}_4$  spectrum, the peak at  $802\text{ cm}^{-1}$  was ascribed to the s-triazine bending mode [30]. The peaks at  $1228$  and  $1311\text{ cm}^{-1}$  were attributed to the C-N stretching vibrations [47, 48]. The peaks at  $1392$ ,  $1535$ , and  $1625\text{ cm}^{-1}$  originated from the -C=N stretching vibrations in aromatic rings. The broad band at  $3000\text{--}3500\text{ cm}^{-1}$  corresponded to the stretching vibrations of the absorbed water hydroxyl group (-O-H) and terminal

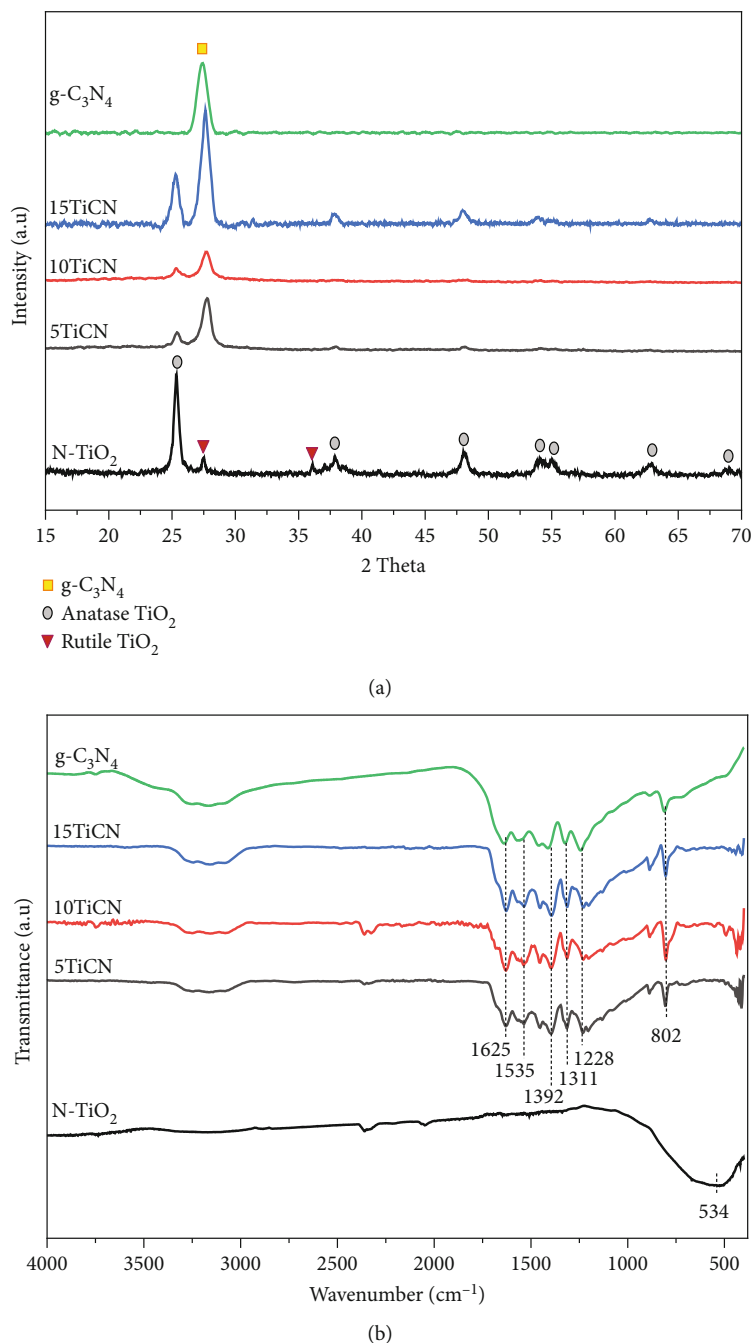


FIGURE 2: XRD patterns (a) and FTIR spectra (b) of  $g\text{-C}_3\text{N}_4$  and  $x\text{TiCN}$  composites.

amino groups ( $-\text{NH}_2$ ) [47, 48]. Finally, the broad peak at  $534\text{ cm}^{-1}$  was attributed to the Ti–O bond vibrations [49].

The light absorption abilities of the composites were analyzed by UV-vis DR spectra. Figure 3(a) shows the UV-vis DR spectra of  $g\text{-C}_3\text{N}_4$  and  $x\text{TiCN}$ . The bandgap energies, calculated using the Kubelka–Munk function (results are shown in Figure 3(b)), were 2.58, 2.60, 2.63, 2.66, and 2.90 eV for  $g\text{-C}_3\text{N}_4$ , 5TiCN, 10TiCN, 15TiCN, and N-TiO<sub>2</sub>, respectively. Increasing the TiO<sub>2</sub> content broadened the composite bandgap energy owing to a greater contribution of the large band gap energy by TiO<sub>2</sub> (3.2 eV) as compared

to  $g\text{-C}_3\text{N}_4$  (2.58 eV). However, generally, all photocatalyst composites could be activated by visible light. The corresponding differential curves of UV-vis DR spectra are displayed in Figure 3(c). The absorption edges ( $\lambda_{\text{abs}}$ ) of pristine TiO<sub>2</sub> (P25) and  $g\text{-C}_3\text{N}_4$  are at wavelengths of 396.3 and 437.5 nm, respectively. In contrast, the  $x\text{TiCN}$  composites exhibit a slight shift of the  $g\text{-C}_3\text{N}_4$  adsorption edge peak to a shorter wavelength, while that of TiO<sub>2</sub> slightly shifts to a longer wavelength. The longer-wavelength-shifted adsorption edge of the TiO<sub>2</sub> constituent is possibly due to nitrogen doping in TiO<sub>2</sub> during the composite synthesis.

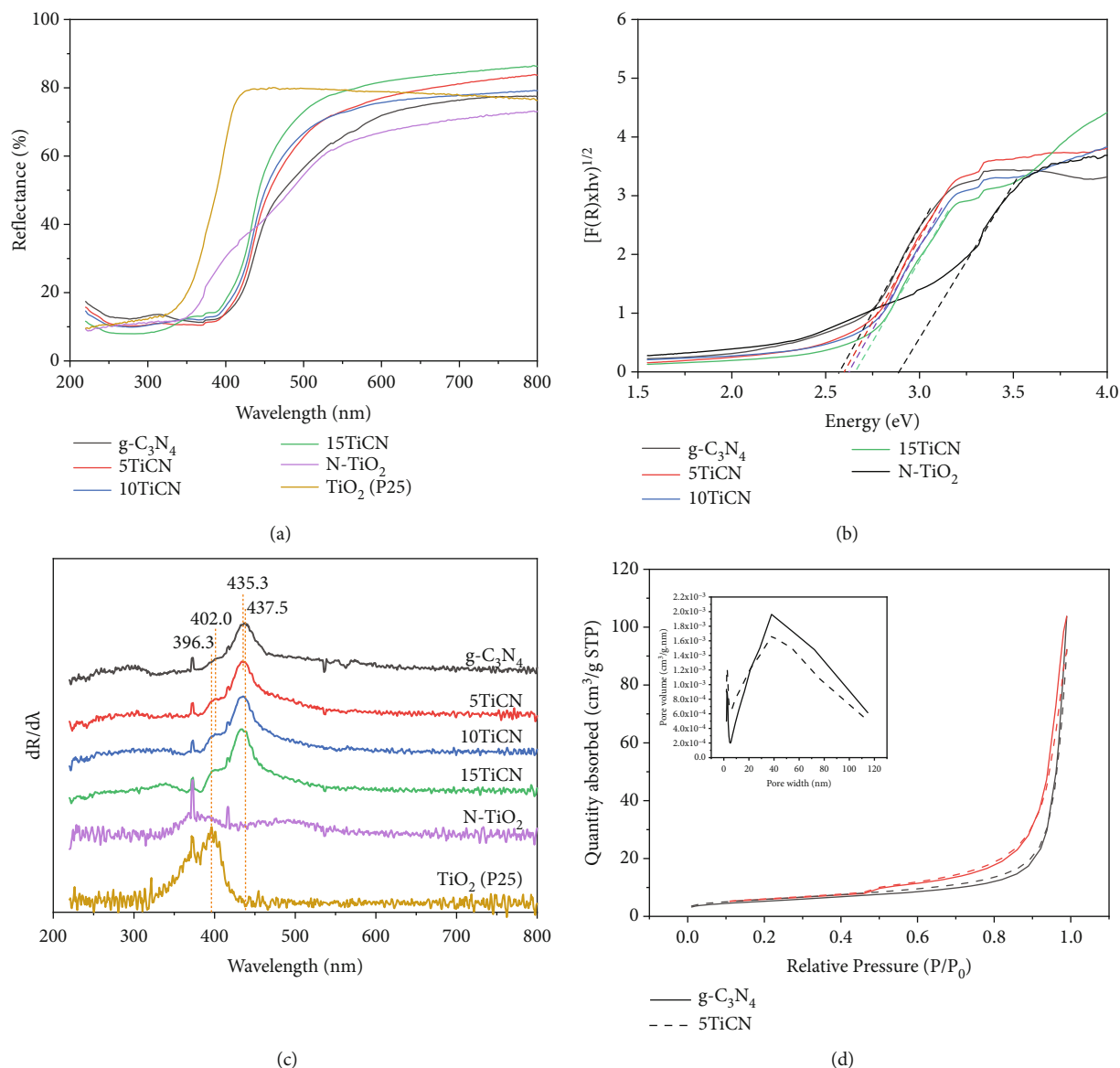


FIGURE 3: UV-vis DR spectra (a), energy bandgap determination by Kubelka–Munk function (b), and its corresponding differential curves (c) of g-C<sub>3</sub>N<sub>4</sub>, N-TiO<sub>2</sub>, and xTiCN composites; N<sub>2</sub> adsorption-desorption isotherms and corresponding pore distribution curves of g-C<sub>3</sub>N<sub>4</sub> (solid line) and 5TiCN composite (dash line) (d).

These observations suggest an interaction between g-C<sub>3</sub>N<sub>4</sub> and TiO<sub>2</sub>, forming in situ-doped N-TiO<sub>2</sub>. In the case of 5TiCN, the observed adsorption edge peaks of TiO<sub>2</sub> and g-C<sub>3</sub>N<sub>4</sub> correspond to wavelengths of 402.0 and 435.3 nm, respectively. Based on the relationship  $E_g = 1240/\lambda_{\text{abs}}$ , the calculated bandgap energies ( $E_g$ ) of TiO<sub>2</sub> and g-C<sub>3</sub>N<sub>4</sub> are 3.08 and 2.85 eV, respectively. For the N-TiO<sub>2</sub> sample prepared by the hydrothermal method, the differential curve of the UV-vis DR spectrum exhibited a single weak and broad peak at 392.5 nm (or  $E_g = 3.16$  eV). This peak is attributed to the adsorption edge of TiO<sub>2</sub>.

The g-C<sub>3</sub>N<sub>4</sub> and 5TiCN composites were selected to characterize its specific surface area, one of the important proper-

ties of heterogeneous catalysis. The results are presented in Figure 3(d). It is observed that two samples show the type-4 isotherms with H3 hysteresis loop, which indicate the presence of a mesopore. This is suitable with the obtained pore distribution curves. The BET surface areas are 18 and 20 m<sup>2</sup>/g for g-C<sub>3</sub>N<sub>4</sub> and 5TiCN, respectively. Hence, the composite preparation did not seem to change the g-C<sub>3</sub>N<sub>4</sub> structure.

The interaction between the TiO<sub>2</sub> and g-C<sub>3</sub>N<sub>4</sub> phases is better understood from the TEM images presented in Figure 4. It is observed that the TiO<sub>2</sub> particles (dark areas in Figures 4(a) and 4(b)) were formed in various sizes and shapes. Some TiO<sub>2</sub> particles were deposited on the g-C<sub>3</sub>N<sub>4</sub> layer (e.g., position of cycle 1), while the others were covered by g-C<sub>3</sub>N<sub>4</sub> multisheets, forming a core-shell structure (e.g.,

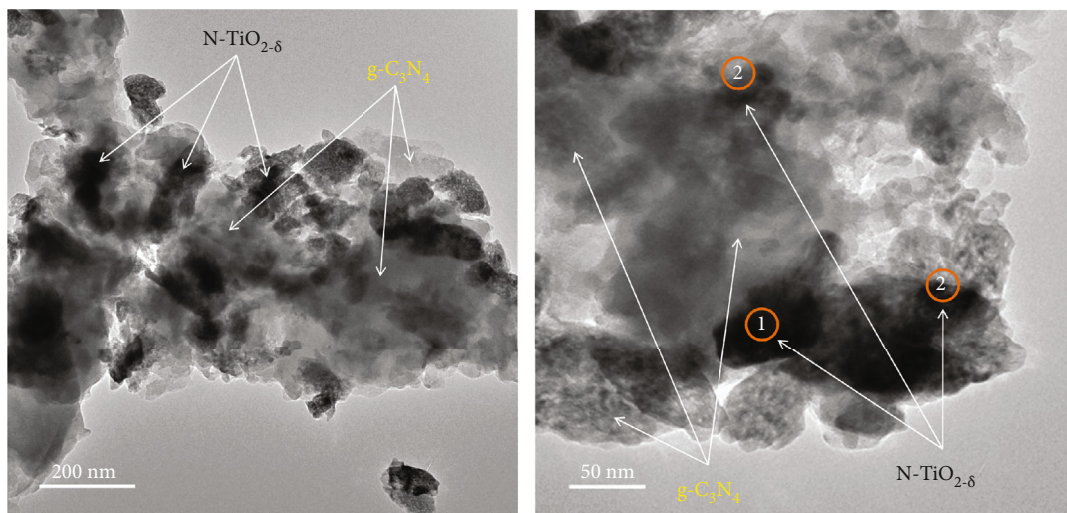


FIGURE 4: TEM images of 5TiCN.

position of cycle 2), thereby enhancing the interaction surface between the  $\text{TiO}_2$  and  $g\text{-C}_3\text{N}_4$  phases.

The elemental composition and oxidation state of the catalyst influence catalytic performance. Therefore, the 5TiCN composite was characterized using XPS, as shown in Figure 5.

Three peaks at binding energies of 458.5, 459.1, and 464.3 eV, corresponding to orbitals  $\text{Ti}^{4+}2p_{3/2}$ ,  $\text{Ti}^{3+}2p_{1/2}$ , and  $\text{Ti}^{4+}2p_{1/2}$ , respectively, were observed in the  $\text{Ti}2p$  high-resolution spectrum [50, 51]. As reported by Jia et al., binding energies of two prominent peaks (at 458.5 and 464.3 eV) exhibited 0.2 eV shifts compared to spectral peaks of pure  $\text{TiO}_2$ . This could be due to the substitution of  $\text{O}^{2-}$  by  $\text{N}^{3-}$ , leading to the formation of N-Ti-O bonds [52]. This indicated N doping of  $\text{TiO}_2$  during composite synthesis, decreasing the  $\text{TiO}_2$  bandgap energy, leading to visible-light activation [17, 18]. The small peak of  $\text{Ti}^{3+}2p_{1/2}$  confirmed oxygen vacancies in  $\text{TiO}_2$  [51]. Hence,  $\text{TiO}_{2-\delta}$  is a more accurate molecular formula than  $\text{TiO}_2$ .

Deconvolution peaks for the O1s spectrum exhibited two peaks at 531 and 532 eV, assigned to O-H of absorbed water and the Ti-O bond [53], respectively. N1s spectrum exhibited three peaks at 398.6, 399.7, and 400.8 eV, ascribed to the  $\text{sp}^2\text{C}$  of C-N=C, tertiary N of N-(C)<sub>3</sub> group, and N-C=N bonds, respectively. The C1s spectrum exhibited three peaks at 284.9, 286.3, and 288.2 eV, corresponding to C-C, C-NH<sub>2</sub>, and N-C=N bonds, respectively [53, 54].

### 3.2. Evaluation of Photocatalytic Activity

**3.2.1. Photooxidation of OTC.** Before performing the photocatalytic test, the adsorption equilibria were carried out (Figure 6(a)). The results demonstrated that all composites reached rapidly the adsorption equilibrium after only about 15 minutes, while 60 minutes was required for N-TiO<sub>2</sub>. The calculation indicated that the equilibrium adsorption quantities of OTC at 60 min were 11%, 14%, 17%, 12%, and 88% for  $g\text{-C}_3\text{N}_4$ , 5TiCN, 10TiCN, 15TiCN, and N-TiO<sub>2</sub>, respec-

tively. It remarked that there was a strong adsorption phenomenon of OTC on N-TiO<sub>2</sub>.

The photocatalytic activity of the catalysts was investigated through OTC photodegradation and CO<sub>2</sub> photoreduction. Figure 6(b) shows the photodegradation of OTC and UV-vis spectra of OTC solutions during test time, using 5TiCN. OTC concentrations were calculated from the absorbance intensity of UV-vis spectra at the 357 nm wavelength.

Figure 7 shows OTC photodegradation efficiency and kinetics. All composite photocatalysts exhibited excellent OTC degradation activity, with yields of 93%, 97%, and 92% for 5TiCN, 10TiCN, and 15TiCN, respectively. For N-TiO<sub>2</sub>, the adsorption phenomenon dominated, reaching 90% adsorbed OTC quantity after 1 hour of equilibrium, and the efficiency of OTC removal increased only ~4% when turning on the light for 5 hours. Hence, the photocatalytic reaction on N-TiO<sub>2</sub> was negligible. This behavior was possibly due to the formation of the melon structure formed during the synthesis, besides the process of nitrogen doping on  $\text{TiO}_2$  [55]. The melon structure, which is not a semiconductor, could cover  $\text{TiO}_2/\text{N-TiO}_2$  particles, preventing the photocatalytic process. A blank test (without catalyst) was also carried out for comparison. In the blank test, the OTC concentration decreased about 9% by photolysis. Hence, after 5 h light irradiation, the 10TiCN composite was slightly more active than those of 5TiCN and 15TiCN. It is noted that the adsorption phenomenon contributes a small part in the conversion calculation, only 14% in the case of 5TiCN as mentioned in the above adsorption equilibrium study. For these OTC conversion reactions, reaction kinetics were described by the following equation [56]:

$$\ln\left(\frac{C_0}{C_t}\right) = kt + \ln\left(\frac{C_0}{C_0'}\right), \quad (1)$$

where  $C_0$ ,  $C_0'$ , and  $C_t$  are the initial, equilibrium, and time  $t$  concentrations of OTC during the test, respectively. Rate

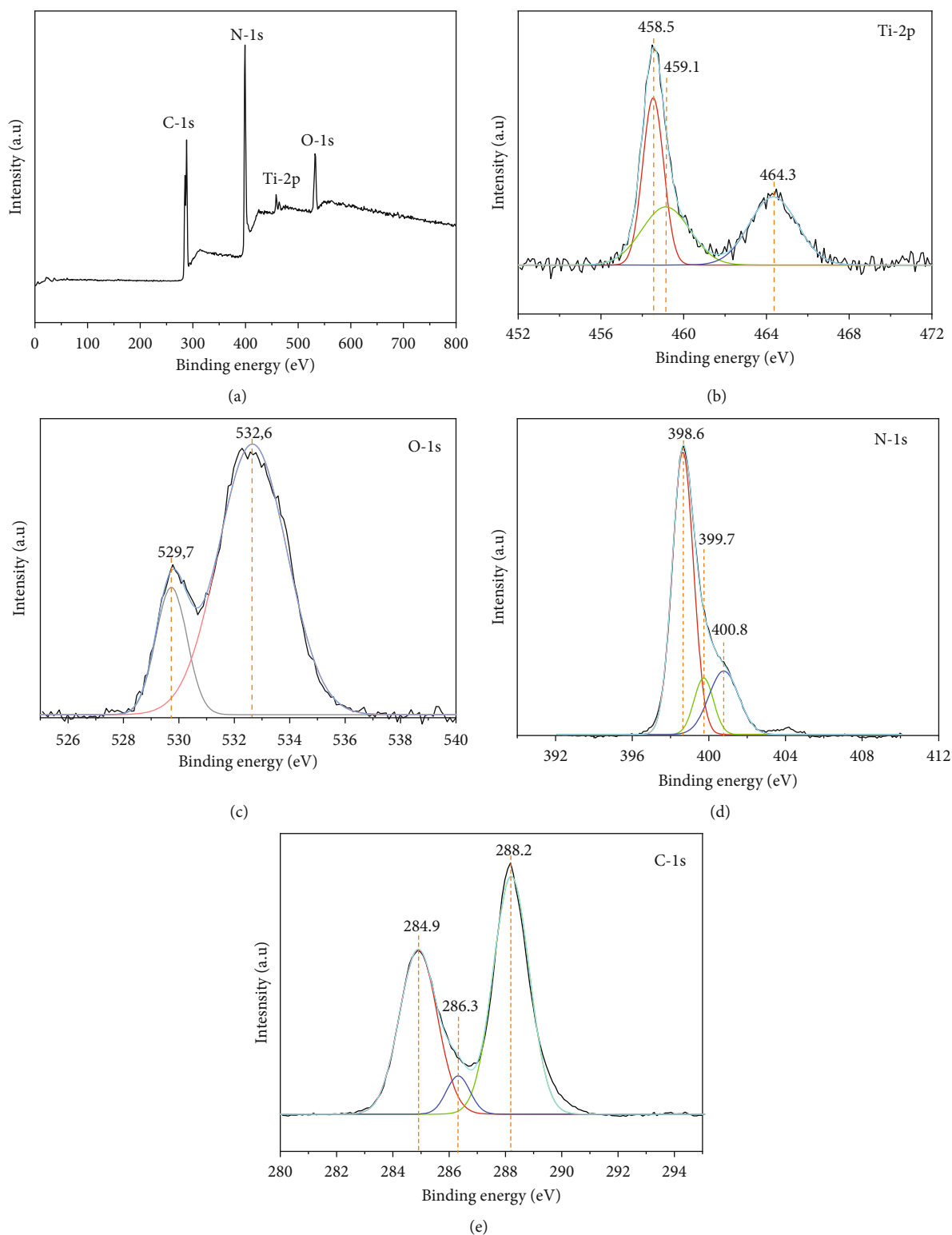


FIGURE 5: X-ray photoelectron spectra of 5TiCN: (a) survey spectra; (b) high-resolution spectra of Ti2p, (c) high-resolution spectra of O1s; (d) high-resolution spectra of N1s; (e) high-resolution spectra of C1s.

constants ( $k$ ) were 0.389, 0.457, 0.647, and 0.451  $\text{h}^{-1}$  for  $\text{g-C}_3\text{N}_4$ , 5TiCN, 10TiCN, and 15TiCN, respectively (from fitted lines in Figure 7(b)). The reaction kinetic on  $\text{N-TiO}_2$  was not investigated as the catalytic activity was negligible

with respect to the adsorption phenomenon. Based on rate constant values, composite activities followed the following order:  $10\text{TiCN} > 5\text{TiCN} \approx 15\text{TiCN} > \text{g-C}_3\text{N}_4$ . The rate constant of 10TiCN was approximately 1.7 times that of  $\text{g-C}_3\text{N}_4$ .

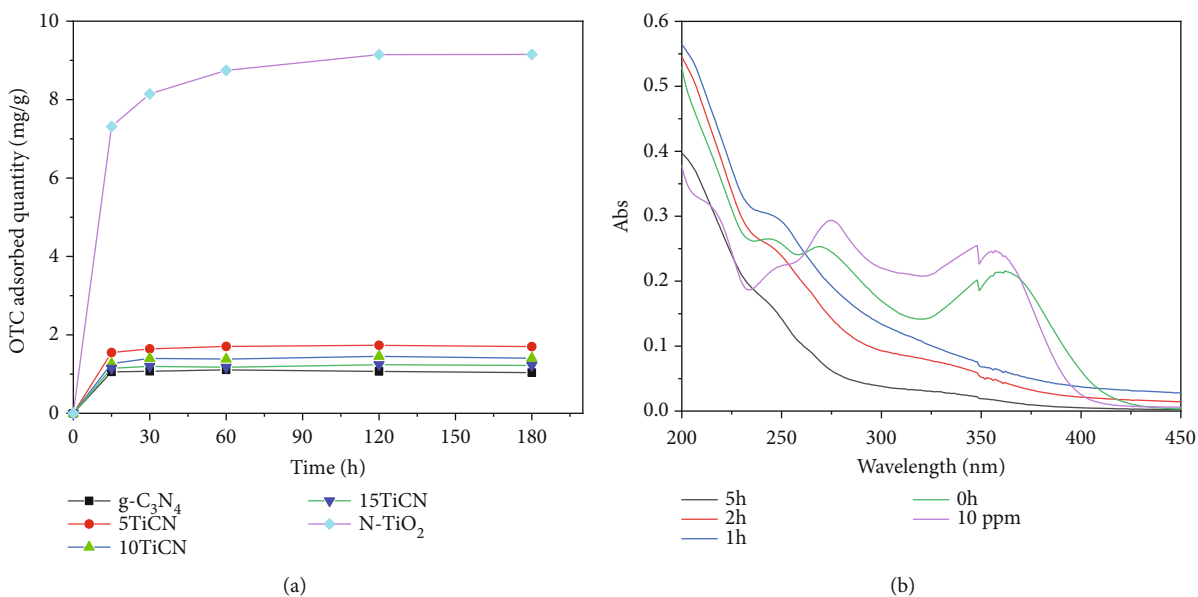


FIGURE 6: OTC adsorption equilibrium (a) on  $x$ TiCN and UV-vis spectra of OTC during test time on 5TiCN composite (b).

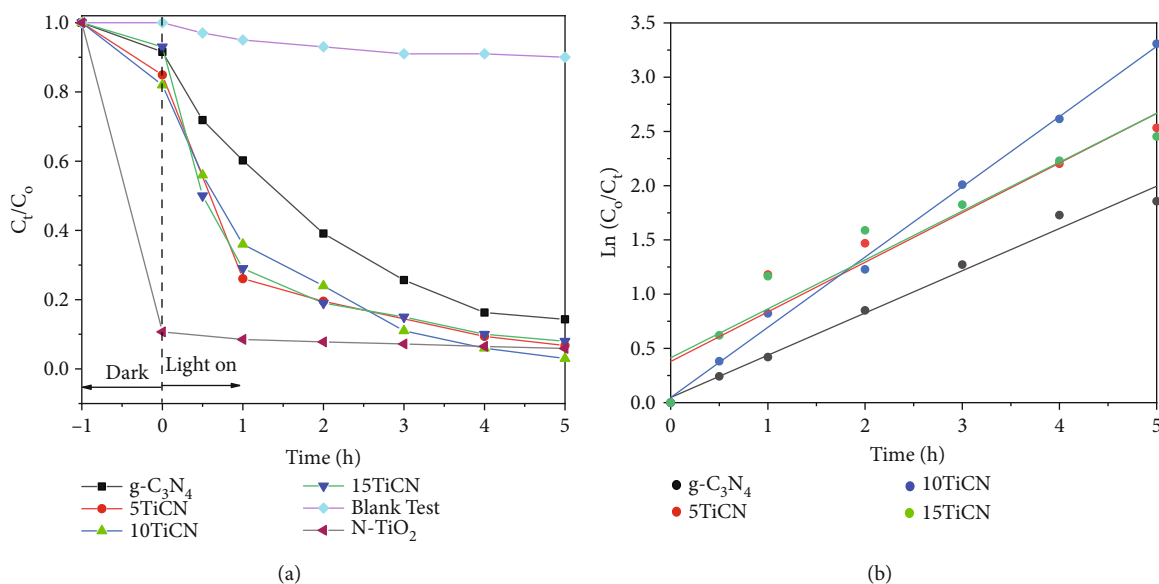


FIGURE 7: (a) Photodegradation efficiency of OTC on  $x$ TiCN composites versus irradiation time and (b) kinetic of OTC degradation reaction on  $x$ TiCN composites.

There are no reports of OTC photodegradation on TiO<sub>2</sub>-g-C<sub>3</sub>N<sub>4</sub> composites, while there are very few reports on tetracycline (TCL) photodegradation using such composites. Wang's research group reported 20 ppm TCL solution photodegradation using composites, such as TiO<sub>2</sub>@g-C<sub>3</sub>N<sub>4</sub> heterojunction, TiO<sub>2</sub>@g-C<sub>3</sub>N<sub>4</sub> core-shell quantum heterojunction, and TiO<sub>2-x</sub>/ultrathin g-C<sub>3</sub>N<sub>4</sub>/TiO<sub>2-x</sub> direct Z-scheme heterojunction [44, 57, 58]. TCL photodegradation rate on the TiO<sub>2</sub>@g-C<sub>3</sub>N<sub>4</sub> core-shell quantum heterojunction composite was 2 and 2.3 times higher than those on TiO<sub>2</sub> and bulk g-C<sub>3</sub>N<sub>4</sub>, respectively. Photoactivity of TiO<sub>2-x</sub>/ultrathin g-C<sub>3</sub>N<sub>4</sub>/TiO<sub>2-x</sub> direct Z-scheme heterojunction system was 20.1 and

1.3 times higher than those of TiO<sub>2</sub> and g-C<sub>3</sub>N<sub>4</sub>, respectively. Wang et al. reported a 3 times higher TCL degradation rate on N-TiO<sub>2</sub>/O-doped N-vacancy g-C<sub>3</sub>N<sub>4</sub> than on N-vacancy g-C<sub>3</sub>N<sub>4</sub> [59]. Rao et al. reported a 4.4 times higher rate constant of 10 ppm TCL solution photodegradation using a hierarchical structure of anatase-rutile TiO<sub>2</sub>/g-C<sub>3</sub>N<sub>4</sub> (ARC), compared to g-C<sub>3</sub>N<sub>4</sub> [60].

In general, the TiO<sub>2</sub>-g-C<sub>3</sub>N<sub>4</sub> heterojunction structure improved photoactivity remarkably compared to those of bulk TiO<sub>2</sub> and g-C<sub>3</sub>N<sub>4</sub>. OTC photodegradation yield reached up to 97%, with a 1.7 times higher rate constant with 10TiCN than with g-C<sub>3</sub>N<sub>4</sub>.

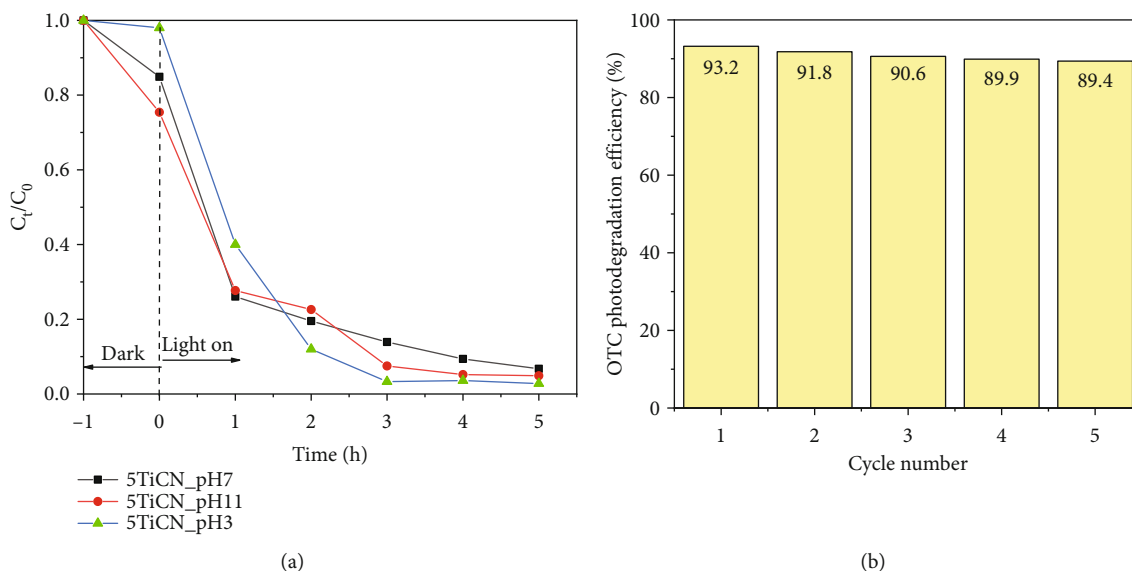


FIGURE 8: Photodegradation efficiency of OTC in function of pH (a) and photostability test on 5TiCN (b).

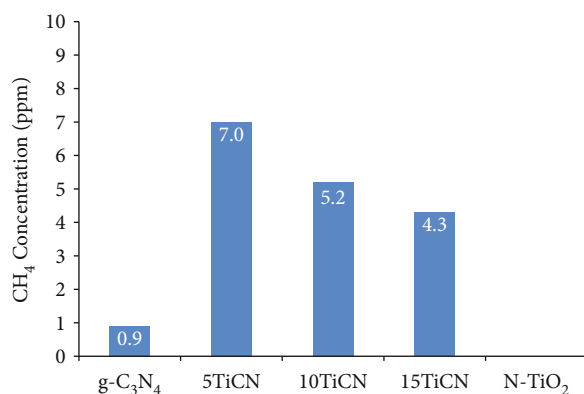


FIGURE 9:  $\text{CH}_4$  concentration on  $\text{g-C}_3\text{N}_4$  and  $x\text{TiCN}$  composite.

The influence of pH on the photoactivity was evaluated. The researches focused on 5TiCN (Figure 8(a)). After 5 hours of irradiation, the photoactivity at pH 11 and 5 was slightly improved, in comparison with pH 7. In the study of Yu et al., the isoelectric point of  $\text{g-C}_3\text{N}_4$  was about pH 5 [61]. It means that the  $\text{g-C}_3\text{N}_4$  surface charge is positive at  $\text{pH} < 5$  and negative at  $\text{pH} > 5$ . The OTC has the  $\text{pK}_{a1} = 3.22$ ,  $\text{pK}_{a2} = 7.68$ , and  $\text{pK}_{a3} = 8.94$  [62]. Therefore, the OTC exhibited a positive charge at  $\text{pH} < 3.22$  in the form of  $\text{H}_3\text{TC}^+$  and negative one at  $\text{pH} > 9$  in the main form of  $\text{OTC}^{2-}$ . Thus, the charges on the  $\text{g-C}_3\text{N}_4$  surface and OTC molecules in experimental pH conditions are the same, which prevent adsorption of OTC on the  $\text{g-C}_3\text{N}_4$  surface by electrostatic repulsion force. That could explain why the pH 3 and pH 7 did not influence strongly on the OTC conversion as observed.

The stability tests were carried out for the 5TiCN composite (Figure 8(b)). The OTC conversion decreased from 93.4% to 89.4% after 5 cycles. This is the promising result in an application view.

**3.2.2. Photoreduction of  $\text{CO}_2$ .** To investigate the dual photocatalytic behavior of  $\text{N-TiO}_{2-6}/\text{g-C}_3\text{N}_4$  composites, they were used in the photoreduction of  $\text{CO}_2$  by  $\text{H}_2\text{O}$  in the gaseous phase (Figure 9). Concentration of  $\text{CH}_4$  (the only product detected) was monitored to analyze the photocatalytic behavior of the synthesized composites. 5TiCN exhibited the highest activity, with 7.0 ppm  $\text{CH}_4$  concentration, followed by 10TiCN (5.2 ppm  $\text{CH}_4$ ), 15TiCN (4.3 ppm  $\text{CH}_4$ ), and  $\text{g-C}_3\text{N}_4$  (0.9 ppm  $\text{CH}_4$ ). No product was detected in the N-TiO<sub>2</sub> test. As mentioned in the OTC photooxidation results above, this low photoactivity of N-TiO<sub>2</sub> could be explained by the formed melon structure that covered  $\text{TiO}_2/\text{N-TiO}_2$  particles and possibly the lower CB potential position of N-TiO<sub>2</sub> than the standard reduction potential of  $\text{CO}_2/\text{CH}_4$  [55]. The detected  $\text{CH}_4$  concentration was quite low over  $\text{g-C}_3\text{N}_4$ . Thus, the test was performed three times, and average value was taken. Hence, the  $\text{CH}_4$  concentration was 7.8 times higher for 5TiCN (composite exhibiting maximum photocatalysis) than for pristine  $\text{g-C}_3\text{N}_4$ .

There are very few reports on photoreduction using a photocatalyst formed by  $\text{TiO}_2$  and  $\text{g-C}_3\text{N}_4$  [45, 63–69].  $\text{CO}_2$  photoreduction in the gaseous phase [45, 63–65] and liquid phase [66–69] has been reported. Gas phase studies, with  $\text{CH}_4$  and CO products, indicate better photocatalytic activity for the  $\text{TiO}_2$ - $\text{g-C}_3\text{N}_4$ -combined photocatalyst, compared to bulk  $\text{TiO}_2$  and  $\text{g-C}_3\text{N}_4$ . Zhou et al. reported a 4 times higher CO formation on  $\text{g-C}_3\text{N}_4$ -N-TiO<sub>2</sub> (14.73  $\mu\text{mol}$ ) than on P25 ( $\text{TiO}_2$ ) [63]. In liquid phase photoreductions, besides  $\text{CH}_4$  and CO, other oxygenated hydrocarbons ( $\text{CH}_3\text{OH}$ ,  $\text{HCOOH}$ , and  $\text{CH}_3\text{COOH}$ ) are formed.  $\text{TiO}_2$ - $\text{g-C}_3\text{N}_4$ -combined photocatalysts exhibit also higher photoactivity compared to single-phase  $\text{TiO}_2$  or  $\text{g-C}_3\text{N}_4$ . Badii et al. reported an 11.3  $\mu\text{mol}\cdot\text{g}^{-1}\cdot\text{h}^{-1}$   $\text{CH}_3\text{OH}$  formation for  $\text{g-C}_3\text{N}_4/\text{TiO}_2$ , which was 5 and 10 times higher than those for  $\text{g-C}_3\text{N}_4$  and P-25 ( $\text{TiO}_2$ ), respectively [66]. Lu et al. reported a 283.9  $\mu\text{mol}\cdot\text{h}^{-1}\cdot\text{g}^{-1}$  CO formation for 2D  $\text{g-C}_3\text{N}_4/$

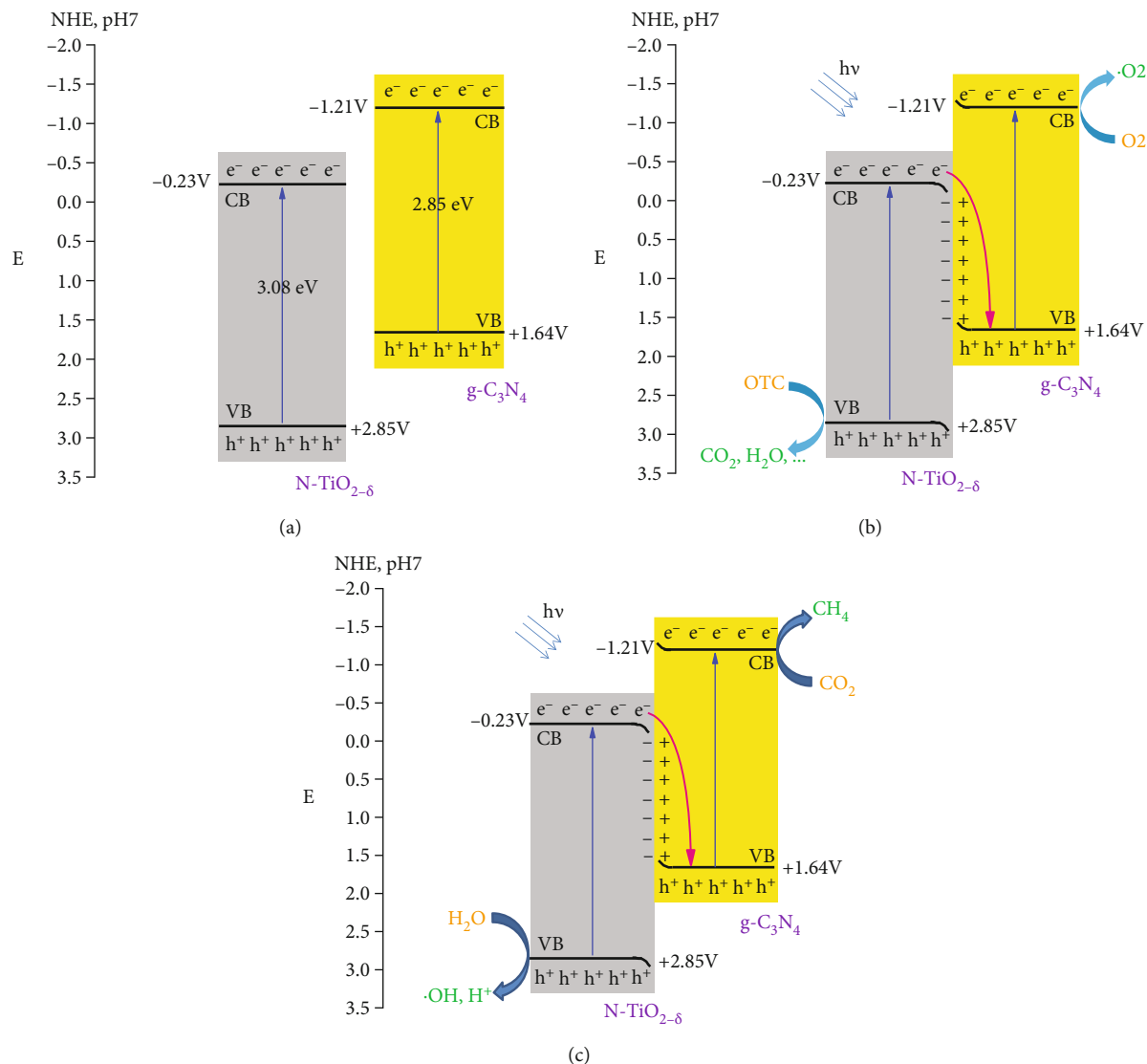


FIGURE 10: Schematic illustrations of the energy band structures of N-TiO<sub>2-δ</sub> and g-C<sub>3</sub>N<sub>4</sub> before contact (a), N-TiO<sub>2-δ</sub>/g-C<sub>3</sub>N<sub>4</sub> heterojunction composite for OTC photooxidation mechanism (b), and CO<sub>2</sub> photoreduction mechanism (c).

TiO<sub>2</sub>, which was 292.2, 6.8, and 5.7 times higher than those for TiO<sub>2</sub>, bulk g-C<sub>3</sub>N<sub>4</sub>, and mechanically mixed TiO<sub>2</sub>/g-C<sub>3</sub>N<sub>4</sub>, respectively [67]. These results cannot be compared due to different experimental conditions. However, all studies indicate higher photoactivity using TiO<sub>2</sub>-g-C<sub>3</sub>N<sub>4</sub>-combined photocatalysts. In this study, CH<sub>4</sub> production on 5TiCN was 7.8 times higher than that on bulk g-C<sub>3</sub>N<sub>4</sub>.

**3.2.3. Photocatalytic Mechanism.** An outstanding photocatalytic activity was exhibited by the *x*TiCN composites during OTC photodegradation and CO<sub>2</sub> photoreduction as compared to the pristine g-C<sub>3</sub>N<sub>4</sub> and N-TiO<sub>2</sub>. Hence, the coupling mechanism of g-C<sub>3</sub>N<sub>4</sub> and TiO<sub>2</sub> is worth investigating. From the UV-vis DR spectrum, the semiconductor conduction/valance edge energies ( $E_{CB}/E_{VB}$ ) can be calculated using the electro-

negativity theory [70]. According to this theory, we have the following empirical formulas:

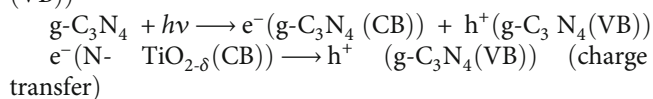
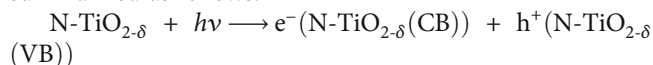
$$E_{CB} = X - E^e - 0.5E_g, E_{VB} = E_{CB} + E_g, \quad (2)$$

where  $X$ ,  $E^e$ , and  $E_g$  are the semiconductor electronegativity (5.81 eV for TiO<sub>2</sub> [71] and 4.72 eV for g-C<sub>3</sub>N<sub>4</sub> [30]), free electron energy corresponding to the hydrogen scale (4.5 eV), and semiconductor bandgap energy, respectively. As determined above from the differential curve of the UV-vis DR spectrum for 5TiCN, the bandgap energies are 3.08 and 2.85 eV, respectively, for the N-TiO<sub>2-δ</sub> and g-C<sub>3</sub>N<sub>4</sub> constituents. Using equation (2),  $E_{CB}/E_{VB}$  is -0.23 V/+2.85 V for N-TiO<sub>2-δ</sub> and -1.21 V/+1.64 V for g-C<sub>3</sub>N<sub>4</sub> (-0.14/+2.76 for separately synthesized N-TiO<sub>2</sub>). With these calculated  $E_g$  and  $E_{CB}/E_{VB}$  values, the

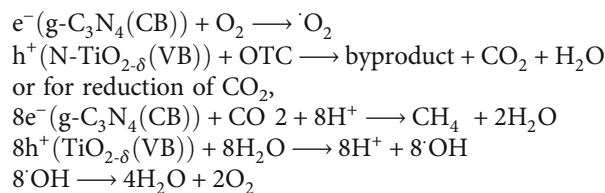
energy band diagram before the coupling of the N-TiO<sub>2-δ</sub> and g-C<sub>3</sub>N<sub>4</sub> phases is presented in Figure 10(a). As thoroughly discussed by Yang [70], when coupling two semiconductors, the built-in electric field formation and photoexcited carrier transfer occur by different routes depending on the semiconductor types, their Fermi level, and CB/VB potential positions. In x TiCN composites, N-TiO<sub>2</sub> and g-C<sub>3</sub>N<sub>4</sub> behave as n-type semiconductors [72, 73], and thus, their Fermi level is near the top conduction edge energy. As the N-TiO<sub>2-δ</sub> Fermi level is higher than that of g-C<sub>3</sub>N<sub>4</sub>, spontaneous electron diffusion from N-TiO<sub>2-δ</sub> to g-C<sub>3</sub>N<sub>4</sub> occurs during their coupling and generates a built-in electric field with positive charge accumulation in the g-C<sub>3</sub>N<sub>4</sub> interface zone and a negative one in the N-TiO<sub>2-δ</sub> interface zone. This diffusion is gradually suppressed by the built-in electric field itself, and finally, a thermal equilibrium state is established in the N-TiO<sub>2-δ</sub>/g-C<sub>3</sub>N<sub>4</sub> heterojunction [70, 74]. On irradiating the composite, photogenerated electron (e<sup>-</sup>) and hole (h<sup>+</sup>) pairs formed on the CB and VB of each constituent. Subsequently, the built-in electric field promoted the photogenerated electrons on the CB of N-TiO<sub>2-δ</sub> to the VB of g-C<sub>3</sub>N<sub>4</sub>. This transfer is displayed in Figures 10(b) and 10(c) and is well-known as the Z-scheme mechanism. In this system, the charge transfer between two phases caused the separation of photogenerated electrons and holes into different zones—electrons in the CB of g-C<sub>3</sub>N<sub>4</sub> and holes in the VB of TiO<sub>2</sub>—preventing their recombination or, simply put, prolonging their lifetime. Notably, this type of charge transfer enriched the photogenerated electrons on the negative CB of g-C<sub>3</sub>N<sub>4</sub> and photogenerated holes on the positive VB of TiO<sub>2</sub>, thereby strengthening the redox property of the composite. Additionally, a low bandgap of g-C<sub>3</sub>N<sub>4</sub> broadened the light absorption region and improved the light utilization efficiency. All these factors contributed to the photocatalytic enhancement of N-TiO<sub>2-δ</sub>/g-C<sub>3</sub>N<sub>4</sub> composites.

Note that the type-II and Z-scheme mechanisms entail a similar photocatalyst composite structure. However, in the type-II mechanism, reduction takes place on the CB of the semiconductor with a less negative CB potential. Hence, for the xTiCN composite, if the type-II mechanism had occurred, the CO<sub>2</sub> would have been reduced on the CB of the N-TiO<sub>2-δ</sub> constituent. This is unlikely as the reduction potential of the N-TiO<sub>2-δ</sub> constituent (-0.23 V) is less negative than that of the CO<sub>2</sub>/CH<sub>4</sub> (-0.24 V) [14]. Nevertheless, the obtained experimental results show a remarkably higher CH<sub>4</sub> content formation than that of bare g-C<sub>3</sub>N<sub>4</sub>. This evidence suggests that the xTiCN photocatalyst composites entail the Z-scheme mechanism. It is also found that CO<sub>2</sub> photoreduction could not take place on separately synthesized N-TiO<sub>2</sub> as its CD potential position (-0.14 V) is less negative than that of CO<sub>2</sub>/CH<sub>4</sub> (-0.24 V).

The photogenerated electron-hole pair transfers are summarized as follows:



Then, for oxidation of OTC,



## 4. Conclusions

Here, x% (wt) N-TiO<sub>2-δ</sub>/g-C<sub>3</sub>N<sub>4</sub> composites were synthesized, and their textural and structural properties were analyzed by XRD, FTIR, UV-DRS, TEM, and XPS. All composites showed better activity than bulk g-C<sub>3</sub>N<sub>4</sub> towards OTC photodegradation and CO<sub>2</sub> photoreduction. OTC photodegradation yields were higher for the composites (93%, 97%, and 92%, on 5TiCN, 10TiCN, and 15TiCN, respectively) than for bulk g-C<sub>3</sub>N<sub>4</sub> (86%). Among these catalysts, the 10TiCN showed the highest rate constant of 0.647 h<sup>-1</sup>. In CO<sub>2</sub> photoreduction, CH<sub>4</sub> was the only product detected. CH<sub>4</sub> concentrations of 0.9, 7.0, 5.2, and 4.3 ppm were detected using bulk g-C<sub>3</sub>N<sub>4</sub>, 5TiCN, 10TiCN, and 15TiCN, respectively. CH<sub>4</sub> formation of 5TiCN was 7.8 times higher than that of bulk g-C<sub>3</sub>N<sub>4</sub>. Enhanced composite photoactivities were attributed to their Z-scheme mechanism. With this structure, charge transfer between N-TiO<sub>2-δ</sub> (CB) and g-C<sub>3</sub>N<sub>4</sub> (VB) occurred, leading to recombination prevention of photogenerated electron-hole pairs and stronger redox abilities. The interesting obtained result above indicates the promising novel dual photocatalysts. Tuning composite morphology (e.g., specific surface area and porosity) and contact surface area between components (e.g., good dispersion phase and core-shell system) could enhance photoactivity of x% (wt) N-TiO<sub>2-δ</sub>/g-C<sub>3</sub>N<sub>4</sub> further.

## Data Availability

The data used to support the findings of this study are included within the article.

## Conflicts of Interest

The authors declare that there is no conflict of interest regarding the publication of this paper.

## Acknowledgments

This research is funded by the Vietnam National Foundation for Science and Technology Development (NAFOSTED) under grant number 104.05-2017.39.

## References

- [1] R. Dagherir and P. Drogui, "Tetracycline antibiotics in the environment: a review," *Environmental Chemistry Letters*, vol. 11, no. 3, pp. 209–227, 2013.
- [2] K. Kummerer, "Antibiotics in the aquatic environment - a review - part I," *Chemosphere*, vol. 75, no. 4, pp. 417–434, 2009.
- [3] L. Xu, H. Zhang, P. Xiong, Q. Zhu, C. Liao, and G. Jiang, "Occurrence, fate, and risk assessment of typical tetracycline

- antibiotics in the aquatic environment: a review,” *Science of the Total Environment*, vol. 753, pp. 141975–141992, 2021.
- [4] S. Suzuki and P. T. P. Hoa, “Distribution of quinolones, sulfonamides, tetracyclines in aquatic environment and antibiotic resistance in Indochina,” *Frontiers in Microbiology*, vol. 3, pp. 1–8, 2012.
  - [5] G. Zhao, X. Huang, X. Wang, and X. Wang, “Progress in the catalyst exploration for heterogenous CO<sub>2</sub> reduction and utilization,” *Journal of Materials Chemistry A*, vol. 5, pp. 21625–21649, 2017.
  - [6] S. Sorcar, S. Yoriya, H. Lee, C. A. Grimes, and S. P. Feng, “A review of recent progress in gas phase CO<sub>2</sub> reduction and suggestions on future advancement,” *Materials Today Chemistry*, vol. 16, p. 100264, 2020.
  - [7] X. Li, J. Xie, C. Jiang, J. Yu, and P. Zhang, “Review on design and evaluation of environmental photocatalysts,” *Frontiers of Environmental Science & Engineering*, vol. 12, no. 5, p. 14, 2018.
  - [8] S. Wageh, A. A. Al-Ghamdi, R. Jafer, X. Li, and P. Zhang, “A new heterojunction in photocatalysis: S-scheme heterojunction,” *Chinese Journal of Catalysis*, vol. 42, pp. 667–669, 2021.
  - [9] L. Liu, T. Hu, K. Dai, J. Zhang, and C. Liang, “A novel step-scheme BiVO<sub>4</sub>/Ag<sub>3</sub>VO<sub>4</sub> photocatalysts for enhanced photocatalytic degradation activity under visible light irradiation,” *Chinese Journal of Catalysis*, vol. 42, pp. 46–55, 2021.
  - [10] Z. Liang, R. Shen, Y. H. Ng, P. Zhang, Q. Xiang, and X. Li, “A review on 2D MoS<sub>2</sub> cocatalysts in photocatalytic H<sub>2</sub> production,” *Journal of Materials Science & Technology*, vol. 56, pp. 89–121, 2020.
  - [11] S. Li, C. Wang, M. J. Cai et al., “Facile fabrication of TaON/Bi<sub>2</sub>MoO<sub>6</sub> core-shell S-scheme heterojunction nanofibers for boosting visible-light catalytic levofloxacin degradation and Cr(VI) reduction,” *Chemical Engineering Journal*, vol. 428, p. 131158, 2022.
  - [12] R. Shen, D. Ren, Y. Ding et al., “Nanostructure CdS for efficient photocatalytic H<sub>2</sub> evolution: a review,” *Science China Materials*, vol. 63, pp. 2153–2188, 2020.
  - [13] X. Yang, Z. Chen, Z. Wan et al., “Recent advances in photodegradation of antibiotic residues in water,” *Chemical Engineering Journal*, vol. 405, p. 126806, 2021.
  - [14] D. Albertus, “Recent progress in artificial photosynthesis: CO<sub>2</sub> photoreduction to valuable chemicals in a heterogeneous system,” *Current Opinion in Chemical Engineering*, vol. 2, no. 2, pp. 200–206, 2013.
  - [15] J. H. Pereira, V. J. Vilar, M. T. Borges, O. González, S. Esplugas, and R. A. Boaventura, “Photocatalytic degradation of oxytetracycline using TiO<sub>2</sub> under natural and simulated solar radiation,” *Solar Energy*, vol. 85, no. 11, pp. 2732–2740, 2011.
  - [16] G. Liu, N. Hoiivik, K. Wang, and H. Jakobsen, “Engineering TiO<sub>2</sub> nanomaterials for CO<sub>2</sub> conversion/solar fuels,” *Solar Energy Materials and Solar Cells*, vol. 105, pp. 53–68, 2012.
  - [17] T. Suwannaruang, J. P. Hildebrand, D. H. Taffa, M. W. K. Kamonsuangkasem, P. Chirawatkul, and K. Wantala, “Visible light-induced degradation of antibiotic ciprofloxacin over Fe–N–TiO<sub>2</sub> mesoporous photocatalyst with anatase/rutile/brookite nanocrystal mixture,” *Journal of Photochemistry and Photobiology A: Chemistry*, vol. 391, p. 112371, 2020.
  - [18] S. Cipagauta-Díaz, A. Estrella-González, M. Navarrete-Magaña, and R. Gómez, “N doped -TiO<sub>2</sub> coupled to BiVO<sub>4</sub> with high performance in photodegradation of Ofloxacin antibiotic and rhodamine B dye under visible light,” *Catalysis Today*, vol. 2021, 2021.
  - [19] F. Li, H. Li, L.-x. Guan, and M.-m. Yao, “Nanocrystalline Co<sup>2+</sup>/F codoped TiO<sub>2</sub>-SiO<sub>2</sub> composite films for environmental applications,” *Chemical Engineering Journal*, vol. 252, pp. 1–10, 2014.
  - [20] O. Ola and M. M. Maroto-Valer, “Transition metal oxide based TiO<sub>2</sub> nanoparticles for visible light induced CO<sub>2</sub> photoreduction,” *Applied Catalysis A: General*, vol. 502, pp. 114–121, 2015.
  - [21] M. Xu, H. Wu, Y. Tang et al., “One-step in-situ synthesis of porous Fe<sup>3+</sup>-doped TiO<sub>2</sub> octahedra toward visible-light photocatalytic conversion of CO<sub>2</sub> into solar fuel,” *Microporous and Mesoporous Materials*, vol. 309, p. 110539, 2020.
  - [22] M. Mgolombane, O. M. Bankole, E. E. Ferg, and A. S. Ogunlaja, “Construction of Co-doped TiO<sub>2</sub>/rGO nanocomposites for high-performance photoreduction of CO<sub>2</sub> with H<sub>2</sub>O: comparison of theoretical binding energies and exploration of surface chemistry,” *Materials Chemistry and Physics*, vol. 268, p. 124733, 2021.
  - [23] A. Tiwari, A. Shukla, D. T. Lalliansanga, and S.-M. Lee, “Aunanoparticle/nanopillars TiO<sub>2</sub> meso-porous thin films in the degradation of tetracycline using UV-A light,” *Journal of Industrial and Engineering Chemistry*, vol. 69, pp. 141–152, 2019.
  - [24] W. Li, B. Li, M. Meng et al., “Bimetallic Au/Ag decorated TiO<sub>2</sub> nanocomposite membrane for enhanced photocatalytic degradation of tetracycline and bactericidal efficiency,” *Applied Surface Science*, vol. 487, pp. 1008–1017, 2019.
  - [25] J. Singh, S. Juneja, R. K. Soni, and J. Bhattacharya, “Sunlight mediated enhanced photocatalytic activity of TiO<sub>2</sub> nanoparticles functionalized CuO-Cu<sub>2</sub>O nanorods for removal of methylene blue and oxytetracycline hydrochloride,” *Journal of Colloid and Interface Science*, vol. 590, pp. 60–71, 2021.
  - [26] X. Hu, C. Li, J. Song, S. Zheng, and Z. Sun, “Multidimensional assembly of oxygen vacancy-rich amorphous TiO<sub>2</sub>-BiOBr-sepiolite composite for rapid elimination of formaldehyde and oxytetracycline under visible light,” *Journal of Colloid and Interface Science*, vol. 574, pp. 61–73, 2020.
  - [27] W. Bi, Y. Hu, N. Jiang et al., “Ultra-fast construction of plaque-like Li<sub>2</sub>TiO<sub>2</sub>/TiO<sub>2</sub> heterostructure for efficient gas-solid phase CO<sub>2</sub> photoreduction,” *Applied Catalysis B: Environmental*, vol. 269, p. 118810, 2020.
  - [28] Q. Wang, P. Dong, Z. Huang, and X. Zhang, “Synthesis of Ag or Pt nanoparticle-deposited TiO<sub>2</sub> nanorods for the highly efficient photoreduction of CO<sub>2</sub> to CH<sub>4</sub>,” *Chemical Physics Letters*, vol. 639, pp. 11–16, 2015.
  - [29] T. Cheng, H. Gao, R. Li, S. Wang, Z. Yi, and H. Yang, “Flexoelectricity-induced enhancement in carrier separation and photocatalytic activity of a photocatalyst,” *Applied Surface Science*, vol. 566, p. 150669, 2021.
  - [30] X. Wang, S. Blechert, and M. Antonietti, “Polymeric graphitic carbon nitride for heterogeneous photocatalysis,” *Acs Catalysis*, vol. 2, pp. 1596–1606, 2012.
  - [31] Y. Zheng, L. Lin, B. Wang, and X. Wang, “Graphitic carbon nitride polymers toward sustainable photoredox catalysis,” *Angewandte Chemie International Edition*, vol. 54, pp. 2868–2884, 2015.
  - [32] O. Timothy, A. T. Kuvarega, and D. C. Onwudiwe, “Graphitic carbon nitride-based catalyst and their application: a review,” *Nano-Structures & Nano-Objects*, vol. 24, p. 10057, 2020.

- [33] M.-M. Fang, J.-X. Shao, X.-G. Huang, J.-Y. Wang, and W. Chen, "Direct Z-scheme CdFe<sub>2</sub>O<sub>4</sub>/g-C<sub>3</sub>N<sub>4</sub> hybrid photocatalysts for highly efficient ceftiofur sodium photodegradation," *Journal of Materials Science & Technology*, vol. 56, pp. 133–142, 2020.
- [34] D. Reh, W. Zhang, Y. Ding et al., "In situ fabrication of robust cocatalyst-free CdS/g-C<sub>3</sub>N<sub>4</sub> 2D-2D step-scheme heterojunction for highly active H<sub>2</sub> evolution," *Solar Rrl*, vol. 4, no. 8, p. 1900423, 2020.
- [35] R. Shen, K. He, A. Zhang et al., "In-situ construction of metallic Ni<sub>3</sub>C@core-shell cocatalysts over g-C<sub>3</sub>N<sub>4</sub> nanosheets for shell-thickness-dependent photocatalytic H<sub>2</sub> production," *Applied Catalysis B: Environmental*, vol. 291, p. 120104, 2021.
- [36] J. Wang, G. Wang, B. Cheng, J. Yu, and J. Fan, "Sulfur-doped g-C<sub>3</sub>N<sub>4</sub>/TiO<sub>2</sub> S-scheme heterojunction photocatalyst for Congo Red photodegradation," *Chinese Journal of Catalysis*, vol. 42, pp. 56–68, 2021.
- [37] P. Suyana, P. Ganguly, B. N. Nair, S. C. Pillai, and U. S. Hareesh, "Structural and compositional tuning in g-C<sub>3</sub>N<sub>4</sub> based systems for photocatalytic antibiotic degradation," *Chemical Engineering Journal Advances*, vol. 8, p. 100148, 2021.
- [38] R. Liu, Z. Chen, Y. Yao et al., "Recent advancements in g-C<sub>3</sub>N<sub>4</sub>-based photocatalysts for photocatalytic CO<sub>2</sub> reduction: a mini review," *RSC Advances*, vol. 10, pp. 29408–29418, 2020.
- [39] J. Lin, W. Tian, H. Zhang, X. Duan, H. Sun, and S. Wang, "Graphitic carbon nitride-based Z-scheme structure for photocatalytic CO<sub>2</sub> reduction," *Energy & Fuels*, vol. 35, no. 1, pp. 7–24, 2021.
- [40] Q. Xu, L. Zhang, J. Yu, S. Wageh, A. A. Al-Ghamdi, and M. Jaroniec, "Direct Z-scheme photocatalysts: principles, synthesis, and applications," *Materials Today*, vol. 21, no. 10, pp. 1042–1063, 2018.
- [41] S. Guan, H. Yang, X. Sun, and T. Xien, "Preparation and promising application of novel LaFeO<sub>3</sub>/BiOBr heterojunction photocatalysts for photocatalytic and photo-Fenton removal of dyes," *Optical Materials*, vol. 100, p. 109644, 2020.
- [42] T. Cheng, H. Gao, G. Liu et al., "Preparation of core-shell heterojunction photocatalysts by coating CdS nanoparticles onto Bi<sub>4</sub>Ti<sub>3</sub>O<sub>12</sub> hierarchical microspheres and their photocatalytic removal of organic pollutants and Cr(VI) ions," *Colloids and Surfaces A: Physicochemical and Engineering Aspects*, vol. 633, p. 127918, 2022.
- [43] L. Li, H. Gao, G. Liu et al., "Synthesis of carnation flower-like Bi<sub>2</sub>O<sub>2</sub>CO<sub>3</sub> photocatalyst and its promising application for photoreduction of Cr(VI)," *Advanced Powder Technology*, vol. 33, p. 103481, 2022.
- [44] W. Wang, J. F. Xinlei, and C. Lu, "TiO<sub>2</sub>@g-C<sub>3</sub>N<sub>4</sub> heterojunction with directional charge migration behavior for photodegradation of tetracycline antibiotics," *Materials Letters*, vol. 236, pp. 622–624, 2019.
- [45] M. Reli, P. Huo, M. Šihor et al., "Novel TiO<sub>2</sub>/g-C<sub>3</sub>N<sub>4</sub> photocatalyst for photocatalytic reduction of CO<sub>2</sub> and photocatalytic decomposition of N<sub>2</sub>O," *The Journal of Physical Chemistry A*, vol. 120, no. 43, pp. 8564–8573, 2016.
- [46] M. Sathish, B. Viswanathan, and R. P. Viswanath, "Characterization and photocatalytic activity of N-doped TiO<sub>2</sub> prepared by thermal decomposition of Ti-melamine complex," *Applied Catalysis. B, Environmental*, vol. 74, no. 3-4, pp. 307–312, 2007.
- [47] A. Majumdar, U. Ghosh, and A. Pai, "Novel 2D/2D g-C<sub>3</sub>N<sub>4</sub>/Bi<sub>4</sub>NbO<sub>8</sub>Cl nano-composite for enhanced photocatalytic degradation of oxytetracycline under visible LED light irradiation," *Journal of Colloid and Interface Science*, vol. 584, pp. 320–331, 2021.
- [48] J. Ni, W. Wang, D. Liu et al., "Oxygen vacancy-mediated sandwich-structural TiO<sub>2-x</sub>/ultrathin g-C<sub>3</sub>N<sub>4</sub>/TiO<sub>2-x</sub> direct Z-scheme heterojunction visible-light-driven photocatalyst for efficient removal of high toxic tetracycline antibiotic," *Journal of Hazardous Materials*, vol. 408, p. 124432, 2021.
- [49] S. El-Sherbiny, F. Morsy, M. Samir, and A. Osama, "Synthesis, characterization and application of TiO<sub>2</sub> nanopowders as special paper coating pigment," *Applied Nanoscience*, vol. 4, pp. 305–313, 2014.
- [50] D. Jimin, "A facile method for synthesis of N-doped TiO<sub>2</sub> nanooctahedra, nanoparticles, and nanospheres and enhanced photocatalytic activity," *Applied Surface Science*, vol. 273, pp. 278–286, 2013.
- [51] B. Bharti, S. Kumar, H.-N. Lee, and R. Kumar, "Formation of oxygen vacancies and Ti<sup>3+</sup> state in TiO<sub>2</sub> thin film and enhanced optical properties by air plasma treatment," *Scientific Reports*, vol. 6, p. 32355, 2016.
- [52] T. Jia, F. Fang, D. Yu, and G. Sun, "Facile synthesis and characterization of N-doped TiO<sub>2</sub>/C nanocomposites with enhanced visible-light photocatalytic performance," *Applied Surface Science*, vol. 430, pp. 438–447, 2018.
- [53] X. Zheng, Y. Liu, X. Liu, Q. Li, and Y. Zheng, "A novel PVDF-TiO<sub>2</sub>@g-C<sub>3</sub>N<sub>4</sub> composite electron spun fiber for efficient photocatalytic degradation of tetracycline under visible light irradiation," *Ecotoxicology and Environmental Safety*, vol. 210, p. 111866, 2021.
- [54] J. Hong, D. K. Hwang, R. Selvaraj, and Y. Ki, "Facile synthesis of Br-doped g-C<sub>3</sub>N<sub>4</sub> nanosheets via one-step exfoliation using ammonium bromide for photodegradation of oxytetracycline antibiotics," *Journal of Industrial and Engineering Chemistry*, vol. 79, pp. 473–481, 2019.
- [55] C. Hu, Y.-C. Chu, M.-S. Wang, and X.-H. Wu, "Rapid synthesis of g-C<sub>3</sub>N<sub>4</sub> spheres using microwave-assisted solvothermal method for enhanced photocatalytic activity," *Journal of Photochemistry and Photobiology A: Chemistry*, vol. 348, pp. 8–17, 2017.
- [56] H. Zhang, G. Zhang, H. Zhang et al., "Facile synthesis hierarchical porous structure anatase-rutile TiO<sub>2</sub>/g-C<sub>3</sub>N<sub>4</sub> composite for efficient photodegradation tetracycline hydrochloride," *Applied Surface Science*, vol. 567, p. 150833, 2021.
- [57] W. Wang, J. Fang, S. Shao, and M. Lai, "Compact and uniform TiO<sub>2</sub>@g-C<sub>3</sub>N<sub>4</sub> core-shell quantum heterojunction for photocatalytic degradation of tetracycline antibiotics," *Applied Catalysis B: Environmental*, vol. 217, pp. 57–64, 2017.
- [58] J. Ni, W. Wang, D. Liu et al., "Oxygen vacancy-mediated sandwich-structural TiO<sub>2-x</sub>/ultrathin g-C<sub>3</sub>N<sub>4</sub>/TiO<sub>2-x</sub> direct Z-scheme heterojunction visible-light-driven photocatalyst for efficient removal of high toxic tetracycline antibiotics," *Journal of Hazardous Materials*, vol. 408, p. 124432, 2021.
- [59] Y. Wang, L. Rao, P. Wang, Z. Shi, and L. Zhang, "Photocatalytic activity of N-TiO<sub>2</sub>/O-doped N vacancy g-C<sub>3</sub>N<sub>4</sub> and the intermediates toxicity evaluation under tetracycline hydrochloride and Cr(VI) coexistence environment," *Applied Catalysis B: Environmental*, vol. 262, p. 118308, 2020.
- [60] H. Zhang, G. Zhang, H. Zhang et al., "Facile synthesis hierarchical porous structure anatase-rutile TiO<sub>2</sub>/g-C<sub>3</sub>N<sub>4</sub> composite for efficient photodegradation tetracycline hydrochloride," *Applied Surface Science*, vol. 567, pp. 473–481, 2019.

- [61] B. Zhu, P. Xia, W. Ho, and J. Yu, "Isoelectric point and adsorption activity of porous g-C<sub>3</sub>N<sub>4</sub>," *Applied Surface Science*, vol. 344, pp. 188–195, 2015.
- [62] Y. Li, H. Wang, X. Liu, G. Zhao, and Y. Sun, "Dissipation kinetics of oxytetracycline, tetracycline, and chlortetracycline residues in soil," *Environmental Science and Pollution Research*, vol. 23, no. 14, pp. 13822–13831, 2016.
- [63] S. Zhou, Y. Liu, J. Li et al., "Facile in situ synthesis of graphitic carbon nitride (g-C<sub>3</sub>N<sub>4</sub>)-N-TiO<sub>2</sub> heterojunction as an efficient photocatalyst for the selective photoreduction of CO<sub>2</sub> to CO," *Applied Catalysis B: Environmental*, vol. 158, pp. 20–29, 2014.
- [64] Q. Wang, L. Zhang, Y. Guo et al., "Multifunctional 2D porous g-C<sub>3</sub>N<sub>4</sub> nano sheets hybridized with 3D hierarchical TiO<sub>2</sub> micro flowers for selective dye adsorption, antibiotic degradation and CO<sub>2</sub> reduction," *Chemical Engineering Journal*, vol. 396, p. 125347, 2020.
- [65] K. Li, B. Peng, J. Jin, L. Zan, and T. Peng, "Carbon nitride nanodots decorated brookite TiO<sub>2</sub> quasi nanocubes for enhanced activity and selectivity of visible-light-driven CO<sub>2</sub> reduction," *Applied Catalysis B: Environmental*, vol. 203, pp. 910–916, 2017.
- [66] A. B. Dehkordi, A. Ziarati, J. B. Ghasemi, and A. Badiei, "Preparation of hierarchical g-C<sub>3</sub>N<sub>4</sub>@TiO<sub>2</sub> hollow spheres for enhanced visible-light induced catalytic CO<sub>2</sub> reduction," *Solar Energy*, vol. 205, pp. 465–473, 2020.
- [67] S. Tang, X. Yin, G. Wang, X. Lu, and T. Lu, "Single titanium-oxide species implanted in 2D g-C<sub>3</sub>N<sub>4</sub> matrix as a highly efficient visible-light CO<sub>2</sub> reduction photocatalyst," *Nano Research*, vol. 12, pp. 457–462, 2019.
- [68] H. Wang, H. Li, Z. Chen, J. Li, P. Huo, and Q. Wang, "TiO<sub>2</sub> modified g-C<sub>3</sub>N<sub>4</sub> with enhanced photocatalytic CO<sub>2</sub> reduction performance," *Solid State Sciences*, vol. 100, p. 106099, 2020.
- [69] J. Wu, Y. Feng, D. Li, X. Han, and J. Liu, "Efficient photocatalytic CO<sub>2</sub> reduction by P-O linked g-C<sub>3</sub>N<sub>4</sub>/TiO<sub>2</sub>-nanotubes Z-scheme composites," *Energy*, vol. 178, pp. 168–175, 2019.
- [70] H. Yang, "A short review on heterojunction photocatalyst: carrier transfer behavior and photocatalytic mechanisms," *Materials Research Bulletin*, vol. 142, p. 11406, 2021.
- [71] M. Navarrete-Magana, A. Estrella-Gonzalez, L. May-Ix, S. Cipagauta-Diaz, and R. Gomeza, "Improved photocatalytic oxidation of arsenic (III) with WO<sub>3</sub>/TiO<sub>2</sub> nanomaterials synthesized by the sol-gel method," *Journal of Environmental Management*, vol. 282, p. 111602, 2021.
- [72] H. Irie, S. Washizuka, Y. Watanabe, T. Kako, and K. Hashimoto, "Photoinduced hydrophilic and electrochemical properties of nitrogen-doped TiO<sub>2</sub> films," *Journal of the Electrochemical Society*, vol. 152, no. 11, pp. E351–E356, 2005.
- [73] A. Wang, C. Wang, F. Li, W. Wong-Ng, and Y. Lan, "Recent advances of graphitic carbon nitride-based structures and applications in catalyst, sensing, imaging, and LEDs," *Nano-Micro Letters*, vol. 9, p. 47, 2017.
- [74] S. Guan, R. Li, X. Sun, T. Xian, and H. Yang, "Construction of novel ternary Au/LaFeO<sub>3</sub>/CuO composite photocatalysts for RhB degradation via photo-Fenton catalysis," *Materials Technology*, vol. 36, no. 10, pp. 603–615, 2021.

## Research Article

# Adsorption Characteristics of Antibiotic Meropenem on Magnetic $\text{CoFe}_2\text{O}_4@Au$ Nanoparticles

Thi Ngoc Mai Pham <sup>1</sup>, Thi Hieu Hoang,<sup>1</sup> Thu Phuong Nguyen,<sup>1</sup> Quang Khanh Nguyen,<sup>1,2</sup> Bach Pham <sup>1</sup>, Quoc Anh Hoang,<sup>1</sup> Tien Duc Pham <sup>1</sup>, Thi Anh Huong Nguyen <sup>1</sup>, Anh Tuan Le <sup>3,4</sup> and Duc Thang Pham <sup>3,4</sup>

<sup>1</sup>Faculty of Chemistry, University of Science, Vietnam National University, Hanoi, 19 Le Thanh Tong, Hoan Kiem, Hanoi 10000, Vietnam

<sup>2</sup>Department of Chemistry, College of Natural Sciences, Hanyang University, Seoul 04763, Republic of Korea

<sup>3</sup>Phenikaa University Nano Institute, Phenikaa University, Yen Nghia, Ha Dong, Hanoi 12116, Vietnam

<sup>4</sup>Faculty of Materials Science and Engineering, Phenikaa University, Yen Nghia, Ha Dong, Hanoi 12116, Vietnam

Correspondence should be addressed to Thi Ngoc Mai Pham; [phamthingocmai@hus.edu.vn](mailto:phamthingocmai@hus.edu.vn) and Duc Thang Pham; [thang.phamduc@phenikaa-uni.edu.vn](mailto:thang.phamduc@phenikaa-uni.edu.vn)

Received 18 November 2021; Revised 16 February 2022; Accepted 25 February 2022; Published 30 March 2022

Academic Editor: George Kyzas

Copyright © 2022 Thi Ngoc Mai Pham et al. This is an open access article distributed under the Creative Commons Attribution License, which permits unrestricted use, distribution, and reproduction in any medium, provided the original work is properly cited.

Adsorption characteristics of the antibiotic meropenem on a novel magnetic material synthesized by surface coating cobalt iron oxide (CFO) with gold nanoparticles (AuNPs) were systematically investigated. The AuNPs can enhance material adsorption capacity by having high affinity towards the thioether and amine groups in the meropenem structure. Au coverage on the CFO surface decreased the saturation magnetization from 55.8 emu/g to 48.8 emu/g, still allowing synthesized CFO@Au nanomaterials to be magnetically recoverable. The CFO@Au nanomaterials showed enhanced adsorption capacity of 25.5 mg/g at optimum conditions of pH 4.0 adsorption time 120 min, and adsorbent mass 0.05 g. Adsorption equilibrium was in accordance with a monolayer Langmuir isotherm, while the adsorption kinetics followed pseudo-first-order kinetics and intraparticle diffusion models. This work provides a simple method to prepare a magnetic composite material with high adsorption efficiency for meropenem and probably other thioether-containing substances.

## 1. Introduction

Recently, the combination of metal oxide materials with other functional components or other materials has been extensively studied to produce composite materials with novel properties and unique applicability. Due to the evident advantages of gold nanoparticles (AuNPs), structures of such nanoparticles on core-shell oxides have attracted great attention [1–3]. As an inert metal, Au is extremely valuable as a material coating for magnetic nanoparticle protection, surface modification versatility, strong catalytic capability, and biocompatibility [4–6]. Applications of Au/metal oxide nanocomposites include removal of toxic substances such as Hg, As [7, 8], catalysts for organic compound reduction [9], or CO oxidation

[10], analysis of various targets including catechols [11], prostate-specific antigen [10], malachite green [12], and drug carriers for biomedical applications [13, 14]. Among different Au-metal oxide composites, Au/magnetic oxide nanoparticles have frequently been studied since these materials can be used in various fields such as protein purification, biological separation, target delivery, magnetic resonance imaging, therapy, and biosensing.  $\text{Fe}_3\text{O}_4$  and other iron-containing compounds such as  $\text{CoFe}_2\text{O}_4$  attract much attention thanks to the capacity for surface functionalization as well as its excellent magnetic properties. In addition, it is easy to separate these compounds from solution using an external magnetic field [4, 15–20].

Many studies have been carried out on  $\text{Fe}_3\text{O}_4/\text{Au}$  nanocomposites, however, not as many studies have focused on

Au and  $\text{CoFe}_2\text{O}_4$  (CFO) composites. Among magnetic oxides, CFO has advantages of large anisotropy, high coercive field, moderate saturation magnetization, high electromagnetic performance, chemical stability, and good electrical conductivity [21–23]. Studies mostly focus on nanocomposite applications for analytical detection, catalysis, and drug delivery, nevertheless, applications for adsorption of -S- or NH- containing substances, exploiting the strong affinity of gold for sulfur or nitrogen atoms has been scarce.

Meropenem is a pyrrolidinyl dimethyl carbamoyl derivative of thienamycin taken from *Streptomyces cattleya*. It is an injectable antibiotic which currently has the broadest antibacterial spectrum in the carbapenem group [24]. Meropenem is one of the strongest antibiotics to kill harmful microorganisms which are resistant to penicillin and cephalosporin antibiotics. Particularly, the carbapenems have been used as last-resort antibiotics for patients in cases of infectious diseases in intensive care units who are seriously infected with multidrug-resistant biota [25]. So far, the analogs of carbapenems in biological and pharmaceutical matrices have mostly been determined with common separation methods include liquid-liquid extraction and solid-liquid extraction (SPE). However, such methods require several steps and have limited selectivity [26]. Sample treatment coupled with magnetic nanoparticles can provide faster phase separation by applying an external magnetic field and is easily reused. To enhance the separation efficiency, magnetic particles have been surface-functionalized with small organic molecules, polymers, aptamers, antibodies, and metal nanoparticles [27].

The present study is aimed at combining magnetic  $\text{CoFe}_2\text{O}_4$  with AuNPs (CFO@Au) and study the adsorption behavior of meropenem on the composite material, which can later be used for separation and enrichment of meropenem from complicated matrices. Since meropenem molecules contain thioether and amine groups, which strongly bind with the Au surface, adsorption of meropenem on Au-modified CFO particles should be enhanced in comparison with bare CFO material. Studies on the adsorptive removal of meropenem have been reported on adsorbents such as multiwalled carbon nanotubes [28] and rice husk functionalized with Mg/Fe-layered double hydroxides [29]. In these cases, the interaction between meropenem and adsorbents is mainly due to electrostatic,  $\pi$ - $\pi$  EDA interactions, hydrophobic interactions, and hydrogen bonding to -OH and -NH- group. To the best of our knowledge, there is as yet no research examining adsorption of meropenem on CFO@Au.

The synthesis of Au/metal oxide composites usually involves mixing gold (III) salts with a suspension containing oxide nanoparticles and then reducing gold (III) by a suitable reductant such as sodium citrate [8], extract of the *Allium Sp* plant [9], or tetrakis (hydroxymethyl) phosphonium chloride (THPC) [12]. Aniline and dithiothreitol are used to stabilize AuNPs while substances like (3-aminopropyl) triethoxysilane (APTES) or polyethyleneimine dithiocarbamate (PEI-DTC) are used to functionalize the magnetic oxide surface to form better linkages with Au particles. In our study, CFO was prepared by a hydrothermal method, while AuNPs were prepared

and stabilized on the CFO surface by using the conventional sodium citrate or sodium borohydride ( $\text{NaBH}_4$ ) reductants and poly (diallyldimethylammonium chloride) PDADMAC polycation as a stabilizer.

## 2. Materials and Methods

**2.1. Reagents and Materials.** All chemicals used were analytical grade and were directly used without further purification. Meropenem sodium salt 98% (Figure S1 of Supplementary data) was purchased from Toronto Research Chemicals (Canada). Other reagents were chloroauric acid tetrahydrate ( $\text{HAuCl}_4 \cdot 4\text{H}_2\text{O}$ ), sodium borohydride ( $\text{NaBH}_4$ ), sodium citrate ( $\text{Na}_3\text{C}_6\text{H}_5\text{O}_7$ ), sodium hydroxide ( $\text{NaOH}$ ), potassium hydroxide ( $\text{KOH}$ ), hydrochloric acid ( $\text{HCl}$ ), poly (diallyldimethylammonium chloride) (PDADMAC) solution with a molecular weight of 400-500 kg/mol (PDADMAC 20 wt% in  $\text{H}_2\text{O}$ ) purchased from Merck (Darmstadt, Germany),  $\text{Fe}(\text{NO}_3)_3 \cdot 9\text{H}_2\text{O}$ ,  $\text{Co}(\text{NO}_3)_2 \cdot 6\text{H}_2\text{O}$ , (3-aminopropyl) triethoxysilane (APTES) and tris(hydroxymethyl) aminomethane (Tris) buffer purchased from Sigma-Aldrich (USA), and Bondesil-C18, 40  $\mu\text{m}$ , 100 gm purchased from Agilent (USA). Deionized water was used for preparing all solutions.

### 2.2. Synthesis of Materials

**2.2.1. Synthesis of  $\text{CoFe}_2\text{O}_4$  Nanoparticles.** Powdered magnetic CFO materials were synthesized by a hydrothermal method. A solution containing  $\text{Co}(\text{NO}_3)_2 \cdot 6\text{H}_2\text{O}$  and  $\text{Fe}(\text{NO}_3)_3 \cdot 9\text{H}_2\text{O}$  with the  $\text{Co}^{2+} : \text{Fe}^{3+}$  molar ratio of 1:2.2 was added to a beaker and adjusted to pH 12 with  $\text{NaOH}$ . This mixture was then transferred to a thermo-hydrolysis vessel and hydrolyzed at 150°C for 2 h. After being hydrolyzed, the sample was taken out and washed several times with distilled water. The precipitate was collected using magnets and dried at 80°C to produce  $\text{CoFe}_2\text{O}_4$  product as a black powder.

### 2.2.2. Synthesis of $\text{CoFe}_2\text{O}_4$ @Au Composites

**(1) PDADMAC-Stabilized Au.** AuNPs were obtained by reducing  $\text{HAuCl}_4$  with  $\text{NaBH}_4$  in the presence of PDADMAC as a stabilizer [30]. The freshly prepared dispersion of CFO (50 mg in 50 mL of water) was acidified with 0.1 M of  $\text{HCl}$  at pH 6.5. While continuous stirring, successively, 152  $\mu\text{L}$  of (3-aminopropyl) triethoxysilane (APTES) and 200  $\mu\text{L}$  of 50 mM  $\text{HAuCl}_4$  were added. Then, 20  $\mu\text{L}$  of PDADMAC was added to the formed dark brown colloidal nanoparticle solution, and the mixture was stirred for 10 minutes. After that, 2 mL of a freshly prepared solution of  $\text{NaBH}_4$  (0.05 M) was added dropwise into the formed reddish-brown colloidal nanoparticle solution, and then, the mixture was stirred for 3 h. The obtained substance was collected with magnets, washed with deionized water and alcohol, and then dried at 80°C for 12 h.

**(2) Citrate-Stabilized Au.** CFO dispersion (0.4 g/100 mL) was mixed with 400  $\mu\text{L}$  of 50 mM  $\text{HAuCl}_4$ . The mixture was heated to boiling under continuous stirring; then, 16 mL of

50 mM sodium citrate was added. The solution was further heated for 20 min to form a reddish-brown colloidal solution. The obtained substance was collected with magnets, washed with deionized water and alcohol, and then was dried at 80°C for 12 h.

**2.3. Material Characterization.** The crystal structures of CFO and CFO@Au were investigated by X-ray diffraction (XRD) using a D8 Advance X-ray diffractometer (Bruker) with wavelength  $\text{Cu}_{K\alpha} = 1.5406 \text{ \AA}$  and the  $2\theta$  angle range of  $20^\circ$  to  $80^\circ$ . The morphology and particle size distribution of CFO and CFO@Au were analyzed on a JEM 1010 transmission electron microscope (TEM, JEOL) operated at an accelerating voltage of 100 keV. The magnetic hysteresis loops were measured by a vibrating sample magnetometer (VSM, Lakeshore) at room temperature and in an external field up to 5 kG. The infrared spectra were recorded on a Fourier transform infrared spectrometer (FTIR-1S, Shimadzu). The absorption spectra of AuNPs, CFO, and CFO@Au were obtained with a UV-Vis spectrophotometer (UV 1601 PC, Shimadzu) using two 1 cm matched quartz cells at room temperature.

**2.4. Meropenem Determination.** The concentrations of meropenem before and after adsorption on adsorbent material are determined by capillary electrophoresis with a capacitively coupled contactless conductivity detector (CE-C<sup>4</sup>D). The CE instrument was built-in house with a commercial C<sup>4</sup>D (ER815, eDAQ, Denistone East, NSW, Australia). Uncoated fused silica capillary (ID of 50  $\mu\text{m}$  and OD of 375  $\mu\text{m}$ ), total length 60 cm, effective length 53 cm, was used with buffered eluent composed of 10 mM Tris adjusted to pH 8.0 with acetic acid. Injection was carried out by siphoning at a height of 20 cm for 20 s. Separation voltage was +20 kV [31].

**2.5. Batch Adsorption of Meropenem on CFO@Au.** To evaluate the adsorption capacity, the adsorbent (0.03–0.1 g) was mixed with 10 mL of meropenem solution (pH from 3.0 to 8.0) having different initial concentrations (30 to 350 mg/L) in 15 mL falcon tubes. These falcon tubes were then shaken in the range of 60 to 300 min. The parameters investigated include solution pH, adsorption time, adsorbent mass, and initial concentration of meropenem.

The concentrations of meropenem after adsorption were determined by using CE-C<sup>4</sup>D measurement. The adsorption efficiency ( $H_{\%}$ ) was evaluated by the following equation:

$$H = \frac{C_0 - C}{C_0} \times 100\%. \quad (1)$$

The adsorption capacity  $q_e$  (mg/g) of meropenem onto CFO@Au was calculated by the following equation:

$$q_e = \frac{C_0 - C_e}{m} \times V, \quad (2)$$

where  $C_0$  (mg/L) and  $C_e$  (mg/L) are the initial concentration and equilibrium concentrations of meropenem, respectively,

$V$  (L) is the volume of the solution, and  $m$  (g) is the adsorbent mass.

Kinetics experiments used initial meropenem concentration of 50 ppm, pH = 4.0 adsorbent mass of 0.05 g, and time ranging 0 to 180 min, while experiments to evaluate adsorption isotherms used initial meropenem concentration varying from 30 to 350 ppm, pH = 4.0, adsorbent mass = 0.05 g, time = 120 min.

**2.6. Adsorption Isotherms.** Langmuir and Freundlich models were investigated for adsorption isotherms. The Langmuir adsorption isotherm is described by the following equation [32–34]:

$$q_e = \frac{q_m K_L C_e}{1 + K_L C_e}, \quad (3)$$

where  $q_e$  and  $q_m$  are equilibrium and maximum adsorption capacities (mg/g), respectively, and  $K_L$  is the Langmuir adsorption constant (L/mg) which relates to energy of adsorption.

The Freundlich model is as follows [33, 35]:

$$q_e = K_F C_e^{1/n}, \quad (4)$$

where  $k_f$  is Freundlich adsorption capacity (L/g) and  $n$  is an indicator for the degree of surface heterogeneity and describes the distribution of the adsorbed molecules on the adsorbent surface. The Freundlich equation is characteristic for a multilayer adsorption isotherm.

**2.7. Kinetic Models.** To evaluate the rate of the adsorption process, the pseudofirst-order, pseudosecond-order, and intraparticle diffusion models are frequently applied to fit the kinetics data. The correlation coefficient ( $R^2$ ) is computed to evaluate how successfully the model fits the data and demonstrate the kinetics of adsorption [33].

The pseudofirst-order model is described by equation (5). This model assumes the physical adsorption of one adsorbate molecule onto one active site on the adsorbent surface [33]:

$$q_t = q_e \left(1 - e^{-k_1 t}\right). \quad (5)$$

The pseudosecond-order model follows equation (6). The pseudosecond-order model assumes the adsorption of one adsorbate molecule onto two active sites on the adsorbent surface, preferentially through chemisorption [33]:

$$q_t = \frac{q_e^2 k_2 t}{1 + q_e k_2 t}, \quad (6)$$

where  $q_e$  and  $q_t$  are equilibrium adsorption capacity (mg/g) and adsorption capacity at different time intervals (mg/g), respectively.  $t$  is adsorption time (min), and  $k_1$  and  $k_2$  are pseudofirst-order (1/s) and pseudosecond-order (g/mg.min) rate constants, respectively.

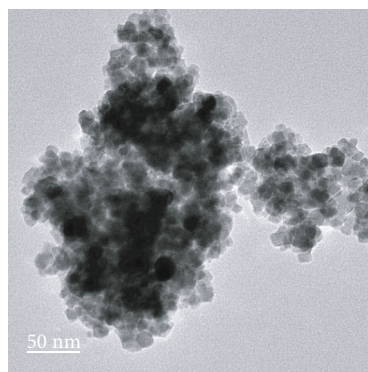
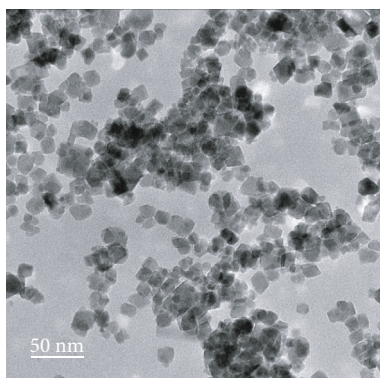
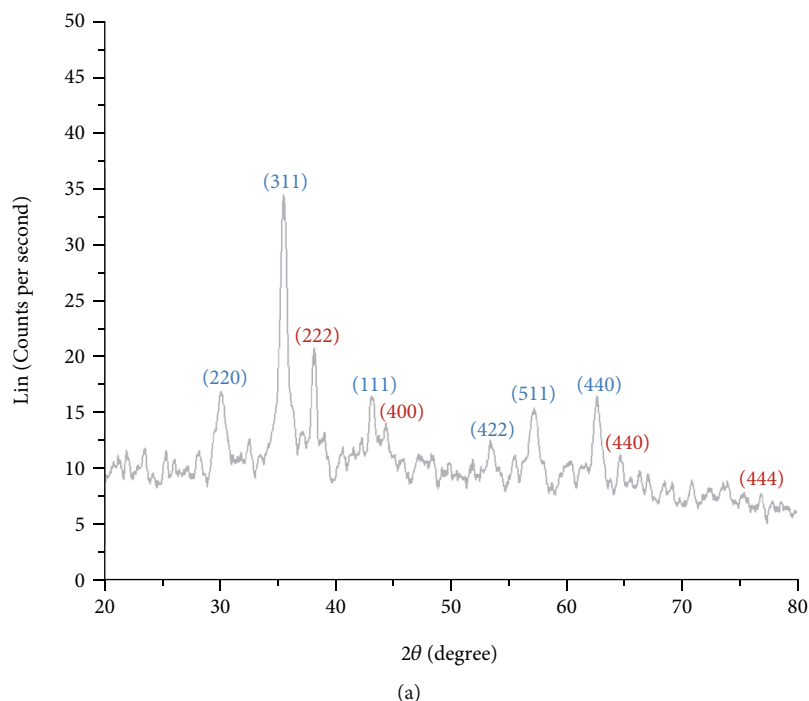


FIGURE 1: Characterization of CFO@Au: (a) X-ray diffraction pattern of the CFO@Au nanocomposites, (b) TEM images of CFO, and (c) TEM images of CFO@Au particles.

Intraparticle diffusion model provides information about the diffusion of adsorbate onto the adsorbent material and whether intraparticle diffusion is the rate-limiting step. Equation (7) describes the intraparticle diffusion model:

$$q_t = k_d t^{1/2}, \quad (7)$$

where  $k_d$  is the intraparticle diffusion rate constant ( $1/\text{min}^{1/2}$ ).

### 3. Results and Discussion

**3.1. Comparison of Meropenem Adsorptivity between CFO@Au-Citrate, CFO@Au-PDADMAC, CFO, and C18 Materials.** The adsorption efficiencies of meropenem on CFO@Au composites, prepared by 2 methods, stabilized with citrate and stabilized with PDADMAC, were compared with bare CFO and conventional adsorption material C18 (10 mL

of 50 ppm meropenem, pH 4.0; contact time 120 min, adsorbent mass 0.10 g) as presented in Figure S2. Among the 4 materials, C18 provides the lowest adsorption efficiency of 24%, followed by CFO (62%), then CFO@Au-PDADMAC (72%), and the highest efficiency was obtained for CFO@Au-citrate (94%). The modification of CFO by AuNPs enhanced the adsorption efficiency of meropenem through affinity interaction between AuNPs on the surface with thioether and amine groups in the meropenem molecular structure.

The CFO and Au composites synthesized by 2 routes demonstrate not only different adsorption efficiencies but also different pH-dependent adsorption behaviors. For CFO@Au-PDADMAC, when the solution pH was varied from 3.0 to 8.0, the adsorption capacity changed insignificantly and had a maximum at pH 6.0. According to our previous research on the PDADMAC-Au system [30], the interaction between the analyte and PDADMAC is mainly hydrophobic interaction. Meropenem has isoelectric point

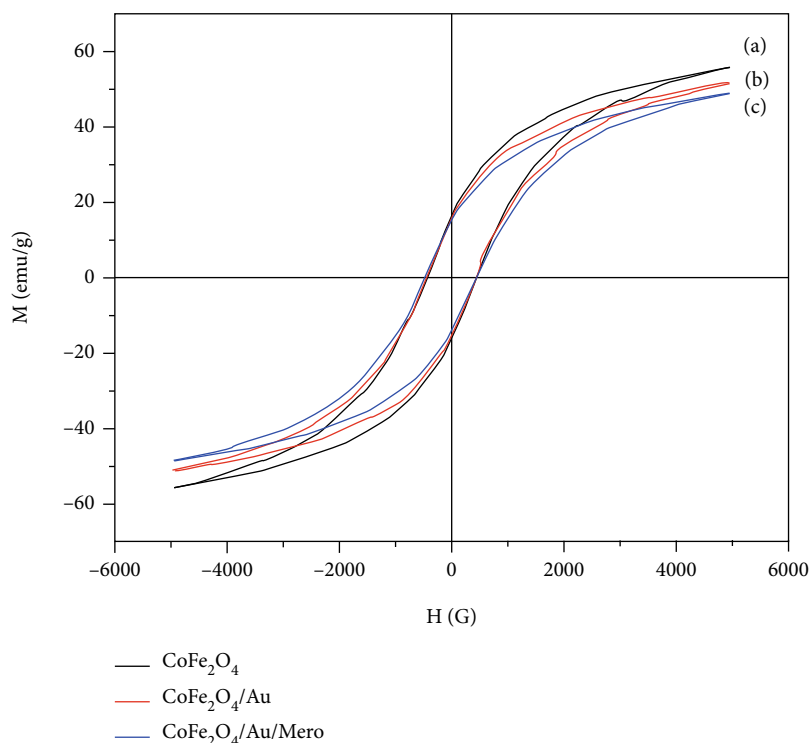


FIGURE 2: Hysteresis loops of (a) CFO, (b) CFO@Au, and (c) CFO@Au-meropenem.

pI~6.0, meaning that at pH 6.0, it is charge neutral. Thus, meropenem can be adsorbed and distributed very well on the hydrophobic surface of CFO@Au-PDADMAC. The maximum adsorption at pH 6.0 suggests the dominant contribution of hydrophobic interaction between meropenem and PDADMAC capped-AuNPs over the electrostatic interaction.

Meanwhile, for CFO@Au-citrate, the maximum adsorption capacity was obtained at pH 4.0 (94%). This is explained by the dominant electrostatic interaction between citrate-AuNPs and meropenem which vary with pH. Citrate-AuNPs are negatively charged at pH > pK = 3.1 of citric acid. For meropenem, at low pH, meropenem is positively charged and hence is well kept on the negatively charged surface of citrate-AuNPs. At higher pH, the positive charge is reduced; hence, the electrostatic attraction decreases, leading to decreased adsorption efficiency. Since the CFO@Au-citrate composite provides higher adsorption efficiencies than the CFO@Au-PDADMAC, in succeeding parts, we will focus our investigation only on the CFO@Au-citrate system, which is denoted simply as CFO@Au.

**3.2. Characterization of CFO@Au.** The XRD pattern of the CFO@Au sample is shown in Figure 1(a). Beside the diffraction peaks at 30.1, 35.4, 43.3, 53.6, 57.5, and 63.0°, corresponding to (220), (311), (111), (422), (511), and (440) planes of cubic spinel CFO, there are additional sharp peaks at 38.5, 44.0, 64.0, and 78.0° assigned to (222), (400), (440), and (444) planes of the face-centered cubic Au lattice [36, 37]. This result indicated that the composite of CFO@Au

has been successfully synthesized, and both phases are in well-developed crystalline structures.

**3.2.1. Surface Morphology.** The TEM images of the CFO material (Figure 1(b)) and the CFO@Au composite (Figure 1(c)) reveal that CFO particles have cubic or rectangular shapes with homogenous sizes from 10-20 nm. After coating with Au, the particles remain the same size but tend to form clusters, covered by additional small and round particles, which may correspond to the morphology of single sphere AuNPs prepared by the citrate method [38, 39].

**3.2.2. Infrared Spectra.** Comparison of FT-IR spectra of CFO@Au (Figure S3a) and CFO@Au-meropenem (Figure S3b) reveals the appearance of several weak bands at 1800-1600 cm<sup>-1</sup>, typical for valence vibration of the C=O group (1620 cm<sup>-1</sup>, 1744 cm<sup>-1</sup>) in spectra of CFO@Au-meropenem [28, 40]. In addition, we have the absorption bands in 1600-1200 cm<sup>-1</sup> regions belonging to aromatic rings (1566 cm<sup>-1</sup>, 1520 cm<sup>-1</sup>, 1398 cm<sup>-1</sup>, 1291 cm<sup>-1</sup>); the bands at >3000 cm<sup>-1</sup> correspond to C-H in aromatic ring (3296 cm<sup>-1</sup>, 3744 cm<sup>-1</sup>) and a wide adsorption band in 3400-2400 cm<sup>-1</sup> to O-H and N-H groups [28, 29]. The existence of organic functional groups belonging to meropenem in FT-IR spectra of CFO@Au-meropenem proves the adsorption of meropenem on the nanocomposite surface.

**3.2.3. UV-Vis Spectra.** UV-Vis absorption spectra of AuNPs, CFO, and CFO@Au particles dispersed in water were recorded in the wavelength range 400-800 nm (Figure S4).

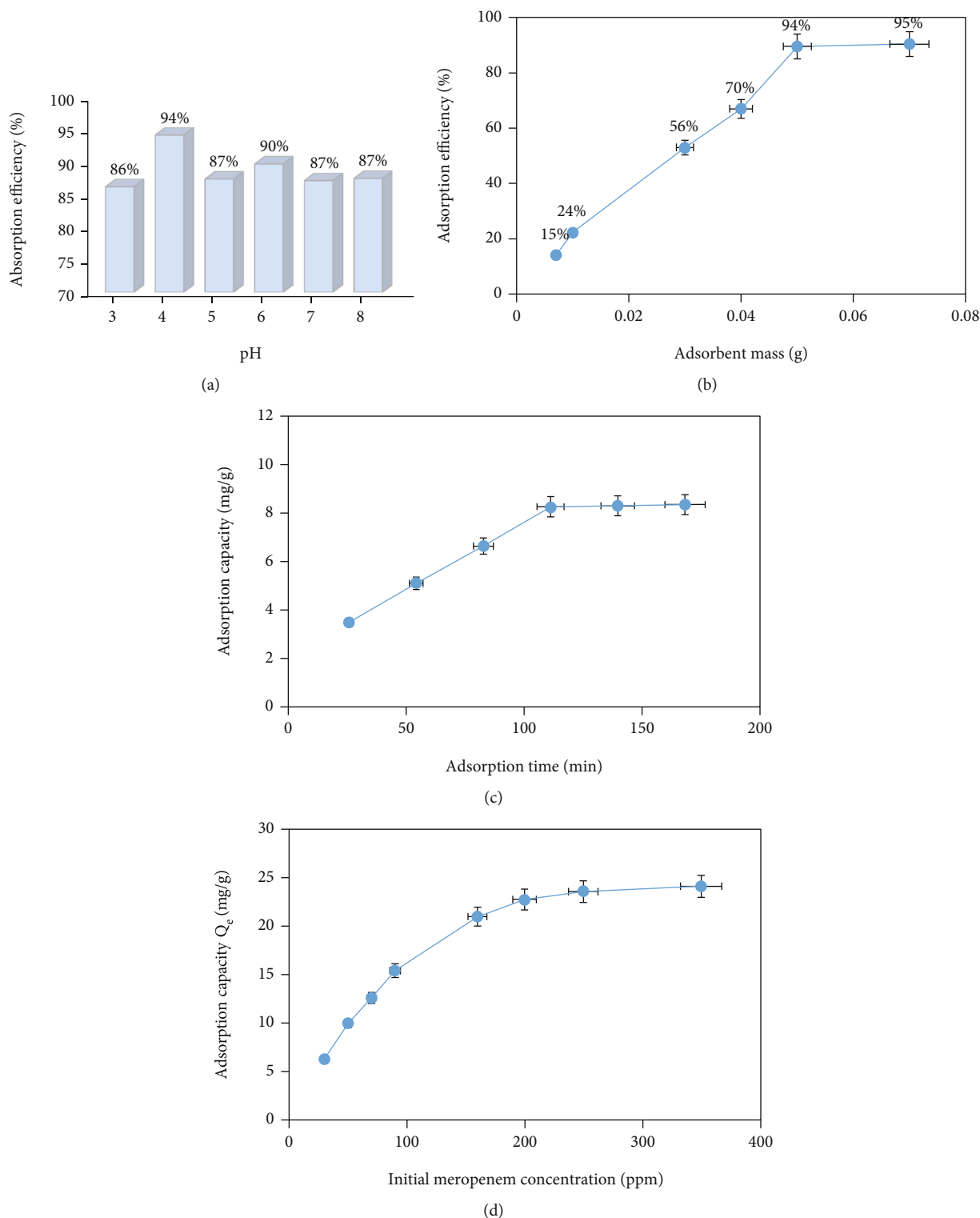


FIGURE 3: (a) The influence of solution pH on meropenem adsorption efficiency of CFO@Au, (b) the influence of adsorbent mass on meropenem adsorption efficiency, (c) the effect of adsorption time on kinetic adsorption, and (d) the effect of initial meropenem concentration on the adsorption capacity of the material.

CFO particles have no surface plasmon resonance (SPR) absorption in the investigated region, while AuNPs have a plasmon band with maximum absorption at 520 nm, typical for AuNPs having sizes of 10-30 nm [41, 42]. For

CFO@Au nanocomposite, a maximum absorption band was detected around 520 nm, but widened and slightly red-shifted. The appearance of the absorption band around 520 nm proved the existence of AuNPs on the surface of

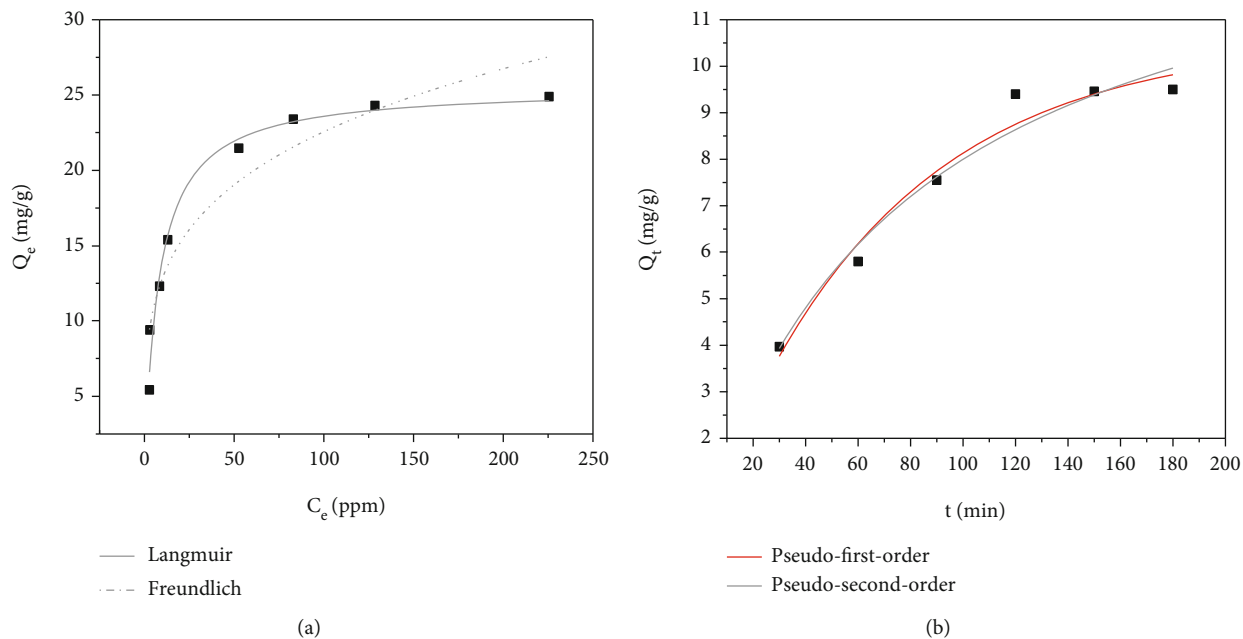


FIGURE 4: Isotherm and kinetic model fit with experimental data of meropenem adsorption on CFO@Au material. (a) Langmuir and Freundlich isotherm. (b) pseudofirst-order and pseudosecond-order kinetic model.

TABLE 1: Isotherm parameters of Langmuir and Freundlich models.

Langmuir model		Freundlich model	
$Q_{\max}$	25.5 mg/g	$K_F$	7.2918
$K_L$	8.15	$1/n$	0.24513
$\chi^2$	1.509	$\chi^2$	5.705
$R^2$	0.97693	$R^2$	0.91281

CFO, as confirmed by XRD measurement. The wavelength shift indicates the change in the dielectric constant of the material, which is inversely proportional to the plasmon vibrational frequency. The widening of the plasmon band is assigned to the decrease of electron exchange of AuNPs adsorbed on the CFO surface [43].

**3.2.4. Magnetic Properties.** In the CFO@Au composites as well as of CFO@Au-meropenem, CFO plays a role as magnetic support, which helps to easily recover material after using. The magnetic properties of CFO, CFO@Au, and CFO@Au-meropenem were characterized based on magnetic hysteresis loops  $M(H)$ . The  $M(H)$  loops provided in Figure 2 show typical soft magnetic behavior. From these curves, characteristic parameters such as remanent magnetizations and coercivities were derived as  $M_r \sim 16$  emu/g and  $H_c \sim 430$  G, respectively. The saturation magnetizations  $M_s$  differ among these samples as 55.8 emu/g, 51.3 emu/g, and 48.8 emu/g for CFO, CFO@Au, and CFO@Au-meropenem, respectively. The decrease in  $M_s$  is due to the coverage of non-magnetic Au as well as meropenem on magnetic core CFO. Despite this change, the composites CFO@Au and CFO@Au-meropenem still possess good magnetic properties.

After meropenem adsorption, CFO@Au powders can be easily separated from the solution after 3 min by using external magnets (Figure S5).

From the above measurements, we confirm that the CFO@Au nanocomposite was successfully fabricated with particle size ranging from 10-20 nm, and that the material has high crystallinity and good magnetic properties. This material was further used to investigate adsorption behavior of meropenem in batch adsorption experiments.

### 3.3. Adsorption of Meropenem on CFO@Au

**3.3.1. Effect of pH.** As mentioned in Section 3.1, for CFO@Au-citrate, the highest adsorption efficiency was obtained at pH 4.0 (Figure 3(a)), which is resulted from the strongest attraction force between negatively charged Au-citrate particles and positively charged meropenem at this pH.

**3.3.2. Effect of Adsorbent Mass.** The adsorbent mass strongly influences the number of adsorption centers, hence, strongly influences the meropenem adsorption capacity. As the adsorbent mass was varied between 0.007 and 0.07 g (see Figure 3(b)), the adsorption efficiency increased and tended to a maximum at 0.05 g. The increase of adsorption capacity with increasing adsorbent mass can be explained by the increase in the number of adsorption centers. However, when the mass of the material is above a certain amount, the adsorption capacity reaches saturation, which corresponds to the saturated adsorption of meropenem. The optimum mass adsorbent was selected as 0.05 g for further studies.

**3.3.3. Effect of Adsorption Time.** The effect of adsorption time on the meropenem adsorption on CFO@Au was

TABLE 2: Pseudofirst-order adsorption and pseudosecond-order adsorption rate constants ( $C_0 = 50$  ppm).

Model	Fit equation	$R^2$	$k$ (g/mg.min)	$q_e$ (exp) (mg/g)	$q_e$ (cal) (mg/g)
Pseudofirst-order adsorption	$q_t = q_e \left(1 - e^{-k_1 t}\right)$	0.97178	0.01466	9.5	10.572
Pseudosecond-order adsorption	$q_t = \frac{q_e^2 k_2 t}{1 + q_e k_2 t}$	0.96455	0.000874	9.5	14.365

investigated in the range from 0 to 180 min with an initial meropenem concentration of 50 ppm, pH 4.0, and adsorbent mass of 0.05 g. Figure 3(c) shows that the uptake of meropenem ( $q_t$ ) (mg/g) increased with increasing adsorption time and remained nearly constant after 120 min. The adsorption is rapid in the initial stages and gradually decreases with the progress of adsorption. All plots are single, smooth, and continuous curves leading to saturation.

**3.3.4. Effect of Initial Meropenem Concentration.** Initial meropenem concentration in the solution plays an important role as the movement of the constituents in the solution controls mass transfer between the solution and the adsorbent surface. Systematic investigation on the initial meropenem concentration was further carried out in a wide concentration range from 30 to 350 ppm, at pH 4.0, adsorbent mass of 0.05 g, and time of 120 min. As can be seen in Figure 3(d), the equilibrium adsorption capacity of meropenem increases significantly at low initial meropenem concentrations from 30 to 160 ppm, from 5.43 to 21.47 mg/g, then increases more slowly and reaches a maximum of 24.89 mg/g at meropenem concentration of 350 ppm. These data are further used to deduce the adsorption isotherms of meropenem on CFO@Au.

**3.4. Study on the Adsorption Isotherms.** The nonlinear regression fit of experimental results with Freundlich and Langmuir adsorption isotherm models are given in Figure 4(a). Comparing the fit parameters of the two models (Table 1), the Langmuir model provides a higher correlation coefficient  $R^2$  of 0.97693 and lower  $\chi^2$  of 1.50 than the Freundlich model ( $R^2$  of 0.91281 and  $\chi^2$  of 5.705), indicating better experimental agreement with the Langmuir rather than the Freundlich model. Hence, we conclude that the isothermal adsorption of meropenem on CFO@Au is by monolayer adsorption rather than multilayer adsorption, and the distribution of active sites on the surface of the adsorbent is uniform. The maximum adsorption capacity calculated from the Langmuir isotherm is rather high as 25.5 (mg/g), which suggests the potential of the composite material for meropenem adsorption in biomedical applications.

**3.5. Study on Kinetic Models of Static Kinetic Adsorption.** Diffusional mechanisms can be studied using three kinetic models including pseudofirst-order, pseudosecond-order, and intraparticle models. The regression correlation coefficient,  $R^2$ , of these models was used to determine the best-fit model.

**3.5.1. The Pseudofirst-Order Model and Pseudosecond-Order Model.** Fitting lines and correlation parameters are presented in Figure 4(b) and Table 2. Both pseudofirst-order and pseudosecond-order models have high correlation factors  $R^2$  (0.97178 for pseudofirst-order model and 0.96455 for pseudosecond-order model), indicating that both models could be satisfied and both physical diffusion and chemical adsorption via bonding between SH- group and gold surface are responsible for meropenem adsorption on CFO@Au material. Since the  $q_e$  value calculated from the fitted pseudofirst-order model (10.572 mg/g) is closer to  $q_e$  experimental (9.5 mg/g), the data seem to better follow the pseudofirst-order model. According to this model, the adsorption of meropenem on CFO@Au was assumed to proceed by diffusion through a boundary, and one adsorbate molecule was adsorbed onto one active site on the adsorbent surface [33].

Our observation on the simultaneous occurrence of physical diffusion and chemical adsorption agrees with other authors [28, 29], however, in their studies, the pseudosecond-order model provides a better account of meropenem adsorption on rice husk functionalized with Mg/Fe layered double hydroxides [29] and on multiwalled carbon nanotubes [28].

**3.5.2. The Intraparticle Diffusion Model.** Because the first two models did not convincingly describe the diffusion of meropenem onto the material surface, the intraparticle diffusion model was then tried as it is a widely used approach for the analysis of adsorption kinetics. This model states that adsorption changes roughly proportionally to  $t^{1/2}$  rather than with contact time  $t$ . The adsorbate was most probably transported into adsorbent through an intraparticle diffusion process with three steps. The first step is instantaneous adsorption or external surface adsorption. The next step is the fast adsorption stage, where intraparticle or pore diffusion is rate-limiting, followed by the final equilibrium step, where intraparticle diffusion begins to decelerate due to extremely low adsorbate concentrations remaining in the solutions adjacent to the particles [44, 45]. Adsorption data for  $q_t$  versus  $t^{1/2}$  is shown in three stages in Figure S6.

According to this model, a plot of  $q_t$  versus  $t^{1/2}$  should be linear if intraparticle diffusion is involved in the adsorption process. The three steps of the adsorption process are shown by the distinct stages in Figure S6. The slope of the graph is steeper at the start, indicating a boundary layer effect. In this stage, meropenem diffuses fast to the sorbent's surface and into the pores thanks to the driving force of electrostatic

attraction between meropenem and CFO@Au and the affinity interaction between meropenem and Au surface. There is also external resistance to mass transfer around the particles [46]. The second region is the gradual adsorption stage, representing micropore diffusion. Intraparticle diffusion is the rate-limiting step in this region. There is also the third stage, as indicated in Figure S6, where intraparticle diffusion began to slow, because the adsorbent was saturated and the concentrations of solutes were low.

#### 4. Conclusions

We have successfully synthesized a magnetic nanocomposite having high adsorptivity (maximum adsorption capacity of 25.5 mg/g) for meropenem, based on magnetic cobalt ferrite (CFO) and gold nanoparticles. Surface modification of CFO by AuNPs significantly enhanced the adsorption capacity efficiency of meropenem in comparison with bare CFO, thanks to affinity interaction between AuNPs on the surface with thioether and amine groups in the molecular structure of meropenem. The optimum conditions for adsorption of meropenem on CFO@Au were found to be pH 4.0, adsorption time 120 minutes, and adsorbent mass 0.05 g. The adsorption isotherm of meropenem CFO@Au follows well the Langmuir model; differences between first and second-order kinetic models are too small to resolve. Despite the presence of non-magnetic gold particles, the composite still possesses good magnetic properties, which is helpful for quickly collecting material after adsorption. CFO@Au material can be used for the separation and enrichment of meropenem from an aqueous solution and is also a potential candidate for other applications such as biological separation and target drug delivery.

#### Data Availability

All the data and supporting materials are included within the article.

#### Conflicts of Interest

All authors declare that there are no conflicts of interest regarding the publication of this paper.

#### Acknowledgments

The authors would like to thank Professor Alexander Scheeline, University of Illinois at Urbana-Champaign for giving valuable comments and revising English.

#### Supplementary Materials

Figure S1: chemical structure of meropenem. Figure S2: adsorption efficiencies of meropenem on C18, CFO, CFO@Au-citrate, and CFO@Au-PDADMAC. Figure S3: IR spectra of (a) CFO@Au; (b) CFO@Au@meropenem. Figure S4: UV-vis absorption spectra of (1) CFO, (2) AuNPs, and (3) CFO@Au solution. Figure S5: separation of CFO@Au-meropenem from aqueous solution using a magnetic stirrer. Figure S6: intraparticle diffusion plots for the adsorption of meropenem. (*Supplementary Materials*)

#### References

- [1] L. Wang, H.-Y. Park, S. I. I. Lim et al., "Core@shell nanomaterials: gold-coated magnetic oxide nanoparticles," *Journal of Materials Chemistry*, vol. 18, no. 23, pp. 2629–2635, 2008.
- [2] L. Wang, J. Luo, M. M. Maye et al., "Iron oxide–gold core–shell nanoparticles and thin film assembly," *Journal of Materials Chemistry*, vol. 15, no. 18, pp. 1821–1832, 2005.
- [3] M. Smith, M. McKeague, and M. C. DeRosa, "Synthesis, transfer, and characterization of core-shell gold-coated magnetic nanoparticles," *MethodsX*, vol. 6, pp. 333–354, 2019.
- [4] C. Karami and M. A. Taher, "A catechol biosensor based on immobilizing laccase to Fe<sub>3</sub>O<sub>4</sub>@Au core-shell nanoparticles," *International Journal of Biological Macromolecules*, vol. 129, pp. 84–90, 2019.
- [5] Y. Xing, Y.-Y. Jin, J.-C. Si et al., "Controllable synthesis and characterization of Fe<sub>3</sub>O<sub>4</sub>/Au composite nanoparticles," *Journal of Magnetism and Magnetic Materials*, vol. 380, pp. 150–156, 2015.
- [6] K. C. Grabar, R. G. Freeman, M. B. Hommer, and M. J. Natan, "Preparation and characterization of Au colloid monolayers," *Analytical Chemistry*, vol. 67, no. 4, pp. 735–743, 1995.
- [7] S.-I. Lo, P.-C. Chen, C.-C. Huang, and H.-T. Chang, "Gold nanoparticle–aluminum oxide adsorbent for efficient removal of mercury species from natural waters," *Environmental Science and Technology*, vol. 46, no. 5, pp. 2724–2730, 2012.
- [8] S. Banerjee, N. P. Kumar, A. Srinivas, and S. Roy, "Core-shell Fe<sub>3</sub>O<sub>4</sub>@Au nanocomposite as dual-functional optical probe and potential removal system for arsenic (III) from water," *Journal of Hazardous Materials*, vol. 375, pp. 216–223, 2019.
- [9] M. S. Najafinejad, P. Mohammadi, M. Mehdi Afsahi, and H. Sheibani, "Biosynthesis of Au nanoparticles supported on Fe<sub>3</sub>O<sub>4</sub>@polyaniline as a heterogeneous and reusable magnetic nanocatalyst for reduction of the azo dyes at ambient temperature," *Materials Science and Engineering: C*, vol. 98, pp. 19–29, 2019.
- [10] S. Wei, W.-W. Wang, X.-P. Fu, S.-Q. Li, and C.-J. Jia, "The effect of reactants adsorption and products desorption for Au/TiO<sub>2</sub> in catalyzing CO oxidation," *Journal of Catalysis*, vol. 376, pp. 134–145, 2019.
- [11] A. Kraus, K. Jainae, F. Unob, and N. Sukpirom, "Synthesis of MPTS-modified cobalt ferrite nanoparticles and their adsorption properties in relation to Au (III)," *Journal of Colloid and Interface Science*, vol. 338, no. 2, pp. 359–365, 2009.
- [12] Z. H. Li, J. H. Bai, X. Zhang et al., "Facile synthesis of Au nanoparticle-coated Fe<sub>3</sub>O<sub>4</sub> magnetic composite nanospheres and their application in SERS detection of malachite green," *Spectrochimica Acta Part A: Molecular and Biomolecular Spectroscopy*, vol. 241, p. 118532, 2020.
- [13] D. T. Nguyen, T. Charinpanitkul, D. W. Park, and K. S. Kim, "Preparation of magnetite hollow structure for drug delivery application," *Journal of Nanoscience and Nanotechnology*, vol. 14, no. 10, pp. 7995–7999, 2014.
- [14] D. T. Nguyen, D. W. Park, and K. S. Kim, "Seed-mediated synthesis of iron oxide and gold/iron oxide nanoparticles," *Journal of Nanoscience and Nanotechnology*, vol. 11, no. 8, pp. 7214–7217, 2011.
- [15] S. Seino, T. Kusunose, T. Sekino et al., "Synthesis of gold/magnetic iron oxide composite nanoparticles for biomedical applications with good dispersibility," *Journal of Applied Physics*, vol. 99, no. 8, p. 08H101, 2006.

- [16] J. Kudr, Y. Haddad, L. Richtera et al., "Magnetic nanoparticles: from design and synthesis to real world applications," *Nanomaterials*, vol. 7, no. 9, p. 243, 2017.
- [17] M. A. M. Tarkistani, V. Komalla, and V. Kayser, "Recent advances in the use of iron-gold hybrid nanoparticles for biomedical applications," *Nanomaterials*, vol. 11, no. 5, p. 1227, 2021.
- [18] S. Karamipour, M. S. Sadjadi, and N. Farhadyar, "Fabrication and spectroscopic studies of folic acid-conjugated  $\text{Fe}_3\text{O}_4/\text{Au}$  core-shell for targeted drug delivery application," *Spectrochimica Acta Part A: Molecular and Biomolecular Spectroscopy*, vol. 148, pp. 146–155, 2015.
- [19] J. Li, Y. Hu, J. Yang et al., "Hyaluronic acid-modified  $\text{Fe}_3\text{O}_4/\text{Au}$  core/shell nanostars for multimodal imaging and photothermal therapy of tumors," *Biomaterials*, vol. 38, pp. 10–21, 2015.
- [20] G. Zhou, Y. Wang, R. Zhou et al., "Synthesis of amino-functionalized bentonite/ $\text{CoFe}_2\text{O}_4/\text{MnO}_2$  magnetic recoverable nanoparticles for aqueous  $\text{Cd}^{2+}$  removal," *Science of the Total Environment*, vol. 682, pp. 505–513, 2019.
- [21] A. Virden, S. Wells, and K. O'Grady, "Physical and magnetic properties of highly anisotropic cobalt ferrite particles," *Journal of Magnetism and Magnetic Materials*, vol. 316, no. 2, pp. e768–e771, 2007.
- [22] Z. Zi, Y. Sun, X. Zhu, Z. Yang, J. Dai, and W. Song, "Synthesis and magnetic properties of  $\text{CoFe}_2\text{O}_4$  ferrite nanoparticles," *Journal of Magnetism and Magnetic Materials*, vol. 321, no. 9, pp. 1251–1255, 2009.
- [23] M. Grigorova, H. J. Blythe, V. Blaskov et al., "Magnetic properties and Mössbauer spectra of nanosized  $\text{CoFe}_2\text{O}_4$  powders," *Journal of Magnetism and Magnetic Materials*, vol. 183, no. 1–2, pp. 163–172, 1998.
- [24] G. G. Zhanel, R. Wiebe, L. Dilay et al., "Comparative review of the carbapenems," *Drugs*, vol. 67, no. 7, pp. 1027–1052, 2007.
- [25] C.-C. Sheu, Y.-T. Chang, S.-Y. Lin, Y.-H. Chen, and P.-R. Hsueh, "Infections caused by carbapenem-resistant enterobacteriaceae: an update on therapeutic options," *Frontiers in Microbiology*, vol. 10, 2019.
- [26] J. Cielecka-Piontek, K. Michalska, P. Zalewski, and S. Zasada, "Comparative review of analytical techniques for determination of carbapenems," *Current Analytical Chemistry*, vol. 8, no. 1, pp. 91–115, 2012.
- [27] C.-H. W. Chen Chun-Chi, K. Po-Yun, and Y.-L. Chen, "Nanomaterial-based adsorbents and optical sensors for illicit drug analysis," *Journal of Food and Drug Analysis*, vol. 28, no. 4, pp. 655–677, 2020.
- [28] M. Shaban, M. Ibrahim, M. M-Ridha, and H. Hussein, "Adsorption of meropenem antibiotics from aqueous solutions on multi-walled carbon nanotube," *International Review of Civil Engineering*, vol. 11, no. 6, pp. 283–293, 2020.
- [29] M. J. M-Ridha, Y. R. Hasan, and M. A. Ibrahim, "Adsorption kinetics and mechanisms for meropenem antibiotic removal in batch mode via rice husk functionalized with Mg/Fe-layered double hydroxides," *Separation Science and Technology*, vol. 56, pp. 2721–2733, 2020.
- [30] Q. K. Nguyen, T. H. Hoang, X. T. Bui, T. A. H. Nguyen, T. D. Pham, and T. N. M. Pham, "Synthesis and application of polycation-stabilized gold nanoparticles as a highly sensitive sensor for molecular cysteine determination," *Microchemical Journal*, vol. 168, p. 106481, 2021.
- [31] T. N. M. Pham, T. B. Le, D. D. Le et al., "Determination of carbapenem antibiotics using a purpose-made capillary electrophoresis instrument with contactless conductivity detection," *Journal of Pharmaceutical and Biomedical Analysis*, vol. 178, p. 112906, 2020.
- [32] I. Langmuir, "The adsorption of gases on plane surfaces of glass, mica and platinum," *Journal of the American Chemical Society*, vol. 40, no. 9, pp. 1361–1403, 1918.
- [33] E. E. Jasper, V. O. Ajibola, and J. C. Onwuka, "Nonlinear regression analysis of the sorption of crystal violet and methylene blue from aqueous solutions onto an agro-waste derived activated carbon," *Applied Water Science*, vol. 10, no. 6, 2020.
- [34] A. M. Brown, "A step-by-step guide to non-linear regression analysis of experimental data using a Microsoft Excel spreadsheet," *Computer Methods and Programs in Biomedicine*, vol. 65, no. 3, pp. 191–200, 2001.
- [35] H. Freundlich, "Über die Adsorption in lösungen," *Über Die Adsorption in Lösungen*, vol. 57U, no. 1, pp. 385–470, 1907.
- [36] W. Khalid, F. Jafar, N. Iqbal et al., "Synthesis of gold-coated  $\text{CoFe}_2\text{O}_4$  and their potential in magnetic hyperthermia," *Applied Physics A*, vol. 124, no. 7, p. 501, 2018.
- [37] M. Muneeswaran, A. Akbari-Fakhrabadi, M. A. Gracia-Pinilla, J. C. Denardin, and N. V. Giridharan, "Realization of structural transformation for the enhancement of magnetic and magneto capacitance effect in  $\text{BiFeO}_3\text{-CoFe}_2\text{O}_4$  ceramics for energy storage application," *Scientific Reports*, vol. 11, no. 1, p. 2265, 2021.
- [38] J. Dong, P. L. Carpinone, G. Pyrgiotakis, P. Demokritou, and B. M. Moudgil, "Synthesis of precision gold nanoparticles using Turkevich method," *Kona Powder and Particle Journal*, vol. 37, pp. 224–232, 2020.
- [39] J. Turkevich, P. C. Stevenson, and J. Hillier, "A study of the nucleation and growth processes in the synthesis of colloidal gold," *Discussions of the Faraday Society*, vol. 11, pp. 55–75, 1951.
- [40] B. Stuart, *Infrared Spectroscopy: Fundamental and Applications*, John Wiley & Sons Ltd., 2004.
- [41] P. K. Jain, K. S. Lee, I. H. El-Sayed, and M. A. El-Sayed, "Calculated absorption and scattering properties of gold nanoparticles of different size, shape, and composition: applications in biological imaging and biomedicine," *The Journal of Physical Chemistry B*, vol. 110, no. 14, pp. 7238–7248, 2006.
- [42] S. Alekseeva, I. I. Nedrygailov, and C. Langhammer, "Single particle plasmonics for materials science and single particle catalysis," *ACS Photonics*, vol. 6, no. 6, pp. 1319–1330, 2019.
- [43] A. O. Baskakov, A. Y. Solov'eva, Y. V. Ioni et al., "Magnetic and interface properties of the core-shell  $\text{Fe}_3\text{O}_4/\text{Au}$  nanocomposites," *Applied Surface Science*, vol. 422, pp. 638–644, 2017.
- [44] M. R. Samarghandi, T. J. Al-Musawi, A. Mohseni-Bandpi, and M. Zarrabi, "Adsorption of cephalixin from aqueous solution using natural zeolite and zeolite coated with manganese oxide nanoparticles," *Journal of Molecular Liquids*, vol. 211, pp. 431–441, 2015.
- [45] F. Kamar, A. Nechifor, G. Nechifor, T. Al-Musawi, and A. Mohammed, "Aqueous phase biosorption of Pb (II), Cu (II), and Cd (II) onto cabbage leaves powder," *International Journal of Chemical Reactor Engineering*, vol. 15, 2017.
- [46] Y. Mao and Q. Yue, "Kinetic modeling of phosphate adsorption by preformed and in situ formed hydrous ferric oxides at circumneutral pH," *Scientific Reports*, vol. 6, no. 1, p. 35292, 2016.

## Research Article

# Synthesis of $\text{CeO}_2\text{-Fe}_2\text{O}_3$ Mixed Oxides for Low-Temperature Carbon Monoxide Oxidation

**Chuc Ngoc Pham,<sup>1</sup> Quyen Van Trinh,<sup>2</sup> Dang Van Thai<sup>3,4</sup>, Nhiem Ngoc Dao<sup>1,5</sup>,  
Bac Quang Nguyen<sup>1,5</sup>, Dung Trung Doan,<sup>1</sup> Hung Bao Le,<sup>5,6</sup> Vinh Van Nguyen,<sup>6</sup>  
Lim Thi Duong,<sup>7</sup> and Lam Dai Tran<sup>8</sup>**

<sup>1</sup>*Institute of Materials Science, Vietnam Academy of Science and Technology, 18 Hoang Quoc Viet, Hanoi 10000, Cau Giay, Vietnam*

<sup>2</sup>*VNU - Hanoi School of Business and Management (VNU- HSB), 144 Xuan Thuy, Cau Giay, Hanoi 100000, Vietnam*

<sup>3</sup>*Institute of Theoretical and Applied Research, Duy Tan University, Hanoi 100000, Vietnam*

<sup>4</sup>*Faculty of Environmental and Chemical Engineering, Duy Tan University, Da Nang 550000, Vietnam*

<sup>5</sup>*Graduate University of Science and Technology, Vietnam Academy of Science and Technology, 18 Hoang Quoc Viet, Cau Giay, Hanoi 10000, Vietnam*

<sup>6</sup>*Vietnam-Russian Tropical Centre, Cau Giay, Hanoi 10000, Vietnam*

<sup>7</sup>*Institute of Geography, Vietnam Academy of Science and Technology, 18 Hoang Quoc Viet, Hanoi 10000, Cau Giay, Vietnam*

<sup>8</sup>*Institute for Tropical Technology, Vietnam Academy of Science and Technology, 18 Hoang Quoc Viet, Cau Giay, Hanoi 10000, Vietnam*

Correspondence should be addressed to Dang Van Thai; [dangvanthai2@duytan.edu.vn](mailto:dangvanthai2@duytan.edu.vn)

Received 7 October 2021; Revised 28 January 2022; Accepted 7 February 2022; Published 10 March 2022

Academic Editor: Ming Hua

Copyright © 2022 Chuc Ngoc Pham et al. This is an open access article distributed under the Creative Commons Attribution License, which permits unrestricted use, distribution, and reproduction in any medium, provided the original work is properly cited.

In this study, the  $\text{CeO}_2\text{-Fe}_2\text{O}_3$  mixed oxide catalysts have been prepared by combustion method using gel-created tartaric acid. The ability of effective carbon monoxide (CO) oxidation to carbon dioxide ( $\text{CO}_2$ ) by  $\text{CeO}_2\text{-Fe}_2\text{O}_3$  catalyst under low-temperature conditions was also demonstrated. The calcined  $\text{CeO}_2\text{-Fe}_2\text{O}_3$  material has a porous honeycomb structure and good gaseous absorption-desorption ability. The solid solution of  $\text{CeO}_2\text{-Fe}_2\text{O}_3$  mixed oxides was formed by the substitution of  $\text{Fe}^{+3}$  ions at some  $\text{Ce}^{4+}$  ion sites within the  $\text{CeO}_2$  crystal lattice. The results also showed that the calcination temperature and the molar ratio of  $\text{Ce}^{3+}$  ions to  $\text{Fe}^{3+}$  ions (CF) affected the formation of the structural phase and the catalytic efficiency. The catalytic properties of the  $\text{CeO}_2\text{-Fe}_2\text{O}_3$  mixed oxide were good at the CF ratio of 1 : 1, the average crystal size was near 70 nm, and the specific surface area was about  $20.22\text{ m}^2\cdot\text{g}^{-1}$ . The full conversion of CO into  $\text{CO}_2$  has been accomplished at a relatively low temperature of  $270\text{ }^\circ\text{C}$  under insufficient  $\text{O}_2$  conditions.

## 1. Introduction

Every year, the world emits a large amount of CO gas from thermal power plants, metallurgical plants, vehicles, wood burning, and waste burning. According to research in several developmental countries, thousands of people are died each year due to CO gas poisoning [1, 2]. The easy cause of CO gas poisoning is because its colorless, odorless, and nontoxic

properties are difficult to recognize. CO gas is the incomplete oxidation product of carbon compounds at low temperatures and  $\text{O}_2$  deficiency [3–5]. Under suitable conditions, CO exhibits strong reducing properties for medium metal oxides, so it has been studied and used in the metallurgical industry early [6]. Because of its possible toxic property to humans, the study and treatment of CO gas together with its secondary  $\text{CO}_2$  product are very important. In some

technical and industrial fields, CO<sub>2</sub> has begun to be captured and applied to reduce the greenhouse effect [7]. There are two popular methods for CO treatment as follows: adsorbing to capture CO gas [8–10] or converting CO to CO<sub>2</sub> by metal oxide catalysts [11].

Nowadays, CeO<sub>2</sub> is one of the important metal oxides in gas conversion catalysis. Cerium (Ce) belongs to the rare earth family and orders the second in the lanthanide series. Ce reserves account for a small proportion of the earth's crust, so exploitation is difficult and expensive. Ce has the electron configuration [Xe]4f<sup>1</sup>5d<sup>1</sup>6s<sup>2</sup>, which it can exist in the oxidation states Ce<sup>+3</sup> ([Xe]4f<sup>1</sup>5d<sup>6</sup>s) and Ce<sup>+4</sup> ([Xe]4f<sup>5</sup>d<sup>6</sup>s). Thus, CeO<sub>2</sub> and Ce<sub>2</sub>O<sub>3</sub> are the compounds of Ce with oxygen, and CeO<sub>2</sub> is more stable due to the electron configuration of Ce<sup>+4</sup> ([Xe]4f<sup>5</sup>d<sup>6</sup>s) being similar to that of the inert xenon gas [12]. The flexible conversion of the two Ce<sup>+4</sup> and Ce<sup>+3</sup> states through the electron donor mechanisms on the surface of CeO<sub>2</sub> makes it widely used in catalytic reactions such as wastewater treatment [13–16], water-gas phase transition [17], and gas conversion [18–21]. CeO<sub>2</sub> oxides can be prepared by hydrothermal method [21, 22], coprecipitation [23–25], sol-gel [19, 26], impregnation [27], and combustion [18]. The choice of the fabrication method decides the crystal structure, morphology, and physicochemical properties of CeO<sub>2</sub>, leading to affect the CO conversion ability of the catalyst [21, 22, 28]. The surface of the fabricated CeO<sub>2</sub> crystals is often imperfect due to lattice defect, vacuous O<sup>2-</sup> ion (denoted V<sub>O</sub>) sites, and unsaturated bonds leading to the existence of Ce<sup>+3</sup> and Ce<sup>+4</sup> states [20, 29]. The ratio between the number of Ce<sup>+3</sup> ions to Ce<sup>+4</sup> ions (Ce<sup>+3</sup>/Ce<sup>+4</sup>) is related to the number of V<sub>O</sub> vacancies on the CeO<sub>2</sub> crystal surface, so it determines the oxygen storage capability and oxygen lease capability [25]. When the Ce<sup>+3</sup>/Ce<sup>+4</sup> ratio is large, the number of V<sub>O</sub> vacancies on the surface is also large [30]. Besides, the number of V<sub>O</sub> also depends on the crystal morphology, and it decreases gradually with nanorods > cubes nanoscale > nanopolyhedra [29]. The density functional theory (DFT) calculations show that for low-index faces, the energy to release an O<sup>2-</sup> ion from the lattice to create a V<sub>O</sub> vacancy of (111) face is the largest in comparison with the (110) and (100) face, so the number of V<sub>O</sub> on the faces decreases in the order (110) > (100) > (111) [29]. In addition, CeO<sub>2</sub> is a direct band-gap semiconductor with bandgap energies of 2.56 eV for the bulk sample and 3.23 eV for the nanoscale, corresponding to the absorption transition energy 2p (O<sup>2-</sup>) → 4f (Ce<sup>+4</sup>) [26, 30]. When an O<sup>2-</sup> ion on the crystal surface gets an excitation agent to promote the electron transition 2p → 4f, it will separate from the crystal lattice leaving a V<sub>O</sub> vacancy in company with the oxidation state transformation Ce<sup>+4</sup>(4f<sup>0</sup>) → Ce<sup>+3</sup>(4f<sup>1</sup>) [11]. V<sub>O</sub> vacancies are capable of adsorbing CO or O<sub>2</sub> molecules at these positions, so they play an important role in catalytic reactions. An O<sub>2</sub> molecule can be captured by a V<sub>O</sub> vacancy to form an O<sup>2-</sup> lattice ion [31]. The combination reactions of CO molecules with the absorbed O<sub>2</sub> molecules on the surface of the oxide catalyst are occurred by the Langmuir-Hinshelwood (L-H) mechanism or with the O<sup>2-</sup> ions of the lattice by the Mars-van Krevelen (M-K) mechanism [29]. The CeO<sub>2</sub> oxide catalyst

material becomes thermal stable, has a fast catalytic rate, and has a low catalytic temperature when combined with some rare metals such as Pt [32], Pd [33], Au [34], and Ag [35]. However, a current trend uses the low-cost transition metal iron (Fe) element to make Fe<sub>2</sub>O<sub>3</sub>-CeO<sub>2</sub> mixed oxides. In nature, iron exists in both Fe<sup>2+</sup> and Fe<sup>3+</sup> oxidation states. The radius of Fe<sup>3+</sup> ion (0.64 Å) is smaller than that of Ce<sup>+4</sup> ion (1.01 Å), so the substitution of Fe<sup>3+</sup> ions in some Ce<sup>+4</sup> ion positions can shrink the CeO<sub>2</sub> crystal lattice, the 2θ diffraction angle positions of the (111) face is shifted towards the larger angle, and the formed possibility of V<sub>O</sub> vacancies is also increased [36]. The optical absorption transition properties of Fe<sub>2</sub>O<sub>3</sub> oxide include the direct charge transition O<sup>2-</sup>(2p) → Fe<sup>3+</sup>(3d) in the ultraviolet region and the indirect charge transition between Fe<sup>3+</sup>(3d) states in the visible region [37]. The conversion ability between Fe<sup>3+</sup> and Fe<sup>2+</sup> ions become even more flexible in Fe<sub>2</sub>O<sub>3</sub>-CeO<sub>2</sub> composition, which is demonstrated through photochemical reactions treating organic pigments [15]. The O<sup>2-</sup> ions of the Fe-O-Ce bonds react better with CO than that of the Ce-O-Ce bonds [38], even so than those of Fe-O-Fe bonds. The energy separates an O<sup>2-</sup> atom from the surface to create a V<sub>O</sub> vacancy of about 3.04 eV [39]. The redox potential of the Fe<sup>+3</sup>/Fe<sup>+2</sup> pair (0.71 eV) is smaller than that of the Ce<sup>+4</sup>/Ce<sup>+3</sup> pair (1.61 eV), which facilitates the electron donor-acceptor processes and the oxidation state transformation of Ce<sup>+4</sup>/Ce<sup>+3</sup> and Fe<sup>+3</sup>/Fe<sup>+2</sup> pairs [20]. Other studies show that the combination of Ce and Fe elements forms CeO<sub>2</sub>-Fe<sub>2</sub>O<sub>3</sub> mixed oxide, which can reduce the reactive catalytic temperature of 50% (T<sub>50</sub>) and 100% (T<sub>100</sub>) CO conversion in comparison with single oxide catalysts of CeO<sub>2</sub> and Fe<sub>2</sub>O<sub>3</sub>, depending on the fabrication method [31, 40, 41].

From the above-mentioned characteristics, it shows that the CeO<sub>2</sub>-Fe<sub>2</sub>O<sub>3</sub> mixed oxide material has many advantageous photochemical properties that need further studying and applying for life. This study was carried out with the purpose of making CeO<sub>2</sub>-Fe<sub>2</sub>O<sub>3</sub> mixed oxide materials from popular Fe metal, reducing the content of rare earth Ce and the reactive catalytic temperature of complete CO conversion to CO<sub>2</sub> while applying to treat the exhaust gas in simple incinerators.

## 2. Chemicals and Experiments

**2.1. Preparation of Mixed Oxide Catalysts.** High-purity chemicals were used as Fe(NO<sub>3</sub>)<sub>3</sub>·6H<sub>2</sub>O (99.98%), Ce(NO<sub>3</sub>)<sub>3</sub>·6H<sub>2</sub>O (99.98%), and tartaric acid (TA) (99.98%). TA was dissolved with twice distilled water at 80 °C to get A solution. The above nitrate salts were also dissolved to give B solution such that the molar ratio of CF mixture to TA solution always was 1:3. A regulator matter was utilized to keep the pH of the solution equal to 2. The B solution was slowly added to the A solution, stirred, and heated at 80 °C for 2 h to obtain a pale-yellow homogeneous gel solution. The gel was then dried at 100 °C for 4 h to obtain a porous shape sample. The obtained sample was analyzed by TGA to investigate the phase transition of the sample in accordance with the calcination temperature. The samples calcined in turn at 450, 550, 650, 750, 850, and 950 °C for 2 h to obtain mixed

oxides which denote as CF450, CF550, CF650, CF750, CF850, and CF950. To investigate the influence of the CF molar ratio on the structural phase formation of mixed oxides, the weight of the nitrate salts in the B solution was calculated so that the CF molar ratio of the obtained gels is in turn 9:1; 3:1; 1:1; 1:3, and 1:9. These gels, calcined at 650 °C for 2 h, received the mixed oxides of CF91, CF31, CF11, CF13, and CF19, respectively.

## 2.2. Analytics

**2.2.1. Differential Thermal Analysis and Thermogravimetric Analysis.** Differential thermal analysis (DTA) and thermogravimetric analysis (TGA) were performed on a Labsys Evo 1600 system. Samples were measured in air, heating rate 10 °C.min<sup>-1</sup>.

**2.2.2. X-Ray Diffraction Analysis.** X-ray diffraction (XRD) measurements of the studied samples were performed on a Siemens D5000 X-meter.

**2.2.3. Scanning Electron Microscopy Image.** The surface morphology of the materials was recorded by scanning electron microscopy (SEM). Samples were measured on a Hitachi S-4800 instrument operating at 10 kV with a magnification of 80000-100000 times.

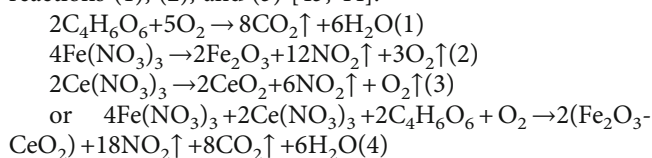
**2.2.4. Determine the Specific Surface Area.** The sample surface area was determined by the Brunauer-Emmett-Teller (BET) method on the Autosorb IQ Station measuring system. BET equation:  $P/[V(P_o - P)] = 1/V_m C + [(C - 1)/V_m C] \cdot P/P_o$ , where  $P$  is the equilibrium pressure,  $P_o$  is the saturated vapor pressure of the adsorbed gas at experimental temperature,  $V$  is the volume of the adsorbed gas at pressure  $P$ , and  $V_m$  is the saturated gas volume of monolayer adsorption per 1 gram of adsorbent, and  $C$  is the BET constant. The specific surface area BET ( $S_{BET}$ ) of the material is calculated according to the equation:  $S_{BET} = (V_m/M) \cdot N A_m d$ , where  $d$  is the density,  $M$  is the molar mass of the adsorbent, respectively,  $N$  is the Avogadro number ( $N = 6.023 \times 10^{23}$  molecules.mol<sup>-1</sup>), and  $A_m$  is the cross-sectional area of 1 molecule occupied on the surface adsorbent.

**2.2.5. Fourier Transform Infrared Spectra.** The Fourier transform infrared (FTIR) spectra of the samples were recorded in the range of wavenumbers from 400 cm<sup>-1</sup> to 4000 cm<sup>-1</sup> on the Impact 410 spectrometer.

**2.2.6. Determination of CO Conversion.** The TPSR temperature surface response program was conducted with a Siemens temperature controller. The CO conversion of the catalytic material performing on the microcurrent device was calculated by the following formula:  $H (\%) = (C_f/C_o) \cdot 100\%$ , where  $H$  is the CO (%) conversion and  $C_o$  and  $C_f$  are the CO concentrations before and after catalysis, respectively.

## 3. Results and Discussions

**3.1. DTA and TGA Spectra of CeO<sub>2</sub>-Fe<sub>2</sub>O<sub>3</sub> Mixed Oxides.** The DTA and TGA spectra of the gel sample with the CF/TA ratio of 1:3 presented in Figure 1. The DTA curve showed the temperature increased from 100 °C to 250 °C. The sample weight decreased by 38.89%, with an endothermic peak at 217 °C. This reduction may be due to the physical evaporation of the adsorbed water on the gel surface [42, 43]. In the temperature range from 250 °C to 550 °C, the sample weight decreased by 34.83% on the TGA curve corresponding to the exothermic peak of 328 °C on the DTA curve, which was caused by the pyrolysis processes of the nitrate salts released O<sub>2</sub> and NO<sub>2</sub> gas; the combustion process of the TA released CO<sub>2</sub> gas and H<sub>2</sub>O according to the following reactions (1), (2), and (3) [43, 44]:



When the temperature increased from 550 °C to 900 °C, the sample weight was almost unchanged, showing that the Fe<sub>2</sub>O<sub>3</sub>-CeO<sub>2</sub> mixed oxide was formed and stable.

**3.2. FTIR Spectra of CeO<sub>2</sub>-Fe<sub>2</sub>O<sub>3</sub> Mixed Oxides.** The appearance of vibrations characterized to the bonds of CeO<sub>2</sub>-Fe<sub>2</sub>O<sub>3</sub> mixed oxide determined via the FTIR spectra. In Figure 2, the FTIR spectra of all samples in the broad absorption range from 3000 cm<sup>-1</sup> to 3500 cm<sup>-1</sup> appeared a peak at about 3378 cm<sup>-1</sup> characterized by the stretching vibration of the O-H group because of the physically adsorbed water; however, this peak intensity decreased gradually as the calcination temperature of samples increased. A peak at about 2337 cm<sup>-1</sup> characterized the stretching vibration of adsorbed CO<sub>2</sub> molecules from the air for CF450, CF550, and CF650 samples, and this peak was completely suppressed for CF750 and CF850 samples. The peaks at 1630, 1380, and 1121 cm<sup>-1</sup> represented the C=O and C-O stretching vibrations of the -COO- group [42, 43]. At the high calcination temperature, the process of CO<sub>2</sub> separation occurred, so the absorption intensity of the band related to -COO- decreased and expanded into a large halo as on the CF850 sample. It is noteworthy that the appearance of the peak at 529 cm<sup>-1</sup> with strong absorption intensity for samples calcined at 850 °C was typical for Fe-O vibrations, the peaks of 643 and 443 cm<sup>-1</sup> were characteristic of Ce-O vibrations [42, 43, 45], and the above peaks appeared clear for the CF650 sample. This also shows that the characteristic phases of the CeO<sub>2</sub>-Fe<sub>2</sub>O<sub>3</sub> mixed oxide were soon formed, and it was also consistent with the result of the TGA-DTA analysis.

**3.3. The Role of Calcination Temperature and Metal Ion Molar Ratio in the Structural Phase Formation of CeO<sub>2</sub>-Fe<sub>2</sub>O<sub>3</sub> Mixed Oxides**

**3.3.1. The Role of Calcination Temperature.** The thermogravimetric analysis shows that the suitable calcination

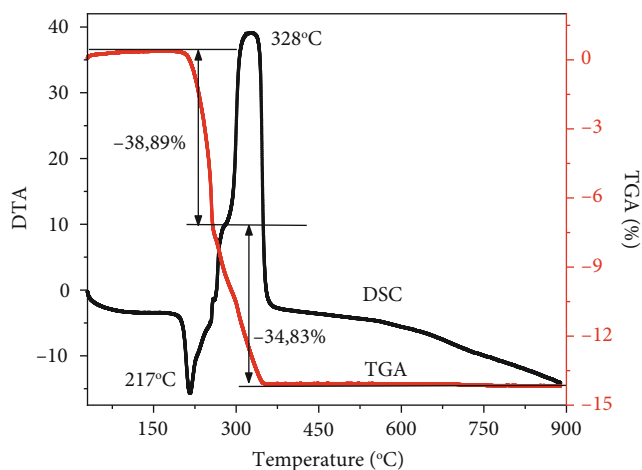


FIGURE 1: TGA and DTA spectra of the gel sample with the CF/TA ratio of 1:3.

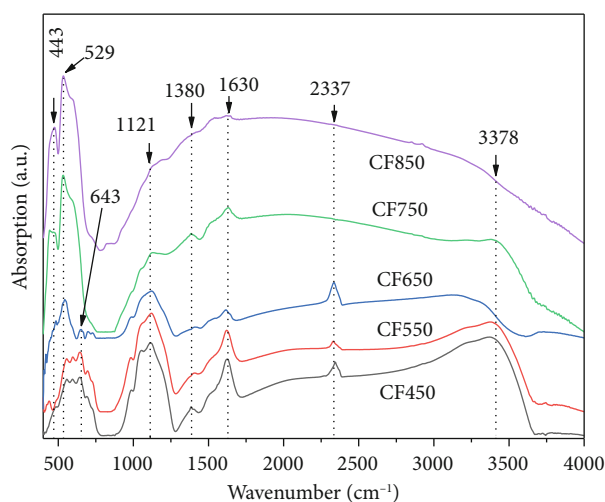


FIGURE 2: FTIR spectra of gel samples with the CF/TA ratio of 1:3 calcined at different temperatures for 2 h.

temperature range was from 450 to 900 °C. Figure 3 presents the XRD pattern of the  $\text{CeO}_2\text{-Fe}_2\text{O}_3$  mixed oxides calcined at 450, 550, 650, 750, 850, and 900 °C for 2 h. At 450 °C and 550 °C, the XRD pattern of CF450 and CF550 only appeared the (111), (200), and (220) faces corresponding to the  $2\theta$  diffraction angles at 28.96°, 33.11°, and 47.47° (JCPDS No. 34-0394), in which the (111) face had the greatest intensity. These faces characterized the face-centered cubic structure of  $\text{CeO}_2$  in mixed oxides [36]. Meanwhile, at these calcination temperatures, there were almost no faces that characterized the structural phase of  $\text{Fe}_2\text{O}_3$ . This may be because the samples had not reached good crystallinity, and the crystal structure was not complete. At 650 °C, the reflection faces characterizing the structural phase of  $\text{Fe}_2\text{O}_3$  also occurred clearly and intertwined with those of  $\text{CeO}_2$  as the represented spectrum of the CF650 sample in Figure 3(b). The (311), (222), (400), (331), (420), (422), and (511) faces corresponded to  $2\theta$  diffraction angles of 56.32°, 59.02°, 69.42°,

76.66°, 79.92°, 88.39°, and 95.04° belonged to the  $\text{CeO}_2$  crystal structure, but the (012), (110), (024), and (116) faces assigned to  $2\theta$  angles of 24.92°, 35.64°, 49.46°, and 54.02°, respectively, representing the hexagonal structure phase of  $\text{Fe}_2\text{O}_3$  (JCPDS No. 33-0664) [14, 19, 27].

The diffraction intensity on all faces became narrower and stronger as the calcination temperature increased. This meant that the samples had better crystallinity, a complete crystal structure, and larger crystal sizes [46]. However, when the samples calcined to 750 °C and 850 °C, a separating tendency of mixed oxide phase into two single oxide phases of  $\text{CeO}_2$  and  $\text{Fe}_2\text{O}_3$  was happened because of these more thermal stable oxides. Based on the XRD pattern and Brass' formula, it is able to determine the  $a$  lattice constant via the (111) face of all the  $\text{CeO}_2\text{-Fe}_2\text{O}_3$  mixed oxides, as seen in Table 1.

The results showed that there was a slight increase of the  $a$  lattice constant from 5.3385 to 5.3530 Å, corresponding to a slight decrease of the  $2\theta$  diffraction angle from 28.96 to 28.89 Å. The increase of the  $a$  lattice constant together with the left shift of the  $2\theta$  angle indicated that the calcination sample at 450 °C had formed in a solution of  $\text{CeO}_2\text{-Fe}_2\text{O}_3$  mixed oxide [23]. It is explained that the  $\text{Fe}^{3+}$  (0.64 Å) ion radius is smaller than the  $\text{Ce}^{4+}$  (1.01 Å) ion radius, so when the  $\text{Ce}^{4+}$  ions are replaced by  $\text{Fe}^{3+}$  ions at some  $\text{CeO}_2$  lattice sites, these substitutions cause the shrink of the crystal lattice [36]. In contrast, the partial separation of the  $\text{CeO}_2$  phase widened the crystal lattice and shifted the  $2\theta$  angle position of the (111) face towards a smaller angle as illustrated by CF450, CF650, and CF850 patterns in the small inset of Figure 3(b). Thus, it can be seen that the change in calcination temperature affected the formation of mixed oxide solution. At 650 °C, the crystal was complete with the appearance of both  $\text{CeO}_2$  and  $\text{Fe}_2\text{O}_3$  phases. When the calcination temperature of the sample increased, the mixed oxides had good crystallization and tended to the segregation of single oxide phases.

**3.3.2. The Role of Metal Ion Molar Ratio.** XRD pattern of  $\text{CeO}_2\text{-Fe}_2\text{O}_3$  mixed oxides with different CF molar ratios calcined at 650 °C for 2 h, as seen in Figure 4. When the molar quantity of  $\text{Ce}^{3+}$  ions was more than that of  $\text{Fe}^{3+}$  ions (CF91 and CF31 samples), the XRD pattern manifested the (111), (200), (220), (311), (222), (400), (331), (422), and (511) faces corresponded to the  $2\theta$  diffraction angles of 28.82°, 33.11°, 47.47°, 56.32°, 59.07°, 69.41°, 76.64°, 79.91°, 88.39°, and 95.04° and characterized the crystalline structure phase of  $\text{CeO}_2$  (for CF91 and CF31 samples in Figure 4(a)) [14, 19, 27].

This may be because with the calcination condition to 650 °C, and the used  $\text{Fe}^{3+}$  ion content was smaller in comparison with the  $\text{Ce}^{4+}$  ion content, so  $\text{Fe}^{3+}$  ions were dissolved in the crystal lattice of  $\text{CeO}_2$  oxide [23]. When the molar quantity of  $\text{Ce}^{3+}$  ion and  $\text{Fe}^{3+}$  ions was equal, the characteristic faces of the  $\text{Fe}_2\text{O}_3$  phase appeared and intertwined with those of  $\text{CeO}_2$ , and the XRD pattern of CF11 was presented again in Figure 4(b). The presence of the typical (110) face of  $\text{Fe}_2\text{O}_3$  shows that the mixed oxide has

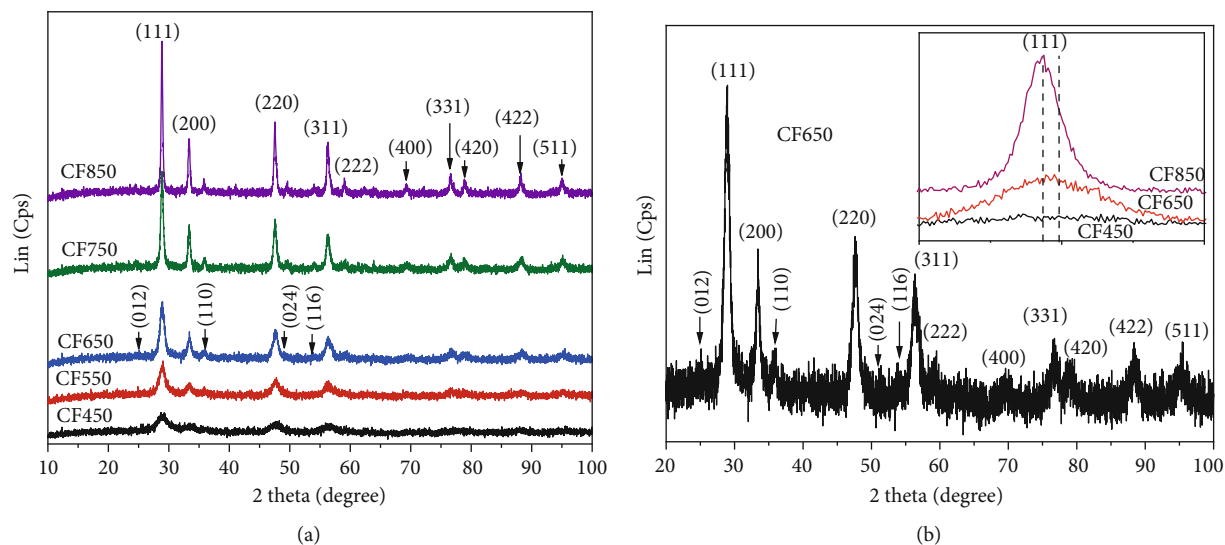


FIGURE 3: XRD pattern of  $\text{CeO}_2\text{-Fe}_2\text{O}_3$  mixed oxides. Samples with the CF molar ratio of 1 : 1 calcined at different temperatures for 2 h (a) and CF650 sample was redrawn (b).

TABLE 1:  $2\theta$  diffraction angle and  $a$  lattice constant of  $\text{CeO}_2\text{-Fe}_2\text{O}_3$  mixed oxides calcined at different temperatures for 2 h.

Sample	CF450	CF550	CF650	CF750	CF850
Diffraction angle $2\theta$ (degree)	28.96	28.94	28.92	28.89	28.88
Lattice constant $a$ (Å)	5.3385	5.3422	5.3458	5.3512	5.3530

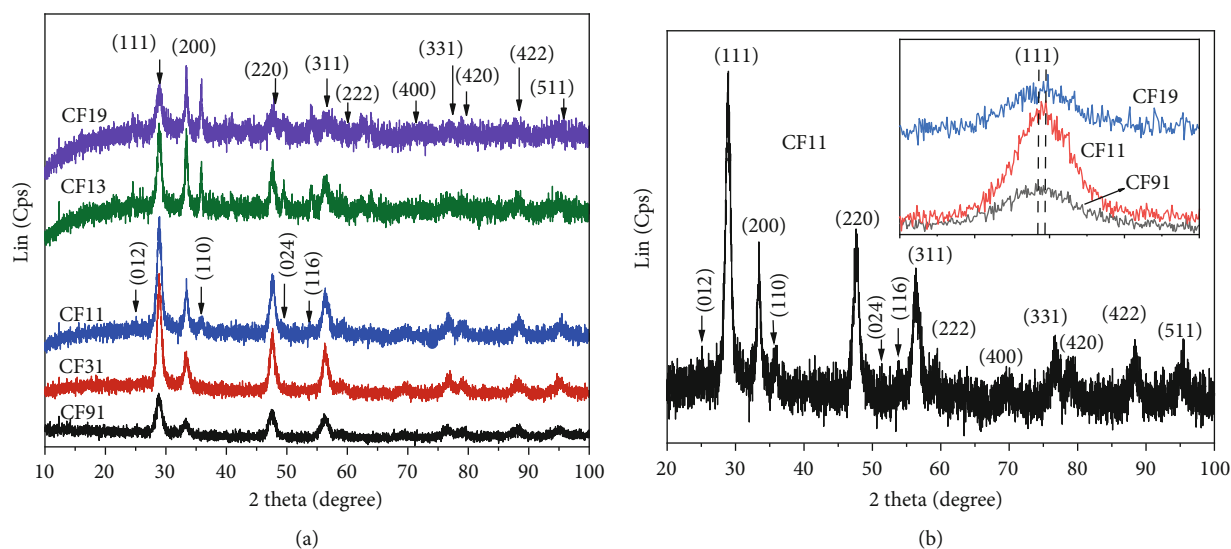


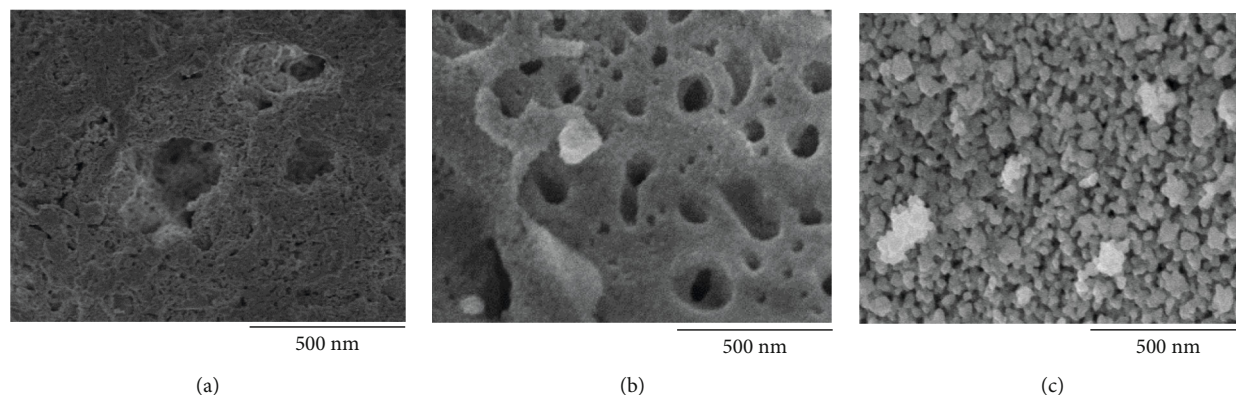
FIGURE 4: XRD patterns of  $\text{CeO}_2\text{-Fe}_2\text{O}_3$  mixed oxides. Samples with different CF molar ratios calcined at  $650^\circ\text{C}$  for 2 h (a) and CF11 sample was redrawn (b).

separated into phases [47]. When the molar quantity of  $\text{Ce}^{3+}$  ions was smaller than those of  $\text{Fe}^{3+}$  ions (for CF13 and CF19 samples), the diffraction intensity on the (110) face became more narrow and stronger. This phenomenon was known that the molar quantity of  $\text{Fe}^{3+}$  ions in mixed oxides was high, which led to the split gradually mixed oxides into

two individual oxide phases of  $\text{CeO}_2$  and  $\text{Fe}_2\text{O}_3$  [23]. The  $a$  lattice constants of  $\text{CeO}_2$  were calculated from the (111) face in Table 2. As a result, there was a slight decrease of  $a$  lattice constant from  $5.3639\text{ \AA}$  to  $5.3385\text{ \AA}$ , while the  $2\theta$  diffraction angle of the (111) face shifted towards the greater diffraction angle from  $28.82^\circ$  to  $28.98^\circ$ , respectively. This

TABLE 2:  $2\theta$  diffraction angle and  $a$  lattice constant of  $\text{CeO}_2\text{-Fe}_2\text{O}_3$  mixed oxides with different CF molar ratios calcined at  $650\text{ }^\circ\text{C}$  for 2 h.

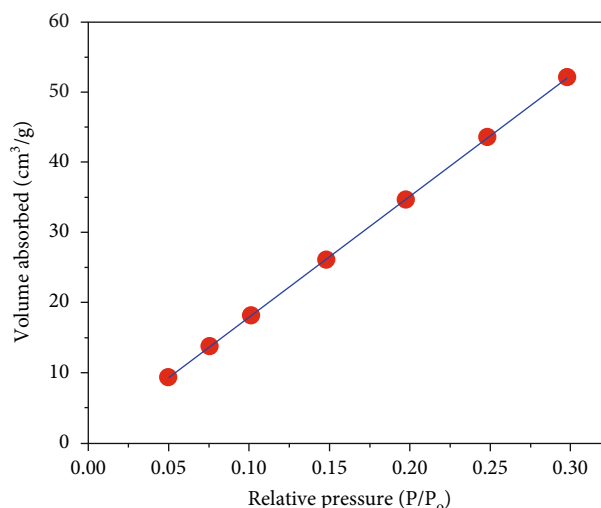
Sample	CF91	CF31	CF11	CF13	CF19
Diffraction angle $2\theta$ (degree)	28.82	28.87	28.92	28.94	28.98
Lattice constant $a$ (Å)	5.3639	5.3548	5.3458	5.3421	5.3385

FIGURE 5: SEM images of  $\text{CeO}_2\text{-Fe}_2\text{O}_3$  mixed oxides with the CF ratio of 1 : 1 calcined at  $450\text{ }^\circ\text{C}$  (a),  $650\text{ }^\circ\text{C}$  (b), and  $850\text{ }^\circ\text{C}$  (c) for 2 h.

shift can observe clearly by CF91, CF11, and CF19, as seen in the small inset in Figure 3(b) [20, 23, 24, 36]. The above results showed that the change in CF molar ratio also affected the formation of the crystal structure phase of the mixed oxides. With a CF molar ratio of 1 : 1, there appeared characteristic reflection faces for the structural phases of  $\text{CeO}_2$  and  $\text{Fe}_2\text{O}_3$ . When the molar quantity of  $\text{Fe}^{3+}$  ions were high, the  $\text{CeO}_2\text{-Fe}_2\text{O}_3$  mixed oxide tended to separate into two oxide phases of  $\text{CeO}_2$  and  $\text{Fe}_2\text{O}_3$ .

**3.4. Morphology of  $\text{Fe}_2\text{O}_3\text{-CeO}_2$  Mixed Oxides.** SEM images of the  $\text{CeO}_2\text{-Fe}_2\text{O}_3$  mixed oxides were shown in Figure 5 with the CF molar ratio of 1 : 1 which were calcined at temperatures of  $450\text{ }^\circ\text{C}$ ,  $650\text{ }^\circ\text{C}$ , and  $850\text{ }^\circ\text{C}$  for 2 h. It is observed that the surface of the CF450 sample was porous. This is the characteristic of materials that are prepared by the combustion method using organic compounds to create gels (Figure 5(a)) [48]. For the CF650 sample, the porous property became clear to many honeycomb-like cavities. It can be explained that the molecular structure of TA consists of strongly polar functional groups  $\text{HOOC}(\text{HO})\text{CC}(\text{OH})\text{COOH}$  that played the role of stretching and uniformly dispersing  $\text{Ce}^{3+}$  and  $\text{Fe}^{3+}$  ions in solution [49]. At  $650\text{ }^\circ\text{C}$ , the decomposition of the organic component and the pyrolysis of nitrate salts led to a decrease in volume and mass, creating a system of space-connected microcapillary tubes (Figure 5(b)). This created a porous property of mixed oxides as well as the obtained result in other reports [50]. The average crystal size of the oxide was determined to be about 70 nm. For the CF850 sample, the crystals tended to break the spatial porous block into discrete nanosized particles (Figure 5(c)) [42].

From the dependence of  $P/[V(P_0 - P)]$  on  $P/P_0$  in the BET equation, the adsorption-desorption isotherm representing the relation between the adsorbed volume and the relative pressure was shown in Figure 6. The linear shape

FIGURE 6: Nitrogen adsorption-desorption isotherms of  $\text{CeO}_2\text{-Fe}_2\text{O}_3$  mixed oxide with the CF molar ratio of 1 : 1 calcined at  $650\text{ }^\circ\text{C}$  for 2 h.

of the isotherm in the low  $P/P_0$  value range indicated that monolayer adsorption occurred on the surface of the porous catalyst, and it is also suitable for the linear region in the range of  $P/P_0$  from 0.05 to 0.35 of this material [51]. The specific surface area of the  $\text{CeO}_2\text{-Fe}_2\text{O}_3$  mixed oxide, CF650 sample, was determined at about  $20.22\text{ m}^2\cdot\text{g}^{-1}$ .

**3.5. Process of CO Conversion to  $\text{CO}_2$ .** The process of CO oxidation by  $\text{CeO}_2\text{-Fe}_2\text{O}_3$  mixed oxide catalysts and the curves of CO conversion according to temperature is described via Figure 7. Under the catalytic temperature condition below  $300\text{ }^\circ\text{C}$  and deficient  $\text{O}_2$  gas, the activities of CO oxidation took place [6]. The CF91, CF31, CF13, and CF19

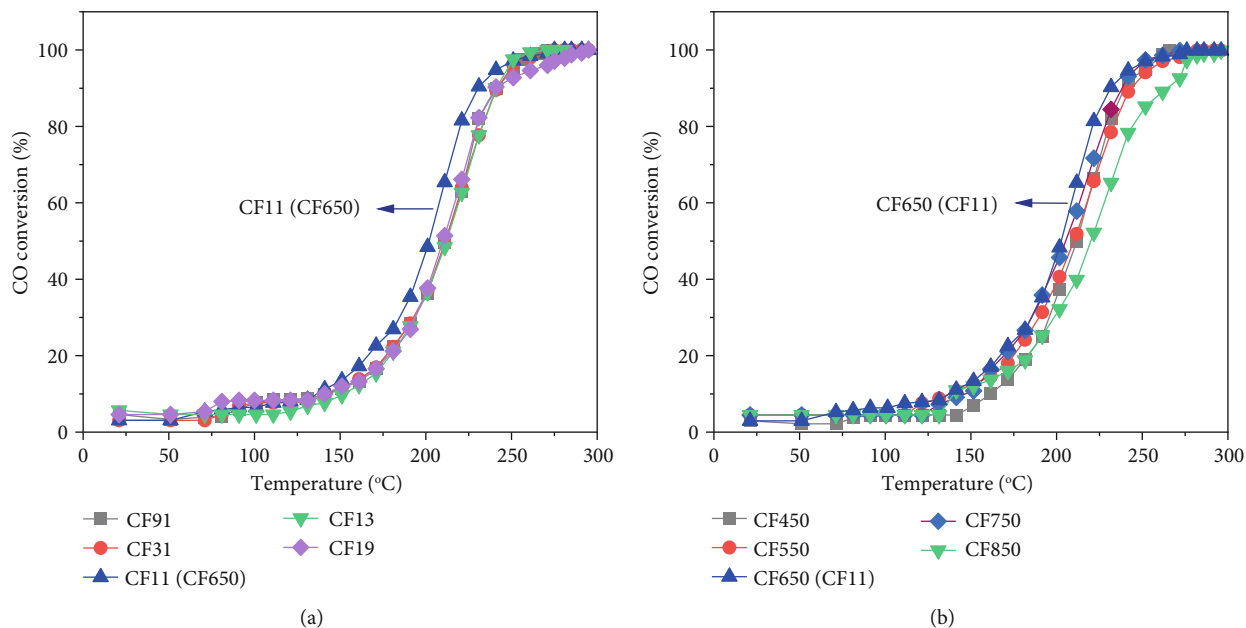
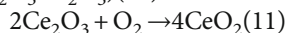
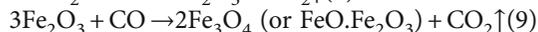
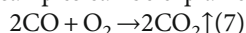


FIGURE 7: CO conversion of CeO<sub>2</sub>-Fe<sub>2</sub>O<sub>3</sub> samples according to temperature. Samples with different CF molar ratios calcined at 650 °C for 2 h (a) and samples calcined at different temperatures for 2 h (b).

samples with the different molar quantities of Ce<sup>3+</sup> and Fe<sup>3+</sup> ions shown that the CO conversion curves were similar variation, and the ability of CO conversion was lower than that of the CF11 sample (Figure 7(a)). For the CF11 sample (also named as CF11(CF650) or CF650(CF11)), the CO conversion curve was left-skewed, meaning that at the same catalytic temperature, the CO conversion of the CF11 sample was higher and finished earlier than other samples. This can be because the molar quantity of Ce<sup>3+</sup> and Fe<sup>3+</sup> ions was the same, the quantity of O<sup>2-</sup> ions in the -Ce-O-Fe- bonds was more dominant than that in two -Ce-O-Ce and -Fe-O-Fe- bonds of other samples, so the catalytic reactions of CF11 sample also happened better than the others [38]. The CO conversion for all samples can be explained by the following reactions:

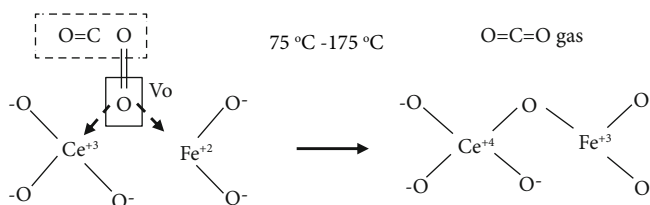


When the catalytic temperature increased from 75 °C to 175 °C, the amount of CO gas was converted about 12%; this may be because a part of CO gas was oxidized by O<sub>2</sub> in (7) [11]. In addition, these reactions can also occur between adsorbed CO and O<sub>2</sub> gases on the surface of the CeO<sub>2</sub>-Fe<sub>2</sub>O<sub>3</sub> catalyst to emit CO<sub>2</sub> by the J-H mechanism. When the temperature increased from 175 °C to 260 °C, the CO conversion was rapid for all samples but reached the fastest 50% at 211 °C for CF11. The intensification of CO oxidation can be because CO combines with an O<sup>2-</sup> at the lattice sites in -Ce-O-Fe-, -Ce-O-Ce- and -Fe-O-Fe- bonds to release CO<sub>2</sub> by the M-K mechanism in (8) and (9) [27, 29]. The Fe<sub>3</sub>O<sub>4</sub> product was a mixture of two FeO·Fe<sub>2</sub>O<sub>3</sub> oxides, meaning that only a part of Fe<sup>3+</sup> ions were reduced to Fe<sup>2+</sup> ions. This low-temperature reaction was also carried out early by another researcher [6].

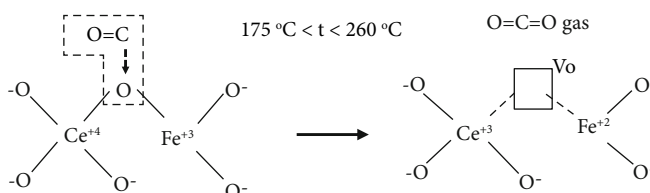
When the temperature was over 260 °C, the CO conversion process slowed down because it needed the recovery of the CeO<sub>2</sub> oxidizing agent from Ce<sub>2</sub>O<sub>3</sub> according to (10) and (11) and then reached 100% at 275 °C faster for the CF11 sample. The recovery here was due to the redox potential of Fe<sup>3+</sup>/Fe<sup>2+</sup> (0.711 V) < Ce<sup>4+</sup>/Ce<sup>3+</sup> (1.61 V) [20], so a tendency happened the redox process Ce<sup>4+</sup> + Fe<sup>2+</sup> → Ce<sup>3+</sup> + Fe<sup>3+</sup> [23, 52], or this was also the process of transferring an O<sup>2-</sup> ion from Ce<sup>4+</sup> ion to a neighboring Fe<sup>2+</sup> ion, creating the charge balance [38]. The (11) reaction turned Ce<sup>3+</sup> into initial Ce<sup>4+</sup>, which was an important agent that helped Fe ion form a closed-loop bridge of oxidation states by the (9) and (10) reactions as follows: Fe<sub>2</sub>O<sub>3</sub> → Fe<sub>3</sub>O<sub>4</sub> → FeO → -Fe<sub>2</sub>O<sub>3</sub>. The participation of Fe<sup>3+</sup> ions in the mixed oxide made the deformation of lattice structure and increased the reaction centers of gases storage and release. Therefore, the conversion of CO to CO<sub>2</sub> became more efficient under low temperatures and O<sub>2</sub> deficiency [4, 5]. It can be seen that thanks to the redox process between Fe<sup>2+</sup> and Ce<sup>4+</sup>, the catalyst system was restored to its original properties and was not degraded.

With the same catalytic mechanisms above, among all CeO<sub>2</sub>-Fe<sub>2</sub>O<sub>3</sub> mixed oxide samples calcined at different temperatures for 2 h, the CO conversion of the CF650 sample was better than all of those (Figure 7(b)). The CF650 curve was also skewed to the left and rapidly reached 100% at 270 °C. It is possible that for the samples CF450 and CF550, the crystallization of the oxides had not been complete, and there were still carbonate components of organic combustion products as analyzed in the TGA-DGT and FTIR spectra, which interfered with the process of CO oxidation. For the CF750 and CF850 samples, the crystal grain size increased, and the surface area decreased, leading to a decrease in the contact and oxidation capacity. Moreover, at high calcination temperature, there was

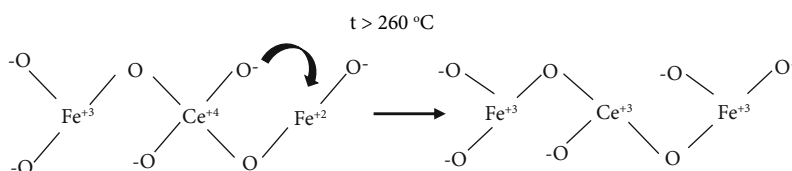
For the J-H mechanism, a CO molecule reacted with adsorbed an  $O_2$  molecule at  $V_O$  vacancy to emit a  $CO_2$  molecule (7):



For the M-K mechanism, a CO molecule combined with an  $O^{2-}$  ion of the crystal lattice to release a  $CO_2$  molecule and a  $V_O$  vacancy (8) and (9):



The transformation of  $Ce^{+4}$  to  $Ce^{3+}$  and  $Fe^{+2}$  to  $Fe^{3+}$  (10):



The transformation of  $Ce^{+4}$  from  $Ce^{+3}$  after an  $O_2$  molecule was captured by a  $V_O$  vacancy (11):

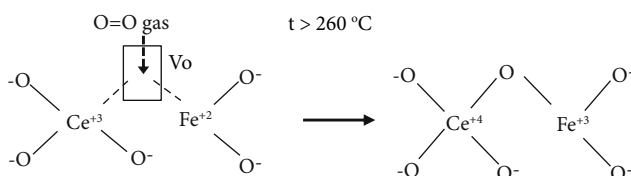


FIGURE 8: The mechanisms of CO oxidation and the oxidation state conversion of metal ions between  $Ce^{+4}/Ce^{+3}$  and  $Fe^{+3}/Fe^{+2}$  pairs on the  $CeO_2-Fe_2O_3$  catalyst surface.

a tendency of phase separation into two single oxides as mentioned in the XRD pattern, so their oxidation ability became less than that of mixed oxide catalysts [23]. Thus, the calcination temperature changed the crystallinity and affected the CO catalytic ability of the  $CeO_2-Fe_2O_3$  mixed oxides. From the above arguments, it is able to describe the mechanisms of CO oxidation, capture  $O_2$ , and release  $O^{2-}$  ions, creating  $V_O$  vacancies on the surface of  $CeO_2$  crystal, as shown in Figure 8.

For the J-H mechanism, a CO molecule reacted with adsorbed an  $O_2$  molecule at  $V_O$  vacancy to emit a  $CO_2$  molecule (7):

For the M-K mechanism, a CO molecule combined with an  $O^{2-}$  ion of the crystal lattice to release a  $CO_2$  molecule and a  $V_O$  vacancy (8) and (9).

The transformation of  $Ce^{+4}$  to  $Ce^{+3}$  and  $Fe^{+2}$  to  $Fe^{+3}$  was in (10).

The transformation of  $Ce^{+4}$  from  $Ce^{+3}$  after an  $O_2$  molecule was captured by a  $V_O$  vacancy (11):

TABLE 3:  $T_{50}$  and  $T_{100}$  temperatures of  $CeO_2-Fe_2O_3$  samples. Samples with different CF molar ratios calcined at  $650^\circ C$  for 2 h (a) and samples calcined at different temperatures for 2 h (b).

a			b		
Sample	$T_{50}$ ( $^\circ C$ )	$T_{100}$ ( $^\circ C$ )	Sample	$T_{50}$ ( $^\circ C$ )	$T_{100}$ ( $^\circ C$ )
CF91	211	275	CF450	211	275
CF31	211	275	CF550	211	280
CF11	200	270	CF650(CF11)	200	270
CF13	211	275	CF750	205	275
CF19	211	295	CF850	221	275

The CO conversion temperatures at  $T_{50}$  and  $T_{100}$  of all  $CeO_2-Fe_2O_3$  samples are shown in Table 3. It can show that the change of the CF molar ratio and calcination temperature of samples affected the CO conversion of  $CeO_2-Fe_2O_3$  mixed oxide catalysts. The  $T_{50}$  and  $T_{100}$  temperatures of all

TABLE 4:  $T_{50}$  and  $T_{100}$  temperatures of  $\text{CeO}_2$ ,  $\text{Fe}_2\text{O}_3$ , and  $\text{CeO}_2\text{-Fe}_2\text{O}_3$  oxides cited in some other references.

Oxide	Fabricated method	$T_{50}$	$T_M/T_{100}$ ( $T_M < T_{100}$ )	Reference
$\text{CeO}_2$	Polyol method	250°C	350°C	[57]
$\text{CeO}_2$	Combustion method	x	~240°C <sup>a</sup>	[58]
$\text{CeO}_2$	Hydrothermal method	216	~230°C	[22]
$\text{CeO}_2$	Combustion method	330°C	~410°C	[52]
$\text{CeO}_2$	Combustion method	~210°C	~260°C <sup>b</sup>	[48]
$\text{CeO}_2$	Co-precipitation method	500 K	700 K	[23]
$\text{CeO}_2$	Microwave and combustion method	362°C	~475°C	[41]
$\text{CeO}_2$	Hydrothermal method	x	~610 K	[55]
$\text{CeO}_2$	Surfactant-templated method	~230°C	~300°C	[46]
$\text{CeO}_2$	Thermal decomposition method	300°C	x	[40]
$\text{CeO}_2$	Solvothermal reaction method	~320°C	~400°C	[56]
$\text{Fe}_2\text{O}_3$	Co-precipitation method	620 K	750 K	[23]
$\text{Fe}_2\text{O}_3$	Co-precipitation method	290°C	450°C	[54]
$\text{Fe}_2\text{O}_3$	Surfactant-assisted method	~220°C	270°C	[53]
$\text{CeO}_2\text{-Fe}_2\text{O}_3$	Co-precipitation method	500 K	600 K	[23]
$\text{CeO}_2\text{-Fe}_2\text{O}_3$	Cyclic molecular designed dispersion method	~465 K	548 K	[27]
$\text{CeO}_2\text{-Fe}_2\text{O}_3$	Co-precipitation method	x	25°C <sup>c</sup>	[25]
$\text{CeO}_2\text{-Fe}_2\text{O}_3$	Hydrothermal method	166°C	~280°C	[19]
$\text{CeO}_2\text{-Fe}_2\text{O}_3$	Co-precipitation method	480 K	~575 K	[24]
$\text{CeFe}_{10}$	Thermal decomposition method	203°C	~280°C	[40]
$\text{Ce}_x\text{Fe}_{1-x}\text{O}_{2-\delta}$	Co-precipitation method	250°C	~450°C	[31]
$\text{Ce}_{0.98}\text{Fe}_{0.03}\text{O}_2$	Microwave and combustion method	298°C	~375°C	[41]

<sup>a,b,c</sup>The maximum CO conversion catalytic temperatures ( $T_M$ ) of 30%, 70%, and 96.17%, respectively. x is the reaction catalyst temperature that is unknown or out of measurement scale.

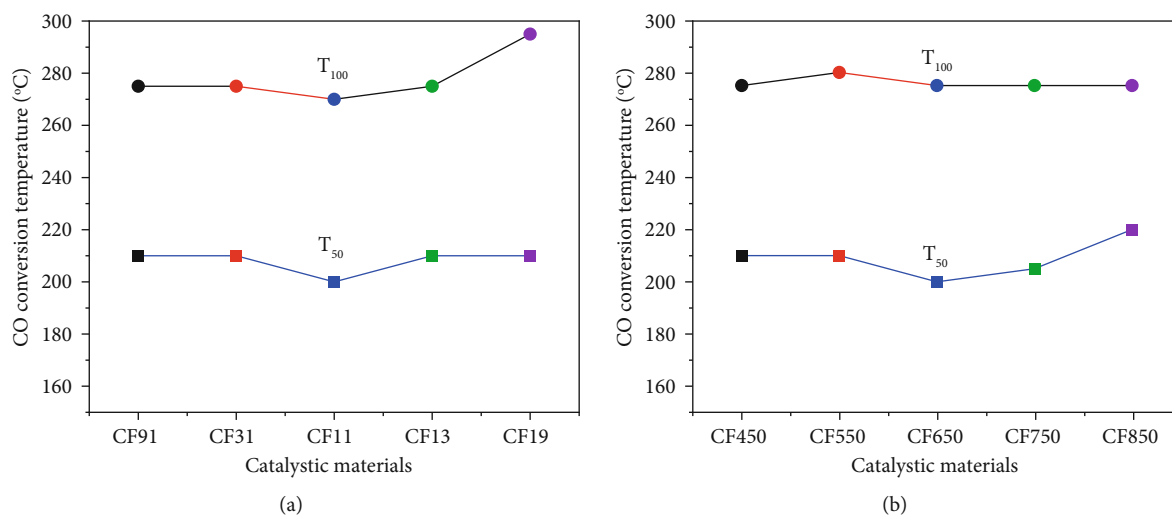


FIGURE 9:  $T_{50}$  and  $T_{100}$  temperatures of  $\text{CeO}_2\text{-Fe}_2\text{O}_3$  samples. Samples with different CF molar ratios calcined at 650 °C for 2 h (a) and samples calcined at different temperatures for 2 h (b).

samples are quite low, so it is considered an advantage of this fabrication method. Of all the samples, the  $T_{50}$  and  $T_{100}$  temperatures of the CF11 (CF650) samples are 200 °C and 270 °C, respectively, which are lower than those of the other samples (Table 3(a) and 3(b)).

Some publications have shown that the  $T_{50}$  and  $T_{100}$  of oxide catalysts are different depending on the fabrication method, as shown in Table 4. In some cases, if the single  $\text{CeO}_2$  or  $\text{Fe}_2\text{O}_3$  oxide is used as a catalyst, the  $T_{50}$  and  $T_{100}$  also decrease quite low [22, 53], but the rest is very high

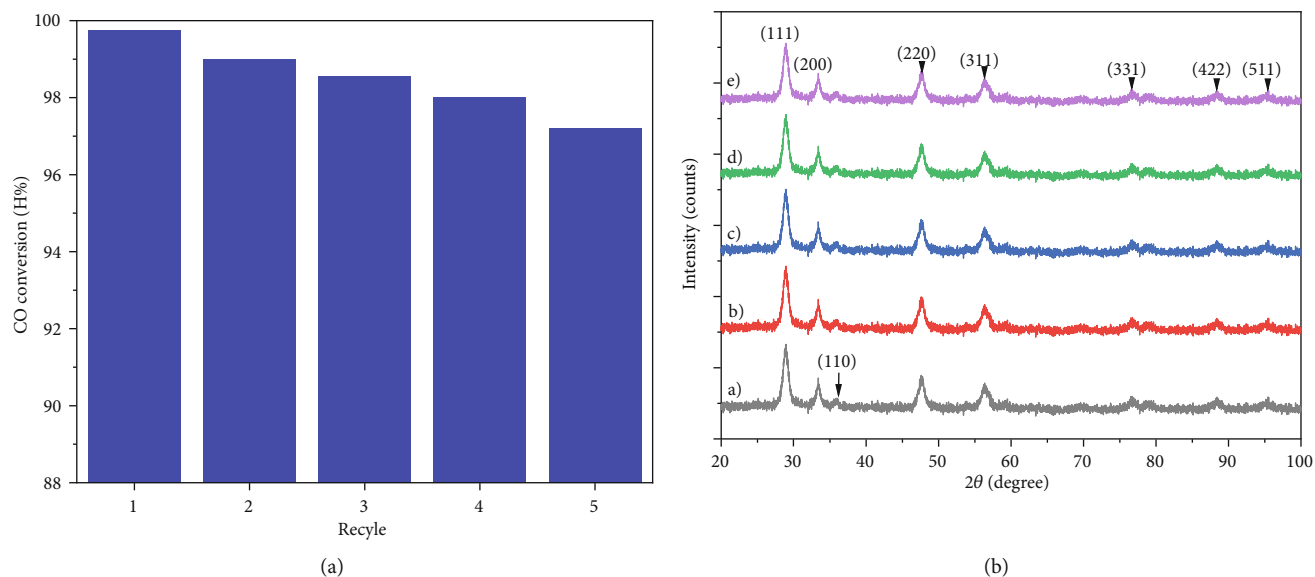


FIGURE 10: CO conversion of sample CF650(CF11) at  $T_{100}$  after 5 recycles (a) and corresponding XRD patterns (A) 1<sup>st</sup>, (B) 2<sup>nd</sup>, (C) 3<sup>rd</sup>, (D) 4<sup>th</sup>, and (E) 5<sup>th</sup> (b).

[23, 41, 46, 52, 54–56]. For  $\text{CeO}_2\text{-Fe}_2\text{O}_3$  catalyst materials, several studies have achieved immediate maximum CO conversion (M) at room temperature but are not capable of 100% CO conversion [25]. Some results are quite similar [19, 27, 40], but the others are very high [23, 24, 31, 41].

The correlation between  $T_{50}$  and  $T_{100}$  temperatures of the  $\text{CeO}_2\text{-Fe}_2\text{O}_3$  mixed oxides is shown in Figure 9. It is seen that the  $T_{50}$  and  $T_{100}$  are quite low for all samples and the conversion ability is the best corresponding to the CF11 sample calcined at  $650^\circ\text{C}$  for 2 h.

Figure 10 shows five oxidation cycles at  $T_{100}$  that were used to study the structural and mixed catalytic stability of sample CF11(650). After 5 oxidation cycles, the CO conversion efficiency was lowered to 97.18% (Figure 10(a)). This reduction in CO oxidation performance might be attributed to phase separation in the mixed oxide, as evidenced by the presence of the  $\text{Fe}_2\text{O}_3$  phase at peak (110) (Figure 10(b)).

The studied results showed that  $\text{Fe}^{3+}$  ions joined in  $\text{CeO}_2$  crystal lattice, which has caused the deformation of the lattice structure, increasing the quantity of  $V_{\text{O}}$  vacancies. The  $V_{\text{O}}$  vacancies acted as the reaction centers, thereby promoting easier oxidation processes. The  $\text{CeO}_2\text{-Fe}_2\text{O}_3$  mixed oxide catalysts are fabricated by the combustion method using gel-created TA matter for CO conversion is effective.

#### 4. Conclusion

$\text{CeO}_2\text{-Fe}_2\text{O}_3$  mixed oxides have been prepared successfully by the combustion method using gel-created tartaric acid. The solid solution of  $\text{CeO}_2\text{-Fe}_2\text{O}_3$  mixed oxides formed a molar ratio of  $\text{Ce}^{+3}$  ions to  $\text{Fe}^{3+}$  ions of 1:1 at  $650^\circ\text{C}$  for 2 h with a uniform average crystal size of 70 nm and a surface area of  $20.22\text{ m}^2\text{g}^{-1}$ . In particular, the transformation of metal-ion states in  $\text{Fe}^{3+}/\text{Fe}^{2+}$  and  $\text{Ce}^{4+}/\text{Ce}^{3+}$  pairs through the redox processes have formed a closed loop

of Fe-ion oxidation states:  $\text{Fe}_2\text{O}_3 \rightarrow \text{Fe}_3\text{O}_4 \rightarrow \text{FeO} \rightarrow \text{Fe}_2\text{O}_3$ , and maintains the catalytic properties of the  $\text{CeO}_2\text{-Fe}_2\text{O}_3$  mixed oxides. The participation of Fe-metal ions in  $\text{CeO}_2\text{-Fe}_2\text{O}_3$  mixed oxide solution enhanced the density of  $V_{\text{O}}$  vacancies and promoted the catalytic reactions of CO conversion. The choice of  $\text{Ce}^{3+}$  to  $\text{Fe}^{3+}$  molar ratio of 1:1 has halved the needed Ce content. The complete conversion of CO into  $\text{CO}_2$  has taken place at a low temperature of  $270^\circ\text{C}$  under deficient  $\text{O}_2$  conditions. The studied results can open a prospect of using  $\text{CeO}_2\text{-Fe}_2\text{O}_3$  mixed oxide catalysts for simple CO emission incinerators.

#### Data Availability

The data used to support the findings of this study are available from the corresponding author upon request.

#### Conflicts of Interest

The authors declare that they have no conflicts of interest.

#### Acknowledgments

This research is funded by the Vietnam Academy of Science and Technology (reference number TĐVLTT.01/21-23).

#### References

- [1] C. Mattiuzzi and G. Lippi, "Worldwide epidemiology of carbon monoxide poisoning," *Human & Experimental Toxicology*, vol. 39, no. 4, pp. 387–392, 2020.
- [2] H. Kinoshita, H. Türkan, S. Vucinic et al., "Carbon monoxide poisoning," *Toxicology Reports*, vol. 7, pp. 169–173, 2020.
- [3] S. R. Eilenberg, K. R. Bilsback, M. Johnson et al., "Field measurements of solid-fuel cookstove emissions from uncontrolled cooking in China, Honduras, Uganda, and India," *Atmospheric Environment*, vol. 190, pp. 116–125, 2018.

- [4] Y. Zhang, Q. Li, A. Meng, and C. Chen, "Carbon monoxide formation and emissions during waste incineration in a grate-circulating fluidized bed incinerator," *Waste Management & Research*, vol. 29, no. 3, pp. 294–308, 2011.
- [5] M. Xiu, S. Stevanovic, M. M. Rahman, A. M. Pourkhesalian, L. Morawska, and P. K. Thai, "Emissions of particulate matter, carbon monoxide and nitrogen oxides from the residential burning of waste paper briquettes and other fuels," *Environmental Research*, vol. 167, pp. 536–543, 2018.
- [6] M. A. Richard, S. L. Soled, R. A. Fiato, and B. A. DeRites, "The behavior of iron oxides in reducing atmospheres," *Materials Research Bulletin*, vol. 18, no. 7, pp. 829–833, 1983.
- [7] J. Vansant and P. W. Koziel, "Technical and industrial applications of CO<sub>2</sub>," in *An Economy Based on Carbon Dioxide and Water*, M. Aresta, I. Karimi, and S. Kawi, Eds., pp. 73–103, Springer, Cham, 2019.
- [8] F. Gao, S. Wang, W. Wang, J. Duan, J. Dong, and G. Chen, "Adsorption separation of CO from syngas with CuCl@AC adsorbent by a VPSA process," *RSC Advances*, vol. 8, no. 69, pp. 39362–39370, 2018.
- [9] J. A. Hogendoorn, W. P. M. van Swaaij, and G. F. Versteeg, "The absorption of carbon monoxide in COSORB solutions: absorption rate and capacity," *The Chemical Engineering Journal*, vol. 59, no. 3, pp. 243–252, 1995.
- [10] C. Xue, W. Hao, W. Cheng et al., "CO adsorption performance of CuCl/activated carbon by simultaneous reduction–dispersion of mixed Cu(II) salts," *Materials*, vol. 12, no. 10, article 1605, 2019.
- [11] G. B. Della Mea, L. P. Matte, A. S. Thill et al., "Tuning the oxygen vacancy population of cerium oxide (CeO<sub>2-x</sub>, 0 < x < 0.5) nanoparticles," *Applied Surface Science*, vol. 422, pp. 1102–1112, 2017.
- [12] S. Scirè and L. Palmisano, *Cerium Oxide (CeO<sub>2</sub>): Synthesis, Properties and Applications*, Elsevier B.V, Amsterdam, Netherlands, first edition, 2020.
- [13] C. Maria Magdalane, K. Kaviyarasu, N. Matinise et al., "Evaluation on La<sub>2</sub>O<sub>3</sub> garlanded ceria heterostructured binary metal oxide nanoplates for UV/ visible light induced removal of organic dye from urban wastewater," *South African Journal of Chemical Engineering*, vol. 26, pp. 49–60, 2018.
- [14] L. He, G. Wang, F. Zhang, Y. Cai, Y. Wang, and I. Djerdj, "Surfactant-assisted synthesis of CeO<sub>2</sub> nanoparticles and their application in wastewater treatment," *RSC Advances*, vol. 2, no. 32, pp. 12413–12423, 2012.
- [15] N. Sabari Arul, D. Mangalaraj, R. Ramachandran, A. Nirmala Grace, and J. In Han, "Fabrication of CeO<sub>2</sub>/Fe<sub>2</sub>O<sub>3</sub> composite nanospindles for enhanced visible light driven photocatalyst and supercapacitor electrode," *Journal of Materials Chemistry A*, vol. 3, no. 29, pp. 15248–15258, 2015.
- [16] S. Tambat, S. Umale, and S. Sontakke, "Photocatalytic degradation of milling yellow dye using sol-gel synthesized CeO<sub>2</sub>," *Materials Research Bulletin*, vol. 76, pp. 466–472, 2016.
- [17] M. Kovacevic, B. L. Mojet, J. G. van Ommen, and L. Lefferts, "Effects of morphology of cerium oxide catalysts for reverse water gas shift reaction," *Catalysis Letters*, vol. 146, no. 4, pp. 770–777, 2016.
- [18] A. F. Zedan and A. S. AlJaber, "Combustion synthesis of non-precious CuO-CeO<sub>2</sub> nanocrystalline catalysts with enhanced catalytic activity for methane oxidation," *Materials*, vol. 12, no. 6, p. 878, 2019.
- [19] M. Lykaki, S. Stefa, S. A. Carabineiro, P. K. Pandis, V. N. Stathopoulos, and M. Konsolakis, "Facet-dependent reactivity of Fe<sub>2</sub>O<sub>3</sub>/CeO<sub>2</sub> nanocomposites: effect of ceria morphology on CO oxidation," *Catalysts*, vol. 9, no. 4, article 371, 2019.
- [20] K. Song, S. Wang, Q. Sun, and D. Xu, "Study of oxidative dehydrogenation of ethylbenzene with CO<sub>2</sub> on supported CeO<sub>2</sub>-Fe<sub>2</sub>O<sub>3</sub> binary oxides," *Arabian Journal of Chemistry*, vol. 13, no. 10, pp. 7357–7369, 2020.
- [21] S. Stefa, M. Lykaki, D. Fragkouli et al., "Effect of the preparation method on the physicochemical properties and the CO oxidation performance of nanostructured CeO<sub>2</sub>/TiO<sub>2</sub> oxides," *PRO*, vol. 8, no. 7, p. 847, 2020.
- [22] G. Feng, W. Han, Z. Wang, F. Li, and W. Xue, "Highly reducible nanostructured CeO<sub>2</sub> for CO oxidation," *Catalysts*, vol. 8, no. 11, p. 535, 2018.
- [23] H. Bao, X. Chen, J. Fang, Z. Jiang, and W. Huang, "Structure-activity relation of Fe<sub>2</sub>O<sub>3</sub>-CeO<sub>2</sub> composite catalysts in CO oxidation," *Catalysis Letters*, vol. 125, no. 1-2, pp. 160–167, 2008.
- [24] P. Sudarsanam, B. Mallesham, D. Naga Durgasri, and B. M. Reddy, "Physicochemical characterization and catalytic CO oxidation performance of nanocrystalline Ce-Fe mixed oxides," *RSC Advances*, vol. 4, no. 22, pp. 11322–11330, 2014.
- [25] Y. Luo, R. Chen, W. Peng, G. Tang, and X. Gao, "Inverse CeO<sub>2</sub>@[single bond](https://sdfstaticassets-us-east-1.science-directassets.com/shared-assets/55/entities/sbnd.gif)Fe<sub>2</sub>O<sub>3</sub> catalyst for superior low-temperature CO conversion efficiency," *Applied Surface Science*, vol. 416, no. C, pp. 911–917, 2017.
- [26] A. A. Ansari, "Optical and structural properties of sol-gel derived nanostructured CeO<sub>2</sub> film," *Journal of Semiconductors*, vol. 31, no. 5, article 053001, 2010.
- [27] A. Tavakoli, N. Nasiri, Y. Mortazavi, and A. A. Khodadadi, "Cyclic molecular designed dispersion (CMDD) of Fe<sub>2</sub>O<sub>3</sub> on CeO<sub>2</sub> promoted by Au for preferential CO oxidation in hydrogen," *International Journal of Hydrogen Energy*, vol. 45, no. 58, pp. 33598–33611, 2020.
- [28] H. Shang, X. Zhang, J. Xu, and Y. Han, "Effects of preparation methods on the activity of CuO/CeO<sub>2</sub> catalysts for CO oxidation," *Frontiers of Chemical Science and Engineering*, vol. 11, no. 4, pp. 603–612, 2017.
- [29] S. Dey and G. C. Dhal, "Cerium catalysts applications in carbon monoxide oxidations," *Materials Science for Energy Technologies*, vol. 3, pp. 6–24, 2020.
- [30] R. A. Vazirov, S. Y. Sokovnin, V. G. Ilves, I. N. Bazhukova, N. Pizurova, and M. V. Kuznetsov, "Physicochemical characterization and antioxidant properties of cerium oxide nanoparticles," *Journal of Physics: Conference Series*, vol. 1115, no. 3, article 032094, 2018.
- [31] D. Li, K. Li, R. Xu et al., "Enhanced CH<sub>4</sub> and CO oxidation over Ce<sub>1-x</sub>Fe<sub>x</sub>O<sub>2</sub> hybrid catalysts by tuning the lattice distortion and the state of surface iron species," *ACS Applied Materials & Interfaces*, vol. 11, no. 21, pp. 19227–19241, 2019.
- [32] A. I. Boronin, E. M. Slavinskaya, A. Figueroba et al., "CO oxidation activity of Pt/CeO<sub>2</sub> catalysts below 0 °C: platinum loading effects," *Applied Catalysis B: Environmental*, vol. 286, article 119931, 2021.
- [33] O. A. Stonkus, T. Y. Kardash, E. M. Slavinskaya, V. I. Zaikovskii, and A. I. Boronin, "Thermally induced structural evolution of palladium-ceria catalysts. Implication for CO oxidation," *ChemCatChem*, vol. 11, no. 15, pp. 3505–3521, 2019.

- [34] K. M. Saoud and M. S. El-Shall, "Physical and chemical synthesis of Au/CeO<sub>2</sub> nanoparticle catalysts for room temperature CO oxidation: a comparative study," *Catalysts*, vol. 10, no. 11, p. 1351, 2020.
- [35] L. S. Kibis, D. A. Svintsitskiy, T. Y. Kardash et al., "Interface interactions and CO oxidation activity of Ag/CeO<sub>2</sub> catalysts: a new approach using model catalytic systems," *Applied Catalysis A: General*, vol. 570, pp. 51–61, 2019.
- [36] V. V. Galvita, H. Poelman, V. Bliznuk, C. Detavernier, and G. B. Marin, "CeO<sub>2</sub>-modified Fe<sub>2</sub>O<sub>3</sub> for CO<sub>2</sub> utilization via chemical looping," *Industrial and Engineering Chemistry Research*, vol. 52, no. 25, pp. 8416–8426, 2013.
- [37] D. H. Taffa, I. Hamm, C. Dunkel, I. Sinev, D. Bahnemann, and M. Wark, "Electrochemical deposition of Fe<sub>2</sub>O<sub>3</sub> in the presence of organic additives: a route to enhanced photoactivity," *RSC Advances*, vol. 5, no. 125, pp. 103512–103522, 2015.
- [38] Z. Zhang, H. Dong, S. Wei, and Y. Zhang, "Determination of active site densities and mechanisms for soot combustion with O<sub>2</sub> on Fe-doped CeO<sub>2</sub> mixed oxides," *Journal of Catalysis*, vol. 276, no. 1, pp. 16–23, 2010.
- [39] S. W. Hoh, L. Thomas, G. Jones, and D. J. Willock, "A density functional study of oxygen vacancy formation on  $\alpha$ -Fe<sub>2</sub>O<sub>3</sub>(0001) surface and the effect of supported Au nanoparticles," *Research on Chemical Intermediates*, vol. 41, no. 12, pp. 9587–9601, 2015.
- [40] O. H. Laguna, M. A. Centeno, G. Arzamendi, L. M. Gandía, F. Romero-Sarria, and J. A. Odriozola, "Iron-modified ceria and Au/ceria catalysts for total and preferential oxidation of CO (TOX and PROX)," *Catalysis Today*, vol. 157, no. 1–4, pp. 155–159, 2010.
- [41] T. R. Sahoo, M. Armandi, R. Arletti et al., "Pure and Fe-doped CeO<sub>2</sub> nanoparticles obtained by microwave assisted combustion synthesis: physico-chemical properties ruling their catalytic activity towards CO oxidation and soot combustion," *Applied Catalysis B: Environmental*, vol. 211, pp. 31–45, 2017.
- [42] S. K. Chawla, K. Prabhjyot, R. K. Mudsainiyan, S. S. Meena, and S. M. Yusuf, "Effect of fuel on the synthesis, structural, and magnetic properties of M-type hexagonal ferrites by sol-gel auto-combustion method," *Journal of Superconductivity and Novel Magnetism*, vol. 28, no. 5, pp. 1589–1599, 2015.
- [43] A. A. Ali, I. S. Ahmed, and E. M. Elfky, "Auto-combustion synthesis and characterization of iron oxide nanoparticles ( $\alpha$ -Fe<sub>2</sub>O<sub>3</sub>) for removal of lead ions from aqueous solution," *Journal of Inorganic and Organometallic Polymers and Materials*, vol. 31, no. 1, pp. 384–396, 2021.
- [44] C. A. Strydom and C. P. J. van Vuuren, "The thermal decomposition of cerium(III) nitrate," *Journal of thermal analysis*, vol. 32, no. 1, pp. 157–160, 1987.
- [45] A. Lassoued, B. Dkhil, A. Gadri, and S. Ammar, "Control of the shape and size of iron oxide ( $\alpha$ -Fe<sub>2</sub>O<sub>3</sub>) nanoparticles synthesized through the chemical precipitation method," *Results in Physics*, vol. 7, no. 7, pp. 3007–3015, 2017.
- [46] M.-N. Guo, C.-X. Guo, L.-Y. Jin, Y.-J. Wang, J.-Q. Lu, and M.-F. Luo, "Nano-sized CeO<sub>2</sub> with extra-high surface area and its activity for CO oxidation," *Materials Letters*, vol. 64, no. 14, pp. 1638–1640, 2010.
- [47] I. Moog, C. Feral-Martin, M. Duttine et al., "Local organization of Fe<sup>3+</sup> into nano-CeO<sub>2</sub> with controlled morphologies and its impact on reducibility properties," *Journal of Materials Chemistry A*, vol. 2, no. 47, pp. 20402–20414, 2014.
- [48] D. N. Nhiem, L. M. Dai, N. D. Van, and D. T. Lim, "Catalytic oxidation of carbon monoxide over nanostructured CeO<sub>2</sub>-Al<sub>2</sub>O<sub>3</sub> prepared by combustion method using polyvinyl alcohol," *Ceramics International*, vol. 39, no. 3, pp. 3381–3385, 2013.
- [49] O. Seibert, J. Grégr, and P. Kejzlar, "The preparation of iron oxide nanoparticles by a self-combustion method," *Manufacturing Technology*, vol. 19, no. 4, pp. 680–684, 2019.
- [50] R. C. Pullar, R. M. Novais, A. P. Caetano, M. A. Barreiros, S. Abanades, and F. A. C. Oliveira, "A review of solar thermochemical CO<sub>2</sub> splitting using ceria-based ceramics with designed morphologies and microstructures," *Frontiers in Chemistry*, vol. 7, article 601, 2019.
- [51] R. Brackmann, F. S. Toniolo, and M. Schmal, "Synthesis and characterization of Fe-doped CeO<sub>2</sub> for application in the NO selective catalytic reduction by CO," *Topics in Catalysis*, vol. 59, no. 19–20, pp. 1772–1786, 2016.
- [52] A. Gupta, A. Kumar, U. V. Waghmare, and M. S. Hegde, "Origin of activation of lattice oxygen and synergistic interaction in bimetal-ionic Ce<sub>0.89</sub>Fe<sub>0.1</sub>Pd<sub>0.01</sub>O<sub>2</sub>- $\delta$ Catalyst," *Maternité*, vol. 21, no. 20, pp. 4880–4891, 2009.
- [53] J.-L. Cao, Y. Wang, X.-L. Yu, S.-R. Wang, S.-H. Wu, and Z.-Y. Yuan, "Mesoporous CuO-Fe<sub>2</sub>O<sub>3</sub> composite catalysts for low-temperature carbon monoxide oxidation," *Applied Catalysis B: Environmental*, vol. 79, no. 1, pp. 26–34, 2008.
- [54] A. Biabani-Ravandi, M. Rezaei, and Z. Fattah, "Catalytic performance of Ag/Fe<sub>2</sub>O<sub>3</sub> for the low temperature oxidation of carbon monoxide," *Chemical Engineering Journal*, vol. 219, pp. 124–130, 2013.
- [55] M. Z. Tana, J. Li, H. Li, Y. Li, and W. Shen, "Morphology-dependent redox and catalytic properties of CeO<sub>2</sub> nanostructures: nanowires, nanorods and nanoparticles," *Catalysis Today*, vol. 148, no. 1–2, pp. 179–183, 2009.
- [56] X. Zhang, F. Hou, Y. Yang et al., "A facile synthesis for cauliflower like CeO<sub>2</sub> catalysts from Ce-BTC precursor and their catalytic performance for CO oxidation," *Applied Surface Science*, vol. 423, pp. 771–779, 2017.
- [57] C. Ho, J. C. Yu, T. Kwong, A. C. Mak, and S. Lai, "Morphology-controllable synthesis of mesoporous CeO<sub>2</sub> nano- and microstructures," *Chemistry of Materials*, vol. 17, no. 17, pp. 4514–4522, 2005.
- [58] R. D. Kerkar and A. V. Salker, "Significant effect of multi-doped cerium oxide for carbon monoxide oxidation studies," *Materials Chemistry and Physics*, vol. 253, p. 123326, 2020.

## Research Article

# Graphene Oxide/Fe<sub>3</sub>O<sub>4</sub>/Chitosan–Coated Nonwoven Polyester Fabric Extracted from Disposable Face Mask for Enhanced Efficiency of Organic Dye Adsorption

Hoang V. Tran , Nhan T. Hoang, Thu D. Le , Luyen T. Tran , and Hue T. M. Dang

*School of Chemical Engineering, Hanoi University of Science and Technology, 1 Dai Co Viet Road, Hanoi, Vietnam*

Correspondence should be addressed to Hoang V. Tran; [hoang.tranvinh@hust.edu.vn](mailto:hoang.tranvinh@hust.edu.vn) and Thu D. Le; [thu.ledieu@hust.edu.vn](mailto:thu.ledieu@hust.edu.vn)

Received 3 November 2021; Revised 9 December 2021; Accepted 23 December 2021; Published 25 January 2022

Academic Editor: Thi Ngoc Mai Pham

Copyright © 2022 Hoang V. Tran et al. This is an open access article distributed under the Creative Commons Attribution License, which permits unrestricted use, distribution, and reproduction in any medium, provided the original work is properly cited.

Owing to the COVID-19 pandemic, huge amounts of disposable face masks have been manufactured and used, and these discarded face masks have to be treated. In this study, we propose a simple approach for reusing the nonwoven polyester fabric (NWPF) from disposable face masks. In this approach, NWPF is utilized as a supporter for coating of a layer of graphene oxide/Fe<sub>3</sub>O<sub>4</sub>/chitosan (GFC) to form a GFC/NWPF adsorbent at room temperature via a simple spray coating method that does not require any solvent. The specific properties of GFC, NWPF, and the GFC/NWPF adsorbent were analysed via X-ray diffraction, transmission electron microscopy, ultraviolet–visible spectroscopy, vibrating sample magnetometry, and field-emission scanning electron microscopy. Results showed that the presence of NWPF enhanced the adsorption capacity of GFC towards organic dyes. At high concentrations of the organic dyes, the adsorption efficiency of the GFC/NWPF adsorbent to the dyes reached 100% within 24 h. The adsorption capacity ( $q_{\max}$ ) of the GFC/NWPF adsorbent to methylene blue, methyl orange, Congo red, and moderacid red was 54.795, 87.489, 88.573, and 29.010 mg g<sup>-1</sup>, respectively, which were considerably higher than that of bulk GFC (39.308, 82.304, 52.910, and 21.249 mg g<sup>-1</sup>, respectively).

## 1. Introduction

Organic dyes are widely used in many industries, such as textile, paper, rubber, plastic, leather, cosmetic, pharmaceutical, and food industries. However, the wastewater produced by these industries contains dyes and their products that contribute to water pollution, causing negative effects on humans and the environment, such as preventing the absorption of oxygen and sunlight and disrupting the respiration and growth of aquatic organisms. Furthermore, it causes adverse effects on the ability of microorganisms to decompose organic substances in wastewater [1–3]. Therefore, researchers have developed various wastewater treatment methods and have successfully applied them in removing colorants. These methods can be divided into three main categories, namely, biological, chemical, and physical methods [1]. Although physical and chemical methods, such as adsorption, photocatalysis, photocatalytic

decomposition, membrane separation, ultrasonication, and wet air oxidation, are effective, they can only be applied when the concentration of the dissolved substances is sufficiently high. Moreover, some methods are expensive and still produce toxic by-products. By comparison, biological treatment methods include removing dyes via anaerobic and aerobic systems and fermenting activated sludge from filamentous fungi, yeasts, bacteria, and bacterial and fungal biomes. However, these methods also have disadvantages, such as long processing time and poor performance in removing dyes with a durable and a high-molecular polymeric structure. Moreover, the composition of these organic dyes in wastewater often harms the microorganism biomes/populations used in the sludge [4]. Among the aforementioned wastewater treatment methods, adsorption is considered one of the preeminent methods owing to its advantages, such as easy implementation, generation of nontoxic substances during the treatment process, high efficiency, and

low cost [5]. Furthermore, various adsorbent materials from traditional materials can be used in adsorption, such as activated carbon, clay, agricultural by-products, banana peels, straw [5], rice husk [6], and red mud [7].

Graphene oxide (GO) and its composite-based adsorbents are excellent in adsorbing organic compounds, including organic dyes, as well as heavy metal ions [8–14]. GO is notable for its simpler fabrication and easier dispersion in water than other materials [15, 16]. Accordingly, GO is easy to use with a high adsorption efficiency. Functional molecules are utilized to generate functional groups to improve the adsorption capacity of GO to heavy metal ions or organic dyes. Chitosan (CS) molecule has several functional groups, such as primary –OH, secondary –OH, and –NH<sub>2</sub> groups. In these groups, the O and N atoms still have undivided electron pairs, making them the chemically active centres of CS. These groups are considered nucleophilic reagents and can participate in several specialized chemical responses [17] or complexed with almost all heavy metals and transition metals to help separate heavy metals from aqueous media easily [18]. Recently, Fe<sub>3</sub>O<sub>4</sub> nanoparticles have been utilized to generate the magnetic property for adsorbents, thereby allowing them to be recovered and reused. In addition, the presence of Fe<sub>3</sub>O<sub>4</sub> nanoparticles can improve the porosity of adsorbents [1, 2, 19, 20]. Therefore, GO/Fe<sub>3</sub>O<sub>4</sub>/CS (GFC) materials have excellent adsorption and recovery and regeneration abilities [21–23]. Hence, they are applied in the removal of organic dyes [2] and heavy metal ions [20].

Nonwoven fabric (NWPFs) is widely used in the production of medical disposable face masks and clothes [24–27]. NWPF can be combined with nanomaterials to enhance their properties, such as antibacterial, waterproof, and fire-proof properties [28, 29]. The COVID-19 pandemic has necessitated the manufacturing and use of huge amounts of disposable face masks, and these discarded masks have to be treated [26]. Several recent reports have proposed using the NWPF extracted from discarded face masks and clothes as an adsorbent for the clean-up of waters polluted with petroleum and oil products [30], as a support of photocatalysts [31–33] or as a reinforcement of cement composites [27].

In this study, we propose a new approach for reusing NWPF. In this approach, NWPF is extracted from discarded disposable face masks as a support of a GFC nanocomposite adsorbent. The GFC/NWPF adsorbent is fabricated by coating GFC onto NWPF via a simple and solvent-free spray coating method at room temperature (RT). Results showed that the presence of NWPF enhanced the adsorption capacity of the GFC adsorbent to various organic dyes. Therefore, the GFC/NWPF adsorbent will not only improve the adsorption capacity of GFC but also contribute to the efficient reuse of NWPF.

## 2. Experimental

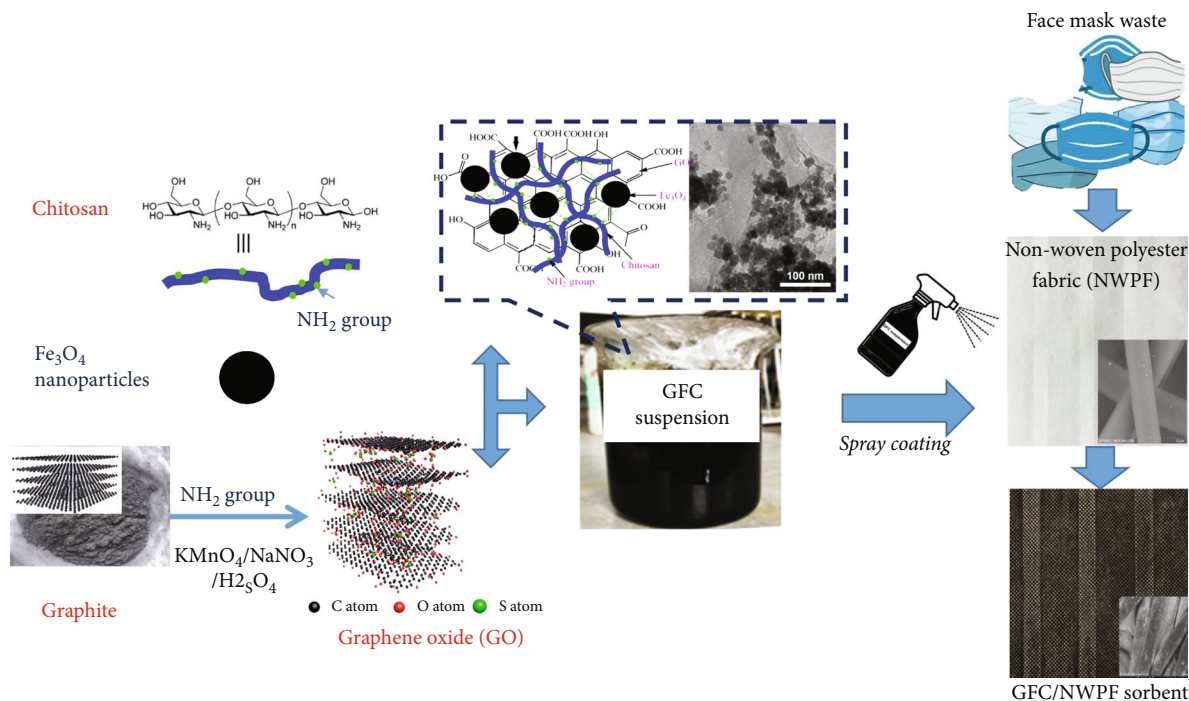
**2.1. Chemicals and Reagents.** Graphite (99 wt.%,  $d = 60$ – $120 \mu\text{m}$ ) was purchased from Vietnam Graphite Group (Vietnam). Sulfuric acid (H<sub>2</sub>SO<sub>4</sub>, 98 wt.%, AR), sodium

nitrate (NaNO<sub>3</sub>, AR), potassium permanganate (KMnO<sub>4</sub>, AR), iron (III) chloride hexahydrate (FeCl<sub>3</sub>·6H<sub>2</sub>O, AR), iron (II) sulfide heptahydrate (FeSO<sub>4</sub>·7H<sub>2</sub>O, AR), sodium hydroxide (NaOH, 99 wt.%, AR), glacial acetic acid (CH<sub>3</sub>COOH, 99 wt.%, AR), and hydrogen peroxide (H<sub>2</sub>O<sub>2</sub>, 33 wt.%, AR) were bought from Xilong Chemical Company (China). Methylene blue (MB), methyl orange (MO), Congo red (CR), and moderacid red (RS) were procured from Van Minh Chemical Company (Vietnam).

GO was prepared from graphite flakes following Hummer's method as described in previous reports [2, 20, 34, 35]. The GO product obtained was characterized via X-ray diffraction (XRD), scanning electron microscopy (SEM), and transmission electron microscopy (TEM) (Fig. SI.1). CS was prepared from shrimp shells in our laboratory in accordance with a previously published procedure [36]. The deacetylation degree (DD%) of CS was 85.0%; its average molecular weight ( $M_w$ ) was 32.8 kDa. A 10 mg mL<sup>-1</sup> CS solution was prepared by dissolving 5 g of CS in 500 mL of 1% (v/v) acetic acid solution and stirring overnight at RT to obtain a homogeneous and colorless solution. Fe<sub>3</sub>O<sub>4</sub> nanoparticles were prepared by coprecipitating a mixture of iron (III) chloride hexahydrate and iron (II) sulfide heptahydrate at the molar ratio of 2:1 [2, 20, 34]. NWPF was extracted from discarded disposable face masks, washed with soap, sonicated with 95% (v/v) ethanol for 5 min, and dried at 80°C.

**2.2. Preparation of the GFC/NWPF Adsorbent.** The GFC/NWPF adsorbent was manufactured by coating a layer of GFC ink onto NWPF via a simple spray coating method. The GFC ink was prepared by mixing 0.22 g GO, 0.85 g Fe<sub>3</sub>O<sub>4</sub>, and 0.36 g CS. Afterwards, the mixture was dissolved in 100 mL 1 wt.% acetic solution and 0.5 mL glycerol by using a homogenizer under ultrasonic conditions for 30 min to obtain a black homogeneous ink of the GFC nanocomposite. The GFC ink was spray-coated onto the NWPF at RT. Finally, the NWPF was dried at 60°C for 2 h. This process was repeated five more times to increase the thickness of the coating. Finally, the NWPF was soaked in 1 M NaOH solution overnight, washed until it reached neutral pH, and dried at 80°C for 24 h to obtain the GFC/NWPF adsorbent. Subsequently, the GFC/NWPF adsorbent was cut into 1 cm × 1 cm samples for later use. The process of preparing the GFC/NWPF adsorbent is illustrated in Scheme 1.

**2.3. Adsorption Procedures.** A piece of 1 cm × 1 cm GFC/NWPF sample (each sample contained 1.49 mg of the GFC powder) was immersed in 10 mL of an organic dye solution (MB, MO, CR, or RS). The mixture was incubated at various contact times at different temperatures. The pH of each solution was adjusted from 2 to 10 by adding 0.1 M HCl and 0.1 M NaOH solutions. The concentration of dye residues in the solution after the adsorption process was measured via UV-Vis spectrometry and by using suitable calibration curves (Figs. SI.3–SI.6). The adsorption capacity of the GFC/NWPF adsorbent to the organic dyes was compared with that of bulk GFC by using 0.0194 g of the GFC powder instead of the GFC/NWPF sample. The dye removal



SCHEME 1: The process of fabricating a new adsorbent by coating graphene oxide/ $\text{Fe}_3\text{O}_4$ /chitosan (GFC) coated onto nonwoven polyester fabric (NWPF) extracted from discarded disposable face masks.

efficiency of each composition in the composite was determined by testing various NWPF samples (Table 1). Dye removal efficiency ( $R$ , %) was calculated using the following equation (1):

$$R(\%) = \left( \frac{C_0 - C_e}{C_0} \right) \times 100. \quad (1)$$

The amount of dye uptake by the GFC adsorbent ( $q_e$ ,  $\text{mg}\cdot\text{g}^{-1}$ ) was calculated as follows (equation (2)):

$$q_e = \frac{C_0 - C_e}{m_a}. \quad (2)$$

The Langmuir equation (3) and the Freundlich equation (4) isotherms were linearized into the following forms:

$$\frac{C_e}{q_e} = \frac{1}{K_L \times q_{\max}} + \frac{1}{q_{\max}} \times C_e, \quad (3)$$

$$\log q_e = \log K_F + \frac{1}{n} \times \log C_e, \quad (4)$$

where  $C_0$  and  $C_e$  ( $\text{mg}\cdot\text{L}^{-1}$ ) are the initial and equilibrium concentrations of organic dyes in solution, respectively;  $m_a$  is the mass of GFC ( $\text{g}\cdot\text{L}^{-1}$ );  $q_e$  and  $q_{\max}$  are the equilibrium organic dye concentration on the adsorbent and the maximum adsorption capacity of the adsorbent ( $\text{mg}\cdot\text{g}^{-1}$ ), respectively;  $K_L$  is the Langmuir constant ( $\text{L}\cdot\text{mg}^{-1}$ ), which is related to the free energy of adsorption;  $K_F$  is the Freundlich constant ( $\text{L}\cdot\text{g}^{-1}$ ); and  $n$  (dimensionless) is the heterogeneity factor.

**2.4. Characterization and Methods.** The XRD patterns of each GFC sample were obtained at RT by using a D8 Advance diffractometer (Bruker ASX) with  $\text{CuK}\alpha$  radiation ( $\lambda = 1.5406 \text{ \AA}$ ) within the range of  $2\theta = 10 - 60^\circ$  at a scanning rate of  $0.02 \text{ s}^{-1}$ . The morphology of the GFC nanocomposite and the GFC/NWPF samples was analysed via TEM (JEOL) at  $100 \text{ kV} \times 200,000$  magnification and FE-SEM (Hitachi S-4500), respectively. The magnetic behaviours of the samples were measured via vibrating sample magnetometry (VSM 880, DMS/ADE Technologies, USA) at fields ranging from  $-10 \text{ kOe}$  to  $10 \text{ kOe}$  at  $25^\circ\text{C}$  with an accuracy of  $10^{-5} \text{ emu}$ . The concentration of organic dye residues in solution after the adsorption process was determined via UV-Vis spectrometry by establishing their calibration curves at the concentrations of  $0.625, 1.25, 2.5, 5, 10,$  and  $20 \text{ mg}\cdot\text{L}^{-1}$ . Moreover, the calibration curves were established at pH 4, 5, 7, and 9. Afterwards, the spectra of these solutions were measured via UV-Vis spectrometry by using an Agilent 8453 UV-Vis spectrophotometer system within the wavelength range of  $200-1200 \text{ nm}$ . Subsequently, their optical density (OD) at the maximum adsorption was used to establish the calibration curves (OD vs.  $C_{\text{mg/L}}$ ). The UV-Vis spectra and calibration curves are shown in the supporting information (SI) from Figs. SI.3 to SI.6.

### 3. Results and Discussion

**3.1. Characterization of GFCs.** The  $\text{Fe}_3\text{O}_4$  nanoparticles agglomerated quite strongly because of their large specific surface energy; thus, the nanoparticles tended to agglomerate to reduce the surface energy (Figure 1(a)). The thickness of GO sheets was thin, only over  $5 \mu\text{m}$  in size (Figure 1(b)).

TABLE 1: Removal efficiency (R%) of MB and MO by various coated NWPF samples at different pH levels.

Sample codes		M2	M3	M4	M5	M6	M7	M8	M9
Compositions	NWPFs	+( <sup>a</sup> )	+	+	+	+	+	+	+
	GO	—( <sup>b</sup> )	+	—	—	+	+	—	+
	CS	—	—	+	—	—	+	+	+
	Fe <sub>3</sub> O <sub>4</sub>	—	—	—	+	+	—	+	+
Acidic medium	R%( <sup>c</sup> ) for MB	31.71	103.70	31.08	26.71	34.68	31.65	25.64	27.04
	R% for MO	4.55	34.65	31.48	14.95	26.07	27.97	57.01	53.51
Neutral medium	R% for MB	29.20	101.32	25.78	35.69	91.54	35.08	31.66	40.33
	R% for MO	4.58	20.73	17.78	6.73	14.67	6.68	9.64	8.19
Basic medium	R% for MB	35.08	105.37	39.78	39.78	99.25	99.82	46.63	86.66
	R% for MO	6.59	17.95	8.49	7.15	13.67	10.99	6.89	7.59

(<sup>a</sup>)Presence; (<sup>b</sup>)absence; (<sup>c</sup>)removal efficiency (R%).

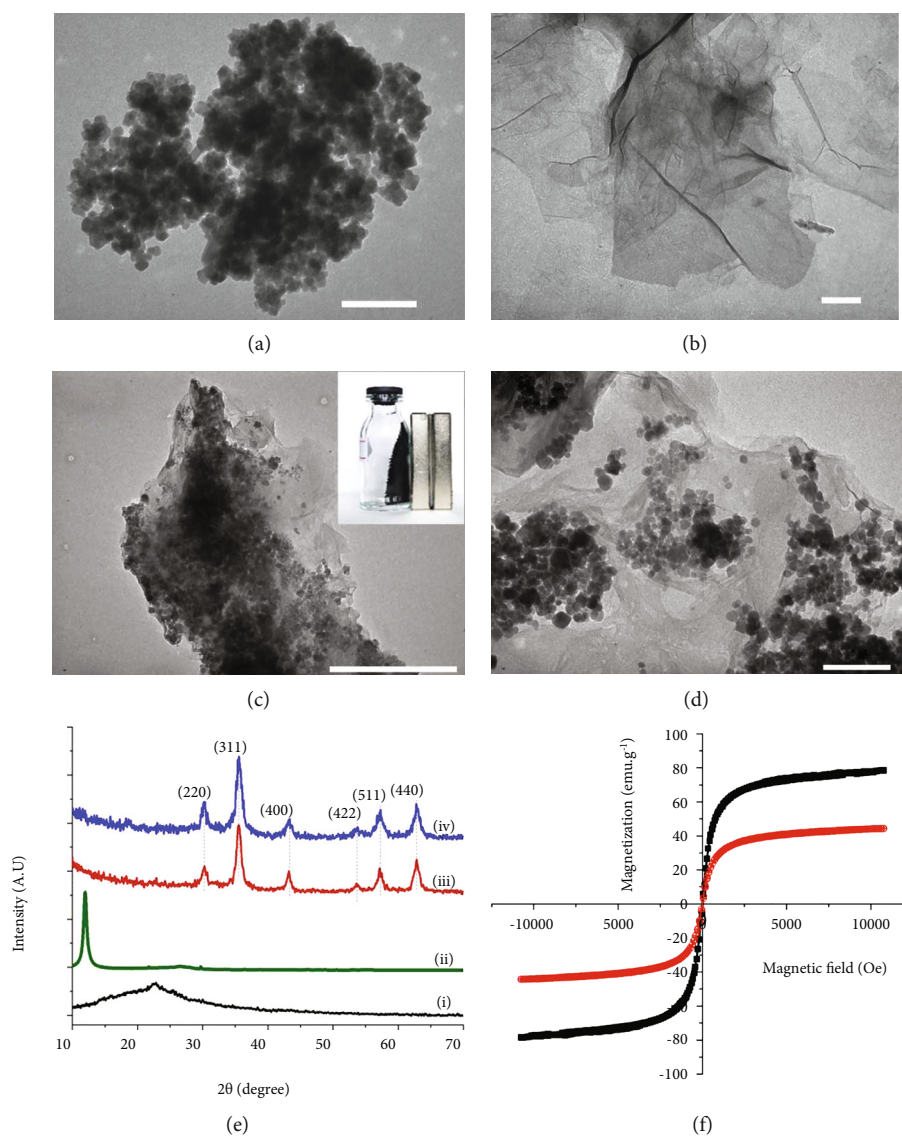


FIGURE 1: (a–d) TEM images of (a) Fe<sub>3</sub>O<sub>4</sub> nanoparticles, (b) GO, and (c, d) GO/Fe<sub>3</sub>O<sub>4</sub>/CS (GFC) nanocomposite (inset: magnetic property of GFC nanocomposite); (e) XRD patterns of (i) CS, (ii) GO, (iii) Fe<sub>3</sub>O<sub>4</sub>, and (iv) GO/Fe<sub>3</sub>O<sub>4</sub>/CS; (f) VSM of (i) Fe<sub>3</sub>O<sub>4</sub> and (ii) GO/Fe<sub>3</sub>O<sub>4</sub>/CS.

Spherical ferromagnetic particles of a fairly uniform size with an average diameter of about 30 nm scattered on the surfaces of GO and CS attached onto the thin GO sheets (Figures 1(c) and 1(d)). These spherical particles helped the  $\text{Fe}_3\text{O}_4$  particles to attach onto the GO layer tightly. TEM results indicated that the GFC materials were successfully synthesized. No obvious peak could be observed from the XRD spectrum of CS (Figure 1(e), curve (i)). By contrast, a strong intensity peak (001) at  $2\theta = 11.90^\circ$  could be observed from the XRD spectrum of GO (Figure 1(e), curve (ii)). The peak (002) of graphite at  $2\theta = 27^\circ$  disappeared (Fig. SI.1b), indicating that GO was successfully synthesized. These results were similar to those of a previous study [37]. Both the XRD spectra of  $\text{Fe}_3\text{O}_4$  (Figure 1(e), curve (iii)) and GO/ $\text{Fe}_3\text{O}_4$ /CS (Figure 1(e), curve (iv)) indicated that the synthesized  $\text{Fe}_3\text{O}_4$  material was a single phase and had a low diffraction baseline, suggesting a complete crystalline phase. In the XRD spectrum of bare  $\text{Fe}_3\text{O}_4$  nanoparticles (Figure 1(e), curve (iii)), six diffraction peaks appeared at  $30.10^\circ$ ,  $35.40^\circ$ ,  $43.10^\circ$ ,  $53.40^\circ$ ,  $57.00^\circ$ , and  $62.50^\circ$ , which corresponded to the (220), (311), (400), (422), (511), and (440) peaks of  $\text{Fe}_3\text{O}_4$  (JCPDS File, PDF No. 65–3107) [11, 13, 22, 23], thereby confirming the formation of the magnetic spinel nanocrystal phase of  $\text{Fe}_3\text{O}_4$ . Comparing with that of pure  $\text{Fe}_3\text{O}_4$ , the diffraction spectrum of the GO/ $\text{Fe}_3\text{O}_4$ /CS sample retained the peaks of  $\text{Fe}_3\text{O}_4$ . Thus, CS and GO coatings did not affect the phase change in  $\text{Fe}_3\text{O}_4$ . The extension line in the figure was evaluated using the Debye–Scherrer equation, which describes the relationship between the width in XRD spectrum and particle size, as follows:  $d = (k\lambda/\beta\cos\theta)$ , where  $d$  is the thickness of the crystal,  $k = 0.89$  (the Debye–Scherrer constant),  $\lambda = 0.15406$  nm (X-ray wavelength),  $\beta$  is the width at half-height of the peak, and  $\theta$  is the Bragg angle. The average crystal size of  $\text{Fe}_3\text{O}_4$  in the bare  $\text{Fe}_3\text{O}_4$  sample was 30 nm, whereas that of the calculated sample was 35 nm. This result was consistent with the TEM images (Figure 1). The magnetic property of GFC was tested with magnets. GFC exhibited strong interactions with the magnets (Figure 1(c), inserted figure). Theoretically, CS and GO are nonmagnetic. Thus, the magnetic property of the GO/ $\text{Fe}_3\text{O}_4$ /CS material was due to the presence of  $\text{Fe}_3\text{O}_4$ . The magnetization curves of the  $\text{Fe}_3\text{O}_4$  and GO/ $\text{Fe}_3\text{O}_4$ /CS samples (Figure 1(f)) demonstrated that they have superparamagnetic properties. The magnetic saturation ( $M_s$ ) of the  $\text{Fe}_3\text{O}_4$  sample was  $\sim 80$  emu  $\text{g}^{-1}$  (Figure 1(f), curve (i)), whereas that of the GFC sample was  $\sim 40$  emu  $\text{g}^{-1}$  (Figure 1(f), curve (ii)). Therefore, the coverage of CS and GO on the  $\text{Fe}_3\text{O}_4$  particles substantially reduced the magnetization. As results show, the  $M_s$  of the GFC sample was still high (40 emu  $\text{g}^{-1}$ ); thus, it was able to coat NWPF and endowed GFC/NWPF with magnetic properties to separate the GFC/NWPF after absorption process using an external magnet for the regeneration and circulation. According to the FTIR spectra of CS and GFC (Fig. SI.2), the main specific groups in CS included an adsorption at  $3578$   $\text{cm}^{-1}$ , which was attributed to the stretching vibration of the O–H group; a band at approximately  $2881$   $\text{cm}^{-1}$ , which was ascribed to the stretching vibration of C–H; and characteristic adsorption bands at  $1674$  and  $1589$   $\text{cm}^{-1}$ , which corresponded to

C=O stretching and N–H blending in the amide groups, respectively [38–41]. However, in the FTIR spectrum of GFC, these specific bands of amide groups shifted to  $1597$ ,  $1516$ , and  $1394$   $\text{cm}^{-1}$ , respectively. The presence of amine and amide groups on the GFC surface plays an important role in organic dye removal [38–43].

**3.2. Characterization of NWPF and the GFC/NWPF Absorbent.** The GO/ $\text{Fe}_3\text{O}_4$ /CS materials were coated onto NWPF via a simple spray coating method. Five coats were applied to create a sufficiently thick and even coating. The mass density ( $d$ ,  $\text{g cm}^{-2}$ ) of the GFC coated onto the  $1$   $\text{cm}^2$  NWPF samples was calculated as follows:

$$d = \frac{m_{\text{GFC(g)}}}{S_{\text{NWPF}}(\text{cm}^2)}, \quad (5)$$

where  $m_{\text{GFC}}$  is the amount of GFC used for coating (g) and  $S_{\text{NWPF}}$  is the total area of NWPF covered ( $\text{cm}^2$ ). In this experiment,  $m_{\text{GFC}} = 0.22$  g of GO +  $0.85$  g of  $\text{Fe}_3\text{O}_4$  +  $0.36$  g of CS ( $=1.43$  g) and  $S_{\text{NWPFs}} = 959$   $\text{cm}^2$ ; hence,  $d = 1.49$  mg GFC  $\text{cm}^{-2}$ .

SEM images of NWPF and the GFC/NWPF absorbent are shown in Figure 2. The polyester fibres in NWPF were slippery and even, their surface was smooth, and it consisted of overlapping nonwoven fibres that were pressed by heat (Figures 2(a), 2(c), 2(e), and 2(g)). By comparison, after GFC was coated onto NWPF, the surface of the polyester fibres in the GFC/NWPF absorbent became rough and rugged (Figures 2(b), 2(d), 2(f), and 2(h)), and the coating cracked at some points (Figures 2(d), 2(f), and 2(h)). Moreover, the size of the fibres considerably increased. By contrast, the GO sheets (Figures 2(d) and 2(h)) and the  $\text{Fe}_3\text{O}_4$  nanoparticles (Figure 2(h), inserted figure) became rumped. These results indicated that GFC was successfully coated onto the surface of NWPF via the simple spray coating method adopted herein. Thus, this method can be employed in fabricating GFC/NWPF absorbents on a large scale.

### 3.3. Adsorption of Organic Dyes on GFC and GFC/NWPF Absorbents

**3.3.1. Optimization of Adsorption Conditions.** The adsorption conditions were optimized including the pH and compositions of the GFC/NWPF adsorbent to enhance its adsorption of organic dyes. Eight coated NWPF samples with different compositions were prepared (Table 1). Their ability to absorb MB (a cationic dye) and MO (an anionic dye) was evaluated at different pH 5, 7, and 9. Organic dyes can be classified into three types: cationic organic dyes with a positive charge, anionic organic dyes with a negative charge, and nonionic organic dyes with no charge. Therefore, the adsorption of the dyes onto the adsorbents can be achieved via electrostatic interactions between dye ions and groups of opposite charge as the functional groups on an adsorbent's surface. However, this classification is only relative because an organic dye can be an anionic or a cationic dye depending on the environment (pH) (Table 2). The surface of the GFC/NWPF adsorbent had abundant amine groups

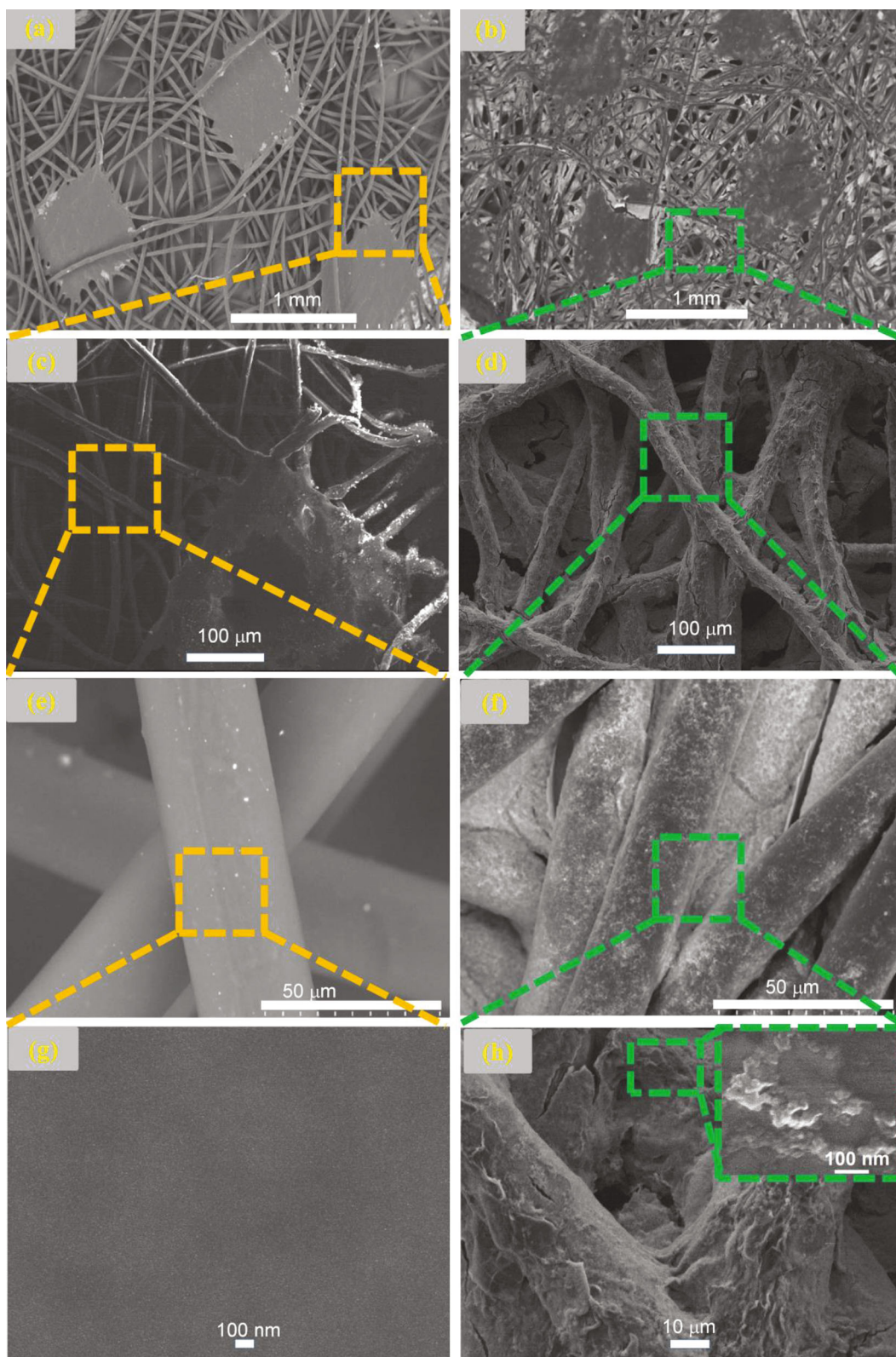


FIGURE 2: SEM and FESEM images of (a, c, e, g) NWPF and (b, d, f, h) GFCs/NWPF.

( $-\text{NH}_2$ ) from CS and  $-\text{COOH}$ . The  $-\text{OH}$  groups of GO are suitable for nonionic dyes when they are in a neutral environment. In an acidic environment, these groups will become  $-\text{NH}_3^{\oplus}$ ,  $-\text{COOH}_2^{\oplus}$ , and  $-\text{OH}_2^{\oplus}$ ; thus, they are suit-

able for absorbing MO, RS, and CR. Moreover, in an alkaline environment, these functional groups will become  $-\text{NH}_2$ ,  $-\text{COO}^{\ominus}$ , and  $-\text{O}^{\ominus}$ , respectively, which are suitable for absorbing MB [1, 2, 35, 44–47].

TABLE 2: Comparison of the adsorption capacity of the adsorbents assessed herein.

Dyes	Conditions	Adsorbents	Langmuir	Freundlich	Comparison of $q_{\max}$ ( $\text{mg g}^{-1}$ ) with that of other adsorbents
Methylene blue (MB)	pH = 9, RT, $T = 2$ h	GFC/NWPPFs	$C_e/q_e = 0.018 * C_e + 0.096$ $R^2 = 0.980$ and $q_{\max} = 54.795 \text{ mg g}^{-1}$	$\log q_e = 0.108 * \log C_e + 1.245$ $R^2 = 0.927$	GO- $\beta$ -cyclodextrin-chitosan@Fe <sub>3</sub> O <sub>4</sub> : $q_{\max} = 84.32 \text{ mg g}^{-1}$ [52]; CS/Fe <sub>3</sub> O <sub>4</sub> /GO: $q_{\max} = 30.01 \text{ mg g}^{-1}$ [2]; Fe <sub>3</sub> O <sub>4</sub> /C core-shell structure: $q_{\max} = 44.38 \text{ mg g}^{-1}$ [53]
		GFC	$C_e/q_e = 0.025 * C_e + 0.125$ $R^2 = 0.970$ and $q_{\max} = 39.308 \text{ mg g}^{-1}$	$\log q_e = 0.193 * \log C_e + 1.245$ $R^2 = 0.742$	
Methyl Orange (MO)	pH = 4, RT, $T = 2$ h	GFC/NWPPF	$C_e/q_e = 0.011 * C_e + 0.401$ $R^2 = 0.9108$ and $q_{\max} = 87.489 \text{ mg g}^{-1}$	$\log q_e = 0.736 * \log C_e + 0.550$ $R^2 = 0.990$	$\gamma$ -Fe <sub>2</sub> O <sub>3</sub> /chitosan composite film: $q_{\max} = 29.41 \text{ mg g}^{-1}$ [54]; amine/Fe <sub>3</sub> O <sub>4</sub> -resin composite: $q_{\max} = 101 \text{ mg g}^{-1}$ [55]
		GFC	$C_e/q_e = 0.012 * C_e + 0.569$ $R^2 = 0.878$ and $q_{\max} = 82.304 \text{ mg g}^{-1}$	$\log q_e = 0.753 * \log C_e + 0.411$ $R^2 = 0.978$	
Congo red (CR)	pH = 4, RT, $T = 2$ h	GFC/NWPPF	$C_e/q_e = 0.011 * C_e + 0.905$ $R^2 = 0.947$ and $q_{\max} = 88.573 \text{ mg g}^{-1}$	$\log q_e = 0.725 * \log C_e + 0.310$ $R^2 = 0.994$	XG-g-PAM/SiO <sub>2</sub> nanocomposite: $q_{\max} = 209.2 \text{ mg g}^{-1}$ [56]; spherical microparticles MgO-GO: $q_{\max} = 227 \text{ mg g}^{-1}$ [57]
		GFC	$C_e/q_e = 0.019 * C_e + 0.212$ $R^2 = 0.945$ and $q_{\max} = 52.910 \text{ mg g}^{-1}$	$\log q_e = 0.388 * \log C_e + 1.020$ $R^2 = 0.9342$	
Moderacid red (RS)	pH = 4, RT, $T = 2$ h	GFC/NWPPF	$C_e/q_e = 0.034 * C_e + 0.433$ $R^2 = 0.939$ and $q_{\max} = 29.010 \text{ mg g}^{-1}$	$\log q_e = 0.548 * \log C_e + 0.545$ $R^2 = 0.963$	Fe <sub>3</sub> O <sub>4</sub> nanoparticles and amine/Fe <sub>3</sub> O <sub>4</sub> -resin composite: $q_{\max} = 40.2$ and $99.4 \text{ mg g}^{-1}$ , respectively [55]; Fe <sub>3</sub> O <sub>4</sub> @GPTMS@P-Lys: $q_{\max} = 134.7 \text{ mg g}^{-1}$ [58]
		GFC	$C_e/q_e = 0.047 * C_e + 0.902$ $R^2 = 0.899$ and $q_{\max} = 21.249 \text{ mg g}^{-1}$	$\log q_e = 0.560 * \log C_e + 0.297$ $R^2 = 0.871$	

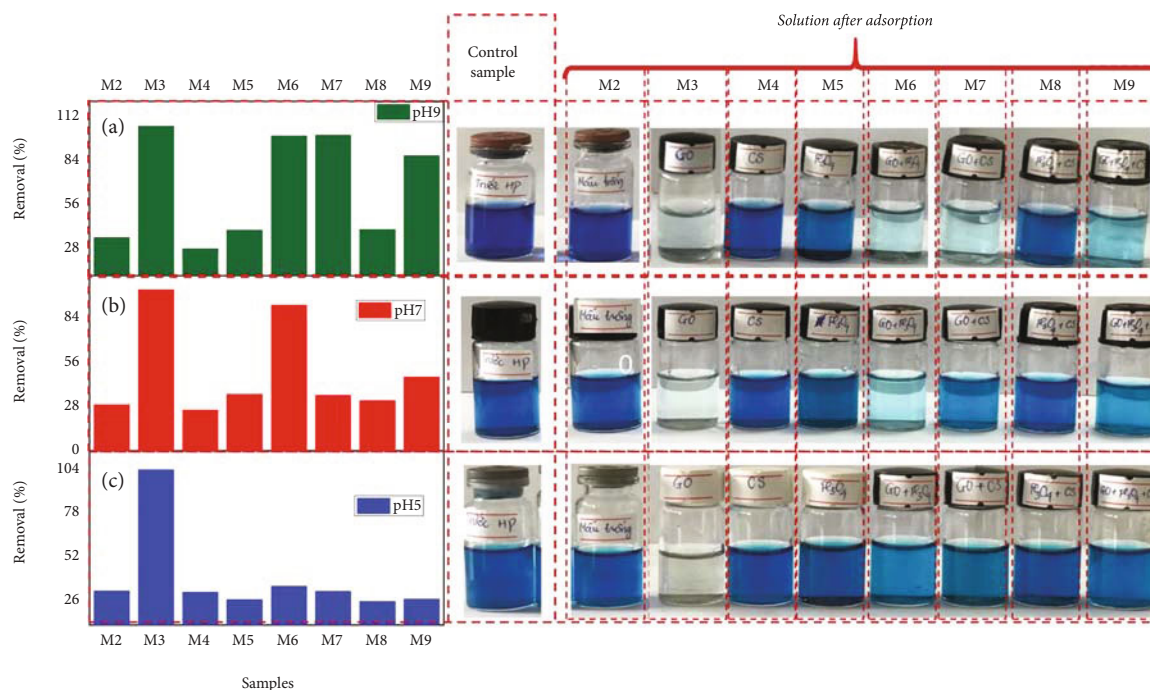


FIGURE 3: Effects of pH on MB adsorption onto the GFC/NWPF adsorbent: (a) pH 5, (b) pH 7, and (c) pH 9 (inserted images: corresponding color of MB solutions before and after the adsorption process).

Figure 3(a) shows that GO/NWPF sample (coded M3) adsorbed MB very well for all medium with removal efficiency ( $R\%$ ) which was 100%. Besides, all adsorbents containing GO, i.e., GO/Fe<sub>3</sub>O<sub>4</sub>/NWPFs (coded M6), GO/CS/NWPFs (coded M7), and GFC/NWPFs (coded M9) samples, performed good adsorption MB in basic medium (pH 9) with the highest  $R\%$  values that were obtained, which were 99%, 99%, and 86%, respectively. On the contrary, without GO, the  $R\%$  values were low for MB adsorption on NWPFs (coded M2) or CS/NWPFs (coded M4), or Fe<sub>3</sub>O<sub>4</sub>/NWPFs (coded M5) or CS/Fe<sub>3</sub>O<sub>4</sub>/NWPFs (coded M8) samples. Figure 3 also shows that the  $R\%$  values were higher than that for neutral medium (pH 7) (Figure 3(b)) or acidic medium (pH 5) (Figure 3(c)). Obtained results imply that, for efficiency removal of MB in solution, the adsorption process should be carried out in alkaline medium, and GO presented in GO/CS/NWPFs played an important role towards MB removal.

In removing the anionic dye MO (Figure 4), the  $R\%$  values for all samples were very low (<20%) at pH 9 (Figure 4(a)) and 7 (Figure 4(b)). However, in an acidic medium (pH 5), their  $R\%$  values were higher (Figure 4(c)). The  $R\%$  value for MO adsorption onto the M6 (GO/Fe<sub>3</sub>O<sub>4</sub>/NWPF) and M7 (GO/CS/NWPF) samples was 26%–27%. Furthermore, the  $R\%$  value was 31%–35% for the M3 (GO/NWPF) and M4 (CS/NWPFs) samples and 53%–58% for the M8 (CS/Fe<sub>3</sub>O<sub>4</sub>/NWPF) and M9 (GFC/NWPFs) samples. The  $R\%$  values were very small for MO adsorption onto the M2 (NWPF) (4%) and M5 (Fe<sub>3</sub>O<sub>4</sub>/NWPF) (14%) samples. These data indicated that MO removal was more difficult to achieve than MB removal in the systems proposed herein. This difference can be attributed to the structure of MO: it

has two oppositely charged centres, namely, a positively charged centre from  $-N^{\oplus}(CH_3)$  and a negatively charged centre from  $-SO_3^{\ominus}$ . Hence, both CS (which contains  $-NH_3^{\oplus}$ ) and GO (which contains  $-COO^{\ominus}$  and  $-OH_2^{\oplus}$ ) play an important role in MO adsorption via electrostatic interactions. Therefore, the M9 sample (GFC/NWPF, which contained both CS and GO components) was able to satisfactorily remove anionic dyes (including MO, RS, and CR) in the acidic medium (pH 5). The attractive forces required to adsorb dye molecules (MB, MO, CR, and RS) onto the surface of the GFC/NWPF adsorbent were not only attributed to electrostatic interactions; it also included due to  $\pi$ - $\pi$  stacking interactions, i.e., the strong interaction between the  $\pi$ -conjugated electron systems of MB, MO, CR, and RS molecules (Table SI.1) with the  $\pi$ -conjugated electrons of GO via  $\pi$ - $\pi$  stacking interactions [1, 2, 31, 32, 42, 43, 48–51]. Accordingly, increasing the content of GO improved the adsorption capacity ( $q_{max}$ ). However, increasing the content of GO should be limited owing to economic (the price of the adsorbent will increase) and technical (the release of GO from the adsorbent into the solution should be avoided) considerations.

The effects of the adsorbents' components on dye adsorption capacity were evaluated. Five coated NWPF samples (S1, S2, S3, S4, and S5) were fabricated and tested for MB adsorption (Figure 5). Figure 5(a) shows the UV-Vis spectrum of the MB solution after adsorption by GFC powder for 2 h at RT and pH 9. The S1, S2, S3, S4, and S5 samples had compositions of GO, Fe<sub>3</sub>O<sub>4</sub>, and CS by mass ( $m_{GO}:m_{Fe_3O_4}:m_{CS}$ ) of 50:40:10, 50:10:40, 0:50:50, 10:60:30, and 10:40:50, respectively. The adsorption efficiency of each sample was very different: the samples with

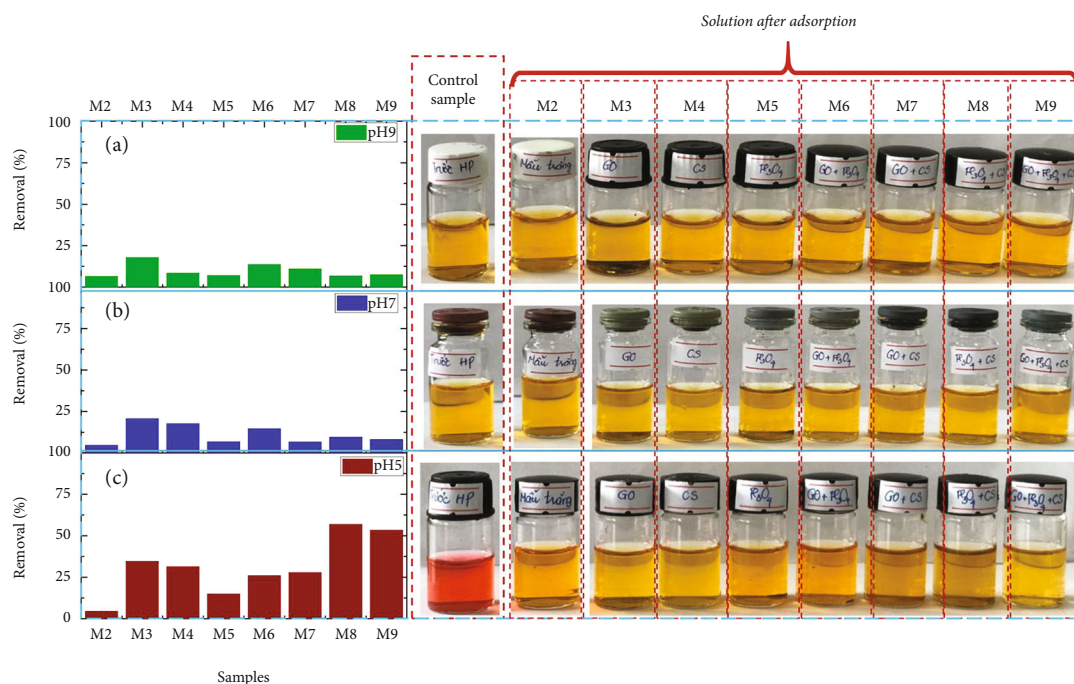


FIGURE 4: Effects of pH on MO adsorption onto the GFC/NWPF absorbent: (a) pH 5, (b) pH 7, and (c) pH 9 (inserted images: corresponding color of MO solutions before and after the adsorption process).

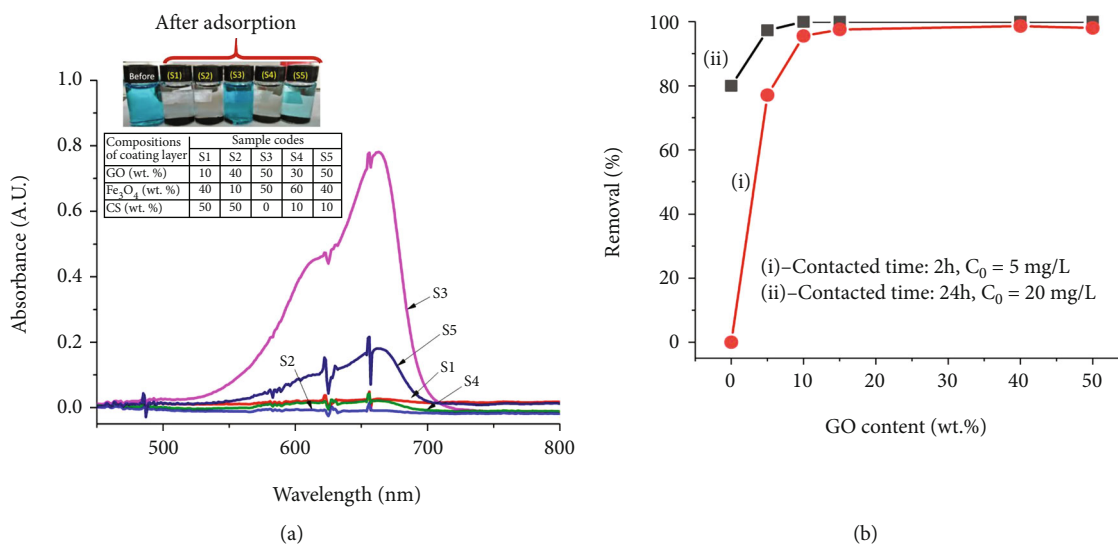


FIGURE 5: (a) UV-Vis spectra of samples after adsorption of MB solutions (inserted images are the colors of the MB solutions before and after adsorption onto GO/Fe<sub>3</sub>O<sub>4</sub>/CS [percent by weight, wt.%]: S1 [50:40:10], S2 [50:10:40], S3 [0:50:50], S4 [10:60:30], and S5 [10:40:50]). (b) Influence of GO content on MB removal at various times and (i) C<sub>0</sub> = 5 mg L<sup>-1</sup> and (ii) C<sub>0</sub> = 20 mg L<sup>-1</sup>.

high GO content (S1 and S2) had very large adsorption capacity (*R*% was 98.03% and 98.0%, respectively). When doped with Fe<sub>3</sub>O<sub>4</sub> and CS, the efficiency of the samples with low GO content substantially increased. The S4 sample had only 10% GO, but its adsorption efficiency was large (*R*% was 95.55%). However, when excessive amounts of CS were added, the *R*% value dramatically decreased to 77.08% in the S5 sample (containing 50 wt.% CS) and even down to 0% in the S3 sample (containing 0 wt.% GO and 50 wt.% CS).

Adding excessive amounts of CS considerably reduced the porosity of the materials. Therefore, GO should be added as much as possible while limiting the content of CS to 10 wt.%–40 wt.%. However, the production costs of GO are high. Thus, instead of adding 40 wt.%–50 wt.% of GO to remove MB at *R*% > 90% in 2 h, *R*% > 90% can still be achieved when 10 wt.% of GO is added by simply extending the adsorption time to 24 h (Figure 5(b)). When the content of GO was increased from 20 wt.% to 50 wt.%, the value of

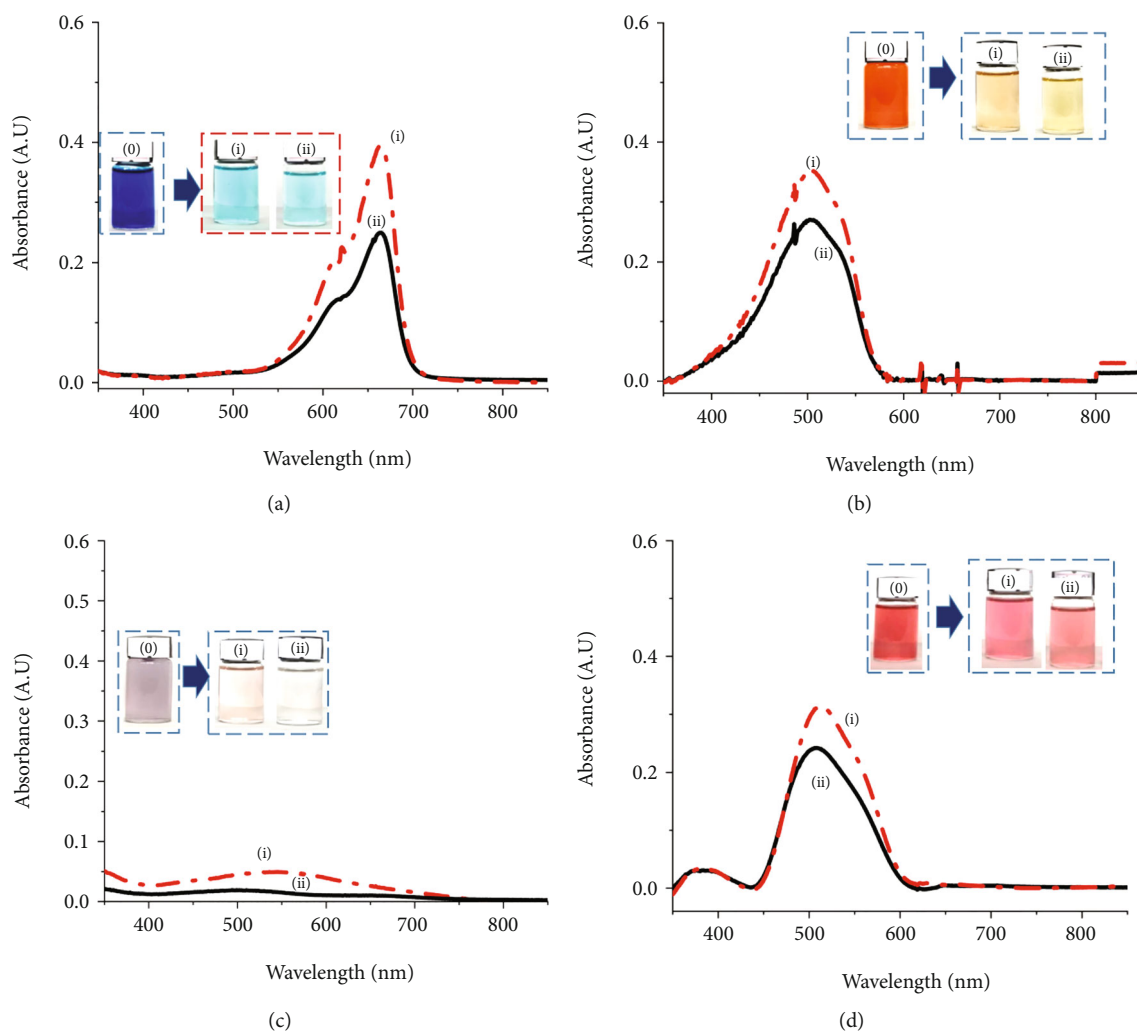


FIGURE 6: UV-Vis spectra of colorant solutions after adsorption of (a) MB, (b) MO, (c) CR, and (d) RS onto (i) GFC (red dot-dash) and (ii) GFC/NWPF (black solid) (inserted image: color of colorant solutions before and after adsorption).

R% did not increase (Figure 5(b)). Therefore, the addition of 10 wt.% of GO is the best level that achieves the optimum technical-economic efficiency.

**3.3.2. Comparison of the Adsorption of MB, MO, CR, and RS onto the GFC/NWPF Absorbent and Bulk GFC.** The adsorption efficiency of bulk GFC was compared with that of the GFC/NWPF absorbent under the same conditions with the same amount of GFC converted. Both the powder and coated samples achieved very good adsorption efficiency for MB, MO, CR, and RS, and the color of the solutions was almost completely eliminated (Figure 6). In all cases, the GFC/NWPF samples seemed to remove the colorants better than the GFC: R% was 97.98% and 96.11% for MB (Figure 6(a)), 96.25% and 94.86% for MO (Figure 6(b)), 97.15% and 84.47% for CR (Figure 6(c)), and 83.68% and 78.22% for RS (Figure 6(d)), respectively. Differences in color could also be observed with the naked eye (pictures inserted in the figures). This result confirmed that coating GFC is necessary to improve its adsorption performance.

**3.3.3. Adsorption Isotherms of MB, MO, CR, and RS onto the GFCs/NWPF Absorbent.** The adsorption isotherms of MB, MO, RS, and CR on both bulk GFC and the GFC/NWPF absorbent were built according to the Langmuir and Freundlich models by using equations (3) and (4) (Table 2 and Figs. SI.7–SI.10). On the basis of the correlation coefficient ( $R^2$ ), the process by which the organic dyes absorb on both bulk GFC and the GFC/NWPF absorbent was more consistent with the Langmuir model than with the Freundlich model. The maximum adsorption capacity ( $q_{max}$ ) of the GFC/NWPF absorbent for all organic dyes was higher than that of bulk GFC (Table 2). Results indicated that the presence of NWPF enhanced  $q_{max}$ . Compared the absorption efficiency for MB, MO, RS, and CR of the various reported materials, the  $q_{max}$  values for MB or MO of the developed hybrid materials herein including bulk GFC and the GFC/NWPF adsorbents are competitive and lower for RS and CR adsorption (Table 2). However, an advantage of the developed bulk GFC and GFC/NWPF adsorbents is they can be made via a simple synthesis process.

## 4. Conclusions

NWPF was extracted from discarded disposable face masks and used as a support to prepare a GFC nanocomposite-based adsorbent. GFC was successfully onto NWPF. The presence of NWPF enhanced the adsorption efficiency of GFC for the organic dyes MB, MO, CR, and RS. In all cases, the coating improved the adsorption performance of the GFC materials. The adsorption efficiency of the GFC/NWPF adsorbent for these organic dyes was higher than that of bulk GFC with the same mass. Obtained results demonstrated that the adsorption efficiency of the GFC/NWPF adsorbent was different for MB, MO, CR, and RS dyes and can be competitive to previously reported materials implying that the GFC/NWPF adsorbent has a high application potential.

## Data Availability

The data used to support the findings of this study are included within the article.

## Conflicts of Interest

The authors declare that they have no conflict of interest.

## Acknowledgments

This work was supported by the Vietnam Ministry of Education and Training (under project number B2020-BKA-15).

## Supplementary Materials

Table IS.1: molecular structure and some specific properties of MB, MO, CR, and RS. Figure SI.1: characterizations of GO: (a) UV-Vis spectrum (inserted figure: digital photo of GO solution and GO flakes), (b) XRD, (c, d) SEM, (e) FE-SEM, and (f) TEM images. Figure SI.2: FT-IR spectra of (a) chitosan (CS) and (b) graphene oxide/Fe<sub>3</sub>O<sub>4</sub>/chitosan (GFC). Figure SI.3: right, UV-Vis spectra of MO solution at various MO concentrations and left, corresponding calibration curves for MO determination at various pH: (i) pH = 4, (ii) pH = 5, (iii) pH = 7, and (iv) pH = 9. Figure SI.4: right, UV-Vis spectra of MB solution at various MB concentrations and left, corresponding calibration curves for MB determination at various pH: (i) pH = 5, (ii) pH = 7, and (iii) pH = 9. Figure SI.5: (i) UV-Vis spectra of CR solution at various CR concentrations and (ii) corresponding calibration curves for CR determination at pH = 4. Figure SI.6: (i) UV-Vis spectra of RS solution at various RS concentrations and (ii) corresponding calibration curves for CR determination at pH = 4. Fig. SI.7: adsorption isotherm according to (a, c) Langmuir and (b, d) Freundlich models of MB on (a, b) GFCs/NWPFs and (c, d) bulk GFCs, respectively. Fig. SI.8: adsorption isotherm according to (a, c) Langmuir and (b, d) Freundlich models of MO on (a, b) GFCs/NWPFs and (c, d) bulk GFCs, respectively. Fig. SI.9: adsorption isotherm according to (a, c) Langmuir and (b, d) Freundlich models of CR on (a, b) GFCs/NWPFs and (c, d) bulk GFCs, respectively. Fig. SI.10: adsorption iso-

therm according to (a, c) Langmuir and (b, d) Freundlich models of RS on (a, b) GFCs/NWPFs and (c, d) bulk GFCs, respectively. (*Supplementary Materials*)

## References

- [1] H. V. Tran, L. T. Hoang, and C. D. Huynh, "An investigation on kinetic and thermodynamic parameters of methylene blue adsorption onto graphene-based nanocomposite," *Chemical Physics*, vol. 535, article 110793, 2020.
- [2] H. V. Tran, L. T. Bui, T. T. Dinh, D. H. Le, C. D. Huynh, and A. X. Trinh, "Graphene oxide/Fe<sub>3</sub>O<sub>4</sub>/chitosan nanocomposite: a recoverable and recyclable adsorbent for organic dyes removal. Application to methylene blue," *Materials Research Express*, vol. 4, no. 3, 2017, Article number 035701.
- [3] S. Vallinayagam, K. Rajendran, S. K. Lakkaboyana et al., "Recent developments in magnetic nanoparticles and nanocomposites for wastewater treatment. Journal of Environmental," *Chemical Engineering*, vol. 9, no. 6, article 106553, 2021.
- [4] C. Fernández, M. S. Larrechi, and M. P. Callao, "An analytical overview of processes for removing organic dyes from wastewater effluents," *TrAC Trends in Analytical Chemistry*, vol. 29, no. 10, pp. 1202–1211, 2010.
- [5] W. Zhang, H. Li, X. Kan et al., "Adsorption of anionic dyes from aqueous solutions using chemically modified straw," *Bioresource Technology*, vol. 117, pp. 40–47, 2012.
- [6] M. Ajmal, R. A. K. Rao, S. Anwar, J. Ahmad, and R. Ahmad, "Adsorption studies on rice husk: removal and recovery of Cd(II) from wastewater," *Bioresource Technology*, vol. 86, no. 2, pp. 147–149, 2003.
- [7] H. Genç, J. C. Tjell, D. McConchie, and O. Schuiling, "Adsorption of arsenate from water using neutralized red mud," *Journal of Colloid and Interface Science*, vol. 264, no. 2, pp. 327–334, 2003.
- [8] S. Debnath, A. Maity, and K. Pillay, "Impact of process parameters on removal of Congo red by graphene oxide from aqueous solution," *Journal of Environmental Chemical Engineering*, vol. 2, no. 1, pp. 260–272, 2014.
- [9] W. Peng, H. Li, Y. Liu, and S. Song, "A review on heavy metal ions adsorption from water by graphene oxide and its composites," *Journal of Molecular Liquids*, vol. 230, pp. 496–504, 2017.
- [10] D. Robati, B. Mirza, M. Rajabi et al., "Removal of hazardous dyes-BR 12 and methyl orange using graphene oxide as an adsorbent from aqueous phase," *Chemical Engineering Journal*, vol. 284, pp. 687–697, 2016.
- [11] J.-S. Choi, L. P. Lingamdinne, J.-K. Yang, Y.-Y. Chang, and J. R. Koduru, "Fabrication of chitosan/graphene oxide-gadolinium nanorods as a novel nanocomposite for arsenic removal from aqueous solutions," *Journal of Molecular Liquids*, vol. 320, article 114410, 2020.
- [12] D. J. Joshi, J. R. Koduru, N. I. Malek, C. M. Hussain, and S. K. Kailasa, "Surface modifications and analytical applications of graphene oxide: a review," *TrAC Trends in Analytical Chemistry*, vol. 144, article 116448, 2021.
- [13] L. P. Lingamdinne, J. R. Koduru, and R. R. Karri, "A comprehensive review of applications of magnetic graphene oxide based nanocomposites for sustainable water purification," *Journal of Environmental Management*, vol. 231, pp. 622–634, 2019.
- [14] L. P. Lingamdinne, J. R. Koduru, Y. Y. Chang, M. Naushad, and J. K. Yang, "Polyvinyl alcohol polymer functionalized

- graphene oxide decorated with gadolinium oxide for sequestration of radionuclides from aqueous medium: Characterization, Mechanism, and Environmental Feasibility Studies,” *Polymers*, vol. 13, no. 21, article 3835, 2021.
- [15] D. R. Dreyer, S. Park, C. W. Bielawski, and R. S. Ruoff, “The chemistry of graphene oxide,” *Chemical Society Reviews*, vol. 39, no. 1, pp. 228–240, 2010.
- [16] J.-G. Yu, L.-Y. Yu, H. Yang et al., “Graphene nanosheets as novel adsorbents in adsorption, preconcentration and removal of gases, organic compounds and metal ions,” *Science of the Total Environment*, vol. 502, pp. 70–79, 2015.
- [17] K. Z. Elwakeel, “Environmental application of chitosan resins for the treatment of water and wastewater: a review,” *Journal of Dispersion Science and Technology*, vol. 31, no. 3, pp. 273–288, 2010.
- [18] P. Szymczyk, U. Filipkowska, T. Józwiak, and M. Kuczajowska-Zadrożna, *The use of chitin and chitosan for the removal of reactive black 5 dye*, Progress on Chemistry and Application of Chitin and Its Derivatives XX, 2015.
- [19] H. V. Tran, L. T. Hoang, and H. T. T. Huyen, *Electrochemical Synthesis of Graphene from Waste Discharged Battery Electrodes and Its Applications to Preparation of Graphene/Fe<sub>3</sub>O<sub>4</sub>/Chitosan-Nanosorbent for Organic Dyes Removal*, Zeitschrift für anorganische und allgemeine Chemie, 2021.
- [20] H. V. Tran, T. L. Tran, T. D. Le, T. D. Le, H. M. T. Nguyen, and L. T. Dang, “Graphene oxide enhanced adsorption capacity of chitosan/magnetite nanocomposite for Cr (VI) removal from aqueous solution,” *Materials Research Express*, vol. 6, no. 2, article 025018, 2019.
- [21] G. Sheng, Y. Li, X. Yang et al., “Efficient removal of arsenate by versatile magnetic graphene oxide composites,” *RSC Advances*, vol. 2, no. 32, pp. 12400–12407, 2012.
- [22] T. N. Nguyen, H. T. B. Pham, H. V. Tran, H. D. Vu, K. V. Nguyen, and L. D. Tran, “Magnetic chitosan nanoparticles for removal of Cr (VI) from aqueous solution,” *Materials Science and Engineering: C*, vol. 33, no. 3, pp. 1214–1218, 2013.
- [23] H. V. Tran, L. D. Tran, and T. N. Nguyen, “Preparation of chitosan/magnetite composite beads and their application for removal of Pb (II) and Ni (II) from aqueous solution,” *Materials Science and Engineering: C*, vol. 30, no. 2, pp. 304–310, 2010.
- [24] M. Elisabeth, “Covid-19: are cloth masks still effective? And other questions answered,” *British Medical Journal*, vol. 372, article n432, 2021.
- [25] N. Karim, S. Afroj, K. Lloyd et al., “Sustainable personal protective clothing for healthcare applications: a review,” *ACS Nano*, vol. 14, no. 10, pp. 12313–12340, 2020.
- [26] F. G. Torres and G. E. De-la-Torre, “Face mask waste generation and management during the COVID-19 pandemic: an overview and the Peruvian case,” *Science of The Total Environment*, vol. 786, article 147628, 2021.
- [27] P. Sadrolodabae, J. Claramunt, M. Ardanuy, and A. de la Fuente, “A textile waste fiber-reinforced cement composite: comparison between short random fiber and textile reinforcement,” *Materials*, vol. 14, article 3742, 2021.
- [28] A. K. M. A. H. Asif and M. Z. Hasan, “Application of nanotechnology in modern textiles: a review,” *International Journal of Current Engineering and Technology*, vol. 8, no. 2, pp. 227–231, 2014.
- [29] M. J. Madou, *Manufacturing Techniques for Microfabrication and Nanotechnology*, CRC press, 2011.
- [30] M. Neznakomova, S. Boteva, L. Tzankov, and M. Elhag, “Non-woven textile materials from waste fibers for cleanup of waters polluted with petroleum and oil products,” *Earth Systems and Environment*, vol. 2, pp. 413–420, 2018.
- [31] M. U. Dao, T. T. T. Nguyen, V. T. Le et al., “Non-woven polyester fabric-supported cuprous oxide/reduced graphene oxide nanocomposite for photocatalytic degradation of methylene blue,” *Journal of Materials Science*, vol. 56, pp. 10353–10366, 2021.
- [32] K. Huo, J. Wang, T. Zhuang et al., “Facile fabrication of recyclable and macroscopic D-g-C<sub>3</sub>N<sub>4</sub>/sodium alginates/non-woven fabric immobilized photocatalysts with enhanced photocatalytic activity and antibacterial performance,” *Journal of Materials Science*, vol. 56, no. 31, pp. 17584–17600, 2021.
- [33] G. Luo, Q. Yu, L. Yu, X. Wang, X. Hao, and J. Fu, “Preparation and characterization of platinum nanoparticles supported by non-woven fabric for formaldehyde decomposition,” *Fibers and Polymers*, vol. 20, pp. 2099–2105, 2019.
- [34] T. D. Le, L. T. Tran, H. T. M. Dang, H. T. T. Tran, and H. V. Tran, “Graphene oxide/polyvinyl alcohol/Fe<sub>3</sub>O<sub>4</sub> nanocomposite: an efficient adsorbent for Co (II) ion removal,” *Journal of Analytical Methods in Chemistry*, vol. 2021, Article ID 6670913, 2021.
- [35] L. T. Tran, H. V. Tran, T. D. Le, G. L. Bach, and L. D. Tran, “Studying Ni (II) adsorption of magnetite/graphene oxide/chitosan nanocomposite,” *Advances in Polymer Technology*, vol. 2019, Article ID 8124351, 2019.
- [36] H. V. Tran, A. X. Trinh, C. D. Huynh, and H. Q. Le, “Facile hydrothermal synthesis of silver/chitosan nanocomposite and application in the electrochemical detection of hydrogen peroxide,” *Sensor Letters*, vol. 14, pp. 32–38, 2016.
- [37] H.-M. Ju, S.-H. Choi, and S. H. Huh, “X-ray diffraction patterns of thermally-reduced graphenes,” *Journal of the Korean Physical Society*, vol. 57, no. 6, p. 1649, 2010.
- [38] Y. Du, M. Pei, Y. He, F. Yu, W. Guo, and L. Wang, “Preparation, characterization and application of magnetic Fe<sub>3</sub>O<sub>4</sub>-CS for the adsorption of orange I from aqueous solutions,” *PLoS One*, vol. 9, no. 10, article e108647, 2014.
- [39] M. Liu, T. Wen, X. Wu et al., “Synthesis of porous Fe<sub>3</sub>O<sub>4</sub> hollow microspheres/graphene oxide composite for Cr(VI) removal,” *Dalton Transactions*, vol. 42, no. 41, pp. 14710–14717, 2013.
- [40] S. ul Haque, A. Nasar, and M. M. R. Inamuddin, “Applications of chitosan (CHI)-reduced graphene oxide (rGO)-polyaniline (PAni) conducting composite electrode for energy generation in glucose biofuel cell,” *Scientific Reports*, vol. 10, article 10428, 2020.
- [41] M. Yadav, Y. Y. Rhee, S. J. Park, and D. Hui, “Mechanical properties of Fe<sub>3</sub>O<sub>4</sub>/GO/chitosan composites,” *Composites Part B: Engineering*, vol. 66, pp. 89–96, 2014.
- [42] X. Rong, F. Qiu, C. Zhang, L. Fu, Y. Wang, and D. Yang, “Adsorption-photodegradation synergetic removal of methylene blue from aqueous solution by NiO/graphene oxide nanocomposite,” *Powder Technology*, vol. 275, pp. 322–328, 2015.
- [43] Y. Yang, Y. Xie, L. Pang et al., “Preparation of reduced graphene oxide/poly(acrylamide) nanocomposite and its adsorption of Pb(II) and methylene blue,” *Langmuir*, vol. 29, pp. 10727–10736, 2013.

- [44] H. C. Vu, A. D. Dwivedi, T. T. Le, S.-H. Seo, E.-J. Kim, and Y.-S. Chang, "Magnetite graphene oxide encapsulated in alginate beads for enhanced adsorption of Cr(VI) and As(V) from aqueous solutions: role of crosslinking metal cations in pH control," *Chemical Engineering Journal*, vol. 307, pp. 220–229, 2017.
- [45] N. T. Nguyen, N. T. Nguyen, and V. A. Nguyen, "In situ synthesis and characterization of ZnO/chitosan nanocomposite as an adsorbent for removal of Congo red from aqueous solution," *Advances in Polymer Technology*, vol. 2020, Article ID 3892694, 2020.
- [46] H. Shi, J. Yang, L. Zhu et al., "Removal of  $Pb^{2+}$ ,  $Hg^{2+}$ , and  $Cu^{2+}$  by chain-like  $Fe_3O_4@SiO_2$ @chitosan magnetic nanoparticles," *Journal of Nanoscience and Nanotechnology*, vol. 16, pp. 1871–1882, 2016.
- [47] H. V. Tran, H. V. Nguyen, D. V. Vu, T. D. Le, B. T. Nguyen, and D. H. Le, "Carbon coated  $MFe_2O_4$  ( $M=Fe, Co, Ni$ ) magnetite nanoparticles: a smart adsorbent for direct yellow and moderacid red dyes," *Korean Journal of Chemical Engineering*, 2021.
- [48] S. Thangavel, S. Thangavel, N. Raghavan, K. Krishnamoorthy, and G. Venugopal, "Visible-light driven photocatalytic degradation of methylene-violet by  $rGO/Fe_3O_4/ZnO$  ternary nanohybrid structures," *Journal of Alloys and Compounds*, vol. 665, pp. 107–112, 2016.
- [49] A. A. Al-Kahtani and M. F. A. Taleb, "Photocatalytic degradation of Maxilon C.I. basic dye using  $CS/CoFe_2O_4/GONCs$  as a heterogeneous photo-Fenton catalyst prepared by gamma irradiation," *Journal of Hazardous Materials*, vol. 309, pp. 10–19, 2016.
- [50] N. Song, X. L. Wu, S. Zhong, H. Lin, and J.-R. Chen, "Biocompatible  $G-Fe_3O_4/CA$  nanocomposites for the removal of methylene blue," *Journal of Molecular Liquids*, vol. 212, pp. 63–69, 2015.
- [51] W. Zhu, X. Jiang, F. Liu, F. You, and C. Yao, "Preparation of chitosan—graphene oxide composite aerogel by hydrothermal method and its adsorption property of methyl orange," *Polymers*, vol. 12, no. 9, p. 2169, 2020.
- [52] L. Fan, C. Luo, M. Sun, H. Qiu, and X. Li, "Synthesis of magnetic  $\beta$ -cyclodextrin—chitosan/graphene oxide as nanoadsorbent and its application in dye adsorption and removal," *Colloids and Surfaces B: Biointerfaces*, vol. 103, pp. 601–607, 2013.
- [53] Z. Zhang and J. Kong, "Novel magnetic  $Fe_3O_4@C$  nanoparticles as adsorbents for removal of organic dyes from aqueous solution," *Journal of Hazardous Materials*, vol. 193, pp. 325–329, 2011.
- [54] R. Jiang, Y.-Q. Fu, H.-Y. Zhu, J. Yao, and L. Xiao, "Removal of methyl orange from aqueous solutions by magnetic magnetite/chitosan nanocomposite films: adsorption kinetics and equilibrium," *Journal of Applied Polymer Science*, vol. 125, no. S2, pp. E540–E549, 2012.
- [55] W. Song, B. Gao, X. Xu et al., "Adsorption–desorption behavior of magnetic amine/ $Fe_3O_4$  functionalized biopolymer resin towards anionic dyes from wastewater," *Bioresource Technology*, vol. 210, pp. 123–130, 2016.
- [56] S. Ghorai, A. K. Sarkar, A. B. Panda, and S. Pal, "Effective removal of Congo red dye from aqueous solution using modified xanthan gum/silica hybrid nanocomposite as adsorbent," *Bioresource Technology*, vol. 144, pp. 485–491, 2013.
- [57] J. Xu, D. Xu, B. Zhu, B. Cheng, and C. Jiang, "Adsorptive removal of an anionic dye Congo red by flower-like hierarchical magnesium oxide ( $MgO$ )-graphene oxide composite microspheres," *Applied Surface Science*, vol. 435, pp. 1136–1142, 2018.
- [58] Y.-R. Zhang, P. Su, J. Huang, Q.-R. Wang, and B.-X. Zhao, "A magnetic nanomaterial modified with poly-lysine for efficient removal of anionic dyes from water," *Chemical Engineering Journal*, vol. 262, pp. 313–318, 2015.

## Research Article

# Characterization of $\text{Co}^{2+}$ - and $\text{Fe}^{3+}$ -Codoped $\text{TiO}_2$ Nanomaterials for Photocatalytic Degradation of Organic Pollutants under Visible Light Irradiation

Nguyen Thi Tuyet Mai,<sup>1</sup> Nguyen Kim Nga ,<sup>1</sup> Dang Thi Minh Hue,<sup>1</sup> Ta Ngoc Dung,<sup>1</sup> Huynh Dang Chinh,<sup>1</sup> and Tran Quang Huy <sup>2</sup>

<sup>1</sup>School of Chemical Engineering, Hanoi University of Science and Technology, 1 Dai Co Viet Road, Hanoi, Vietnam

<sup>2</sup>Phenikaa University Nano Institute (PHENA), Phenikaa University, Hanoi 12116, Vietnam

Correspondence should be addressed to Nguyen Kim Nga; [nga.nguyenkim@hust.edu.vn](mailto:nga.nguyenkim@hust.edu.vn)

Received 1 August 2021; Revised 4 October 2021; Accepted 11 October 2021; Published 18 November 2021

Academic Editor: Tien Duc Pham

Copyright © 2021 Nguyen Thi Tuyet Mai et al. This is an open access article distributed under the Creative Commons Attribution License, which permits unrestricted use, distribution, and reproduction in any medium, provided the original work is properly cited.

In this study,  $\text{TiO}_2$  nanomaterials were prepared using a solvothermal method and codoped with  $\text{Co}^{2+}$  and  $\text{Fe}^{3+}$  ions for the photocatalytic degradation of organic pollutants under visible light. The physicochemical properties of the obtained materials were studied by powder X-ray diffraction, field emission electron scanning microscopy, energy-dispersive X-ray spectroscopy, and nitrogen adsorption isotherms. Optical absorption was characterized by UV-vis absorption spectroscopy. The photocatalytic activities of the prepared materials were evaluated through methylene blue (MB) degradation under visible light irradiation. Results showed the excellent performance of MB degradation investigated on  $\text{TiO}_2$  samples codoped with  $\text{Co}^{2+}$  and  $\text{Fe}^{3+}$  in comparison with undoped and  $\text{Co}^{2+}$ -doped  $\text{TiO}_2$  samples. The codoped  $\text{TiO}_2$  samples degraded 85%–90% of MB after 120 min, whereas all the prepared  $\text{TiO}_2$  samples were composed of pure anatase phase and had a spherical-like shape and mean crystalline size ranging from 6.2 nm to 7.8 determined by Scherrer's equation. The optical absorption of the  $\text{TiO}_2$  codoped with  $\text{Co}^{2+}$  and  $\text{Fe}^{3+}$  was significantly enhanced toward the visible light region. The pseudo-second-order kinetic model fits well for the degradation of MB on as-prepared  $\text{TiO}_2$  codoped with  $\text{Co}^{2+}$  and  $\text{Fe}^{3+}$ .

## 1. Introduction

The development of metal oxide nanoparticles has been extensively attracted as adsorbents and photocatalysts for the treatment of dye-containing wastewater [1–3]. Titanium dioxide ( $\text{TiO}_2$ ) nanoparticles have considerable attention because of their long-term stability, low cost, and nontoxicity [4]. However, the major drawback of  $\text{TiO}_2$  is a large bandgap energy (~3.2 eV and 3.0 eV for anatase and rutile phases, respectively), and it requires ultraviolet (UV) irradiation (wavelength,  $\lambda < 387$  nm) for activation. Many attempts have been conducted to extend the photocatalytic activity of  $\text{TiO}_2$  from a UV to visible light region (wavelength,  $\lambda$ : 400–700 nm). Doping of  $\text{TiO}_2$  with transition metals or nonmetals is the most promising approach used to activate it due to the bandgap energy reduction [5]. Tran-

sition metals can provide additional energy levels within the bandgap of a  $\text{TiO}_2$  photocatalyst. Electron transfer from one of these levels to the conduction band requires lower photon energy than those of undoped  $\text{TiO}_2$  [6]. Various transition metal ions have been studied to dope with  $\text{TiO}_2$ , including Co [7], Fe [8], Cr [9], Ni [10], and V [11], etc. Furthermore, many researchers have also focused on codoping of  $\text{TiO}_2$  with two or more metal ions for enhancement of photocatalytic degradation of organic pollutants under solar light irradiation such as Mn and Co [12]; Ni and Cr [13]; Fe, Co, and S [14]; and Fe and Pr [15]. It indicated that codoped  $\text{TiO}_2$  could expand its light absorption range toward visible light and thus enhance its photocatalytic efficiency, which is higher than that of single-doped  $\text{TiO}_2$ . It was reported that  $\text{Mn}^{2+}$ - and  $\text{Co}^{2+}$ -codoped  $\text{TiO}_2$  could degrade about 97% of enoxacin, which was higher than that of  $\text{Co}^{2+}$  single-

doped TiO<sub>2</sub> (degradation percentage ~48%) after 80 min of exposure to solar light [12]. A recent work also demonstrated that Ni/Cr-codoped TiO<sub>2</sub> exhibited a higher efficiency of 95.6% for MB degradation after 90 min under sunlight, compared to Ni-doped TiO<sub>2</sub> (Ni-doped TiO<sub>2</sub> degraded ~28%-59% of MB depending on the amount of Ni doping) [13]. The photocatalytic degradation of Acid Orange 7 azo dye under visible light using Fe<sup>3+</sup>- and Pr<sup>3+</sup>-codoped TiO<sub>2</sub> was much more enhanced compared to undoped TiO<sub>2</sub> and Fe<sup>3+</sup>-single-doped TiO<sub>2</sub> [15]. Those studies indicated that the photocatalytic activity of doped TiO<sub>2</sub> material is greatly dependent on the nature of the dopant ions and their doping concentration and preparation, in which optimal conditions for the synthesis decide the ability of nanomaterials applied for the photodegradation of organic pollutants in wastewater. Fe<sup>3+</sup> has been considered the best dopant among the transition metals used for increasing the photocatalytic activity of TiO<sub>2</sub> thanks to its similar radius to Ti<sup>4+</sup> (0.63 Å and 0.60 Å, respectively). TiO<sub>2</sub> doping with Co<sup>2+</sup> showed excellent degradation activity of dye molecules; however, the optimal concentration of Co<sup>2+</sup> is needed to enhance activity, because the high percentage of Co<sup>2+</sup> leads to a reduction in the photocatalytic activity [14].

In this study, we aimed to synthesize and characterize TiO<sub>2</sub> nanoparticles codoped with Co<sup>2+</sup> and Fe<sup>3+</sup> ions using the solvothermal method. The effect of the doping concentration of Co<sup>2+</sup> was investigated to determine the optimal condition for preparing a photocatalyst with high activity in the visible light region. The obtained nanomaterials were investigated by various physicochemical methods, including XRD, FE-SEM, EDXS, nitrogen adsorption-desorption isotherms, and UV-vis absorption. Photocatalytic activities of prepared nanomaterials were evaluated for degradation of methylene blue (MB). Our results indicated that the prepared TiO<sub>2</sub> materials codoped with Co<sup>2+</sup> and Fe<sup>3+</sup> showed a highly photocatalytic efficiency compared to single-doped TiO<sub>2</sub>. This nanomaterial could be an effective alternative for the treatment of wastewater in the textile industry.

## 2. Materials and Methods

**2.1. Chemicals and Preparation.** All chemicals were of analytical grade and used as received without further purification. Tetraisopropyl orthotitanate (Ti(*i*-OC<sub>3</sub>H<sub>7</sub>)<sub>4</sub>), acetylacetone (C<sub>5</sub>H<sub>8</sub>O<sub>2</sub>), ethanol (C<sub>2</sub>H<sub>5</sub>OH), and methylene blue C<sub>16</sub>H<sub>18</sub>ClN<sub>3</sub>S (MB) were obtained from Merck. Cobalt (II) acetate tetrahydrate ((CH<sub>3</sub>COO)<sub>2</sub>Co·4H<sub>2</sub>O) and iron (III) nitrate nonahydrate (Fe(NO<sub>3</sub>)<sub>3</sub>·9H<sub>2</sub>O) were purchased from China. Double-distilled water was used for preparing all solutions.

Single doping of TiO<sub>2</sub> with Co<sup>2+</sup> and codoping with Co<sup>2+</sup> and Fe<sup>3+</sup> were conducted by the solvothermal synthesis. The obtained samples were referred to as TiO<sub>2</sub>-*x*%Co-*y*%Fe, with *x* and *y* showing the molar Co/Ti and Fe/Ti ratio in the starting materials, respectively. In a typical experiment, a mixture consisting of 14.5 mL of C<sub>2</sub>H<sub>5</sub>OH and 0.5 mL of C<sub>5</sub>H<sub>8</sub>O<sub>2</sub> was stirred for 15 min. The mixture was slowly added with 2.96 mL of Ti(*i*-OC<sub>3</sub>H<sub>7</sub>)<sub>4</sub> as a precursor

and stirred for another 30 min (mixture 1). Desired amounts of (CH<sub>3</sub>COO)<sub>2</sub>Co·4H<sub>2</sub>O and Fe(NO<sub>3</sub>)<sub>3</sub>·9H<sub>2</sub>O were dissolved in another mixture consisting of 5 mL of C<sub>2</sub>H<sub>5</sub>OH, 1 mL of C<sub>5</sub>H<sub>8</sub>O<sub>2</sub>, and 0.18 mL of H<sub>2</sub>O for 30 min. The mixed solution was then dropped into mixture 1 with continuous stirring for 30 min and then transferred to a 100 mL Teflon-lined stainless-steel autoclave maintained at 180°C for 12 h. The product was washed several times with double-distilled water until pH 7, dried at 100°C for 24 h, and ground on agate mortar. Single-doped and codoped TiO<sub>2</sub> samples were designated as TiO<sub>2</sub>-1%Co, TiO<sub>2</sub>-2.5%Co, TiO<sub>2</sub>-5%Co, TiO<sub>2</sub>-1%Co-2.5%Fe, and TiO<sub>2</sub>-2.5%Co-2.5%Fe. TiO<sub>2</sub> nanoparticles were also prepared as a control and denoted as undoped TiO<sub>2</sub>.

**2.2. Material Characterization.** X-ray diffraction (XRD) patterns of the prepared TiO<sub>2</sub> samples were recorded with a D8 ADVANCE Bruker Diffractometer within 2θ range of 20°–80° with a scan step of 0.03°·s<sup>-1</sup> under Cu-Kα radiation (λ = 0.154056 nm). The surface morphology of the TiO<sub>2</sub> samples and representative doped TiO<sub>2</sub> samples was observed by field emission scanning electron microscopy (FE-SEM, Hitachi S-4800, Japan). The average nanoparticle sizes were calculated from the scanning electron microscopic (SEM) images by using ImageJ software. The elemental composition of the samples was analyzed through energy-dispersive X-ray spectroscopy (EDXS, Nova NanoSEM 450, FEI). The nitrogen adsorption-desorption isotherms of the representative TiO<sub>2</sub> samples were measured at -196°C with a Micromeritics ASAP 2020 apparatus. The total surface areas of the samples were determined by the Brunauer–Emmett–Teller (BET) method, and the pore size distribution was determined through the Barrett–Joyner–Halenda (BJH) method using desorption curves. UV-vis absorption spectra were recorded on the Jasco V-670 spectrometer.

The photocatalytic activity of the prepared TiO<sub>2</sub> samples was evaluated by degradation of MB under visible light irradiation. A 250 W Osram mercury lamp equipped with a UV cut-off filter was used as a visible light source. In a typical experiment, 40 mg of the prepared TiO<sub>2</sub> sample was added into a 100 mL quartz photoreactor containing 50 mL of 14 mg·L<sup>-1</sup> MB solution. The reaction mixture was then stirred in the dark at a constant speed of 150 rpm for 30 min to reach the adsorption-desorption equilibrium. The resulting mixture was irradiated under the visible light source for up to 120 min. After predefined intervals (30, 60, 90, and 120 min), the samples were removed from the photoreactor and centrifuged. The residual concentration in the supernatant was measured with a UV-vis spectrometer (Agilent 8453, USA) at a wavelength of 665 nm. MB concentration was determined using a linear regression equation obtained by plotting a calibration curve of MB within a range of known concentrations. The photocatalytic ability of the TiO<sub>2</sub> samples was evaluated through the percentage of MB degradation as follows:

$$\text{Degradation percent} = \frac{C_0 - C}{C_0} \cdot 100\%, \quad (1)$$

where  $C_0$  is the initial concentration of MB and  $C$  is the remaining concentration of MB at a specific time of measurement.

### 3. Results and Discussion

**3.1. Characterization of the Synthesized Materials.** The XRD patterns of the synthesized samples (undoped, single-doped, and codoped  $\text{TiO}_2$ ) are shown in Figure 1. The results demonstrated the formation of monocrystalline  $\text{TiO}_2$  in the anatase phase in all samples. The XRD pattern of undoped  $\text{TiO}_2$  samples (Figure 1(a)) shows typically crystalline peaks at  $2\theta = 25.1^\circ$ ,  $37.67^\circ$ ,  $47.71^\circ$ , and  $54.11^\circ$  corresponding to crystal planes (101), (111), (200), and (211), respectively, which can be indexed to the anatase phase of  $\text{TiO}_2$  (JCPDS card no. 21-1272). For single-doped and codoped  $\text{TiO}_2$  samples, those diffraction peaks are observed at  $2\theta = 25.22^\circ$ ,  $25.25^\circ$ ,  $25.30^\circ$ ,  $25.34^\circ$ , and  $25.37^\circ$ ;  $37.85^\circ$ ,  $37.90^\circ$ ,  $38^\circ$ ,  $38.09^\circ$ , and  $38.12^\circ$ ;  $47.82^\circ$ ,  $47.88^\circ$ ,  $47.92^\circ$ ,  $47.99^\circ$ , and  $48.11^\circ$ ; and  $54.35^\circ$ ,  $54.41^\circ$ ,  $54.44^\circ$ ,  $54.46^\circ$ , and  $54.51^\circ$  (see Figures 1(b)–1(f)) for  $\text{TiO}_2$ -1%Co,  $\text{TiO}_2$ -2.5%Co,  $\text{TiO}_2$ -5%Co,  $\text{TiO}_2$ -1%Co-2.5%Fe, and  $\text{TiO}_2$ -2.5%Co-2.5%Fe, respectively. The data indicated that the typical peaks of the anatase  $\text{TiO}_2$  in single-doped and codoped  $\text{TiO}_2$  samples were slightly shifted to higher values than those of undoped  $\text{TiO}_2$  samples. The codoped  $\text{TiO}_2$  samples (Figures 1(e) and 1(f)) exhibited a decrease in peak intensity and slight broadening of the peaks compared with those of undoped  $\text{TiO}_2$  and single-doped  $\text{TiO}_2$  samples (Figures 1(a)–1(d)). Moreover, no characteristic peaks attributed to cobalt and iron compounds were detected in the XRD patterns, which can be attributed to the very low dopant amount in the samples. The observations suggested that  $\text{Co}^{2+}$  and  $\text{Fe}^{3+}$  cations were successfully introduced into the lattice of  $\text{TiO}_2$ . The average particle sizes of the samples were calculated from the full width at half maximum (FWHM) of the (101) diffraction peak according to the Debye–Scherrer equation [16]:

$$D = \frac{0.9\lambda}{\beta \cos \theta} \quad (2)$$

where  $\lambda$  is the X-ray wavelength (0.15406 nm),  $\beta$  is the line width at half maxima of peaks, and  $\theta$  represents the Bragg angle of X-ray diffraction. The obtained results (Table 1) showed that the average particle sizes of all samples were at a nanosized scale ranging from 6.2 nm to 7.8 nm. The single-doped and codoped  $\text{TiO}_2$  samples had a smaller size than the undoped  $\text{TiO}_2$  samples. The undoped  $\text{TiO}_2$  samples had the largest mean particle size of 7.8 nm. Among the three Co-doped  $\text{TiO}_2$  samples,  $\text{TiO}_2$ -1%Co samples had the smallest particle size with a mean particle size of 6.8 nm. The average particle size of Co-doped  $\text{TiO}_2$  samples increased from 6.8 nm to 7.5 nm with an increasing Co/Ti molar ratio from 1% to 5% in the samples. The high doping amount of Co resulted in an increase in the particle size, which was attributed to the larger radius of  $\text{Co}^{2+}$  (0.74 Å) than that of  $\text{Ti}^{4+}$  (0.60 Å). Therefore, the Co/Ti molar ratio of 1% was considered to be optimal. This ratio was further used to prepare  $\text{TiO}_2$  codoped with Co and Fe with varying

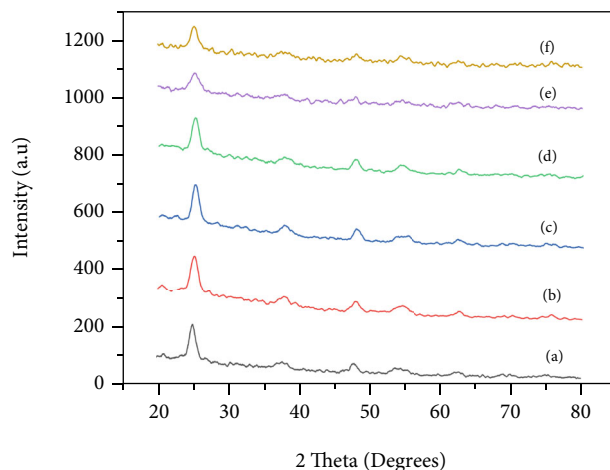


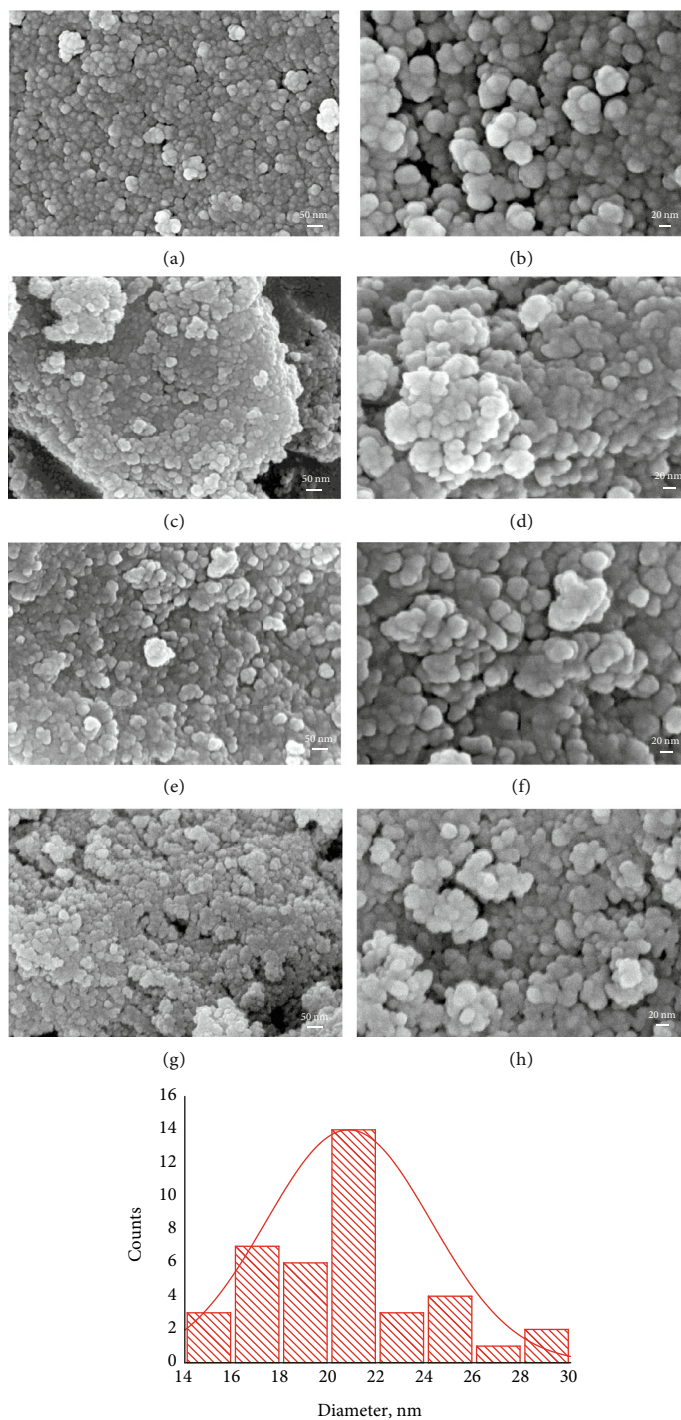
FIGURE 1: XRD patterns of (a) undoped  $\text{TiO}_2$ , (b)  $\text{TiO}_2$ -1%Co, (c)  $\text{TiO}_2$ -2.5%Co, (d)  $\text{TiO}_2$ -5%Co, and co-doped  $\text{TiO}_2$ : (e)  $\text{TiO}_2$ -1%Co-2.5%Fe and (f)  $\text{TiO}_2$ -2.5%Co-2.5%Fe.

Co/Ti molar ratios from 1% to 2.5% and a fixed Fe/Ti molar ratio of 2.5%. Previous studies [14, 15] reported that the Fe-doped  $\text{TiO}_2$  can extend more excellent absorption in the longer wavelength range than  $\text{TiO}_2$ . As a result, we chose iron as a codopant element with cobalt for extending the light absorption of  $\text{TiO}_2$  nanoparticles toward the visible region. The Fe/Ti molar ratio of 2.5% was used in the synthesis of codoped  $\text{TiO}_2$  samples, because the higher Fe content may lead to the formation of iron oxide during thermal treatment at  $180^\circ\text{C}$ , decrease the synthesis yield, and/or distort the lattice of  $\text{TiO}_2$ . As shown in Table 1,  $\text{TiO}_2$ -1%Co-2.5%Fe samples had smaller sizes (their mean particle sizes are 6.2 nm) than  $\text{TiO}_2$ -2.5%Co-2.5%Fe samples (their mean particle sizes are 7.6 nm). These results demonstrated that  $\text{TiO}_2$  codoped with Co and Fe inhibited the crystal growth of the particles and effectively decreased the particle size; the high doping amount of Co also resulted in an increase in the particle size of the codoped  $\text{TiO}_2$  samples.

The morphology of the synthesized  $\text{TiO}_2$  samples was further observed through FE-SEM imaging. Figure 2 presents the FE-SEM images of the representative samples: undoped  $\text{TiO}_2$  (Figures 2(a) and 2(b)),  $\text{TiO}_2$ -1%Co (Figures 2(c) and 2(d)),  $\text{TiO}_2$ -5%Co (Figures 2(e) and 2(f)), and  $\text{TiO}_2$ -1%Co-2.5%Fe (Figures 2(g) and 2(h)) at magnifications of 100k and 200k. The results indicated that the synthesized  $\text{TiO}_2$  samples consisted of numerous crystalline particles that agglomerated to form tiny clusters. The FE-SEM images demonstrated that the particles were spherical and had uniform size distribution. The calculations from the FE-SEM images confirmed that the average sizes were 26.5, 23.8, 27, and 20.8 nm for undoped  $\text{TiO}_2$ ,  $\text{TiO}_2$ -1%Co,  $\text{TiO}_2$ -5%Co, and  $\text{TiO}_2$ -1%Co-2.5%Fe samples, respectively. These results showed deviations from the data obtained from XRD due to the agglomeration of the nanoparticles in the FE-SEM images. However, the results were in agreement with the XRD results, confirming that Co and Fe doping can suppress  $\text{TiO}_2$  particle growth and the  $\text{TiO}_2$ -1%Co-2.5%Fe sample had the smallest particle size with a narrow distribution of the particle size (inset in Figure 2).

TABLE 1: Mean crystalline size and phase of the prepared TiO<sub>2</sub> samples.

Samples	Undoped TiO <sub>2</sub>	TiO <sub>2</sub> -1%Co	TiO <sub>2</sub> -2.5%Co	TiO <sub>2</sub> -5%Co	TiO <sub>2</sub> -1%Co-2.5%Fe	TiO <sub>2</sub> -2.5%Co-2.5%Fe
Crystalline phase	Anatase	Anatase	Anatase	Anatase	Anatase	Anatase
Mean crystalline size	7.8 nm	6.8 nm	7.4 nm	7.5 nm	6.2 nm	7.6 nm

FIGURE 2: FE-SEM images of undoped TiO<sub>2</sub> (a, b), TiO<sub>2</sub>-1%Co (c, d), TiO<sub>2</sub>-5%Co (e, f), and TiO<sub>2</sub>-1%Co-2.5%Fe (g, h) samples with magnifications of 100 k and 200 k. Inset shows a particle size distribution of TiO<sub>2</sub>-1%Co-2.5%Fe samples.

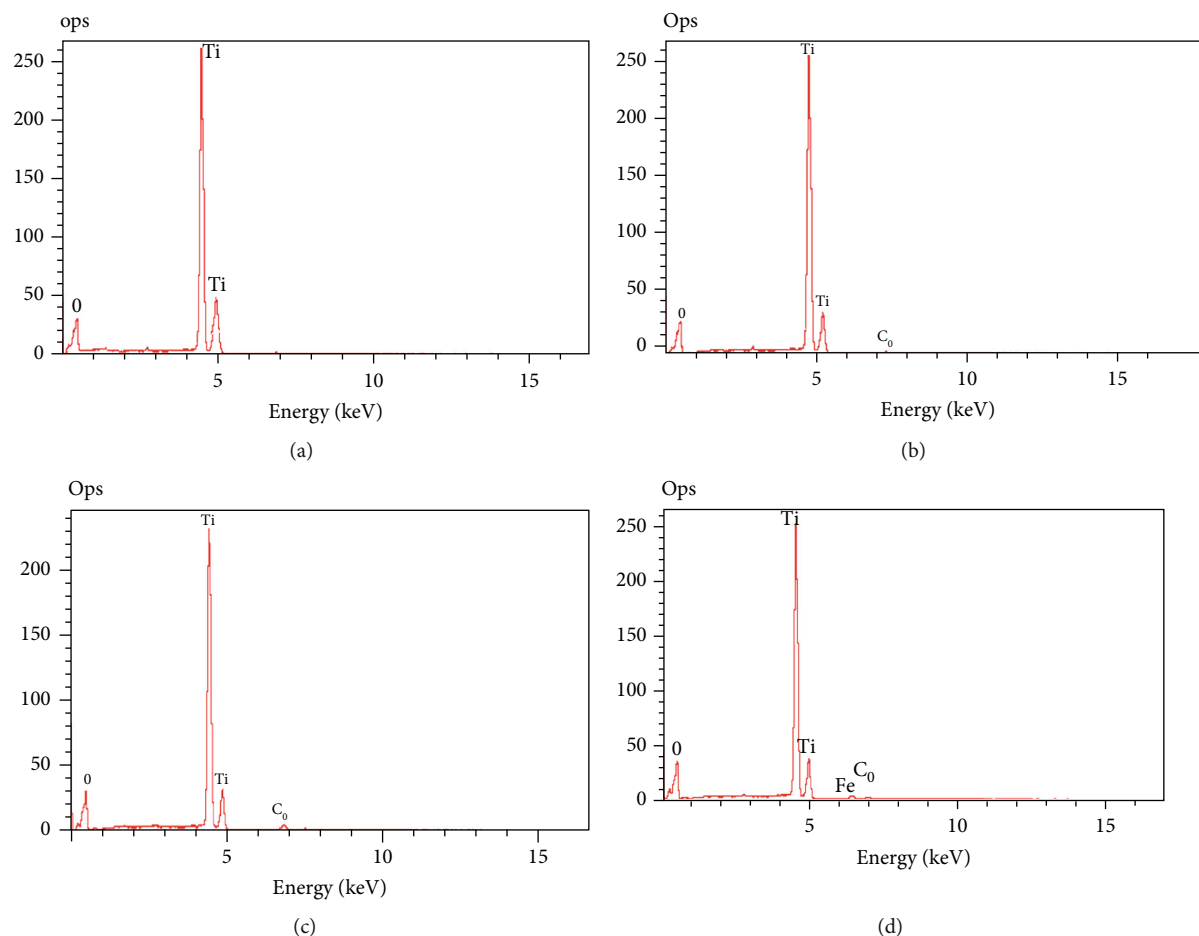


FIGURE 3: EDXS spectra of (a) undoped  $\text{TiO}_2$ , (b)  $\text{TiO}_2$ -1%Co, (c)  $\text{TiO}_2$ -5%Co, and (d)  $\text{TiO}_2$ -1%Co-2.5%Fe samples.

The presence of doping metals on the  $\text{TiO}_2$  samples was determined through EDXS analyses. The EDXS spectra of the representative  $\text{TiO}_2$  samples (undoped  $\text{TiO}_2$ ,  $\text{TiO}_2$ -1%Co,  $\text{TiO}_2$ -5%Co, and  $\text{TiO}_2$ -1%Co-2.5%Fe) are presented in Figure 3. As shown in Figures 3(a), O and Ti were found to be the major components of undoped  $\text{TiO}_2$  with 65.35 at% and 33.65 at%, respectively. Co was detected as the doping component of  $\text{TiO}_2$ -1%Co and  $\text{TiO}_2$ -5%Co samples because tiny peaks were observed in the EDXS spectra (Figures 3(b) and 3(c)), which were attributed to the presence of Co in the samples (0.21 at% and 0.89 at%, respectively). The contents of Co and Fe in  $\text{TiO}_2$ -1%Co-2.5%Fe samples were 0.28 at% and 0.74 at%, respectively (Figure 3(d)). The results confirmed that Co and Fe were successfully doped in the  $\text{TiO}_2$  samples.

Nitrogen adsorption-desorption isotherms were determined for the representative samples to analyze and quantify the pore structure and surface area of doped and codoped  $\text{TiO}_2$  samples. Figure 4 presents the nitrogen adsorption-desorption isotherms of three selected samples:  $\text{TiO}_2$ -1%Co (Figure 4(a)),  $\text{TiO}_2$ -5%Co (Figure 4(b)), and  $\text{TiO}_2$ -1%Co-2.5%Fe (Figure 4(c)). Results in Figure 4 indicate that the three samples had a similar hysteresis loop, which could be associated with capillary condensation in mesopores. The hysteresis loops of these samples, which were observed in the  $P/P_0$  range of 0.42–0.82, were characterized by a type

IV isotherm with an  $\text{H}_2$  hysteresis loop [17]. The results suggested that the  $\text{TiO}_2$  samples contained ink-bottle pores, leading to pore blocking/percolation effects during desorption in mesopore networks. Pore size distribution was calculated by the BJH method using data on the desorption curves (Figure 5). The surface areas of the synthesized  $\text{TiO}_2$  samples were determined by using the BET method. The surface characteristics of these samples are summarized in Table 2 and compared with those of undoped  $\text{TiO}_2$ .  $\text{TiO}_2$ -1%Co and  $\text{TiO}_2$ -1%Co-2.5%Fe samples showed a narrow pore size distribution (Figures 5(a) and 5(c)) with average mesopore diameters of 3.97 and 4.1 nm, respectively (Table 2).  $\text{TiO}_2$ -5%Co samples exhibited a wider pore size distribution that scattered from 2.5 nm to 6.5 nm and mainly concentrated at 5.1 nm (Figure 5(b) and Table 2). Undoped  $\text{TiO}_2$  showed a larger mean pore size of 6.7 nm than the doped and codoped  $\text{TiO}_2$ . As shown in Table 2, the prepared  $\text{TiO}_2$  samples did not have significant discrepancies in their BET surface area. Relatively high BET surface areas were determined as follows:  $170 \text{ m}^2/\text{g}$  for  $\text{TiO}_2$ -1%Co,  $164 \text{ m}^2/\text{g}$  for  $\text{TiO}_2$ -5%Co, and  $174 \text{ m}^2/\text{g}$  for  $\text{TiO}_2$ -1%Co-2.5%Fe, which are slightly higher than that of undoped  $\text{TiO}_2$  ( $160 \text{ m}^2/\text{g}$ ). The large BET surface areas of the doped and codoped  $\text{TiO}_2$  samples confirmed the better adsorption ability of the frameworks of  $\text{TiO}_2$ . This finding may be due to the linkage between the dopant ions ( $\text{Co}^{2+}$  and  $\text{Fe}^{3+}$ ) and titanium by an

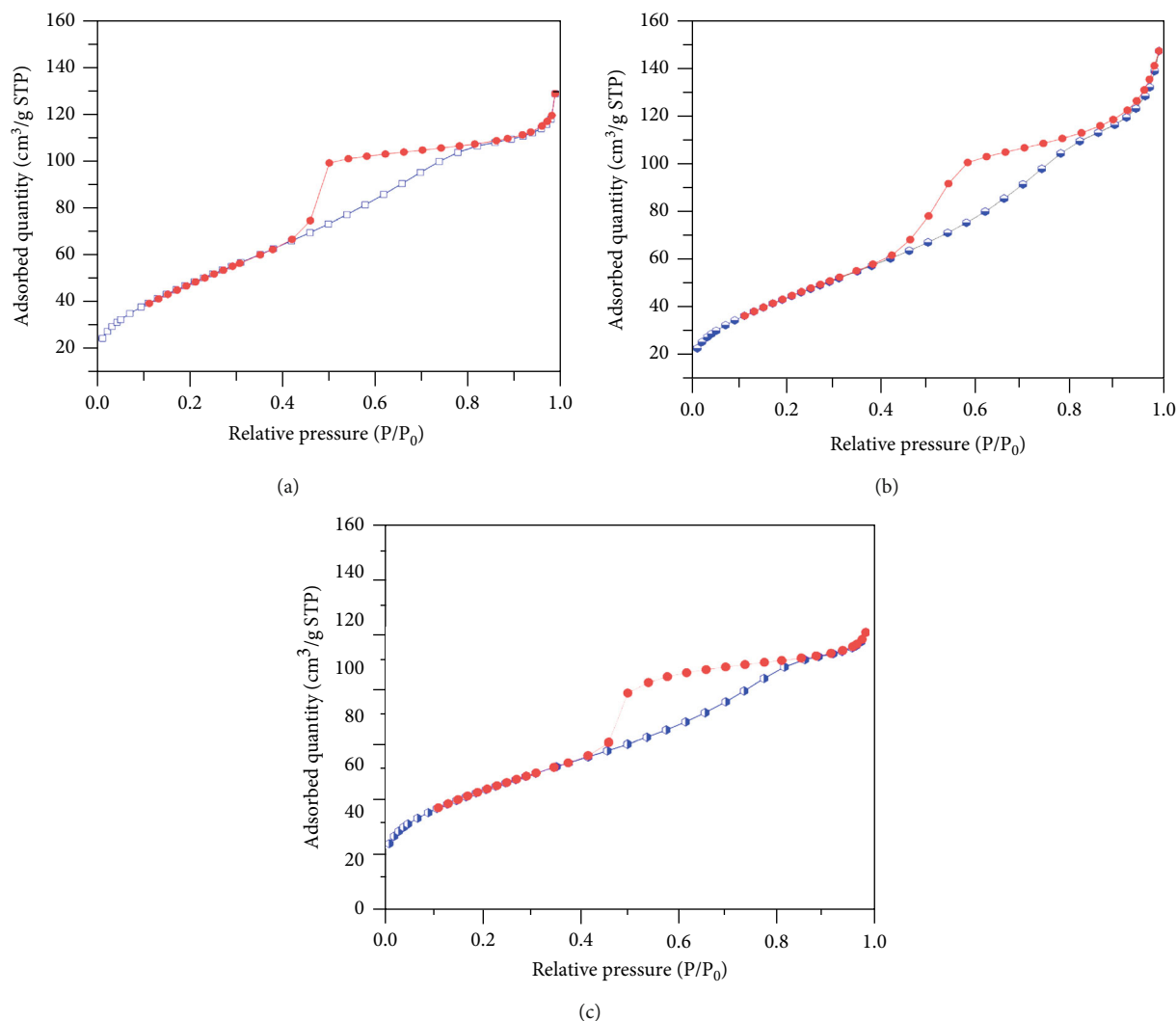


FIGURE 4: Nitrogen adsorption-desorption isotherms of representative samples: (a)  $\text{TiO}_2$ -1%Co, (b)  $\text{TiO}_2$ -5%Co, and (c)  $\text{TiO}_2$ -1%Co-2.5%Fe samples.

oxygen bridge, which effectively increased their specific surface areas.

Table 3 compares the BET surface areas of doped and codoped  $\text{TiO}_2$  materials of the present work with those of other doped and codoped  $\text{TiO}_2$  materials reported previously. The BET surface areas of doped and codoped  $\text{TiO}_2$  materials of our work were within  $164\text{--}174\text{ m}^2/\text{g}$ , which were higher than those of Fe-doped  $\text{TiO}_2$  materials [18, 19], Codoped  $\text{TiO}_2$  materials [20], Cr- and Fe-doped  $\text{TiO}_2$  materials [18], and Fe- and La-doped  $\text{TiO}_2$  materials [19] (Table 3). The larger BET surface areas of the doped and codoped  $\text{TiO}_2$  materials of the present work were possibly due to their smaller particle sizes ranging from  $6.2\text{ nm}$  to  $7.5\text{ nm}$  (Table 3), depending on the doping amount. The doped  $\text{TiO}_2$  materials of our work were prepared under more favorable conditions (solvothermal treatment at  $180^\circ\text{C}$  without calcination). The other  $\text{TiO}_2$  materials were prepared by hydrothermal treatment or sol-gel method, followed by calcination, which resulted in the formation of larger particle sizes and significant loss of the BET surface area (Table 3).

The UV-vis absorption spectra of undoped  $\text{TiO}_2$ , doped  $\text{TiO}_2$ , and codoped  $\text{TiO}_2$  samples were recorded to study their optical properties (Figure 6). As shown in Figure 6 (curve a), the undoped  $\text{TiO}_2$  sample was characterized by a narrow absorption spectrum, ranging from  $250\text{ nm}$  to  $370\text{ nm}$  in the UV region. No visible light absorption was observed for the undoped  $\text{TiO}_2$  sample. Co-doped  $\text{TiO}_2$  (Figure 6, curves b–d) and Co- and Fe-doped  $\text{TiO}_2$  samples (Figure 6, curves e and f) had broader absorption spectra, which shifted toward longer wavelengths in the visible light region. The absorption spectra of Co-doped  $\text{TiO}_2$  samples had maximum peaks at about  $330\text{--}340\text{ nm}$ , but the shoulder of the peaks shifted to the visible range ( $400\text{--}700\text{ nm}$ ).  $\text{TiO}_2$  samples codoped with Co and Fe were characterized by a broader maximum peak at  $400\text{--}500\text{ nm}$  and stronger intensity of the absorption shoulder in the visible region compared with those of single-doped  $\text{TiO}_2$  samples. Figure 6 shows that the absorption edges of  $\text{TiO}_2$  codoped with Co and Fe moved remarkably, with a redshift to the visible region in comparison with undoped  $\text{TiO}_2$ . These optical

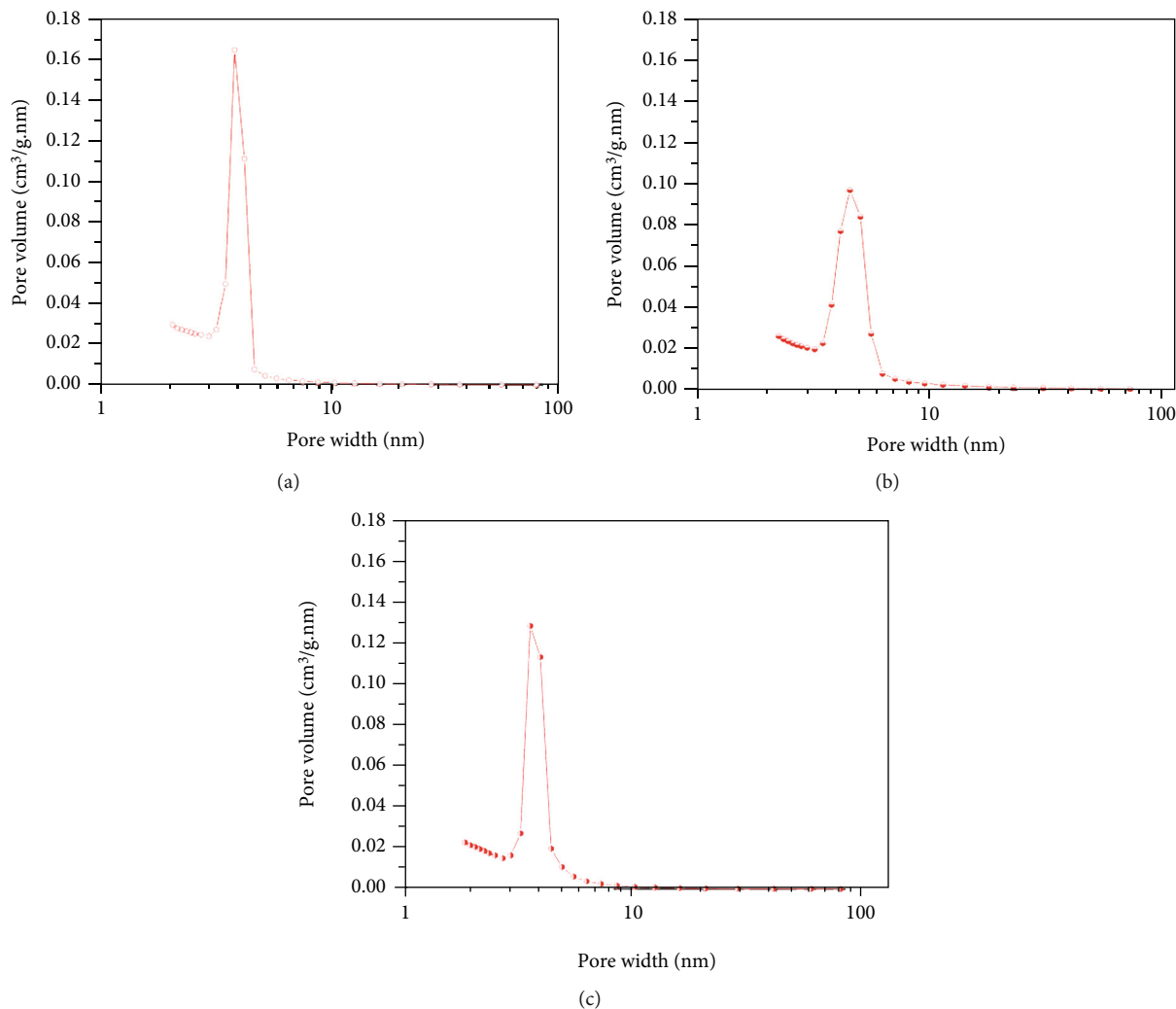


FIGURE 5: Pore size distributions of representative samples: (a)  $\text{TiO}_2$ -1%Co, (b)  $\text{TiO}_2$ -5%Co, and (c)  $\text{TiO}_2$ -1%Co-2.5%Fe samples.

TABLE 2: Surface characteristics of the representative  $\text{TiO}_2$  samples.

Samples	$S_{\text{BET}}^{\text{a}}$ ( $\text{m}^2/\text{g}$ )	$V_{\text{BJH}}^{\text{b}}$ ( $\text{cm}^3/\text{g}$ )	$D_{\text{p}}^{\text{c}}$ (nm)
$\text{TiO}_2$ -1%Co	170	0.18	3.97
$\text{TiO}_2$ -5%Co	164	0.23	5.1
$\text{TiO}_2$ -1%Co-2.5%Fe	174	0.16	4.1
Undoped $\text{TiO}_2$	160	0.29	6.7

<sup>a</sup>BET surface area. <sup>b</sup>Total pore volume determined using desorption curves of the isotherms. <sup>c</sup>Peak pore sizes from the pore size distributions.

absorption characteristics of  $\text{TiO}_2$  codoped with Co and Fe were possibly due to absorption induced by dopants. The absorption edges can be extrapolated by making a tangent line of the UV-vis absorption spectra [21]. Therefore, the bandgap energies of the prepared  $\text{TiO}_2$  samples were estimated from the UV-vis spectra via the following equation:

$$E_g = \frac{1240}{\lambda} \quad (3)$$

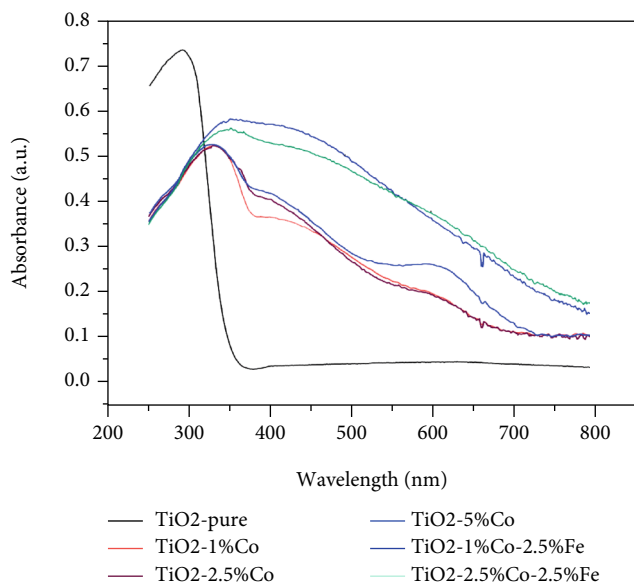
The bandgap energy levels of Co-doped  $\text{TiO}_2$  samples

were estimated to be 2.03 eV, 2.00 eV, and 1.99 eV (for  $\text{TiO}_2$ -1%Co,  $\text{TiO}_2$ -2.5%Co, and  $\text{TiO}_2$ -5%Co, respectively), which were higher than those of Co- and Fe-codoped  $\text{TiO}_2$  samples (their bandgap energies are 1.65 eV and 1.59 eV for  $\text{TiO}_2$ -1%Co-2.5%Fe and  $\text{TiO}_2$ -2.5%Co-2.5%Fe, respectively). The calculated bandgap energies of single-doped and codoped  $\text{TiO}_2$  samples were lower than that of undoped  $\text{TiO}_2$  samples ( $\sim 3.25$  eV). The results revealed that the dopant elements were successfully incorporated into the  $\text{TiO}_2$  crystal lattice and extended the optical absorption toward the visible light region.  $\text{TiO}_2$  samples codoped with Co and Fe had stronger optical absorption of the visible light than single-doped and undoped  $\text{TiO}_2$  samples. This means that the  $\text{TiO}_2$  codoped with Co and Fe can absorb visible light in a much wider range of wavelengths than undoped  $\text{TiO}_2$  and single-doped  $\text{TiO}_2$  samples, which is beneficial for increasing the photocatalytic efficiency under visible light.

**3.2. Photocatalytic Activities of the Prepared  $\text{TiO}_2$  Materials for Degradation of MB.** Before the photocatalytic reaction, the adsorption for MB removal on the synthesized  $\text{TiO}_2$  materials was conducted under dark conditions. Results

TABLE 3: Comparison of the BET surface areas of the TiO<sub>2</sub> samples prepared in this work with those of previous works.

Materials	Synthetic conditions	S <sub>BET</sub> (m <sup>2</sup> /g)	Particle size (nm)	References
TiO <sub>2</sub> -1%Co	Solvothermal treatment at 180°C without calcination	170	6.8	This work
TiO <sub>2</sub> -5%Co	Solvothermal treatment at 180°C without calcination	164	7.5	This work
TiO <sub>2</sub> -1%Co-2.5%Fe	Solvothermal treatment at 180°C without calcination	174	6.2	This work
TiO <sub>2</sub> -Fe	Hydrothermal treatment at 180°C, calcined at 400°C	89	18	[18]
TiO <sub>2</sub> -0.2%Fe	Sol-gel, calcined at 500°C	78	12	[19]
TiO <sub>2</sub> -0.2%Fe-2%La	Sol-gel, calcined at 500°C	84	10	[19]
TiO <sub>2</sub> -0.085%Co	Sol-gel, with following heat treatment from 200°C to 900°C for 30 min	39.7	25	[20]
Fe-Cr-codoped TiO <sub>2</sub>	Hydrothermal treatment at 180°C, calcined 500°C	93		[18]

FIGURE 6: UV-vis spectra of undoped TiO<sub>2</sub>, TiO<sub>2</sub>-1%Co, TiO<sub>2</sub>-2.5%Co, TiO<sub>2</sub>-5%Co, TiO<sub>2</sub>-1%Co-2.5%Fe, and TiO<sub>2</sub>-2.5%Co-2.5%Fe samples.

obtained showed that the percentages of MB removal were only 5%–6% after 60 min for all the synthesized materials, but desorption of MB was observed by prolonging adsorption time for those materials. Therefore, the photocatalytic activities of the prepared TiO<sub>2</sub> samples were evaluated by degrading MB solution under visible light irradiation. The reaction mixture was first stirred in the dark for 30 min to reach the adsorption-desorption equilibrium and to ensure that the degradation of MB obtained is due to the photocatalytic reaction with the presence of the synthesized TiO<sub>2</sub> materials, but not due to the adsorption. Figure 7 shows the percentage of MB degradation over all of the TiO<sub>2</sub> samples (undoped TiO<sub>2</sub>, TiO<sub>2</sub>-1%Co, TiO<sub>2</sub>-2.5%Co, TiO<sub>2</sub>-5%Co, TiO<sub>2</sub>-1%Co-2.5%Fe, and TiO<sub>2</sub>-2.5%Co-2.5%Fe samples) as a function of irradiation time. For comparison, control experiments were performed under the same conditions but without the presence of a photocatalyst (Figure 7, curve MB). As shown in Figure 7 (curve MB), almost no degradation of MB was observed without the photocatalyst (only 7.95% of MB was degraded after 120 min of exposure to visible light irradiation), indicating that MB was unable to self-

degrade. Undoped TiO<sub>2</sub> and Co-doped TiO<sub>2</sub> with low doping concentration (TiO<sub>2</sub>-1%Co and TiO<sub>2</sub>-2.5%Co) showed pure photocatalytic activity. The degradation efficiencies of MB on undoped TiO<sub>2</sub> samples were comparable with those of Co-doped TiO<sub>2</sub> samples with low Co doping concentration for all the tested time points (Figure 7, curves undoped TiO<sub>2</sub>, TiO<sub>2</sub>-1%Co, and TiO<sub>2</sub>-2.5%Co). The degradation percentages of MB were 10.95%, 17.85%, and 17.5% after 120 min of irradiation for undoped TiO<sub>2</sub>, TiO<sub>2</sub>-1%Co, and TiO<sub>2</sub>-2.5%Co, respectively. However, the degradation of MB is enhanced with higher Co doping concentration. The degradation percentages of MB increased three times on TiO<sub>2</sub>-5%Co samples and were higher than those on TiO<sub>2</sub>-1%Co and TiO<sub>2</sub>-2.5%Co samples for all the tested time points. About 39.8% of MB was degraded within 30 min on TiO<sub>2</sub>-5%Co and then gradually increased to ~50% by increasing irradiation time up to 120 min. Moreover, the significantly enhanced degradation of MB was observed on codoped TiO<sub>2</sub> samples (Figure 7, curves TiO<sub>2</sub>-1%Co-2.5%Fe and TiO<sub>2</sub>-2.5%Co-2.5%Fe). The highest degradation of MB was obtained by TiO<sub>2</sub> codoped with 1%Co and 2.5%Fe for all the time points tested. The degradation of MB was almost complete on codoped TiO<sub>2</sub> samples for the tested time; 90% and 85% of MB were degraded on TiO<sub>2</sub>-1%Co-2.5%Fe and TiO<sub>2</sub>-2.5%Co-2.5%Fe after 120 min, respectively.

The results showed that TiO<sub>2</sub> samples codoped with Co and Fe exhibited higher photocatalytic degradation of MB under visible light than the undoped and single-doped TiO<sub>2</sub> samples, which could be attributed to their lower bandgap values compared to those of the undoped and single-doped TiO<sub>2</sub> samples. These observations indicated that codopant ions had a favorable effect on the photocatalytic performance of the prepared TiO<sub>2</sub> materials. These ions can provide additional energy levels within the bandgap of TiO<sub>2</sub>. The bandgap of TiO<sub>2</sub> consists of a contribution from the 2p orbitals of O for the valence band and the 3d orbitals of Ti toward the conduction band, which have a large difference in energy, leading to the activation of TiO<sub>2</sub> in the UV light region with extremely high energy. The band structures of codoped TiO<sub>2</sub> materials are mainly affected by the 3d energy states of the transitional metal ions (Co<sup>2+</sup> and Fe<sup>3+</sup>). In fact, the UV-vis absorption studies (Figure 6) revealed that the respective absorption bands of codoped TiO<sub>2</sub> samples effectively shifted toward wavelengths longer

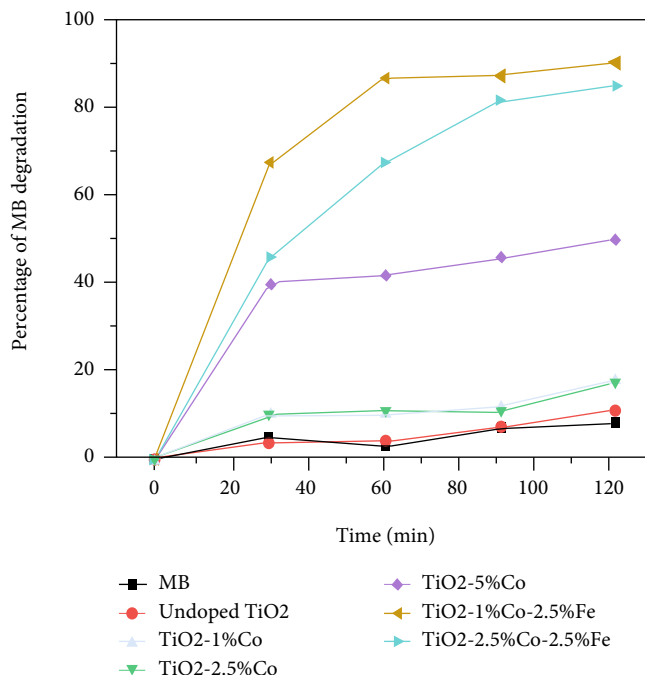
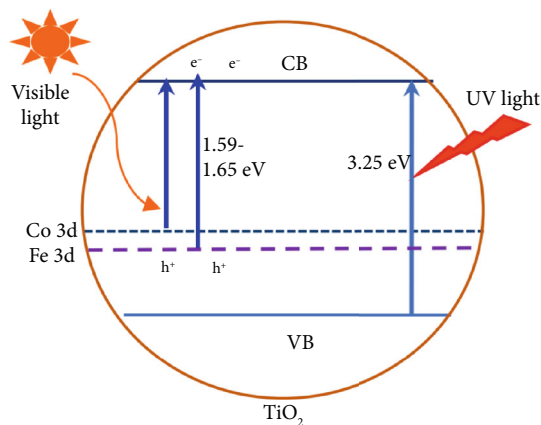


FIGURE 7: The degradation of MB using different catalysts: undoped TiO<sub>2</sub>, TiO<sub>2</sub>-1%Co, TiO<sub>2</sub>-2.5%Co, TiO<sub>2</sub>-5%Co, TiO<sub>2</sub>-1%Co-2.5%Fe, and TiO<sub>2</sub>-2.5%Co-2.5%Fe samples under visible light irradiation.



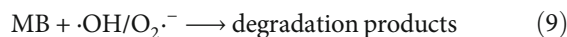
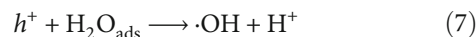
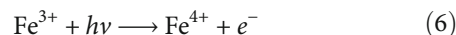
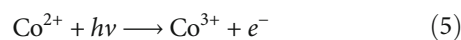
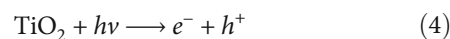
SCHEME 1: Band structure of TiO<sub>2</sub> and TiO<sub>2</sub> codoped with Co<sup>2+</sup> and Fe<sup>3+</sup>. VB: valence band; CB: conduction band.

than 400 nm. Thus, the partially filled Co/Fe 3d bands were located below the conduction band of TiO<sub>2</sub>. Hence, when photons with wavelengths longer than 400 nm are used for illumination, the electrons in the Co 3d and Fe 3d bands, instead of electrons in the valence band of TiO<sub>2</sub>, are excited to the conduction band, while Co<sup>2+</sup> and Fe<sup>3+</sup> loses one electron and becomes Co<sup>3+</sup> and Fe<sup>4+</sup> (see Scheme 1). This phenomenon can induce more photogenerated electrons and holes to participate in the photocatalytic reaction.

As calculated above, the bandgap energy values of codoped TiO<sub>2</sub> samples (1.59 eV-1.65 eV) were lower than those of single-doped TiO<sub>2</sub> samples (1.99-2.03 eV) and undoped TiO<sub>2</sub> (3.25 eV), indicating the lower energy of pho-

tons necessary to generate electron transition and holes ( $h^+$ ) for codoped TiO<sub>2</sub> samples compared to single-doped and undoped TiO<sub>2</sub>. These holes can react with water to produce the highly reactive  $\cdot\text{OH}$ , and both holes and  $\cdot\text{OH}$  have a strong oxidation potential for the degradation of MB.

The plausible reaction mechanism of the photodegradation is given below:



It is suggested that the photodegradation of MB can be divided into three main steps: (1) the initial step is the formation of electrons ( $e^-$ ) in the CB and holes ( $h^+$ ) in the VB upon a light incident on the photocatalyst surface (see equations (4), (5), (6)); (2) the intermediate step includes the formation of  $\cdot\text{OH}$  and  $\text{H}^+$  through the interaction between the holes and H<sub>2</sub>O adsorbed on the photocatalyst surface (equation (7)) and of  $\text{O}_2^{\cdot-}$  due to the reduction of the adsorbed O<sub>2</sub> molecule (equation (8)) that has strong oxidation power, which in turn promotes the decomposition of MB; and (3) the final step is the degradation of MB by  $\cdot\text{OH}/\text{O}_2^{\cdot-}$  radicals.

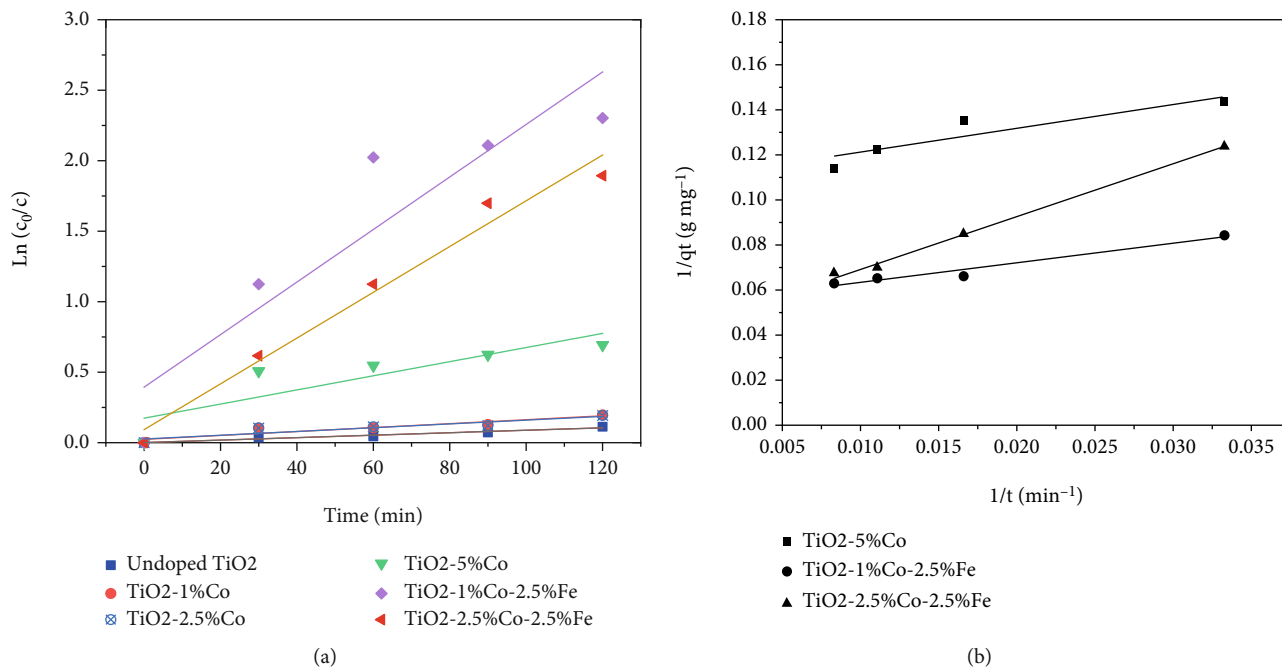


FIGURE 8: Plots of (a) first- and (b) second-order reaction rates for the degradation of MB over as-prepared TiO<sub>2</sub> materials.

Thus, this work proposed a study to understand the role of Co and Fe in codoped TiO<sub>2</sub> nanoparticles in yielding better performance as a visible light-driven photocatalyst.

The kinetics of photodegradation of MB on as-prepared TiO<sub>2</sub> materials was further investigated using the pseudo-first-order kinetic model [22] as follows:

$$\ln \frac{C_0}{C} = k_1 t, \quad (10)$$

where  $C_0$  is the initial concentration of MB,  $C$  is the concentration of MB at time  $t$ , and  $k_1$  is the apparent reaction rate constant. According to equation (10), a linear regression plot of  $\ln(C_0/C)$  vs. time  $t$  gives the value of  $k_1$ . The experimental data were analyzed using the pseudo-first-order equation; the resulting plots of  $\ln(C_0/C)$  vs. time  $t$  are shown in Figure 8(a). From the obtained plots in Figure 8(a), the rate constants were found to be 0.0009 min<sup>-1</sup>, 0.0014 min<sup>-1</sup>, 0.0013 min<sup>-1</sup>, 0.005 min<sup>-1</sup>, 0.0186 min<sup>-1</sup>, and 0.0162 min<sup>-1</sup> with correlation coefficients ( $R^2$ ) of 0.96, 0.91, 0.90, 0.78, 0.85, and 0.98 for the undoped TiO<sub>2</sub>, TiO<sub>2</sub>-1%Co, TiO<sub>2</sub>-2.5%Co, TiO<sub>2</sub>-5%Co, TiO<sub>2</sub>-1%Co-2.5%Fe, and TiO<sub>2</sub>-2.5%Co-2.5%Fe, respectively. The experimental degradation data of all the TiO<sub>2</sub> samples were also analyzed using the pseudo-second-order kinetic equation proposed by Blanchard et al. [23]:

$$\frac{1}{q_t} = \frac{1}{k_2 q_e^2} + \frac{1}{q_e} t, \quad (11)$$

where  $q_t$  and  $q_e$  are the amounts of dye adsorbed at time  $t$  and at equilibrium (mg·g<sup>-1</sup>) and  $k_2$  is the pseudo-second-order rate constant (g·mg<sup>-1</sup>·min<sup>-1</sup>) for the adsorption pro-

cess. The linear plots of  $1/q_t$  vs. time  $1/t$  shown in Figure 8(b) give the values of  $k_2$  and  $q_e$ . It could be seen that three TiO<sub>2</sub> samples: TiO<sub>2</sub>-5%Co, TiO<sub>2</sub>-1%Co-2.5%Fe, and TiO<sub>2</sub>-2.5%Co-2.5%Fe showed the best fit in the linear plots of  $1/q_t$  vs.  $1/t$  with higher values of  $R^2$  (0.83, 0.95, and 0.99, respectively) than those of the pseudo-first-order equation (0.78, 0.85, and 0.98). The values of  $q_e$  obtained from the linear plots are 9.03 mg·g<sup>-1</sup>, 18.28 mg·g<sup>-1</sup>, and 21.78 mg·g<sup>-1</sup> for TiO<sub>2</sub>-5%Co, TiO<sub>2</sub>-1%Co-2.5%Fe, and TiO<sub>2</sub>-2.5%Co-2.5%Fe, which were higher than those of the experimental values (8.75 mg·g<sup>-1</sup>, 14.86 mg·g<sup>-1</sup>, and 15.75 mg·g<sup>-1</sup> for TiO<sub>2</sub>-5%Co, TiO<sub>2</sub>-1%Co-2.5%Fe, and TiO<sub>2</sub>-2.5%Co-2.5%Fe, respectively), whereas the undoped TiO<sub>2</sub>, TiO<sub>2</sub>-1%Co, and TiO<sub>2</sub>-2.5%Co samples did not follow the pseudo-second-order equation because of smaller values of  $R^2$  (0.82, 0.55, and 0.54) of the plots  $1/q_t$  vs.  $1/t$  (not shown), compared to those of the pseudo-first-order plots.

The observations revealed that the degradation of MB on the undoped TiO<sub>2</sub> and Co single-doped TiO<sub>2</sub> samples with 1% Co and 2.5% Co doping can be described by the pseudo-first-order equation. Meanwhile, the pseudo-second order fits better compared to the pseudo-first order for describing the degradation of MB on the TiO<sub>2</sub> doped with 5%Co and codoped with Co and Fe, considering that  $R^2$  of the pseudo-second-order equation was greater than that of the first order for those samples. This clearly explains that the enhanced degradation efficiency of MB is attributed to the high surface area of the TiO<sub>2</sub> codoped with Co and Fe and their reduced bandgap energies.

Table 4 compares the degradation of MB on the TiO<sub>2</sub> materials as prepared in this work with those published in previous works [24–28]. It was found that the TiO<sub>2</sub> codoped with 1%Co and 2.5%Fe in this work showed the highest

TABLE 4: Comparison of MB degradation of the TiO<sub>2</sub>-codoped samples of this work with other materials.

Materials	Synthetic conditions	S <sub>BET</sub> (m <sup>2</sup> ·g <sup>-1</sup> )	Degradation percentage of MB	References
Bi <sub>2</sub> O <sub>3</sub>	Calcination method at 500°C for 6 h	2.9	70% after 4 h under visible light irradiation	[24]
CaBi <sub>6</sub> O <sub>10</sub>	Impregnation-calcination method at 650°C for 12 h	2.5	97% after 4 h under visible light irradiation	[24]
CeO <sub>2</sub> /V <sub>2</sub> O <sub>5</sub>	Thermal decomposition at 400°C for 30 min	—	64.2% after 4 h under visible light	[25]
CeO <sub>2</sub> /CuO	Thermal decomposition at 400°C for 30 min	—	70.1% after 4 h under visible light	[25]
ZnO/CdO	Thermal decomposition at 350°C for 3 h	—	75% after 4 h under visible light	[26]
g-C <sub>3</sub> N <sub>4</sub> -CdS	Precipitation method	166.5	90.45% after 3 h under visible light	[27]
F-doped TiO <sub>2</sub>	Sol-gel method, calcined at 500°C for 1 h	39.6	90% after 4 h under visible light	[28]
TiO <sub>2</sub> -1%Co-2.5%Fe	Solvothermal method at 180°C	174	90% after 2 h under visible light	This work

photocatalytic efficiency with 90% of MB degraded after visible light irradiation of 2 h. The metal oxide (Bi<sub>2</sub>O<sub>3</sub>) [24] and mixed metal oxides (e.g., CeO<sub>2</sub>/V<sub>2</sub>O<sub>5</sub> [24], CeO<sub>2</sub>/CuO [25], and ZnO/CdO [26]) exhibited much lower degradation efficiency of MB compared with the TiO<sub>2</sub> materials of our work, which degraded about 64.2%–75% of MB for a longer irradiation time of 4 h. The complex metal oxide CaBi<sub>6</sub>O<sub>10</sub> [24] and nanocomposite g-C<sub>3</sub>N<sub>4</sub>-CdS [27] demonstrated relatively high degradation percentages of MB (~97% and 90.45% for CaBi<sub>6</sub>O<sub>10</sub> and g-C<sub>3</sub>N<sub>4</sub>-CdS, respectively), which could be comparable with that of the TiO<sub>2</sub> codoped with 1%Co and 2.5%Fe of our work, but these materials require a quite long irradiation time of 4 h (for CaBi<sub>6</sub>O<sub>10</sub>) and 3 h (g-C<sub>3</sub>N<sub>4</sub>-CdS) to obtain the complete degradation of MB under visible light. Moreover, a similar study reported that TiO<sub>2</sub> doped with 10% F [28] also revealed a high degradation percentage of MB (~90%), but after a much longer irradiation time of 4 h, compared to that of the TiO<sub>2</sub> codoped with Co and Fe of our work. The comparison revealed that the photocatalytic efficiency of the materials depends not only on their band structure but also on their surface characteristics. The excellent photocatalytic performance of the TiO<sub>2</sub> codoped with Co and Fe of our work could be attributed to their larger BET surface area compared to those of the other materials. As a result, the TiO<sub>2</sub> codoped with Co and Fe has more active sites and simultaneously can absorb much more visible light and generate more electron-hole pairs, which in turn enhanced the photocatalytic activity and reduced the reaction time as compared to the other materials.

#### 4. Conclusions

In this work, we presented the characterization of TiO<sub>2</sub> nanoparticles codoped with Co<sup>2+</sup> and Fe<sup>3+</sup> synthesized through solvothermal treatment at 180°C without further calcination at high temperatures. Undoped TiO<sub>2</sub> and Co single-doped TiO<sub>2</sub> materials were also prepared using the same procedure to compare with codoped TiO<sub>2</sub> in terms of optical absorption and photocatalytic efficiency for MB degradation. The doped and codoped TiO<sub>2</sub> materials of the present work exhibited better adsorption characteristics (e.g., their BET surface areas of 164–174 m<sup>2</sup>/g) than doped

and codoped TiO<sub>2</sub> materials of previous works; as-prepared codoped TiO<sub>2</sub> materials had significantly enhanced optical adsorption toward the visible light region. Among the TiO<sub>2</sub> samples studied, the codoped TiO<sub>2</sub> materials showed the highest photocatalytic activity for the degradation of MB; they degraded about 90% of MB within 120 min under visible light irradiation. The TiO<sub>2</sub> samples codoped with Co and Fe in this work showed higher photocatalytic efficiency for the degradation of MB than those of metal oxides, mixed metal oxides, and other materials in the previous works. The pseudo-second-order kinetic model fits well for describing the degradation of MB on the TiO<sub>2</sub> codoped with Co and Fe. Hence, this study provides a simple route to synthesize an effective photocatalyst for the degradation of dye compounds under visible light for wastewater treatment.

#### Data Availability

All the data used to support the findings of this study are included within the article.

#### Conflicts of Interest

There are no conflicts of interest to declare.

#### Acknowledgments

This study was funded by the Vietnam National Foundation for Science and Technology Development (NAFOSTED) under grant number 104.03-2019.313.

#### References

- [1] D. Chen, Y. Cheng, N. Zhou et al., “Photocatalytic degradation of organic pollutants using TiO<sub>2</sub>-based photocatalysts: a review,” *Journal of Cleaner Production*, vol. 268, p. 121725, 2020.
- [2] M. Sun, Y. Fang, S. Sun, and Y. Wang, “Surface modification of TiO<sub>2</sub> with N doping and Ag loading for enhanced visible-light photoactivity,” *RSC Advances*, vol. 6, no. 15, pp. 12272–12279, 2016.
- [3] N. T. T. Mai, N. K. Nga, D. T. M. Hue et al., “Effect of calcination temperature on the structure and characteristics of

- cuprous oxide ( $\text{Cu}_2\text{O}$ -ONPs),” in *Proceedings of Second Annual Conference on Materials, Machine. Meth. for Sustainable Development (MMMS2020)*, pp. 375–383, 2021.
- [4] Q. Sun, K. Li, S. Wu, B. Han, L. Sui, and L. Dong, “Remarkable improvement of  $\text{TiO}_2$  for dye photocatalytic degradation by a facile post-treatment,” *New Journal of Chemistry*, vol. 44, no. 5, pp. 1942–1952, 2020.
- [5] M. K. Singh and M. S. Mehata, “Enhanced photoinduced catalytic activity of transition metal ions incorporated  $\text{TiO}_2$  nanoparticles for degradation of organic dye: absorption and photoluminescence spectroscopy,” *Optical Materials*, vol. 109, p. 110309, 2020.
- [6] M. A. Rauf, M. A. Meetani, and S. Hisaindee, “An overview on the photocatalytic degradation of azo dyes in the presence of  $\text{TiO}_2$  doped with selective transition metals,” *Desalination*, vol. 276, no. 1–3, pp. 13–27, 2011.
- [7] P. Jiang, W. Xiang, J. Kuang, W. Liu, and W. Cao, “Effect of cobalt doping on the electronic, optical and photocatalytic properties of  $\text{TiO}_2$ ,” *Solid State Sciences*, vol. 46, pp. 27–32, 2015.
- [8] J.-H. Shen, H.-Y. Chuang, Z.-W. Jiang, X.-Z. Liu, and J.-J. Horng, “Novel quantification of formation trend and reaction efficiency of hydroxyl radicals for investigating photocatalytic mechanism of Fe-doped  $\text{TiO}_2$  during UV and visible light-induced degradation of acid orange 7,” *Chemosphere*, vol. 251, p. 126380, 2020.
- [9] C. Gomez-Polo, S. Larumbe, A. Gila et al., “Improved photocatalytic and antibacterial performance of Cr doped  $\text{TiO}_2$  nanoparticles,” *Surfaces and Interfaces*, vol. 22, p. 100867, 2021.
- [10] A. Barmeh, M. R. Nilforoushan, and S. Otraj, “Wetting and photocatalytic properties of Ni-doped  $\text{TiO}_2$  coating on glazed ceramic tiles under visible light,” *Thin Solid Films*, vol. 666, pp. 137–142, 2018.
- [11] T. Wang, D. Shena, T. Xua, and R. Jiang, “Photocatalytic degradation properties of V-doped  $\text{TiO}_2$  to automobile exhaust,” *Science of the Total Environment*, vol. 586, pp. 347–354, 2017.
- [12] M. Sayed, A. Arooj, N. S. Shah et al., “Narrowing the band gap of  $\text{TiO}_2$  by co-doping with  $\text{Mn}^{2+}$  and  $\text{Co}^{2+}$  for efficient photocatalytic degradation of enoxacin and its additional peroxidase like activity: a mechanistic approach,” *Journal of Molecular Liquids*, vol. 272, pp. 403–412, 2018.
- [13] M. Shaban, A. M. Ahmed, N. Shehata, M. A. Betiha, and A. M. Rabie, “Ni-doped and Ni/Cr co-doped  $\text{TiO}_2$  nanotubes for enhancement of photocatalytic degradation of methylene blue,” *Journal of Colloid and Interface Science*, vol. 555, pp. 31–41, 2019.
- [14] M. Imran, Z. Saeed, M. Pervaiz et al., “Enhanced visible light photocatalytic activity of  $\text{TiO}_2$  co-doped with Fe, Co, and S for degradation of Congo red,” *Spectrochimica Acta Part A: Molecular and Biomolecular Spectroscopy*, vol. 255, p. 119644, 2021.
- [15] A. Mancuso, O. Sacco, V. Vaiano et al., “Visible light active Fe-Pr co-doped  $\text{TiO}_2$  for water pollutants degradation,” *Catalysis Today*, vol. 380, pp. 93–104, 2021.
- [16] U. Holzwarth and N. Gibson, “The Scherrer equation versus the 'Debye-Scherrer equation',” *Nature Nanotechnology*, vol. 6, no. 9, p. 534, 2011.
- [17] S. J. Gregg and K. S. W. Sing, *Adsorption, Surface Area and Porosity*, Academic Press, London, 2nd edition, 1982.
- [18] E. D. Jeong, P. H. Borse, J. S. Jang et al., “Hydrothermal synthesis of Cr and Fe co-doped  $\text{TiO}_2$  nanoparticle photocatalyst,” *Journal of Ceramic Processing Research*, vol. 9, pp. 250–253, 2008.
- [19] Q. Wang, S. Xu, and F. Shen, “Preparation and characterization of  $\text{TiO}_2$  photocatalysts co-doped with iron (III) and lanthanum for the degradation of organic pollutants,” *Applied Surface Science*, vol. 257, no. 17, pp. 7671–7677, 2011.
- [20] M. A. Barakat, G. Hayes, and S. I. Shah, “Effect of cobalt doping on the phase transformation of  $\text{TiO}_2$  nanoparticles,” *Journal of Nanoscience & Nanotechnology*, vol. 5, no. 5, pp. 759–765, 2005.
- [21] T. Sun, J. Fan, E. Liu et al., “Fe and Ni co-doped  $\text{TiO}_2$  nanoparticles prepared by alcohol-thermal method: application in hydrogen evolution by water splitting under visible light irradiation,” *Powder Technology*, vol. 228, pp. 210–218, 2012.
- [22] S. Iyyapushpam, S. T. Nishanthi, and D. Pathinettam Padiyan, “Photocatalytic degradation of methyl orange using  $\alpha\text{-Bi}_2\text{O}_3$  prepared without surfactant,” *Journal of Alloys and Compounds*, vol. 563, pp. 104–107, 2013.
- [23] G. Blanchard, M. Maunaye, and G. Martin, “Removal of heavy metals from waters by means of natural zeolites,” *Water Research*, vol. 18, no. 12, pp. 1501–1507, 1984.
- [24] Y. Wang, Y. He, T. Li, J. Cai, M. Luo, and L. Zhao, “Novel  $\text{CaBi}_6\text{O}_{10}$  photocatalyst for methylene blue degradation under visible light irradiation,” *Catalysis Communication*, vol. 18, pp. 161–164, 2012.
- [25] R. Saravanan, S. Joicy, V. K. Gupta, V. Narayanan, and A. Stephen, “Visible light induced degradation of methylene blue using  $\text{CeO}_2/\text{V}_2\text{O}_5$  and  $\text{CeO}_2/\text{CuO}$  catalysts,” *Materials Science and Engineering C*, vol. 33, no. 8, pp. 4725–4731, 2013.
- [26] R. Saravanan, H. Shankar, T. Prakash, V. Narayanan, and A. Stephen, “ZnO/CdO composite nanorods for photocatalytic degradation of methylene blue under visible light,” *Materials Chemistry and Physics*, vol. 125, no. 1–2, pp. 277–280, 2011.
- [27] F. Jiang, T. Yan, H. Chen, A. Sun, C. Xu, and X. Wang, “A  $\text{g-C}_3\text{N}_4\text{-CdS}$  composite catalyst with high visible-light-driven catalytic activity and photostability for methylene blue degradation,” *Applied Surface Science*, vol. 295, pp. 164–172, 2014.
- [28] W. Yu, X. Liu, L. Pan et al., “Enhanced visible light photocatalytic degradation of methylene blue by F-doped  $\text{TiO}_2$ ,” *Applied Surface Science*, vol. 319, pp. 107–112, 2014.

## Research Article

# Preparation and Characterization of Biochar Derived from Agricultural By-Products for Dye Removal

**Phuong Thu Le** <sup>1</sup>, **Huyen Thuong Bui**,<sup>1</sup> **Duy Ngoc Le**,<sup>1</sup> **Thi Hue Nguyen**,<sup>2</sup> **Le Anh Pham**,<sup>1</sup> **Hong Nam Nguyen**,<sup>1</sup> **Quoc Son Nguyen**,<sup>1</sup> **Thu Phuong Nguyen**,<sup>3</sup> **Ngoc Trinh Bich**,<sup>1</sup> **Thi Thuy Duong**,<sup>2</sup> **Marine Herrmann**,<sup>1,4</sup> **Sylvain Ouillon** <sup>1,4</sup> and **Thi Phuong Quynh Le**<sup>5</sup>

<sup>1</sup>University of Science and Technology of Hanoi, Vietnam Academy of Science and Technology, 18 Hoang Quoc Viet Road, Cau Giay, Hanoi, Vietnam

<sup>2</sup>Institute of Environmental Technology, Vietnam Academy of Science and Technology, 18 Hoang Quoc Viet Road, Cau Giay, Hanoi, Vietnam

<sup>3</sup>Institute for Tropical Technology, Vietnam Academy of Science and Technology, 18 Hoang Quoc Viet Road, Cau Giay, Hanoi, Vietnam

<sup>4</sup>UMR LEGOS, Université de Toulouse, IRD, CNES, CNRS, UPS, 14 avenue Edouard Belin, 31400 Toulouse, France

<sup>5</sup>Institute of Natural Products Chemistry, Vietnam Academy of Science and Technology, 18 Hoang Quoc Viet Road, Cau Giay, Hanoi, Vietnam

Correspondence should be addressed to Phuong Thu Le; [le-phuong.thu@usth.edu.vn](mailto:le-phuong.thu@usth.edu.vn)

Received 27 August 2021; Revised 30 September 2021; Accepted 1 November 2021; Published 11 November 2021

Academic Editor: Thanh Son Le

Copyright © 2021 Phuong Thu Le et al. This is an open access article distributed under the Creative Commons Attribution License, which permits unrestricted use, distribution, and reproduction in any medium, provided the original work is properly cited.

In this study, biochar was derived from the agricultural by-products coconut coir (BC1) and rice husk (BC2) activated with NaOH 25%. This material was characterized through analytical methods such as SEM images, XRD, FTIR, and Raman. Analysis results indicated that the carbon structure carbon is amorphous and with many graphene layers. A high specific surface area was detected with  $364.22 \text{ m}^2 \cdot \text{g}^{-1}$  for BC1 and  $329.71 \text{ m}^2 \cdot \text{g}^{-1}$  for BC2 with many meso and micropores when analyzed by  $\text{N}_2$  and  $\text{CO}_2$  adsorption. The material also showed anionic and cationic dye adsorption capacity for textile wastewater following both Langmuir and Freundlich models where BC2 had better max adsorption capacity compared to BC1,  $6.519 \text{ mg} \cdot \text{g}^{-1}$  for MO and  $8.612 \text{ mg} \cdot \text{g}^{-1}$  for MB.

## 1. Introduction

Textile is one of the largest industries in the globe. Vietnam was ranked 8th in exporting textile and dye products in 2018 according to the WTO, which provided over 1.6 million employments [1]. However, this industry emits huge amounts of wastewater that need to be treated. Many solutions such as biological treatments [2, 3], electrocoagulation [4–6], membrane bioreactors [7–9], or photochemical methods [10] have been developed. [11] combined a coagulation-flocculation treatment with alkali-activated carbon made from sand with a TAN efficiency of 70%. Compared to other methodologies, many studies have confirmed that adsorption methods with

activated carbon from agricultural by-products are highly effective when treating textile dyeing wastewater.

Various studies have shown that agricultural by-products such as straw, rice husks, corn cobs, or coir have a high potential for adsorption of pollutants, especially pesticides and dyes in wastewater [12, 13]. The superiority of these types of material lies in the fact that it is inexpensive or even free, is available in abundance, especially in countries with strong agricultural economies like Vietnam, and is easily biodegradable in the environment. Vietnam is classified among the top five rice-producing countries in the world with an output of 38 million tons $\cdot$ year<sup>-1</sup> (GSO, 2009), equivalent to 38 million tons of straw and 6–7 million

tons of rice husks. Common agricultural by-products from rice production straw, rice husk ash, and rice hulls [14] have all been shown to be beneficial in removing pesticides [14–16] and dyes [17–19]. Rice husk-derived biochar has also been studied and applied to remove contaminants from polluted water with an adsorption capacity of 123.03 mg.g<sup>-1</sup> for glyphosate [20] and 9.73 mg.g<sup>-1</sup> for the methylene blue [21].

In addition to rice, Vietnam is also known as one of the ten largest manufacturers of coconut-related products in the world with an output of around 1.5 million tons in 2017, the second-largest producer of coir in the world with 36,000 tons in 2017 (FAO, 2018). The primary by-product of coconut is coconut shell which has a high adsorption capacity and is hence widely used in biofilter systems for the purpose of pesticides removal [22–24]. Other studies have proven its usefulness in textile wastewater treatments [25–27]. Results all showed that biochar has a high ability to remove pollutants in general. The vast majority of agricultural by-products are lignocellulose materials composed largely of polysaccharides (cellulose and hemicelluloses) and lignins with a chemical composition of hydroxyl and carboxyl groups [28]. Interactions between these functional groups and pesticides are also expected to be the primary mechanism for adsorption of agricultural by-products [29]. Agricultural by-products have received much attention from scientists as a source for biochar [30]. For a long time, combining biochar with the right measurement of soil has been used to increase the water holding capacity as well as soil nutrients and crop yield [31]. Furthermore, recent studies have demonstrated the high efficiency and feasibility of biochar-soil blending at laboratory and field scales for the purpose of preventing glyphosate-containing pesticides in soil from leaking into natural water sources [32–35]. However, De Gisi et al. [36] showed that there is a lack of data concerning the characteristics of the new by-products studied such as their average particle size or specific surface area.

With the abundance of input materials as well as the necessity to recycle such a valuable agricultural waste, biochar derived from rice husk and coconut coir is expected to be the answer to the demand for an economically and environmentally friendly material that has effective pollutants adsorption ability for application in surface water treatment.

In this study, biochar was prepared in the laboratory from agricultural by-products in Vietnam such as coconut coir (named BC1) and rice husks (named BC2) by a pyrolysis method to investigate its potential in water pollution treatment. To be more specific, this research is designed to test the adsorbability of the biochar towards two different dyes, i.e., methylene blue—a cationic dye, and methyl orange—an anionic dye.

## 2. Chemicals and Methodology

**2.1. Chemicals.** Methylene blue trihydrate (MB, C<sub>16</sub>H<sub>18</sub>ClN<sub>3</sub>S·3H<sub>2</sub>O, ≥98.5%)—a cationic dye and methyl orange (MO, C<sub>14</sub>H<sub>14</sub>N<sub>3</sub>NaO<sub>3</sub>S, ≥98.5%)—an anionic dye represent both types of separate functional group and were purchased from Xilong Chemical Co., Ltd. (China). We used sodium chloride (NaCl, ≥99.5%) and sodium hydroxide

(NaOH, ≥99.5%) from Merck (Germany), and hydrochloric acid (HCl, 35.0–37.0%) and nitric acid (HNO<sub>3</sub>, 65%) from Daejung chemicals and metals (Korea).

### 2.2. Methodology

**2.2.1. Biochar Production.** Rice husk was collected from Bac Ninh province, Northern Vietnam, and thoroughly sieved to keep only the 5 mm diameter husk for use. Coconut fiber was collected from Hoai Duc district, Hanoi city, cut into small pieces, and sieved into coir less than 2 mm and more than 1 mm in diameter.

Rice husk and coconut coir were carefully washed three times with tap water and twice with distilled water to remove impurities. After that, the coir and the husk were dried at 105°C in the oven for 5 hours until they were completely dried. The husk (or coir) was then placed in a stainless steel pot and covered on the surface with commercial charcoal to prevent the formation of ash and coke during carbonization. Next, the pot was sealed and put into the Nabertherm furnace (Germany) under limited oxygen conditions. The material heating program used is shown in the diagram in Figure 1. At the end of the carbonization, the biochars' weight, density, and mass loss (%) were calculated (Table 1).

Biochar after carbonization is activated by NaOH 25%: biochar's specific surface area, ion-exchange capacity, and the number of oxygen-containing functional groups all raise after it is treated with NaOH [37, 38]. It can simultaneously be used as an effective, inexpensive, and ecologically acceptable activator [39]. A mixture of 18 g biochar and 300 mL of NaOH 25% solution were thus added into a Duran bottle of 500 mL, and the mixture was shaken at 250 rpm in an IKA KS 4000i incubator shaker for 4 hours at room temperature. The material was then filtered out and washed with distilled water (with a conductivity less than 18 megaohms), dried naturally at room temperature, and stored in a brown bottle.

**2.2.2. Characterization of Biochars.** A temperature-induced mass loss of 0.7 g each raw material (rice husk and coconut shell) was determined by thermogravimetric analysis and differential gravimetric analysis (TGA/DTG) using a CIRAD-designed Macro-TGA from 25°C to 800°C at a heating rate of 5°C.min<sup>-1</sup> under air. Every 5 seconds, mass loss data and temperature changes were recorded by the MTG software and analyzed on the Origin software. The functional groups and characterizing covalent bonding information of the different biochars after the pyrolysis were analyzed by FT-IR spectrometer (Thermo scientific iS50). Information on the crystal structure, phase, orientation, and molecular interactions of the biochars after fabrication were studied on the Equinox 5000-XRD Spectrometreler and the Raman spectrometer NRS-5100 from JASCO Corporation, Japan. The surface morphology and porous structure were observed by a scanning electron microscope (SEM, Hitachi S-4800). This instrument is also integrated with Energy Dispersive X-ray Spectroscopy for the analysis of the surface elemental composition of materials.

N<sub>2</sub> and CO<sub>2</sub> adsorption isotherms of samples processed under vacuum conditions at 300°C were analyzed. The

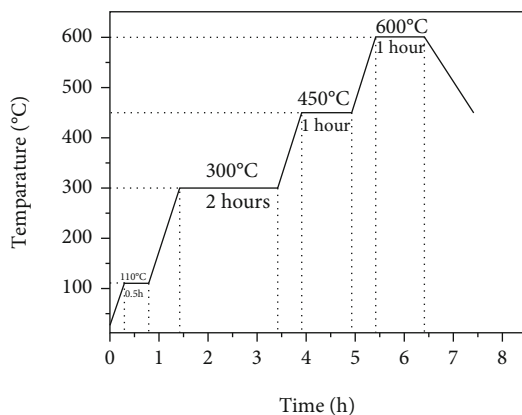


FIGURE 1: Biochar production process diagram.

TABLE 1: Density and weight loss of each material before and after carbonization.

Material	Density before carbonization (g.mL <sup>-1</sup> )	Density after carbonization (g.mL <sup>-1</sup> )	Weight loss (%)
Coir/biochar 1	0.1309	0.1044	60
Husk/biochar 2	0.2259	0.1309	57

measurement was performed by a Belsorp minill Microtrac-BEL device at  $-196^{\circ}\text{C}$  (for  $\text{N}_2$  sorption) and  $25^{\circ}\text{C}$  (for  $\text{CO}_2$  sorption), pressure 1 bar. The Belsorp software (BEL master TM) was used to analyze the porosity properties of carbon materials. Application of  $\text{N}_2$  adsorption isotherm by the BET equation and graph data allowed calculation of the specific surface area, total pore volume, and micrometer-sized pore distribution. The  $\text{CO}_2$  adsorption isotherm by the Dubinin-Astakhov (DA) method was used to determine the pore volume of the sample.

To determine pH<sub>pzc</sub>, two different solutions of sodium chloride (NaCl) were prepared at  $10^{-2}\text{M}$  and  $5 \times 10^{-2}\text{M}$  with purged deionized water ( $\text{CO}_2$ -free) and adjusted with pure hydrochloric acid (HCl) and pelleted sodium hydroxide (NaOH) to different pH values, i.e. 2, 4, 6, 8, 10, and 12. Then, each biochar was added into separated bottles at a ratio of 5 g of biochar to 1 L of pH-adjusted sodium chloride solution of 70 mL total. The bottles were secured in the incubator shaker for 24 hours. After shaking, the pH value was recorded in order to sketch an initial and final pH diagram.

**2.2.3. Adsorbability of Biochars.** MB and MO dyes were used to study the adsorption capacity of the biochar prepared at room temperature. These experiments were carried out in a 70 mL solution containing a  $10\text{ mg.L}^{-1}$  dye solution and a  $5\text{ mg.L}^{-1}$  biochar in a 100 mL Duran bottle. The initial pH was chosen based on the BC pH<sub>pzc</sub> data adjusted by using a solution of  $\text{H}_2\text{SO}_4$  and NaOH. A mixing series was set up, and the solution was shaken in the incubator shaker IKA KS 4000i at 250 rpm. All experiments were carried out at room temperature. Each sample was collected after 2

hours. The adsorbents were centrifuged in Hermle centrifuge Z 366 K at 4500 rpm for 20 minutes, separated by Whatman cellulose acetate paper with a pore size of  $0.45\ \mu\text{m}$ , and dried at  $105^{\circ}\text{C}$  for 2 hours. The concentration changes of the dye solutions were measured by Shimadzu UV-1800 UV-Vis spectrometer.

**2.2.4. Determination of MB and MO Concentrations by UV-Vis Spectrophotometry.** For the study of MB removal efficiency, the absorbance of the samples at maximum wavelength  $\lambda_{\text{max}} = 664\text{ nm}$  was measured. Calibration curves for MB were prepared with 7 different standard concentrations ranging from  $0\text{ mg.L}^{-1}$  to  $12\text{ mg.L}^{-1}$ . Since the color of MO is pH-dependent, the absorbance of the solution was measured at  $\lambda_{\text{max}} = 507\text{ nm}$  for  $\text{pH} = 2$ , and at  $\lambda_{\text{max}} = 464\text{ nm}$  for both  $\text{pH} = 12$ , the natural pH value of the solution.

The  $H$  removal efficiency (%) can be calculated based on the dye concentration:

$$H = \frac{C_0 - C_t}{C_0} \times 100, \quad (1)$$

where  $C_0$  and  $C_t$  are the dye concentrations at initial time and time  $t$ , respectively.

According to Lambert Beer's law:  $\text{Abs} = \epsilon bC$ , the dye concentration  $C$  is directly proportional to the absorbance since the molar attenuation coefficient  $\epsilon$  and the path length  $b$  (size of cuvette) remain constant. Therefore, the  $H$  removal efficiency (%) can be calculated based on the absorbance of the solution:

$$H = \frac{\text{Abs}_0 - \text{Abs}_t}{\text{Abs}_0} \times 100, \quad (2)$$

where  $\text{Abs}_0$  and  $\text{Abs}_t$  are the absorbances measured at initial time and time  $t$ , respectively.

Batch adsorption experiments for MB and MO removal were conducted in triplicates. In this study, the pH value of the research samples was determined by Hana instrument HI98197 portable multiparameter meter according to TCVN 6492:2011, ISO 10523:2008.

### 3. Results and Discussion

**3.1. TGA/DTG and Biochar Density.** The biochar carbonization process was set up based on the result of TGA/DTG analysis, shown in Figure 2.

The TGA/DTG diagram shows the mass loss curves of both materials (coir and husk) as a function of temperature at the heating rate of  $5^{\circ}\text{C.min}^{-1}$ . The materials were dried before carbonization, so in the temperature range from  $100^{\circ}\text{C}$  to  $250^{\circ}\text{C}$ , the mass does not change much, indicating the absence of free water molecules in the materials. The biggest mass loss occurs at  $250\text{--}300^{\circ}\text{C}$ , with a loss greater than 60% and 40% for coir and husk, respectively, suggesting that water and bounds organic compounds have been decomposed. In the temperature range of  $300^{\circ}\text{C}\text{--}450^{\circ}\text{C}$ , the pyrolysis process continues at a slower rate, with the final yield reaching about 5% for coir and 25% for husk. Both

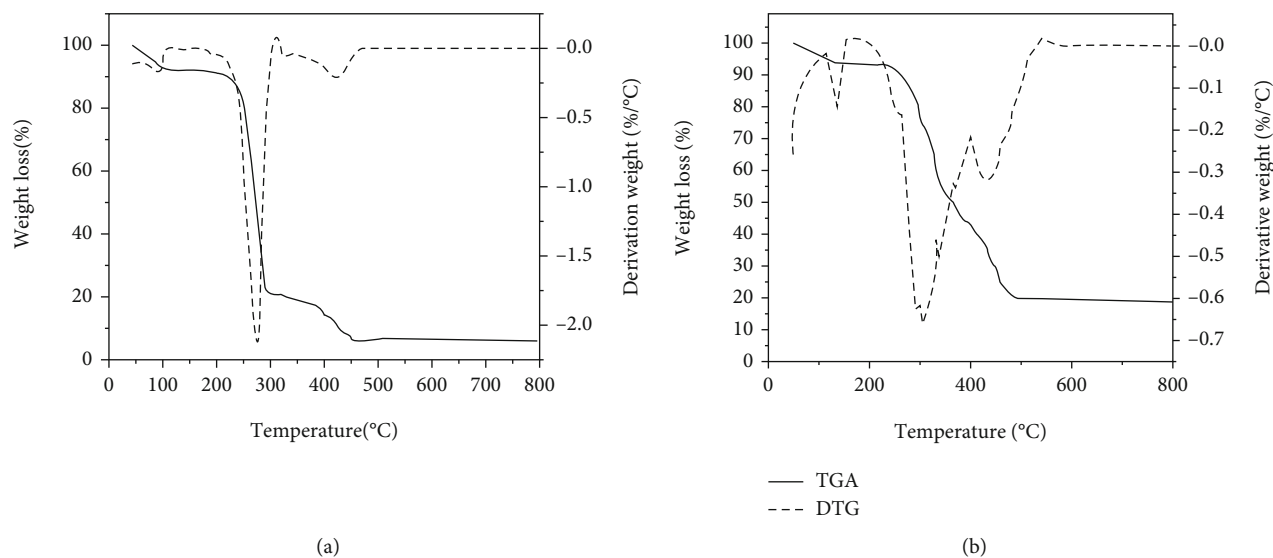


FIGURE 2: DTG/TGA diagram of coir (a) and rice husk (b).

TGA/DTG diagrams of coir and husk indicate that the mass yield hardly changes at temperatures above 450°C, which suggests that only ash remains.

These results show that although the DTG/TG curve of husk is a little different from that of coir, they are very similar at the first order, which justifies that the same calcination process was used for both materials (Figure 1).

Before and after the carbonization process, each mass and volume of each material were measured to calculate the initial and final density (before/after carbonization). The density of each material is recorded in Table 1.

There is no common pattern for the variation of density of the two materials before and after the carbonization process. For coconut coir (biochar 1 or BC1) and husk (biochar 2 or BC2), the density decreases by 20% and almost 50%, respectively. This is due to the fact that during calcination, water and organic compounds bound in the structure of the material were lost in gases and water vapor. However, the shape of the coconut coir (BC1) and the husk (BC2) was not altered much after the carbonization process, especially for the husk (which retained the shape of rice grains). Therefore, the density of both materials decreased slightly.

As can be seen clearly from Table 1, the actual mass loss after the carbonization of coir and husk was only 60% and 57%, respectively, much lower than when doing the TGA/DTG analysis (respectively, 95% and 75%, Figure 2). This can be explained by the formation of ash during TGA/DTG analysis, while during calcination, ashes were significantly reduced by covering the surface material with coal in the calcination process.

**3.2. Point of Zero Charge (PZC).** The pH of the solution (methylene blue and methyl orange) has a great influence on the adsorption capacity of the adsorbent on the adsorbate [40]. In order to optimize this capacity, the point of zero charge (PZC) should be analyzed and used. When pH values are below the PZC of an adsorbent, anions are attracted to its surface; cations experience the same effect when pH values

exceed the PZC [41]. Therefore, several experiments were carefully carried out to determine the PZC value for three types of biochar made from coir of two different sizes and from husk. The results on PZC are shown in Figures 3(a) and 3(b).

A buffer solution was used for the determination of PZC: a solution of NaCl with NaOH or HCl provided a buffer to stabilize and ensure the desired pH values so that the PZC result was correct.

For initial pH values of 2 and 12, the final pH values were almost identical to the initial values. Differences were only observed for initial pH values of 4, 6, and 10, where the final pH values remained stable around 9. This indicated that biochar 1 has an estimated PZC value at pH = 9, at which the biochar surface reaches electrically neutral state. In addition, according to the PZC theory, at pH values above the PZC value, the materials are negatively charged, and vice versa for pH values below the PZC.

For biochar 2, the initial–final pH curve is also similar to that of biochar 1; however, the PZC obtained for biochar 2 was lower than that of the biochar 1, at pH = 8.

**3.3. Fourier-Transform Infrared Spectroscopy (FTIR).** All FTIR spectra of the obtained biochars were collected in the midinfrared from 4000  $\text{cm}^{-1}$  to 390  $\text{cm}^{-1}$  and are shown in Figure 4.

The two spectra showed similarities, in the single bond region, a wideband showing up at 3500  $\text{cm}^{-1}$  attributed to the O–H stretching mode of hydroxyl groups, and in the double bond region. At about 1650  $\text{cm}^{-1}$ , the adsorption band was attributed to C=O stretching. For the spectrum of biochar 2, the greatest bands were observed at 1050  $\text{cm}^{-1}$ , which was in the fingerprint region, and it was attributed to the C–O stretching. In the wavenumber range of 900  $\text{cm}^{-1}$  to 400  $\text{cm}^{-1}$ , the spectrum was quite complex and hard to observe. However, in particular, when observing the spectrum of biochar 2, some peaks could be clearly seen at 1087, 800, and 460  $\text{cm}^{-1}$ , which were attributed to the carbon-silicon

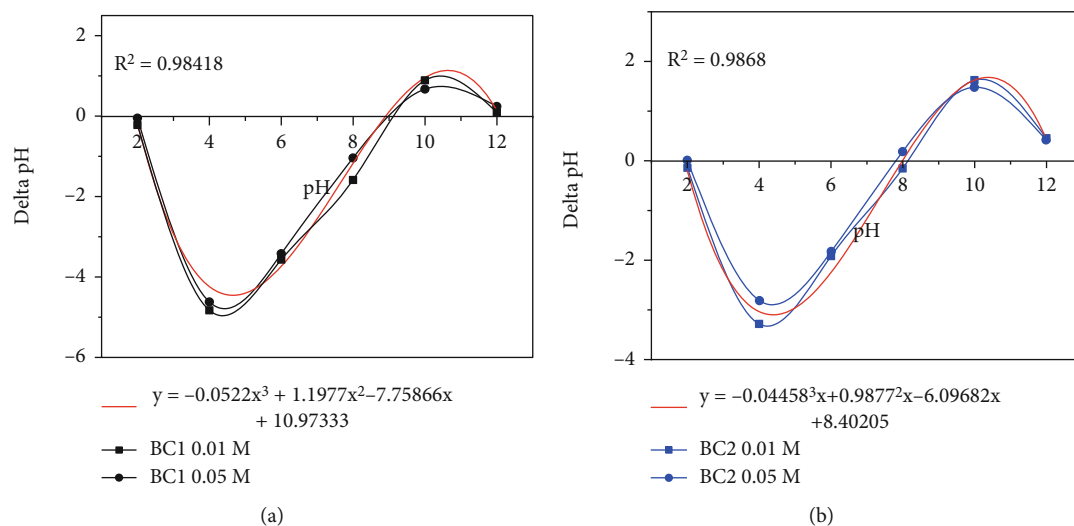


FIGURE 3: PZC of BC1 (a) and PZC of BC2 (b) in a buffer solution containing, respectively, 0.05 M and 0.01 M NaCl.

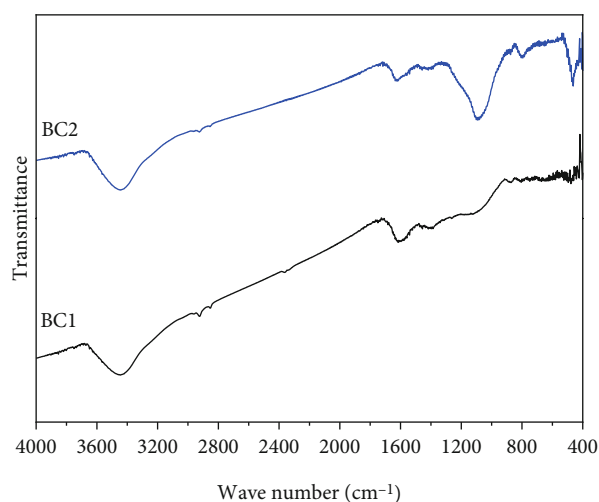


FIGURE 4: FTIR analysis on the biochar.

group (C-Si) (Pankaj [42, 43]). This carbon-silicon group is often found on the husk surface and is not found in coir. The spectra of biochar 1 did not show many differences. Besides the two spectral bands observed at  $3500 \text{ cm}^{-1}$  and  $1650 \text{ cm}^{-1}$ , the fingerprint region was also complex and hard to assign.

**3.4. X-Ray Diffraction Spectroscopy (XRD) Results.** The diffraction diagram of the biochars is presented in Figure 5. Two wide peaks range at  $2\theta = 22.5^\circ$  and  $2\theta = 43^\circ$  and the absence of peak showing the formation of the crystal phase indicates that the BCs were amorphous carbon. In addition, the diagrams revealed the presence of graphene structure in all biochar samples. The formation of graphene structures can occur during the pyrolysis of materials derived from agricultural by-products [44]. This result is similar to the conclusions of BC diffraction studies from [44]. The diagram also showed that graphene is the only crystal structure that appears in the BCs. In other words, no crystal structure of

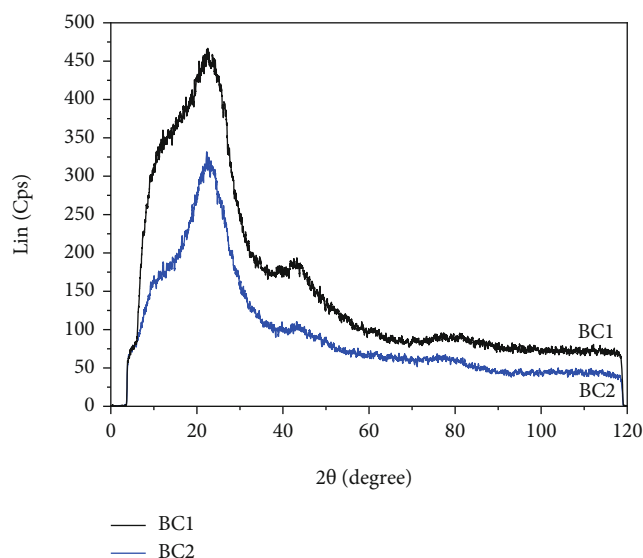


FIGURE 5: Diffraction diagram of biochars 1 and 2.

other metals could be found on the BC samples. Many studies have also shown that silica compounds in rice husk can form crystals when the temperature reaches  $800^\circ\text{C}$ .

**3.5. Raman Spectrum.** The carbon structure of biochar was also determined using Raman spectroscopy, complementing the results obtained from XRD (Figure 6).

Raman spectroscopy showed two main peaks at D band ( $1361 \text{ cm}^{-1}$ ) and G band ( $1591 \text{ cm}^{-1}$ ), corresponding to the graphene layer edge and an ideal lattice carbon, respectively [45]. Both peaks showed the presence of carbon atoms ( $sp^2$ ) in an aromatic compound that corresponds to the amorphous form of the benzene ring [46, 47]. Despite being different raw materials, the two biochars derived from rice husk and coir had the same shape spectrum, proving that the formation of biochar structure by pyrolysis from different agricultural by-products is the same. This result was also

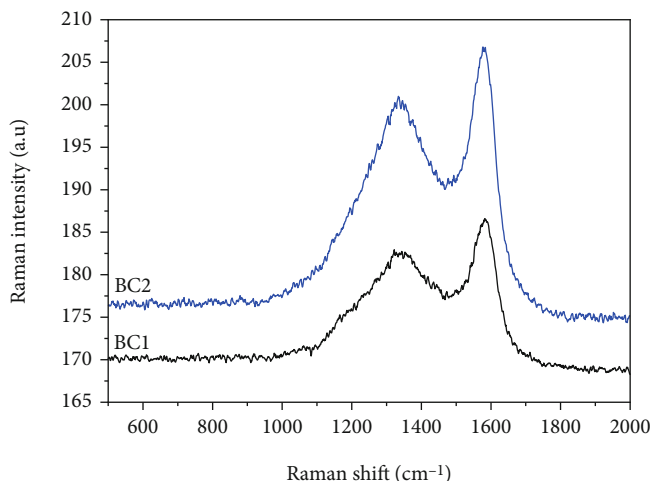


FIGURE 6: Raman spectrum of difference BCs.

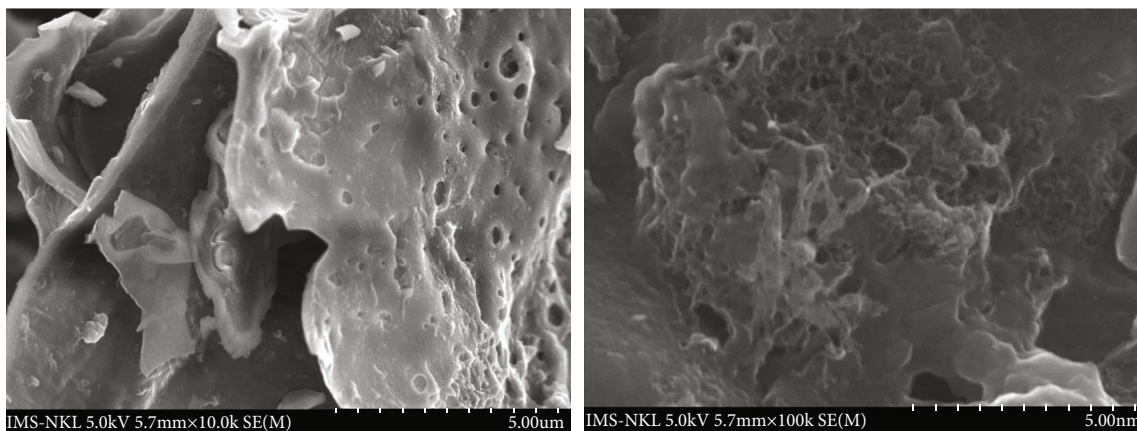


FIGURE 7: SEM images of BC1.

confirmed by the X-ray diffraction method of biochar. Biochar after pyrolysis has an amorphous form with several layers of graphene to create the porous structure of the material.

**3.6. Surface Morphology of Biochars.** Surface morphology and porous structure are important features in the adsorption process. In particular, for biochar, solids are obtained from the pyrolysis of rice husks and coir in an anaerobic environment (lack of oxygen and high pressure). The surface morphology, as well as the main surface elemental composition, was investigated by scanning electron microscopy (SEM) (Figures 7 and 8) and energy dispersive X-ray emission (EDX).

Generally, all BCs had porous meso and micropore structures with different shapes and sizes. SEM image observation of both BC types also showed the structure of the graphene layers formed along with the field structure of BC. These results also correspond to the results of [44].

The SEM image of rice husk biochar (BC2) showed that it remained intact in its structure (fiber shape) of the original husk, and the pores were fairly uniform. After being broken

in half, the cross-section image of BC2 revealed a series of pores with a capillary structure on the BC2 wall, about 5 to 10  $\mu\text{m}$  in diameter. Besides, although the mesopore structure was uneven, the micropore size was quite uniform with a diameter of approximately 50 nm.

In contrast, the results for BC1 yielded a greater variety of pore sizes. Specifically, the surface morphology of biochar from coconut coir showed many pores of fairly nonuniform size with a large structure.

The average percentage values of surface elemental composition in biochars, corresponding to the SEM micrographs analysis positions and dispersive spectrum are presented in Figure 9 and Table 2.

The obtained results showed that the main component of all BCs was carbon, which confirmed the decomposition of cellulose, lignin, and organic matters contained in agricultural by-products at high-temperature 500-600°C. Besides, they revealed a significant content of oxygen. Combined with the results of the FTIR analysis, the oxygen content in the BCs was confirmed to come from the functional groups -COO- and -OH existing on the surface of BCs. Specifically, Si content included in the BC2 structure was consistent with the results

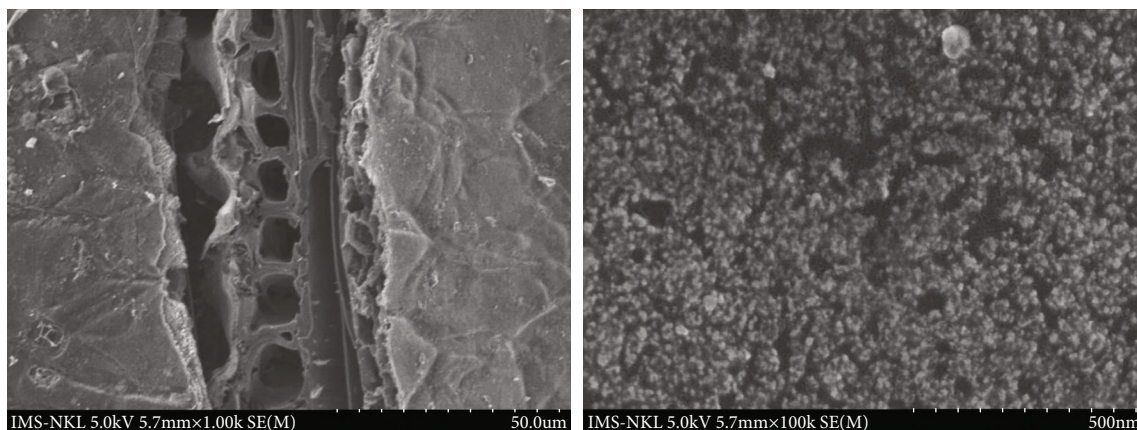


FIGURE 8: SEM images of BC2.

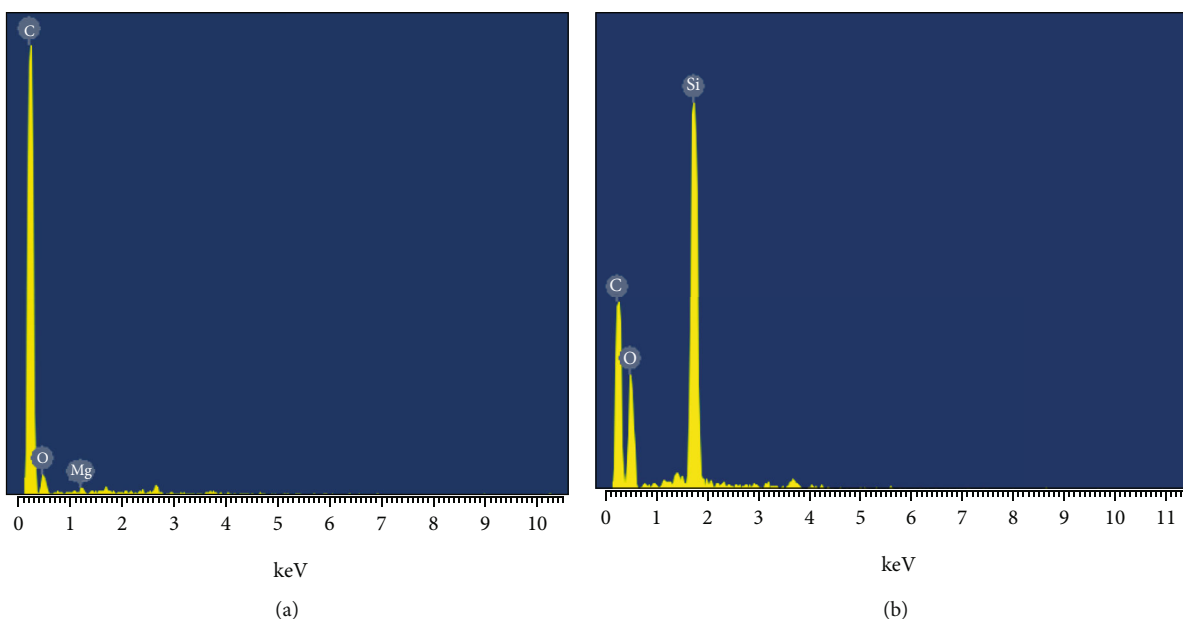


FIGURE 9: Energy dispersive spectrum corresponding to a SEM image analysis position of BC1 (a) and BC2 (b).

TABLE 2: Average mass percentage of surface elemental composition in biochar.

Components	BC1	BC2
C K (%)	82.93	40.27
O K (%)	16.76	44.92
Mg K (%)	0.31	0.00
Si K (%)	0.00	14.81
Total	100.00	100.00

of the FTIR analysis, indicating the bond between silicon and carbon (Si-C). However, the contents of C, O, and Si are unevenly distributed at different locations of the BCs.

3.7. *Specific Surface Area and Pore Volume.* The N<sub>2</sub> adsorption-desorption isotherms (Figure 10) were used to determine the porosity of the BCs. The specific surface area

and pore volume are significant parameters that have a strong link with the adsorption ability of the material. Micropores (diameter < 2 nm) and mesopores (between 2 and 50 nm) actively participate in the sorption capacity of biochar, while larger pores usually have a much smaller effect [48].

The BC2 had a higher microporosity compared to that of the BC1, as shown by the higher position of the corresponding isotherm and the larger slope at relative pressures  $p/p_o$  above 0.1. The N<sub>2</sub> adsorption-desorption isotherm of the BC1 exhibited type I isotherms in the IUPAC classification [49], which indicated that the microporous structure was dominant in the BC1. Meanwhile, the BC2's isotherms exhibited type IV with a large range for the hysteresis loop. This can be explained by the capillary condensation phenomenon, whereby a gas in a pore condenses into a liquid phase at a pressure  $p < p_o$  of the bulk liquid [49]. This result strongly suggests that in the case of BC2, besides micropores, mesopores were also present.

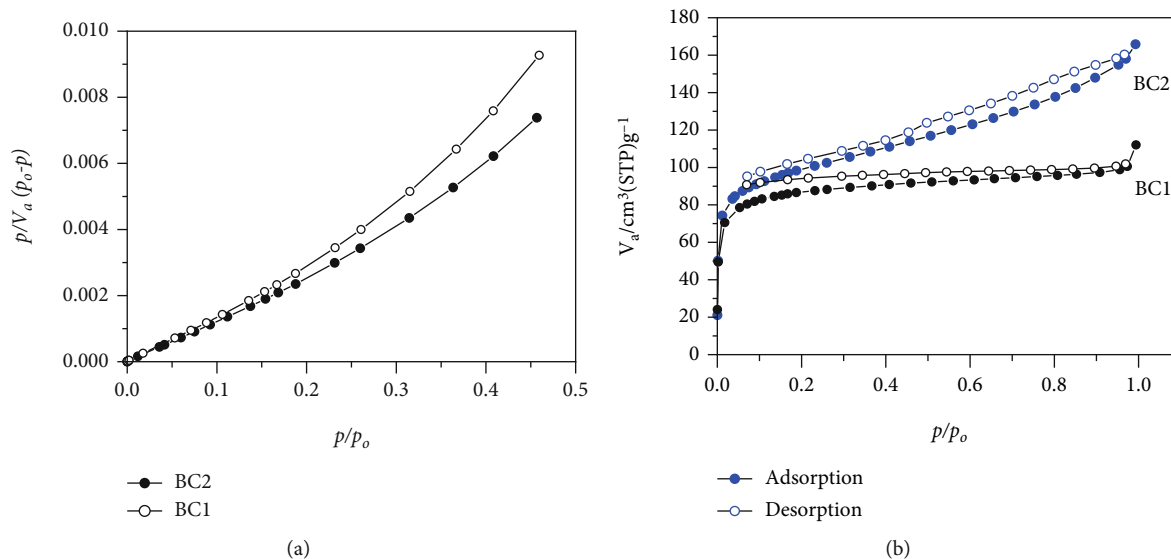


FIGURE 10: BET-plot (a) and adsorption/desorption isotherm (b) of BC1 and BC2 in  $N_2$ .

TABLE 3: Parameters of specific surface area and pore of biochar.

Sample	$S_{BET}$ ( $m^2 \cdot g^{-1}$ )	$V_{BET}$ ( $cm^3 \cdot g^{-1}$ )	$V_{meso}$ ( $cm^3 \cdot g^{-1}$ )	$V_{Micro}$ (BET) ( $cm^3 \cdot g^{-1}$ )	$V_{Micro}$ (DA) ( $cm^3 \cdot g^{-1}$ )
BC1	329.7	0.17	0.03	0.14	0.21
BC2	364.2	0.26	0.14	0.15	0.26

Table 3 shows the results of total surface area ( $S_{BET}$ ) and total pore volume ( $V_{BET}$ ), estimated by the BET method, and micropore volume ( $V_{Micro}$ ) and mesopore volume ( $V_{Meso}$ ), estimated by the t-plot and BJH methods, respectively.

The  $S_{BET}$  of BC2 was higher than that of BC1 ( $364.2 m^2 \cdot g^{-1}$  vs.  $329.7 m^2 \cdot g^{-1}$ ). Similarly, the pore volume of BC2 was  $0.26 cm^3 \cdot g^{-1}$  compared to  $0.17 cm^3 \cdot g^{-1}$  for BC1. Compared to other biomass chars produced under similar carbonization conditions, such as fern char [50] or cashew nutshell char [51], BCs produced in this study achieved higher porosity levels. The  $V_{Micro}$  (estimated by BET technique) of BC1 and BC2 is similar. However, the large size of the  $N_2$  molecules prevents them from entering the ultra-micropores, i.e., pores with diameters less than 1 nm. Therefore,  $CO_2$  adsorption/desorption was performed to fully reflect the microporous structures of these BCs (Figure 11).

The adsorption/desorption isotherm plot of  $CO_2$  of BC2 is above that of BC1, indicating a higher micropore volume. Moreover, both isotherms showed hysteresis at low-pressure. This indicates that the  $CO_2$  molecules were in a metastable state, and the gas was not readily released at the level corresponding to the value of thermodynamic equilibrium at pressure decrease [52]. In other words, both BCs exhibited heterogeneous surface properties with bottleneck shapes at the micropore entrance. This pore shape is known to be favorable for long particule capture.

The  $V_{Micro}$  (estimated by DA method) reached  $0.26 cm^3 \cdot g^{-1}$  for BC2 and  $0.21 cm^3 \cdot g^{-1}$  for BC1. The smaller kinetic diameter of  $CO_2$  (0.3 nm) compared to  $N_2$  (0.36 nm) gave a much higher  $V_{Micro}$  calculated by the DA

method than by the t-plot method. This indicates that the microporous structures were better developed in rice husk biochar than in coir biochar.

### 3.8. Biochar Adsorbability

**3.8.1. General Evaluation of BC1 Adsorbability with Methylene Blue (MB).** Evaluation of the effect of pH on biochar 1 adsorbability of methylene blue was first performed. Experiments were carried out to evaluate the effect of varying pH values of dye solution on the ability of biochar to adsorb methylene blue ions. The results are shown in Figure 12.

The effect of pH on methylene blue adsorption was not significant for biochar 1 as there was little difference between the three efficiency lines. At pH = 2, the adsorbability of BC1 was however slightly weaker than at other pH values for the first hours of the time series, which accurately reflects the point of zero charge principle. The difference between the efficiency lines of BC1 was more distinct for the efficiency lines at pH = 2 and at other pH values. The efficiency reached 66% at pH 2 and 87% at both pH 6 and pH 12 after 30 minutes of adsorption. When the adsorption time was increased to 1 hour, the adsorption efficiency showed similar differences, 87% at pH 2 and 94% at the other two pH values. It was found that dye adsorption increases with pH, with a maximum adsorption at pH 6. This could be due to the fact that the surface of the adsorbent becomes negative at higher pH values, favoring the adsorption of positively charged MB cationic dye via electrostatic attraction. Moreover, there is a

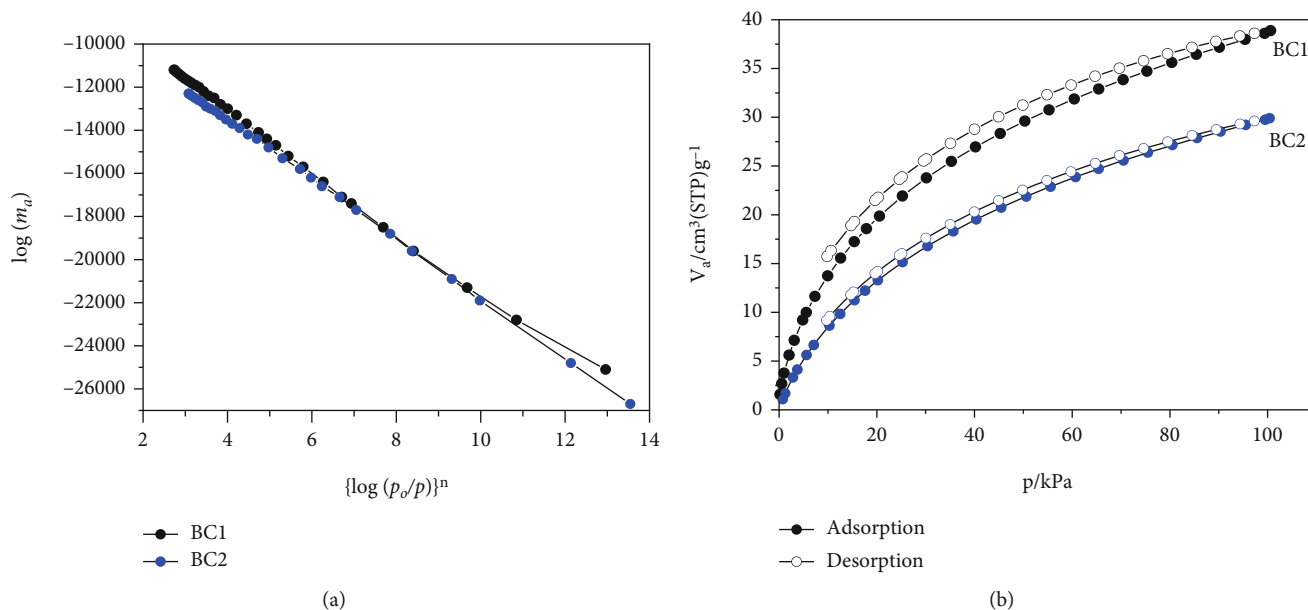


FIGURE 11: DA-plot (a) and adsorption/desorption isotherm (b) of BC1 and BC2 in  $\text{CO}_2$ .

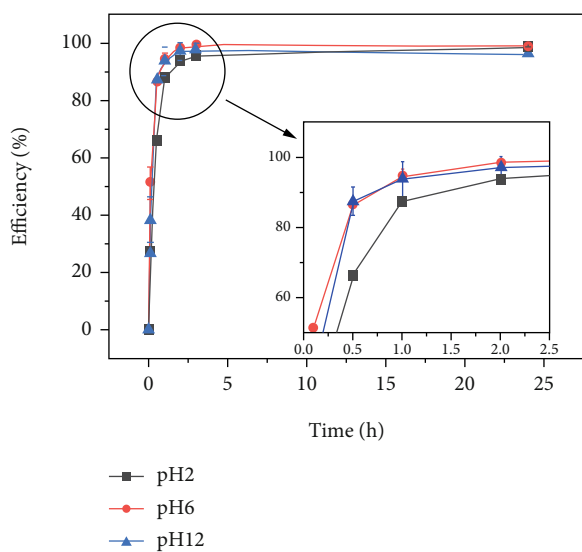


FIGURE 12: Evaluation of the effect of pH on biochar 1 ( $5 \text{ g.L}^{-1}$ ) adsorbability of methylene blue ions.

slight reduction in adsorption at pH 12 due to the repulsion of adsorbent surface and the existence of a partial negative charge ( $\text{Cl}^-$ ) on MB [42].

**3.8.2. Evaluation of the Effect of Biochar Dosage on Adsorbability with Methylene Blue.** The effect of varying biochar concentration on the adsorption of dye ions on the biochar surface was studied with methylene blue. The results are given in Figure 13.

As expected, the higher the biochar concentration, the better the adsorbability. However, the differences are not really significant. Based on these results, a catalyst concentration of  $5 \text{ g.L}^{-1}$  was selected for further studies.

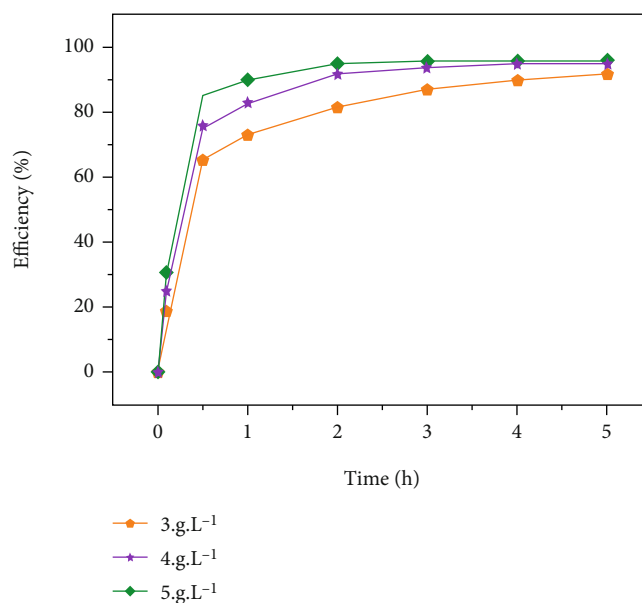


FIGURE 13: Evaluation of the effect of biochar 1 dosage on adsorbability.

**3.8.3. Evaluation of the Effect of pH on Biochar Adsorbability with Methyl Orange.** The laboratory-synthesized biochar BC1 was studied for its ability to remove not only methylene blue but also methyl orange, an anionic dye. The results are shown in Figure 14.

At pH 2, it took less than an hour to reach 80% efficiency, and after 5 hours, biochar 1 had removed over 96% of the MO in the solution. In contrast, the efficiency of dye removal at pH 6 and 12 was approximately half that at pH 2, 49%, and 47%, respectively. At pH 6 and pH 12, the surface was, respectively, neutral and positively charged; therefore; adsorption efficiency is much lower.

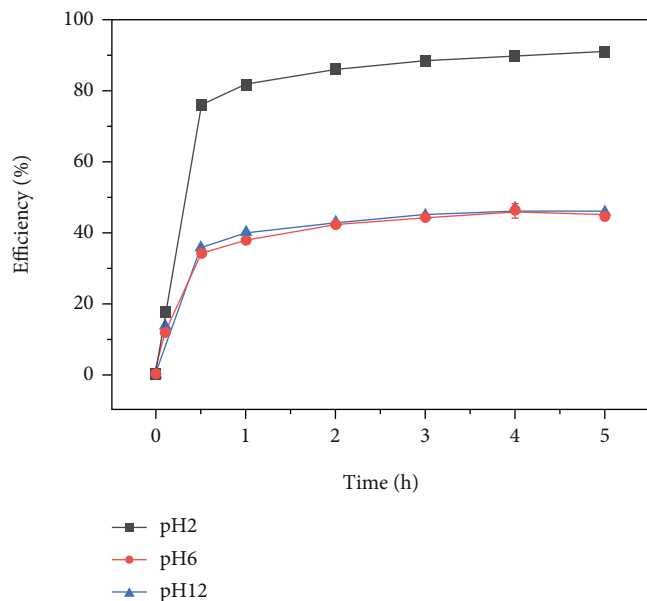


FIGURE 14: Evaluation of the effect of pH on biochar 1 ( $5 \text{ g.L}^{-1}$ ) adsorbability of methyl orange.

In addition to the electrostatic interaction following the PZC principle, many functional groups exist on the biochar surface and bind to methylene blue or methyl orange, thus, facilitating the adsorption on the biochar surface. When the pH of the solution was decreased significantly, the positive surface charge of the BC increased and, consequently, the adsorption of methyl orange anions on the BC surface increased significantly. On the contrary, when the pH of the solution was increased, the adsorption of methyl orange on BC1 decreased due to the repulsive force between the adsorbent and the negatively charged adsorbate. However, the adsorption of methylene blue at high pH was enhanced due to the strong electrostatic interaction between the cationic groups of MB molecule and the negatively charged BC surface. Therefore, this could be the main mechanism of the adsorption. The results showed that the highest adsorption efficiency of BC was obtained at basic pH values for MB and at acidic pH for MO.

In consequence, the influence of the two different biochars on dye adsorbability was investigated at pH 6 for MB and at pH 2 for MO (Figure 15).

Figure 15 clearly demonstrates that the adsorption of BC2 was superior to that of BC1 under the same conditions with a peak efficiency of nearly 100%. This difference is also partly due to the physical characteristics of the adsorbent. BC2 is derived from the rice husk with a much higher number of pores than BC1 which is coconut coir. It has both meso and micropores, so the total BET and total porous volume of BC2 are larger than BC1,  $364.22 \text{ m}^2 \cdot \text{g}^{-1} > 329.71 \text{ m}^2 \cdot \text{g}^{-1}$  and  $0.26 \text{ m}^3 \cdot \text{g}^{-1} > 0.17 \text{ m}^3 \cdot \text{g}^{-1}$ .

Moreover, biochar 2 has a relatively high microporous and mesoporous area,  $0.15 \text{ cm}^3 \cdot \text{g}^{-1}$  and  $0.14 \text{ cm}^3 \cdot \text{g}^{-1}$  compared to  $0.14 \text{ cm}^3 \cdot \text{g}^{-1}$  and  $0.03 \text{ cm}^3 \cdot \text{g}^{-1}$  for biochar 1, respectively. Apart from those factors, these two types of biochar

had similar surface functional groups, and the only difference was the silicon components found in BC2.

The MB adsorption efficiency of BC1 was close to 94%, much higher than that of MO (about 82%) after 1 hour of the reaction. BC2 also showed a similar trend with the adsorption efficiency slightly higher for MB than for MO, about 100% and 96%, respectively. Both materials had better electronic interactions with MB than with MO. This suggested that the adsorption capacity of both biochars was more efficient for MB than for MO. Considering the physicochemical properties of the adsorbent surface, although MO ( $1.31 \times 0.55 \times 0.18 \text{ nm}$ ) has a smaller molecular size than MB ( $1.26 \times 0.77 \times 0.65 \text{ nm}$ ), which means that MO molecules were able to enter the pores and being retained in more micro and mesopores; however, MB ions were more selectively adsorbed.

This result is consistent with the study of Phuong et al. [53] who obtained an average surface area including micropore and mesopore of rice husk-derived biochar of  $118 \text{ m}^2 \cdot \text{g}^{-1}$ . Since the volume of mesopore was quite small and most of the pore volume was micropore, MB ions took longer to be adsorbed into the BCA pores, so the adsorbability rate was slowed down. In our study, the dye adsorption rate of BC1 was slower than that of BC2 because BC2 had a larger BET volume and much larger pore volume, as mentioned above. Both dyes can be completely adsorbed.

**3.8.4. Isothermal Adsorption.** The results of the physicochemical characteristics analysis showed that BC2 had a higher adsorption capacity than BC1 due to its larger surface area and pore volume, a larger number of surface functional groups, and a lower pH of PZC. Therefore, the adsorption isotherm of MB and MO adsorption was also evaluated through two popular adsorption models, Langmuir and Freundlich isotherm models. Figure 16 shows the isotherm of MB and MO adsorption on BC1 material according to Langmuir and Freundlich models.

The parameters of Langmuir and Freundlich adsorption isotherms were calculated from the slope values and the vertical cut and are presented in Table 4.

Langmuir and Freundlich adsorption isotherms are two chemisorption models in which Langmuir is a monolayer adsorption process while Freundlich describes a multilayer adsorption capacity of the material.

The results demonstrated that the adsorption capacity of BC2 followed both Langmuir and Freundlich models with MO adsorbent. The regression coefficients  $R^2$  were both high (0.97 and 0.99 for Langmuir and Freundlich, respectively), revealing that the adsorption process follows both models. In contrast, with the MB adsorbent, the adsorption isotherm followed the Langmuir model with a regression coefficient of 0.99. For BC1 adsorption, MO followed the Langmuir model with  $R^2$  of 0.99 and MB followed Freundlich with the same  $R^2$  value. Overall, in this study, the dye removal efficiency of BC2 was higher than that of BC1, both following the Langmuir and Freundlich isotherm models.

Remind that the Freundlich model suggests multilayer physisorption on the surface of the material with different adsorption energy levels whereas the Langmuir model

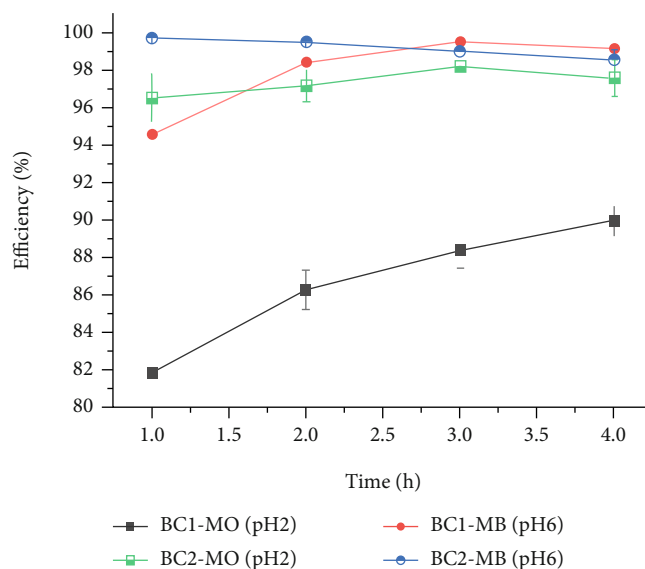


FIGURE 15: Effect of two different biochars on adsorbability of dyes molecules.

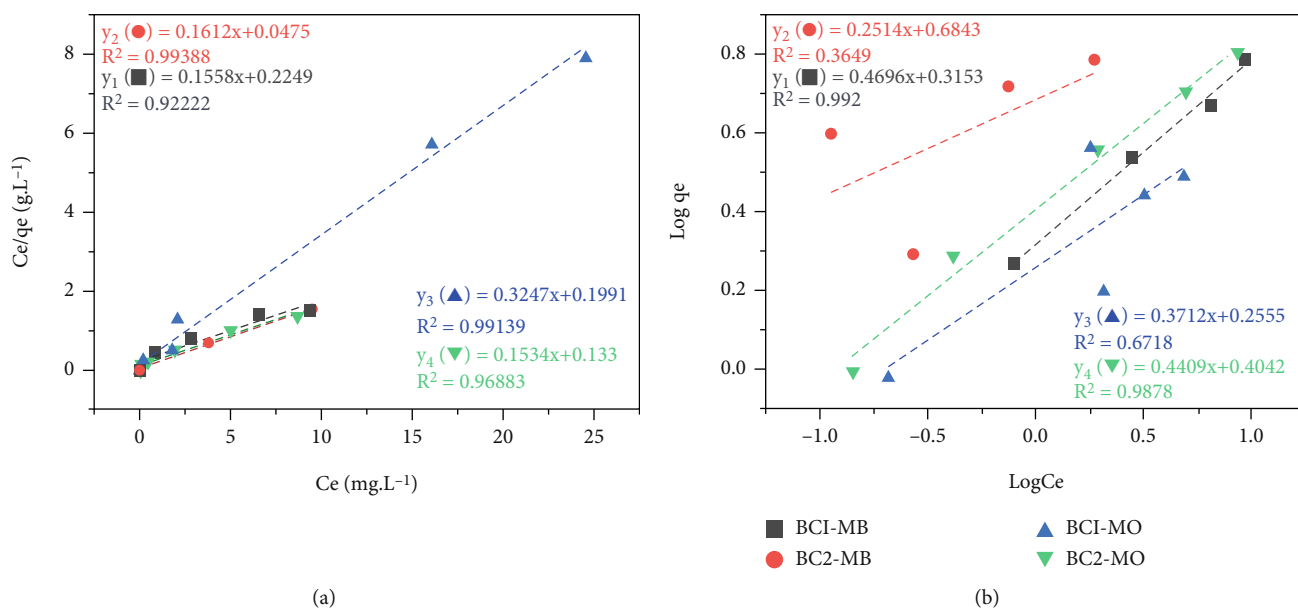


FIGURE 16: Langmuir (a) and Freundlich (b) adsorption isotherm model fittings for the adsorption of MB and MO on BC1 and BC2 at 25°C.

TABLE 4: The adsorption isotherm of MO and MB adsorbed on BC2 and BC2 materials according to Langmuir and Freundlich models.

Model	Parameters	MB		MO	
		BC1	BC2	BC1	BC2
Langmuir isotherm parameters	$R^2$	0.922	0.994	0.991	0.969
	$q_{max}$ ( $mg.g^{-1}$ )	6.418	8.612	3.080	6.519
	$B$ ( $L.mg^{-1}$ )	0.693	2.445	1.631	1.153
Freundlich isotherm parameters	$R^2$	0.992	0.365	0.672	0.988
	$K_F$ [( $mg.g^{-1}$ ) ( $L.mg^{-1}$ )] <sup>n</sup>	2.067	4.834	1.801	2.536
	$n$	2.129	3.978	2.694	2.268

proposes monolayer chemisorption by the donor-acceptor interaction based on electrophilic addition [54, 55]. This was because the charge-rich carbonized surface created bonds with protonated amino groups in the acidic medium. In addition, H-H and H-O bonding between the carbon-silicon group on the surface of biochar with the phenolic group of dye molecules could also be able to occur [56].

Rodriguez also indicated that the mechanism of dye adsorption on biochars may be classified into two types of interactions: nonelectrostatic and electrostatic. Adsorption is affected by the pH of the solution as well as the  $pH_{pZC}$ . Therefore, at  $pH < pH_{pZC}$ , the surface of the biochar is positively charged, promoting anionic species adsorption, and negatively charged at  $pH > pH_{pZC}$ , favoring cationic species adsorption [57]. Furthermore, all biochar samples had  $pH_{pZC}$  values of 8 and 9 for BC1 and BC2, respectively, higher than the pH values of MB (6.0) and MO (2) solutions. Biochar has a positive charge, MB is a cation dye that has a positive charge when dissolved in water, and MO is an anion dye that becomes negatively charged when dissolved in water. The adsorption mechanism is therefore dominated by the dispersion interaction between the dissociated electrons on the surface of the activated carbon and the free electrons of the dye molecule contained in the aromatic ring [58].

The  $R_L$  separation factor values for dye adsorption on the particular adsorbent were all positive and less than unity in all cases, suggesting extremely favorable adsorption under all circumstances. This is furthermore consistent with the results for the  $1/n_F$  values, which were less than unity, suggesting that the dye is preferentially absorbed by biochar.

In terms of the maximum adsorption capacity of a material, BC2 adsorbs both dyes well and better than BC1 with a  $q_{max}$  value of  $8.612 \text{ mg.g}^{-1}$  and  $6.519 \text{ mg.g}^{-1}$  for MB and MO, respectively. These values are quite low compared to that of various adsorbents, such as bamboo-activated carbon [59], pea shells [60], modified clay-ball [61], and activated biochar derived from wakame [62]. However, biochars prepared with a particle size of 1-2 mm for coir and 5 mm for rice husk are more ecologically friendly and economically effective compared to other adsorbents. First, the granular nature of the adsorbent is useful since it can be easily separated after filtration and sedimentation without creating sludge. Second, in terms of recycling, using an agricultural by-product allows waste to be a valued resource to reduce environmental risks [12].

#### 4. Conclusions

Biochars derived from agricultural by-products including coconut coir and rice husk were successfully produced in large quantity, homogenized following the calcination process, and then activated by  $H_2$  25%. The biochars had a high specific surface area of  $364.22 \text{ m}^2.\text{g}^{-1}$  and  $329.71 \text{ m}^2.\text{g}^{-1}$  for rice husk and coconut coir biochars, respectively. All biochars had micro and mesopore structures but with different amounts. SEM images as well as XRD and Raman analysis of different biochars also showed various graphene layers with an amorphous structure. These results suggest that the bio-

char obtained in this study could have a high adsorbability for small to large molecules. Indeed, both biochar BC1 and BC2 showed good adsorption ability for MB and MO. In addition, BC2 had a better performance in dye adsorption than BC1.

The results of adsorption isotherm experiments indicated BC2 material followed Langmuir and Freundlich isotherms when adsorbing MO with a maximal adsorption volume of  $6.519 \text{ mg.g}^{-1}$ . In the case of MB adsorption, BC2 only followed the Langmuir isotherm with a maximal adsorption volume of  $8.612 \text{ mg.g}^{-1}$ . On the contrary, BC1 adsorbed MB following the Freundlich isotherm while its MO adsorption followed the Langmuir isotherm. In general, the agricultural by-products can be reused after treatment as adsorbents for persistent organic pollutants, including those found in wastewater from the textile industry.

#### Data Availability

The data used to support the findings of this study are included in the article.

#### Conflicts of Interest

The authors declare that they have no conflicts of interest.

#### Acknowledgments

This research was funded by the Vietnam Academy of Science and Technology (VAST), code: VAST07.04/20-21. The authors wish to acknowledge the support of the International Joint Laboratory LOTUS (Land-Ocean aTmosphere regional coUPled System) as well as the Institute of Research of Environment (IRD). The authors greatly appreciate the editorial team as well as reviewers who have devoted their time and expertise to improve the quality of this publication.

#### References

- [1] B. Nhung and T. Thuy, "Vietnam's textile and garment industry: an overview," in *Business and IT*, vol. VIII, no. 2, pp. 45–53, 2018.
- [2] K. Sarayu and S. Sandhya, "Current technologies for biological treatment of textile wastewater—a review," *Applied Biochemistry and Biotechnology*, vol. 167, no. 3, pp. 645–661, 2012.
- [3] H. Wang, X.-W. Zheng, J.-Q. Su, Y. Tian, X.-J. Xiong, and T.-L. Zheng, "Biological decolorization of the reactive dyes Reactive Black 5 by a novel isolated bacterial strain *Enterobacter* sp. EC3," *Journal of Hazardous Materials*, vol. 171, no. 1-3, pp. 654–659, 2009.
- [4] M. S. Mahmoud, J. Farah, and T. E. Farrag, "Enhanced Removal of Methylene Blue by Electrocoagulation Using Iron Electrodes," *Egyptian Journal of Petroleum*, vol. 22, no. 1, pp. 211–216, 2013.
- [5] A. S. Naje, S. Chelliapan, Z. Zakaria, M. A. Ajeel, and P. A. Alaba, "A review of electrocoagulation technology for the treatment of textile wastewater," *Reviews in Chemical Engineering*, vol. 33, pp. 263–292, 2017.
- [6] U. Tezcan Un and E. Aytac, "Electrocoagulation in a packed bed reactor-complete treatment of color and COD from real

- textile wastewater,” *Journal of Environmental Management*, vol. 123, pp. 113–119, 2013.
- [7] V. Jegatheesan, B. K. Pramanik, J. Chen, D. Navaratna, C.-Y. Chang, and L. Shu, “Treatment of textile wastewater with membrane bioreactor: a critical review,” *Bioresource Technology*, vol. 204, pp. 202–212, 2016.
- [8] A. H. Konsowa, M. G. Eloffy, and Y. A. El-Taweel, “Treatment of dyeing wastewater using submerged membrane bioreactor,” *Desalination Water Treat*, vol. 51, no. 4-6, pp. 1079–1090, 2013.
- [9] B. X. Thanh, N. P. Dan, and N. T. Binh, “Fouling mitigation in a submerged membrane bioreactor treating dyeing and textile wastewater,” *Desalination Water Treat*, vol. 47, no. 1-3, pp. 150–156, 2012.
- [10] M. R. Al-Mamun, S. Kader, M. S. Islam, and M. Z. H. Khan, “Photocatalytic activity improvement and application of UV-TiO<sub>2</sub> photocatalysis in textile wastewater treatment: a review,” *Journal of Environmental Chemical Engineering*, vol. 7, no. 5, p. 103248, 2019.
- [11] A. Sharma, Z. Syed, U. Brighu, A. B. Gupta, and C. Ram, “Adsorption of textile wastewater on alkali-activated sand,” *Journal of Cleaner Production*, vol. 220, pp. 23–32, 2019.
- [12] J. O. Quansah, T. Hlaing, F. N. Lyonga et al., “Nascent rice husk as an adsorbent for removing cationic dyes from textile wastewater,” *Applied Sciences*, vol. 10, no. 10, p. 3437, 2020.
- [13] B. Srivastava, V. Jhelum, D. D. Basu, and P. K. Patanjali, “Adsorbent for pesticide uptake from contaminated water: a review,” *Journal of Scientific and Industrial Research*, vol. 68, pp. 839–850, 2009.
- [14] A. Bhatnagar and M. Sillanpää, “Utilization of agro-industrial and municipal waste materials as potential adsorbents for water treatment—a review,” *Chemical Engineering Journal*, vol. 157, no. 2-3, pp. 277–296, 2010.
- [15] M. Akhtar, S. M. Hasany, M. I. Bhangar, and S. Iqbal, “Low cost sorbents for the removal of methyl parathion pesticide from aqueous solutions,” *Chemosphere*, vol. 66, no. 10, pp. 1829–1838, 2007.
- [16] S. Deokar and S. Mandavgane, “Rice husk ash for fast removal of 2,4-dichlorophenoxyacetic acid from aqueous solution,” *Adsorption Science and Technology*, vol. 33, no. 5, pp. 429–440, 2015.
- [17] M. L. Firdaus, N. Krisnanto, W. Alwi, R. Muhammad, and M. A. Serunting, “Adsorption of textile dye by activated carbon made from rice straw and oil palm midrib,” *Aceh International Journal of Science and Technology*, vol. 6, no. 1, pp. 1–7, 2017.
- [18] M. Ghorbani and H. Eisazadeh, “Removal of COD, color, anions and heavy metals from cotton textile wastewater by using polyaniline and polypyrrole nanocomposites coated on rice husk ash,” *Composites. Part B, Engineering*, vol. 45, no. 1, pp. 1–7, 2013.
- [19] M. Muneer, I. A. Bhatti, and S. Adeel, “Removal of Zn, Pb and Cr in textile wastewater using rice husk as a biosorbent,” *Asian Journal of Chemistry*, vol. 22, pp. 7453–7459, 2010.
- [20] I. Herath, P. Kumarathilaka, M. I. Al-Wabel et al., “Mechanistic modeling of glyphosate interaction with rice husk derived engineered biochar,” *Microporous and Mesoporous Materials*, vol. 225, pp. 280–288, 2016.
- [21] Y. C. Sharma and S. N. Upadhyay, “An economically viable removal of methylene blue by adsorption on activated carbon prepared from rice husk,” *Canadian Journal of Chemical Engineering*, vol. 89, no. 2, pp. 377–383, 2011.
- [22] J. S. Chin-Pampillo, K. Ruiz-Hidalgo, M. Masis-Mora, E. Carazo-Rojas, and C. E. Rodríguez-Rodríguez, “Design of an optimized biomixture for the degradation of carbofuran based on pesticide removal and toxicity reduction of the matrix,” *Environmental Science and Pollution Research*, vol. 22, no. 23, pp. 19184–19193, 2015.
- [23] T. De Wilde, P. Spanoghe, J. Ryckeboer, P. Jaeken, and D. Springael, “Sorption characteristics of pesticides on matrix substrates used in biopurification systems,” *Chemosphere*, vol. 75, no. 1, pp. 100–108, 2009.
- [24] G. D. Gikas, M. Pérez-Villanueva, M. Tsioras et al., “Low-cost approaches for the removal of terbuthylazine from agricultural wastewater: constructed wetlands and biopurification system,” *Chemical Engineering Journal*, vol. 335, pp. 647–656, 2018.
- [25] A. K. Samanta, G. Basu, and L. Mishra, “Role of major constituents of coconut fibres on absorption of ionic dyes,” *Industrial Crops and Products*, vol. 117, pp. 20–27, 2018.
- [26] N. L. P. A. Saraswati and I. D. K. Sastrawidana, “Absorption of Remazol Red dye from textile waste using activated carbon from coconut shell,” *IOP Conference Series: Materials Science and Engineering*, vol. 1115, no. 1, article 012076, 2021.
- [27] Y. C. Wong, M. S. R. Senan, and N. A. Atiqah, “Removal of methylene blue and malachite green dye using different form of coconut fibre as adsorbent,” *Journal of Basic & Applied Sciences*, vol. 9, pp. 172–177, 2013.
- [28] A. Demirbas, “Agricultural based activated carbons for the removal of dyes from aqueous solutions: a review,” *Journal of Hazardous Materials*, vol. 167, no. 1-3, pp. 1–9, 2009.
- [29] T. Ahmad, M. Rafatullah, A. Ghazali, O. Sulaiman, R. Hashim, and A. Ahmad, “Removal of pesticides from water and wastewater by different adsorbents: a review,” *Journal of Environmental Science and Health, Part C*, vol. 28, no. 4, pp. 231–271, 2010.
- [30] O. A. Ioannidou, A. A. Zabaniotou, G. G. Stavropoulos, M. A. Islam, and T. A. Albanis, “Preparation of activated carbons from agricultural residues for pesticide adsorption,” *Chemosphere*, vol. 80, no. 11, pp. 1328–1336, 2010.
- [31] S. P. Sohi, E. Krull, E. Lopez-Capel, and R. Bol, “A review of biochar and its use and function in soil,” *Advances in Agronomy*, vol. 105, pp. 47–82, 2010.
- [32] H. Cederlund, E. Börjesson, and J. Stenström, “Effects of a wood-based biochar on the leaching of pesticides chlorpyrifos, diuron, glyphosate and MCPA,” *Journal of Environmental Management*, vol. 191, pp. 28–34, 2017.
- [33] M. Hagner, S. Hallman, L. Jauhiainen et al., “Birch (*Betula spp*) wood biochar is a potential soil amendment to reduce glyphosate leaching in agricultural soils,” *Journal of Environmental Management*, vol. 164, pp. 46–52, 2015.
- [34] X. Jiang, Z. Ouyang, Z. Zhang et al., “Mechanism of glyphosate removal by biochar supported nano-zero-valent iron in aqueous solutions,” *Colloids and Surfaces A: Physicochemical and Engineering Aspects*, vol. 547, pp. 64–72, 2018.
- [35] S. S. Mayakaduwa, P. Kumarathilaka, I. Herath et al., “Equilibrium and kinetic mechanisms of woody biochar on aqueous glyphosate removal,” *Chemosphere*, vol. 144, pp. 2516–2521, 2016.
- [36] S. De Gisi, G. Lofrano, M. Grassi, and M. Notarnicola, “Characteristics and adsorption capacities of low-cost sorbents for wastewater treatment: a review,” *Sustainable Materials and Technologies*, vol. 9, pp. 10–40, 2016.

- [37] Z.-L. Chen, J.-Q. Zhang, L. Huang, Z.-H. Yuan, Z.-J. Li, and M.-C. Liu, "Removal of Cd and Pb with biochar made from dairy manure at low temperature," *Journal of Integrative Agriculture*, vol. 18, no. 1, pp. 201–210, 2019.
- [38] Q.-P. Zhang, Q.-C. Liu, B. Li et al., "Adsorption of Cd(II) from aqueous solutions by rape straw biochar derived from different modification processes," *Chemosphere*, vol. 175, pp. 332–340, 2017.
- [39] H. Pouretedal and N. Sadegh, "Effective removal of amoxicillin, cephalexin, tetracycline and penicillin G from aqueous solutions using activated carbon nanoparticles prepared from vine wood," *Journal of Water Process Engineering*, vol. 1, pp. 64–73, 2014.
- [40] P. K. Malik, "Dye removal from wastewater using activated carbon developed from sawdust: adsorption equilibrium and kinetics," *Journal of Hazardous Materials*, vol. 113, no. 1-3, pp. 81–88, 2004.
- [41] B. A. T. Mehrabadi, S. Eskandari, U. Khan, R. D. White, and J. R. Regalbuto, "A review of preparation methods for supported metal catalysts," *Advances in catalysis*, vol. 61, pp. 1–35, 2017.
- [42] P. Sharma, R. Kaur, C. Baskar, and W.-J. Chung, "Removal of methylene blue from aqueous waste using rice husk and rice husk ash," *Desalination*, vol. 259, no. 1-3, pp. 249–257, 2010.
- [43] K. Zhang, P. Sun, M. C. A. S. Faye, and Y. Zhang, "Characterization of biochar derived from rice husks and its potential in chlorobenzene degradation," *Carbon*, vol. 130, pp. 730–740, 2018.
- [44] M. Zhang, B. Gao, Y. Yao, Y. Xue, and M. Inyang, "Synthesis, characterization, and environmental implications of graphene-coated biochar," *Science of the Total Environment*, vol. 435-436, pp. 567–572, 2012.
- [45] G. E. Tranter and D. D. Le Pevelen, "Chiroptical spectroscopy and the validation of crystal structure stereochemical assignments," *Tetrahedron Asymmetry*, vol. 28, pp. 1192–1198, 2017.
- [46] A. B. Fuertes, M. C. Arbestain, M. Sevilla et al., "Chemical and structural properties of carbonaceous products obtained by pyrolysis and hydrothermal carbonisation of corn stover," *Soil Research*, vol. 48, no. 7, pp. 618–626, 2010.
- [47] E. Pusceddu, S. F. Santilli, G. Fioravanti, A. Montanaro, F. Miglietta, and P. U. Foscolo, "Chemical-physical analysis and exfoliation of biochar-carbon matter: from agriculture soil improver to starting material for advanced nanotechnologies," *Materials Research Express*, vol. 6, no. 11, p. 115612, 2019.
- [48] H. N. Nguyen, D. A. Khuong, T. T. H. Vu et al., "Kinetic and structural changes during gasification of cashew nut shell char particles," *Environmental Progress & Sustainable Energy*, vol. 40, no. 3, article e13580, 2021.
- [49] J. B. Condon, *Surface Area and Porosity Determinations by Physisorption: Measurement, Classical Theories and Quantum Theory*, Elsevier, 2006.
- [50] A. T. Q. Nguyen, T. A. Bui, N. T. Mai et al., "Release kinetics of potassium from silica-rich fern-derived biochars," *Agronomy Journal*, vol. 112, no. 3, pp. 1713–1725, 2020.
- [51] N. H. Nam, K. D. Anh, L. G. T. Truc, T. A. Ha, and V. T. T. Ha, "Pyrolysis of cashew nut shell: a parametric study," *Vietnam Journal of Chemistry*, vol. 58, pp. 506–511, 2020.
- [52] M. Abunowara, M. A. Bustam, S. Sufian, and U. Eldemerdash, "Description of carbon dioxide adsorption and desorption onto Malaysian coals under subcritical condition," *Procedia engineering*, vol. 148, pp. 600–608, 2016.
- [53] H. T. Phuong, M. A. Uddin, and Y. Kato, "Characterization of biochar from pyrolysis of rice husk and rice straw," *Journal of Biobased Materials and Bioenergy*, vol. 9, no. 4, pp. 439–446, 2015.
- [54] H. M. F. Freundlich, "Over the adsorption in solution," *The Journal of Physical Chemistry*, vol. 57, pp. 385–471, 1906.
- [55] I. Langmuir, "The constitution and fundamental properties of solids and liquids Part I. Solids," *Journal of the American chemical society*, vol. 38, no. 11, pp. 2221–2295, 1916.
- [56] S. S. Mayakaduwa, M. Vithanage, A. Karunaratna, D. Mohan, and Y. S. Ok, "Interface interactions between insecticide carbofuran and tea waste biochars produced at different pyrolysis temperatures," *Chemical Speciation & Bioavailability*, vol. 28, no. 1-4, pp. 110–118, 2016.
- [57] F. Rodríguez-reinoso, "The role of carbon materials in heterogeneous catalysis," *Carbon*, vol. 36, no. 3, pp. 159–175, 1998.
- [58] M. Belhachemi and F. Addoun, "Comparative adsorption isotherms and modeling of methylene blue onto activated carbons," *Applied Water Science*, vol. 1, no. 3-4, pp. 111–117, 2011.
- [59] Q.-S. Liu, T. Zheng, N. Li, P. Wang, and G. Abulikemu, "Modification of bamboo-based activated carbon using microwave radiation and its effects on the adsorption of methylene blue," *Applied Surface Science*, vol. 256, no. 10, pp. 3309–3315, 2010.
- [60] Ü. Geçgel, G. Özcan, and G. Ç. Gürpınar, "Removal of methylene blue from aqueous solution by activated carbon prepared from pea shells (*Pisum sativum*)," *Journal of Chemistry*, vol. 2012, Article ID 614083, 2010.
- [61] M. Auta and B. H. Hameed, "Modified mesoporous clay adsorbent for adsorption isotherm and kinetics of methylene blue," *Chemical Engineering Journal*, vol. 198-199, pp. 219–227, 2012.
- [62] X. Yao, L. Ji, J. Guo et al., "An abundant porous biochar material derived from wakame (*Undaria pinnatifida*) with high adsorption performance for three organic dyes," *Bioresource Technology*, vol. 318, p. 124082, 2020.

## Research Article

# Crosslinking, Mechanical Properties, and Antimicrobial Activity of Photocurable Diacrylate Urethane/ZnO-Ag Nanocomposite Coating

Truc Vy Do <sup>1,2</sup>, Minh Nguyet Ha <sup>1,2</sup>, Tuan Anh Nguyen <sup>1</sup>, Hoang Thu Ha <sup>3</sup>,  
and Thien Vuong Nguyen <sup>1,2</sup>

<sup>1</sup>Institute for Tropical Technology, VAST, 18 Hoang Quoc Viet, Cau Giay, Hanoi, Vietnam

<sup>2</sup>Graduate University of Science and Technology, VAST, 18 Hoang Quoc Viet, Cau Giay, Hanoi, Vietnam

<sup>3</sup>University of Education-Vietnam National University, 144 Xuan Thuy, Cau Giay, Hanoi, Vietnam

Correspondence should be addressed to Hoang Thu Ha; [hoangthuhavnuued@gmail.com](mailto:hoangthuhavnuued@gmail.com)  
and Thien Vuong Nguyen; [vuongvast@gmail.com](mailto:vuongvast@gmail.com)

Received 22 June 2021; Revised 4 August 2021; Accepted 26 October 2021; Published 9 November 2021

Academic Editor: George Kyzas

Copyright © 2021 Truc Vy Do et al. This is an open access article distributed under the Creative Commons Attribution License, which permits unrestricted use, distribution, and reproduction in any medium, provided the original work is properly cited.

In this article, ZnO-Ag nanohybrids were chemically synthesized in the aqueous medium by reducing silver nitrate with sodium borohydride NaBH<sub>4</sub>. These nanohybrids were then homogeneously dispersed into the diacrylate urethane/1,6-hexanediol diacrylate resin system at a content of 2 wt%. The structural morphology, mechanical resistances, and crosslinking of the as-prepared nanocomposite coating (nanocoating) were evaluated. The antimicrobial characteristic was tested by keeping track of the lag-log growth phase of *E. coli* bacteria in the coating existence among cell cultures. The obtained data indicated that the nanohybrids added into the UV curing diacrylate urethane matrices had significantly increased the abrasion resistance, relative hardness, and conversion of the acrylate groups of the nanocoating. In addition, the antibacterial test revealed that the nanocoating had good antibacterial property against *E. coli*, whereas for the pure coating (without ZnO-Ag nanoparticles), there was no antibacterial activity observed.

## 1. Introduction

UV curable acrylate resin-based paints exhibit many advantages, such as transparency, moisture resistance, chemical resistance, and being environmentally friendly, since they do not contain the organic solvents and can be processed at normal temperatures. Consequently, they have been widely applied to various finish surfaces, such as steel or wooden floors [1–4].

Nowadays, nanomaterials attract strong research and application interest. The addition of nanoscale additives to the polymer matrix significantly enhanced the properties of the material [5–12]. Enhancing the properties of coatings with antibacterial function has become a social demand; thus, there is an attempt to mix inorganic nanoparticles (like Ag, ZnO, and TiO<sub>2</sub>) as antibiotics into paint [13–19]. Among those, Ag nanoparticles showed the highest anti-

microbial effectiveness against most bacteria. In order to improve the antimicrobial activity of nano-Ag, Ag particles are often attached to nanosized transition metal oxides (such as Fe<sub>3</sub>O<sub>4</sub> and MnO<sub>2</sub> nanoparticles). In the previously published paper, we reported the antimicrobial activity of Fe<sub>3</sub>O<sub>4</sub>-Ag hybrid nanoparticles which was clearly more efficient than that of the single Ag nanoparticles [20–23]. The plausible explanation for this observation is that (1) Ag<sup>+</sup> ions were released faster from the hybrid nanoparticles and (2) the ionization of nano-Ag was accelerated by the presence of Fe<sup>3+</sup> ions. Moreover, the absorbed radiation range of the nanohybrids can shift to the UV and visible light region [20].

However, the addition of nanoparticles (as nanofillers) can affect the curing reaction of thermoset resin systems depending on the intrinsic composition of the nanoparticles. In case of the epoxy matrix, Fe<sub>3</sub>O<sub>4</sub> nanoparticles can act as a

bridging link molecule, leading to reduce the total free mass and increase the cross-linking density [24, 25]. Herein, to explore the healing dynamics of the epoxy/amine system, Fe<sub>3</sub>O<sub>4</sub> nanoparticles played a role as nanocontainers for carrying functional groups such as the carboxylic acid [26], amino [27, 28], or hydroxyl [27, 29]. The authors found that reaction between carboxylic acid and amine functional groups of curing agent could impact hardener activation [26]. In contrast, hydroxyl and amine groups could increase the amount of thermal curing by gaining access to the epoxy groups [27]. It was reported that nano-SiO<sub>2</sub> might cause an incomplete crosslinking stage of clearcoat based on acrylic-melamine resin, reducing the crosslinking density of the neat clearcoat, and enhancing the weathering durability of the clearcoats. One possible explanation is that nano-SiO<sub>2</sub> absorbed the UV light, thus protecting the clearcoat from the impact of weathering degradation [30]. In our previous works [31–33] when examining the curing reaction of acrylic polyols with isocyanate, we found that isocyanate groups are also involved in reaction with OH groups of nano-SiO<sub>2</sub> to form a tight inorganic-organic hybrid material. For UV curing systems, the degree of influence of additives depends not only on the content but also on their ability to absorb UV rays and photocatalytic activity. Fe<sub>3</sub>O<sub>4</sub>-Ag hybrid nanoparticles, despite a strong UV absorption, their low content (0.1 wt%) might not significantly affect the kinetics of curing reaction [23]. The organic UV absorber T384 reduced the efficiency of double bonds while nanoparticles absorb UV anatase TiO<sub>2</sub> and ZnO increased the conversion of the acrylate groups of the system due to strong photocatalytic activity [34].

In this work, ZnO-Ag nanohybrids were chemically synthesized in the aqueous medium by reducing silver nitrate with sodium borohydride NaBH<sub>4</sub>. Their structural morphology had been characterized. These nanohybrids were then homogeneously dispersed into the diacrylate urethane/1,6-hexanediol diacrylate resin system. The photocrosslinking polymerization process of the system of acrylate urethane resin and 1,6 hexanediol diacrylate diluent in the presence of ZnO-Ag nanohybrids had been investigated by using various measurements, such as the quantitative infrared spectra, coating hardness, and coating gel fraction. In addition, morphology, abrasion resistance, and antimicrobial activity of nanocomposite coating were also evaluated.

## 2. Experiments

**2.1. Chemicals.** NaBH<sub>4</sub>, AgNO<sub>3</sub>, and nano-ZnO were ordered from Sigma-Aldrich.

A photocurable resin system includes (i) Ebecryl 284 diacrylate urethane resin (abbrev. E284) ordered from a Radcure Specialties, (ii) 1,6-hexanediol diacrylate diluent (abbrev. HDDA, 80%, Sigma), and (iii) 1-hydroxy-cyclohexyl-phenyl-ketone photoinitiator, Irgacure 184 (I-184, CIBA). Figure 1 represents chemical structure of components of the photocurable resin system.

**2.2. Synthesis of ZnO-Ag Nanohybrids.** ZnO-Ag nanohybrids are chemically synthesized in the aqueous medium by reduc-

ing silver nitrate with sodium borohydride NaBH<sub>4</sub> [11]. Firstly, nano-ZnO (1.5 g) is added in 300 ml of distilled water, then dispersed homogeneously with aid of the ultrasonication 35 kHz for 60 min. Next, 30 ml of AgNO<sub>3</sub> solution (1.67 mg/ml) is dripped into the above-prepared dispersion of ZnO nanoparticles by further sonication for 40 min. The mixture is then placed into the 500 ml glass flask for the next synthesis step. To fabricate ZnO-Ag nanohybrids, NaBH<sub>4</sub> solution formed by dissolving 0.024 g of reductant into 50 ml water is then dripped (1 drop/s) to the reaction flask. The mixed solution is stirred (120 rpm for 60 min) at 4°C. The nanoparticles were obtained by repeatedly adding fresh distilled water and then centrifuging the solution at 10,000 rpm for 5 min for several times until the total removal of the residual precursors and agents.

**2.3. Preparation of Nanocomposite Coating.** ZnO-Ag nanohybrids at the 2 wt% content of HDDA and E284 are added into HDDA, then ultrasonicated during 3 hrs. Thereafter, this mixture is mixed with E284 and I.184 by mechanical stirring in the Ika RW16 Basic Mixer (England) for 30 min. The ratio of HDDA/E284/I.184 was 45/55/3.

The paint films are prepared on different surfaces with varied sizes depending on investigation purposes. In detail, for IR spectral analysis, paint layers with a 25 μm thickness are coated on KBr pellets. For gel fraction examination and morphology observation, the coatings were made on Teflon sheets with the size of 100 × 100 × 10. The coatings were deposited on glass plates (100 × 100 × 3 mm) for testing the abrasion resistance and relative hardness.

The coating samples are exposed to UV light (250 mW/cm<sup>2</sup>) using the FUSION UV system (F300S, USA) at 25°C in air by passing several times with a 5–40 m/s rate of web. The time of UV exposure can calculate from the web rate, for example, UV exposure time of 0.15 s corresponds to a web pass at 40 m/s.

### 2.4. Characterizations

**2.4.1. FTIR Spectrum Analysis.** A decrease of characteristic IR absorption bands of acrylate groups during the crosslinking reaction is quantitatively studied according to the method described in previous papers [23, 34] by using a FTIR spectroscopy Nicolet iS10 (USA).

**2.4.2. Gel Fraction Analysis.** The gel fraction (GEL) of coatings is analyzed according to ASTM D 2765. The cured samples are carried out in a Soxhlet tool in CH<sub>3</sub>COCH<sub>3</sub> for 24 h [23]. The GEL is determined by the following formula:

$$\text{The GEL(\%)} = \left( \frac{m_t}{m_0} \right) \times 100, \quad (1)$$

where  $m_t$  is the weight of insoluble part which was heated at 50°C until completely dry and  $m_0$  was the weight of initial coating (before analysis).

**2.4.3. Study on Hardness and Abrasion Resistance of Coatings.** The hardness of paint film is evaluated based on the NF T 30-016 standard by using a pendulum damping

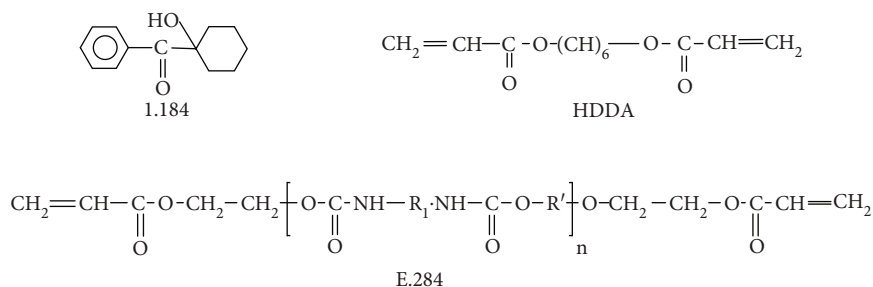


FIGURE 1: Chemical structure of the photocurable resin system.

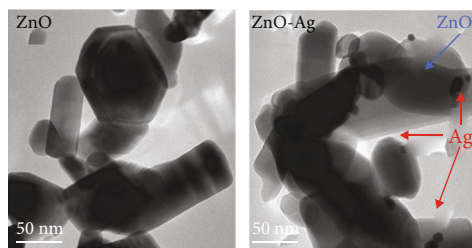


FIGURE 2: TEM images of pure ZnO nanoparticles (ZnO) and self-synthesis ZnO-Ag nanohybrids.

tester (model 300). The relative hardness (RH) is calculated by the formula as follows:

$$RH = \frac{\text{Absolute hardness of the film}}{425 \text{ (425 was absolute hardness of standard glass)}} \quad (2)$$

The abrasion resistance of the films is determined according to the abrasive falling methods (ASTM D968). Each sample was tested 3 times, and the illustrated results were the average values.

**2.4.4. Microstructural Examination.** The morphology of the self-synthesized ZnO-Ag nanohybrids has been analyzed by transmission electron microscopy (JEM 1010, JEOL Ltd., Tokyo, Japan). The crystallinity and crystalline phase of the fabricated nanoparticle structures were examined using an X-ray diffractometer (XRD, Philips X'Pert MPD) with  $\text{CuK}\alpha$  radiation (0.1540 nm) in the range of  $20^\circ$ – $60^\circ$ .

The morphology of the nanocomposite coating has been studied using Field Emission Scanning Electron Microscopy S 4800 (FE-SEM) (Hitachi, Japan).

**2.4.5. Antimicrobial Assay.** For antimicrobial assay, *E. coli* strain DH5 $\alpha$  is received from Invitrogen (USA); LB medium including yeast extract and Bacto tryptone are ordered from Merck (Germany). *E. coli* strain DH5 $\alpha$  is inoculated into 2 ml of LB medium and shacked overnight at 200 rpm while the temperature remained  $37^\circ\text{C}$ . Another cell suspension at 1% *v/v* cultured cell suspension: LB medium is prepared by inoculating the cells into 100 ml of fresh LB medium. The incubation underwent the same conditions as presented above. Once the value of optical density value ( $\lambda = 600 \text{ nm}$ ,  $\text{OD}_{600}$ ) was 0.3, the coatings are placed into incubation-

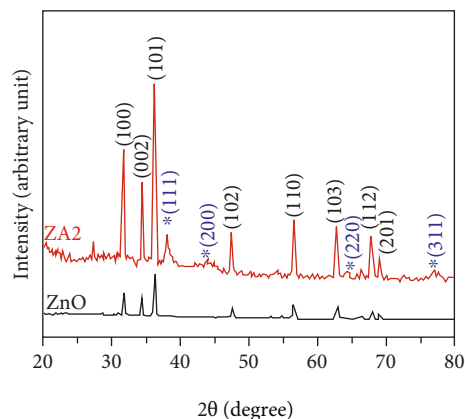


FIGURE 3: XRD diffraction diagrams of pure ZnO nanoparticles (ZnO) and ZnO-Ag nanohybrids (ZA2).

flagon and kept cultivating. The suspension of cultured cell suspension is then collected at various time scales (from 30 to 300 min) after adding either UVAU or UVAU/ZnO-Ag nanocoatings (with the same size of  $100 \times 100 \times 0.03 \text{ mm}$ ); then, their  $\text{OD}_{600}$  values were determined. All experiments were conducted in triplicate for determining the mean value [19, 23].

### 3. Results and Discussions

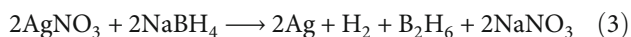
**3.1. Study on Characteristics of ZnO-Ag Nanohybrids.** The structural morphology of pure ZnO nanoparticles (ZnO) and ZnO-Ag nanohybrids is characterized by TEM and XRD analyses and shown in Figures 2 and 3.

Figure 2 shows that the used commercial ZnO nanoparticles were cylindrical in shape and have dimensions of about 30–70 nm in width and about 100–200 nm in length; Ag nanoparticles are spherical in shape with a size of about 10–30 nm attached to ZnO nanoparticles. Because these two types of particles are different in shape and size, it is easy to see the presence of both types of particles on TEM image.

The crystalline phase structure of the self-synthesized ZnO-Ag nanohybrids is analyzed by the X-ray diffraction method. XRD diffraction diagrams of ZnO-Ag nanohybrids and pure ZnO nanoparticles are presented in Figure 3.

From the obtained results, it can be seen that the XRD diagrams of both particles show characteristic diffraction peaks corresponding to the lattice faces (100), (002), (101), (102), (110), (103), (112), and (201) of ZnO nanoparticles

(JCPDS No. 36-1451). Apart from the spectral lines that characterize the hexagonal crystal structure of pure ZnO compounds, no other peaks or spectra of the impurity were observed. On the XRD diffraction pattern of ZnO-Ag hybrid nanoparticles, the characteristic diffraction peaks of ZnO remain the same, which shows that Ag ions are not substituted for ZnO in the crystal lattice of ZnO. In addition, on the XRD pattern of ZnO-Ag nanohybrid nanoparticles, diffraction peaks appear at angular positions corresponding to the lattice planes (111), (200), (220), and (311) in the face center cubic structure of Ag (JCPDS No. 04-0783). Thus, the method of using  $\text{NaBH}_4$  reducing agent to reduce  $\text{Ag}^+$  ions to Ag atoms is described by the following reaction equation:



### 3.2. Study on Crosslinking and Characteristics of Photocuring Acrylate Urethane/ZnO-Ag Nanocoating

**3.2.1. Conversion of the Acrylate Groups.** Using the IR spectral method to study the crosslinking of the curing resin system is one of the most simple and effective methods. It allows to assess both the rate of polymerization reaction and the conversion of the reacted functional groups [1, 23, 34]. In the current paper, the photocrosslinking polymerization reaction of the coating base on E.284 resin, HDDA diluent, and I.184 photoinitiator in the presence of 2 wt% ZnO-Ag nanohybrids is investigated by analyzing the changes of IR absorption density of acrylate double bonds. IR spectra of the photocurable diacrylate urethane/1,6-hexanediol diacrylate/1-hydroxy-cyclohexyl-phenyl-ketone systems without (UVAU) and with 2 wt% ZnO-Ag nanohybrids (UVAU/ZnO-Ag) before and after UV exposure of 4.8 s are presented in Figure 4.

Figure 4 shows that after 4.8 s exposed to UV, IR bands at 1632, 1409, 984, and 811  $\text{cm}^{-1}$  which are assigned to the double bonds of acrylate groups in E.284 and HDDA molecules decreased. Among those, the absorption band at 811  $\text{cm}^{-1}$  is chosen to study numerically the transformation of the acrylate groups throughout the crosslinking process of the coatings because of its most clearly decrease. The calculated data are presented in Figure 5.

As shown in Figure 5, the conversion of the acrylate groups occurs rapidly in the first 0.15 s and then slows down. The acrylate double bond conversion at the coating containing 2 wt% ZnO-Ag nanohybrids was higher than that at neat coating (without ZnO-Ag nanohybrids). After 4.8 s exposed to UV light, most of the acrylate double bonds were covered by 93.53 and 95.82% for neat and nanocomposite coatings, respectively. Thus, ZnO-Ag nanoparticles enhanced the transformation of acrylate double bonds.

**3.2.2. Variation of Gel Fraction.** To have further information of the photopolymerization reaction of the system in the presence of ZnO-Ag nanohybrids, the GEL of the coatings was determined. Figure 6 visualizes the obtained results.

Figure 6 indicates that, after 0.3 s of crosslinking, the GEL of the films without and with 2 wt% the nanohybrids appeared. The GEL increased rapidly in the first 2.4 s; after

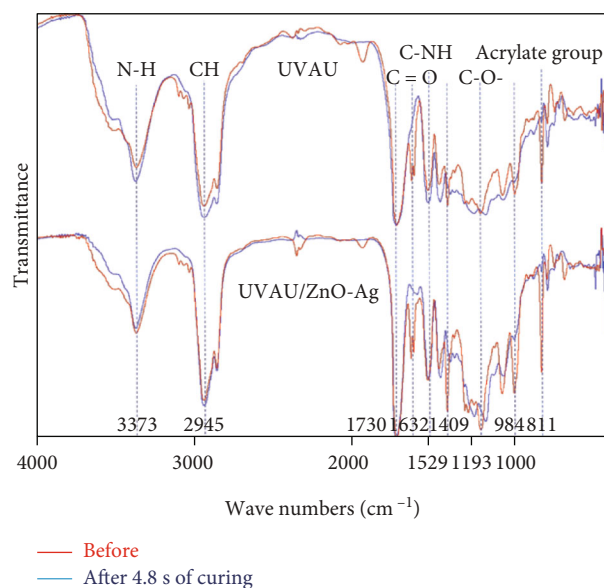


FIGURE 4: IR spectra of the UV-curable E.284/HDDA/I.184 systems without (UVAU) and with 2 wt% ZnO-Ag nanohybrids (UVAU/ZnO-Ag) before and after 4.8 s UV light irradiation.

then, it slowed down. In the presence of 2 wt% of the nanohybrids, the GEL of the film was increased in comparison with that of the neat film. After 4.8 s of the crosslinking, the GEL of the films got the highest value of approximately 95.3 (without the nanohybrids) and 96.7% (with 2 wt% ZnO-Ag nanohybrids). Thus, 2 wt ZnO-Ag nanohybrids increased the GEL of the films.

**3.2.3. Hardness Evaluation.** For the thermoset resin system, the hardness of the coating increased with the crosslinking density, and thus, it is possible to study the polymerization reaction by keeping track of the growth of the coatings' hardness. Figure 7 represents the relative hardness of coatings varied over time range of 0-4.8 s. It is clear that the hardness values rose rapidly in the first 1.2 s of the reaction before slowing down. The hardness of the coating containing 2 wt% ZnO-Ag nanohybrids was higher than that of the neat coating (without the nanohybrids). After 4.8 s of crosslinking reaction, the hardness of the coating and ZnO-Ag hybrid-reinforced coating reached the highest value of around 0.72 and 0.76, respectively. The incorporation of the nanoparticles in the coating matrix increased slightly the coating hardness.

It is well known that the outstanding characteristic of a photoinitiator is susceptible to UV light [2, 27]. When being exposed to UV light in FUSION UV equipment, the I 184 photoinitiator is destructed into free radicals which then attack the acrylate group, initiating the crosslinking polymerization. At first (in the first 0.15 s of UV exposure), the content of photoinitiators is high (about 3%) and the curing system is relatively flexible (low viscosity) so the reaction of the acrylate double bonds is inconsiderably impacted by UV absorbers of ZnO-Ag nanohybrids. However, concentration of the photoinitiators and the acrylate groups reduce rapidly by time, and thus, the conversion of the acrylate groups

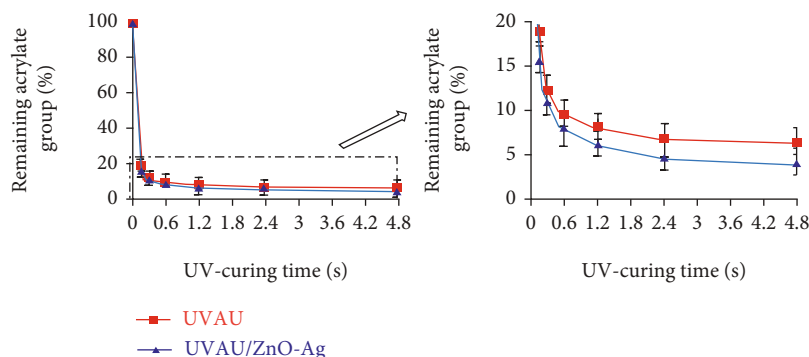


FIGURE 5: Conversion of the acrylate groups under the UV light irradiation.

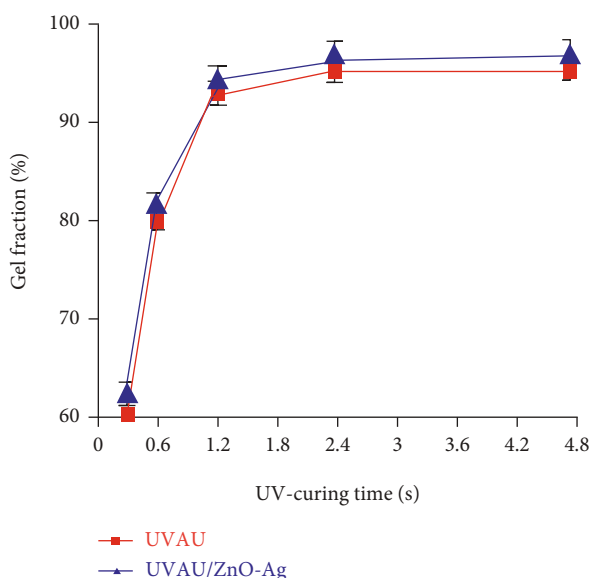


FIGURE 6: Variations of GEL of the photocurable acrylate urethane coating without (UVAU) and with 2 wt% ZnO-Ag nanohybrids (UVAU/ZnO-Ag).

slowed down. In the presence of 2 wt% ZnO-Ag nanohybrids, the conversion of the acrylate groups is affected by photocatalytic characteristic of nano ZnO-Ag hybrid structure. This effect is similar to the case of photocatalyst nanoparticles (A-TiO<sub>2</sub>, ZnO) [34–37]. The difference is that due to the hybridization with Ag, the photocatalytic activity of ZnO is reinforced. When absorbing UV energy, an electron jumps from the valence band to the conduction band, resulting in the formation of an electron-hole pair. These electron and positive hole pairs reacted with hydroxyl functional groups, water and oxygen molecules attached to the nanoparticles' surface, generating free radicals (·OH) [38–40] which could also initiate the crosslinking polymerization reaction of acrylate double bonds, leading to the increase of its conversion as well as the increase in the GEL and relative hardness of the film.

3.2.4. Study on Abrasion Resistance of the Paint Film. Abrasion resistance of the films without (UVAU) and with 2 wt% ZnO-Ag nanohybrids (UVAU/ZnO-Ag) after 4.8 s of crosslinking is presented in Figure 8.

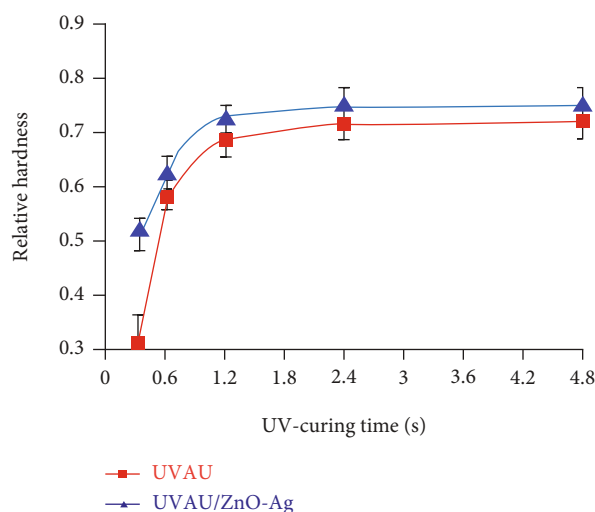


FIGURE 7: Variation of hardness of the films without (UVAU) and with 2 wt% ZnO-Ag nanohybrids (UVAU/ZnO-Ag).

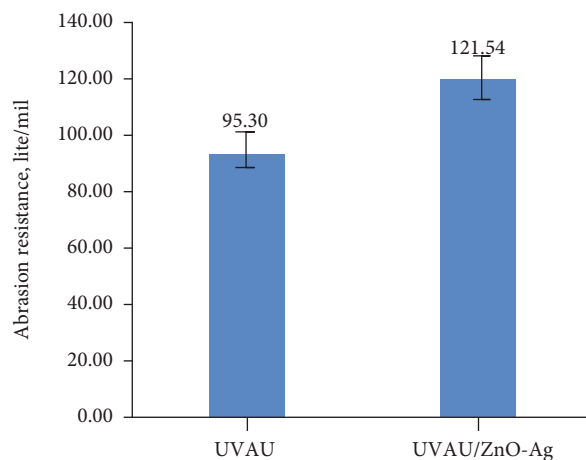


FIGURE 8: Abrasion resistance of the coating without (UVAU) and with 2 wt% ZnO-Ag nanohybrids (UVAU/ZnO-Ag) after 4.8 s of curing.

Figure 8 demonstrates that the incorporation of 2 wt% ZnO-Ag hybrid nanoparticles into polymer network helped gain the abrasion resistance of the paint film from 95.30 to 121.54/lite/mil. To explain the enhancement of abrasion

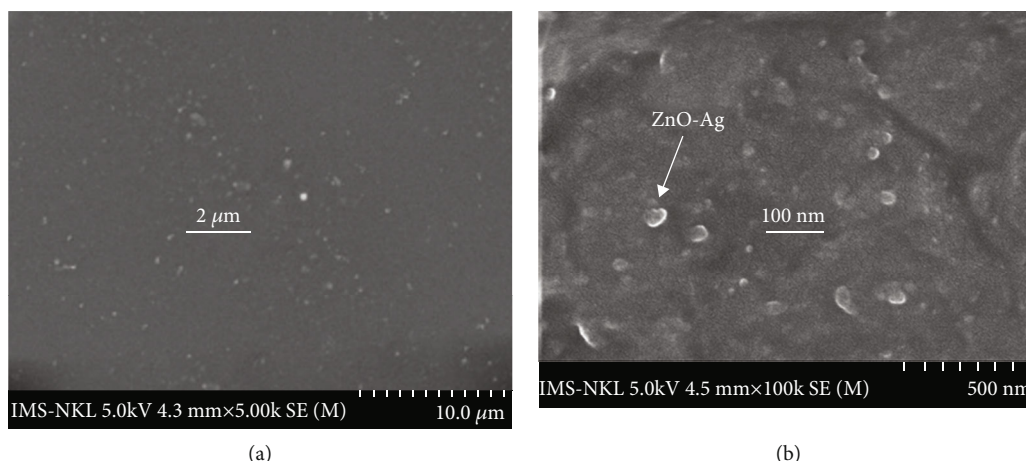


FIGURE 9: FE-SEM image of the photocurable acrylate urethane/ZnO-Ag nanocoating in surface (a) and in cross-section (b).

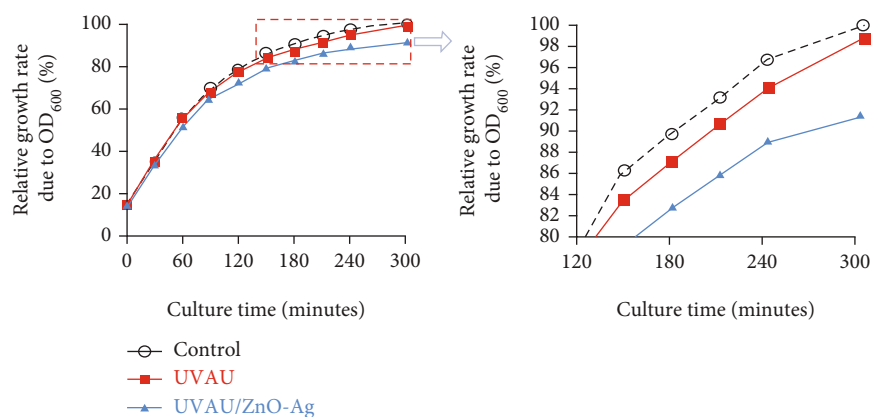


FIGURE 10: The growth rate of *E. coli* bacteria in liquid culture without (control) or with the presence of the coating films not containing (UVAU) or containing 2 wt% ZnO-Ag nanohybrids (UVAU/ZnO-Ag).

resistance of the photocurable acrylate urethane/ZnO-Ag nanocoating, its FE-SEM images are analyzed and indicated in Figure 9.

As can be seen from Figure 9, the coating possessed tight structures with no defects or cracks. Additionally, the nanohybrids are well-dispersed into the coating with a size of about 40-250 nm. The abrasion resistance of the nanocoating is enhanced by tough ZnO-Ag nanohybrids which had high hardness. This is also the reason for the increase in the relative hardness of the nanocoating in Figure 7.

**3.3. Antimicrobial Activity of the Nanocoating.** The growth rate of *E. coli* bacteria in liquid culture without (control) or with the presence of the coating films not containing (UVAU) or containing ZnO-Ag nanohybrids (UVAU/ZnO-Ag) during 300 min (5 h) is presented in Figure 10.

As shown in Figure 10, after 5 h of test, the growth rate of *E. coli* bacteria was only ~91% in the culture with added UVAU/ZnO-Ag coating (containing 2 wt% ZnO-Ag nanohybrids), whereas it was 98.5% in the culture with the presence of UVAU films (not containing 2 wt% ZnO-Ag nanohybrids). These results have proved that the UVAU/ZnO-Ag nanocomposite film has obviously stronger antibiotic effect against *E.*

*coli* bacteria than that of the UVAU/ZnO-Ag nanocomposite film [19].

## 4. Conclusion

ZnO-Ag nanohybrids were chemically synthesized in the aqueous medium by reducing silver nitrate with sodium borohydride  $\text{NaBH}_4$ . Their structural morphology had been characterized by FE-SEM, TEM, and XRD. These nanohybrids (2 wt%) were then homogeneously dispersed into the diacrylate urethane/1,6-hexanediol diacrylate resin system. Photopolymerization, morphology and mechanical properties, and antimicrobial activity of UV curing acrylate urethane coating in the presence of 2 wt% ZnO-Ag nanohybrids were investigated. The analysis results show that ZnO-Ag nanohybrids are dispersed well in polymer matrix, with a size of about 40-250 nm. The nanohybrids enhance significantly both the conversion of acrylate groups, gel fraction, relative hardness, abrasion resistance, and antimicrobial activity of the coating. After 4.8 s crosslinking reaction, the conversion of acrylate groups, gel fraction, abrasion resistance, and hardness of the paint film increases from 93.53 to 95.82%, from 95.3 to 96.7%, from 0.72 to 0.76,

and from 95.28 to 121.54 l/mil, respectively. After 5 h of the antimicrobial test, the growth rate of *E. coli* bacteria is only ~91% in the culture with the presence of the paint films containing 2 wt% ZnO-Ag nanohybrids, while it is 98.5% in the culture with the presence of the films not containing the nanohybrids.

## Data Availability

All the data and supporting materials are included within the article.

## Conflicts of Interest

The authors declare no conflicts of interest.

## Acknowledgments

The authors would like to thank the financial support of the Vietnam National Foundation for Science and Technology Development (NAFOSTED, Grant # 104.02-2018.19).

## References

- [1] M. D. Brito, X. Allonas, C. Croutxé-Barghorn, M. Palmieri, and I. Alig, "Kinetic study of photoinduced quasi-simultaneous interpenetrating polymer networks," *Progress in Organic Coatings*, vol. 73, no. 2–3, pp. 186–193, 2012.
- [2] T. P. Nguyen-Tri and T. V. Nguyen, "Radically curable nano-based coatings (chapter 10)," in *Nanomaterials Based Coatings*, T. P. Nguyen, S. Rtimi, and C. Ouellet-Plamondon, Eds., pp. 339–372, Elsevier, 2019.
- [3] T. V. Nguyen, X. H. Le, P. H. Dao, C. Decker, and T. P. Nguyen, "Stability of acrylic polyurethane coatings under accelerated aging tests and natural outdoor exposure: the critical role of the used photo-stabilizers," *Progress in Organic Coatings*, vol. 124, pp. 137–146, 2018.
- [4] X. H. Le, T. V. Nguyen, M. T. Le, and T. V. T. Nguyen, "Study of photocrosslinking reaction of the resin system on the base of copolymer of tung and soybean oils, methyl methacrylate, styrene," *Vietnam Journal of Science Technology*, vol. 48, no. 3A, pp. 150–157, 2010.
- [5] C. M. Vu, L. T. Nguyen, T. V. Nguyen, and H. J. Choi, "Effect of additive-added epoxy on mechanical and dielectric characteristics of glass fiber reinforced epoxy composites," *Polymer Korea*, vol. 38, no. 6, pp. 726–734, 2014.
- [6] Q. V. Bach, C. M. Vu, H. T. Vu, T. Hoang, T. V. Dieu, and D. D. Nguyen, "Epoxidized soybean oil grafted with CTBN as a novel toughener for improving the fracture toughness and mechanical properties of epoxy resin," *Polymer Journal*, vol. 52, pp. 345–357, 2020.
- [7] C. M. Vu, V. H. Nguyen, and Q. V. Bach, "Phosphorous-jointed epoxidized soybean oil and rice husk-based silica as the novel additives for improvement mechanical and flame retardant of epoxy resin," *Journal of Fire Sciences*, vol. 38, no. 1, pp. 3–27, 2020.
- [8] Q. V. Bach, C. M. Vu, H. T. Vu, and D. D. Nguyen, "Enhancing mode I and II interlaminar fracture toughness of carbon fiber-filled epoxy-based composites using both rice husk silica and silk fibroin electrospun nanofibers," *High Performance Polymers*, vol. 31, no. 9–10, pp. 1195–1203, 2019.
- [9] D. D. Nguyen, C. M. Vu, and H. J. Choi, "Improvement of the mode I interlaminar fracture toughness of glass fiber/epoxy composites using polystyrene electrospun nanofibers," *Polymer Bulletin*, vol. 75, pp. 5089–5102, 2018.
- [10] C. M. Vu, Q. V. Bach, H. T. Vu, D. D. Nguyen, B. X. Kien, and S. W. Chang, "Carbon-fiber-reinforced epoxy resin with sustainable additives from silk and rice husks for improved mode-I and mode-II interlaminar fracture toughness," *Macromolecular Research*, vol. 28, no. 1, pp. 33–41, 2020.
- [11] C. M. Vu and H. J. Choi, "Fracture toughness and surface morphology of micro/nano sized fibrils-modified epoxy resin," *Polymer Science Series A*, vol. 58, no. 3, pp. 464–470, 2016.
- [12] C. M. Vu and Q. V. Bach, "Effects of DOPO-grafted epoxidized soybean oil on fracture toughness and flame retardant of epoxy resin/rice husk silica hybrid," *Macromolecular Research*, vol. 28, no. 9, pp. 826–834, 2020.
- [13] T. V. Nguyen, T. A. Nguyen, P. H. Dao et al., "Effect of rutile titania dioxide nanoparticles on the mechanical property, thermal stability, weathering resistance and antibacterial property of styrene acrylic polyurethane coating," *Advances in Natural Sciences: Nanoscience and Nanotechnology*, vol. 7, no. 4, 2016.
- [14] A. M. El Saeed, M. A. El-Fattah, and A. M. Azzam, "Synthesis of ZnO nanoparticles and studying its influence on the antimicrobial, anticorrosion and mechanical behavior of polyurethane composite for surface coating," *Dyes and Pigments*, vol. 121, pp. 282–289, 2015.
- [15] H. Barani, "Preparation of antibacterial coating based on in situ synthesis of ZnO/SiO<sub>2</sub> hybrid nanocomposite on cotton fabric," *Applied Surface Science*, vol. 320, pp. 429–434, 2014.
- [16] P. Dallas, V. K. Sharma, and R. Zboril, "Silver polymeric nanocomposites as advanced antimicrobial agents: classification, synthetic paths, applications, and perspectives," *Advances in Colloid and Interface Science*, vol. 166, no. 1–2, pp. 119–135, 2011.
- [17] M. Akbarian, M. E. Olya, M. Ataefard, and M. Mahdavian, "The influence of nanosilver on thermal and antibacterial properties of a 2 K waterborne polyurethane coating," *Progress in Organic Coatings*, vol. 75, no. 4, pp. 344–348, 2012.
- [18] R. D. Toker, N. Kayaman-Apohan, and M. V. Kahraman, "UV-curable nano-silver containing polyurethane based organic-inorganic hybrid coatings," *Progress in Organic Coatings*, vol. 76, no. 9, pp. 1243–1250, 2013.
- [19] T. T. Le, T. V. Nguyen, T. A. Nguyen et al., "Thermal, mechanical and antibacterial properties of water-based acrylic polymer/SiO<sub>2</sub>-Ag nanocomposite coating," *Journal of Materials Chemistry and Physics*, vol. 232, pp. 362–366, 2019.
- [20] T. P. Nguyen, T. A. Nguyen, T. H. Nguyen, and P. Carriere, "Antibacterial behavior of hybrid nanoparticles (Chapter 7)," in *Noble Metal-Metal Oxide Hybrid Nanoparticles: Fundamentals and Applications*, S. Mohapatra, T. A. Nguyen, and T. P. Nguyen, Eds., pp. 141–155, Woodhead Publishing, 2019.
- [21] T. D. Ngo, T. M. H. Le, T. H. Nguyen et al., "Antibacterial nanocomposites based on Fe<sub>3</sub>O<sub>4</sub>-Ag hybrid nanoparticles and natural rubber-polyethylene blends," *International Journal of Polymer Science*, vol. 2016, Article ID 7478161, 9 pages, 2016.
- [22] T. N. L. Nguyen, T. V. Do, T. V. Nguyen et al., "Antimicrobial activity of acrylic polyurethane/Fe<sub>3</sub>O<sub>4</sub>-Ag nanocomposite coating," *Progress in Organic Coatings*, vol. 132, pp. 15–20, 2019.
- [23] T. V. Nguyen, T. V. Do, M. H. Ha et al., "Crosslinking process, mechanical and antibacterial properties of UV-curable acrylate/Fe<sub>3</sub>O<sub>4</sub>-Ag nanocomposite coating," *Journal of Progress in organic coating*, vol. 139, p. 105325, 2020.

- [24] N. Huong, "Improvement of bearing strength of laminated composites by nanoclay and Z-pin reinforcement," *PhD. Dissertation*, University of New South Wales, Australia, 2006.
- [25] O. Becker, R. Varley, and G. Simon, "Morphology, thermal relaxations and mechanical properties of layered silicate nanocomposites based upon high-functionality epoxy resins," *Polymer*, vol. 43, no. 16, pp. 4365–4373, 2002.
- [26] M. Jouyandeh, M. Shabaniyan, M. Khaleghi et al., "Acid-aided epoxy-amine curing reaction as reflected in epoxy/Fe<sub>3</sub>O<sub>4</sub> nanocomposites: chemistry, mechanism, and fracture behavior," *Progress in Organic Coatings*, vol. 125, pp. 384–392, 2018.
- [27] M. Jouyandeh, S. M. R. Paran, M. Shabaniyan et al., "Curing behavior of epoxy/Fe<sub>3</sub>O<sub>4</sub> nanocomposites: a comparison between the effects of bare Fe<sub>3</sub>O<sub>4</sub>, Fe<sub>3</sub>O<sub>4</sub>/SiO<sub>2</sub>/chitosan and Fe<sub>3</sub>O<sub>4</sub>/SiO<sub>2</sub>/chitosan/imide/phenylalanine-modified nanofillers," *Progress in Organic Coatings*, vol. 123, pp. 10–19, 2018.
- [28] M. R. Saeb, M. Nonahal, H. Rastin et al., "Calorimetric analysis and molecular dynamics simulation of cure kinetics of epoxy/chitosan-modified Fe<sub>3</sub>O<sub>4</sub> nanocomposites," *Progress in Organic Coatings*, vol. 112, pp. 176–186, 2017.
- [29] M. R. Saeb, H. Rastin, M. Shabaniyan, M. Ghaffari, and G. Bahlakeh, "Cure kinetics of epoxy/β-cyclodextrin-functionalized Fe<sub>3</sub>O<sub>4</sub> nanocomposites: Experimental analysis, mathematical modeling, and molecular dynamics simulation," *Progress in Organic Coatings*, vol. 110, pp. 172–181, 2017.
- [30] H. Yari, S. Moradian, and N. Tahmasebi, "The weathering performance of acrylic melamine automotive clearcoats containing hydrophobic nanosilica," *Journal Coating Technology and Research*, vol. 11, no. 3, pp. 351–360, 2014.
- [31] T. M. A. Bui, T. V. Nguyen, T. M. Nguyen et al., "Investigation of crosslinking, mechanical properties and weathering stability of acrylic polyurethane coating reinforced by SiO<sub>2</sub> nanoparticles issued from rice husk ash," *Journal of Materials Chemistry and Physics*, vol. 241, p. 122445, 2020.
- [32] P. H. Dao, T. V. Nguyen, M. H. Dang et al., "Effect of silica nanoparticles on properties of coatings based on acrylic emulsion resin," *Vietnam Journal of Science and Technology*, vol. 56, no. 3B, pp. 117–125, 2018.
- [33] T. V. Nguyen, T. A. Nguyen, and T. H. Nguyen, "The synergistic effects of SiO<sub>2</sub> nanoparticles and organic photostabilizers for enhanced weathering resistance of acrylic polyurethane coating," *Journal of Composites Science*, vol. 4, no. 1, p. 23, 2020.
- [34] T. V. Nguyen, T. P. Nguyen, S. Azizi et al., "The role of organic and inorganic UV-absorbents on photopolymerization and mechanical properties of acrylate-urethane coating," *Journal of Materials Today Communications*, vol. 22, p. 100780, 2020.
- [35] T. V. Nguyen, P. H. Dao, T. A. Nguyen et al., "Photocatalytic degradation and heat reflectance recovery of water-borne acrylic polymer/ZnO nanocomposite coating," *Journal of Applied Polymer Science*, vol. 137, no. 37, p. 49116, 2020.
- [36] P. H. Dao, T. V. Nguyen, T. A. Nguyen et al., "Acrylic polymer/TiO<sub>2</sub> nanocomposite coatings: mechanism for photo-degradation and solar heat reflective recovery," *Journal of Materials Chemistry and Physics*, vol. 272, p. 124984, 2021.
- [37] T. V. Vu, T. V. Nguyen, M. Tabish et al., "Water-borne ZnO/acrylic nanocoating: fabrication, characterization, and properties," *Polymers*, vol. 13, no. 5, p. 717, 2021.
- [38] T. V. Nguyen, T. P. Nguyen, T. D. Nguyen, R. Aidani, V. T. Trinh, and C. Decker, "Accelerated degradation of water borne acrylic nanocomposites used outdoor protective coatings," *Polymer Degradation and Stability*, vol. 128, pp. 65–76, 2016.
- [39] T. V. Nguyen, P. H. Dao, K. L. Duong et al., "Effect of R-TiO<sub>2</sub> and ZnO nanoparticles on the UV-shielding efficiency of water-borne acrylic coating," *Progress in Organic Coatings*, vol. 110, pp. 114–121, 2017.
- [40] T. A. T. Pham, V. A. Tran, V. D. Le et al., "Facile preparation of ZnO nanoparticles and Ag/ZnO nanocomposite and their photocatalytic activities under visible light," *International Journal of Photoenergy*, vol. 2020, Article ID 8897667, 2020.

## Research Article

# Improving SERS Sensing Efficiency and Catalytic Reduction Activity in Multifunctional Ternary Ag-TiO<sub>2</sub>-GO Nanostructures: Roles of Electron Transfer Process on Performance Enhancement

Mai Quan Doan <sup>1</sup>, Nguyen Ha Anh <sup>1</sup>, Hoang Van Tuan <sup>1</sup>, Nguyen Cong Tu <sup>2</sup>,  
Nguyen Huu Lam <sup>2</sup>, Nguyen Tien Khi <sup>1,3</sup>, Vu Ngoc Phan <sup>1,3</sup>, Pham Duc Thang<sup>1,4</sup>  
and Anh-Tuan Le <sup>1,4</sup>

<sup>1</sup>Phenikaa University Nano Institute (PHENA), Phenikaa University, Hanoi 12116, Vietnam

<sup>2</sup>School of Engineering Physics (SEP), Hanoi University of Science and Technology, Hanoi 10000, Vietnam

<sup>3</sup>Faculty of Biotechnology, Chemistry and Environmental Engineering, Phenikaa University, Hanoi 12116, Vietnam

<sup>4</sup>Faculty of Materials Science and Engineering, Phenikaa University, Hanoi 12116, Vietnam

Correspondence should be addressed to Mai Quan Doan; [doan.maiquan@phenikaa-uni.edu.vn](mailto:doan.maiquan@phenikaa-uni.edu.vn)  
and Anh-Tuan Le; [tuan.leanh@phenikaa-uni.edu.vn](mailto:tuan.leanh@phenikaa-uni.edu.vn)

Received 10 August 2021; Revised 7 September 2021; Accepted 9 September 2021; Published 1 October 2021

Academic Editor: Ngo Nghia Pham

Copyright © 2021 Mai Quan Doan et al. This is an open access article distributed under the Creative Commons Attribution License, which permits unrestricted use, distribution, and reproduction in any medium, provided the original work is properly cited.

Multifunctional nanocomposites have received great attention for years; electron transfer (ET) is considered as an explanatory mechanism for enhancement of performance of these nanostructures. The existence of this ET process has been proved in many studies using either experimental or computational approaches. In this study, a ternary nanocomposite system of Ag/TiO<sub>2</sub>/GO was prepared to evaluate the performance enhancement in two experimental models: a physical model (i.e., surface-enhanced Raman scattering (SERS) sensor) and a chemical one (i.e., catalytic reduction reaction). The metal/semiconductor heterojunction between Ag and TiO<sub>2</sub>, as well as Ti-O-C bonds, has allowed plasmonic hot electrons to be transferred in the internal structure of the material. An investigation on the role of Ag content on the SERS sensing and catalytic reduction efficiency of Ag/TiO<sub>2</sub>/GO was performed in both models. Interestingly, they all resulted in the same optimal Ag content of 50 wt%. It was then further discussed to provide a convincing evidence for the plasmon-induced electron transfer phenomena in the Ag/TiO<sub>2</sub>/GO nanostructure. These findings also suggest a pathway to design and develop high-performance, cost-effective, facile-preparation, and eco-friendly multifunctional nanostructures for detecting and removing contaminants in environment.

## 1. Introduction

It is now widely accepted that electron-transfer (ET) mechanism in metal-semiconductor (MS) nanocomposites/nano-hybrids must be involved to explain the enhancement of their contaminant detection/degradation performance, in comparison to single metals or semiconductors [1–5]. ET naturally occurs in connection with the transduction of energy. In MS materials, ET process takes place in a dual-mode pathway. It means electrons can be transferred from metals to semiconductors or from semiconductors to metals,

which depends directly on the wavelengths of excitation sources [2–4, 6]. When a metal nanostructure contacts with a semiconductor, a specific space-charge region is created in MS interface, which leads to the band bending in the semiconductor and gives rise to a Schottky transition [2, 6]. Due to the light-matter interaction between ultraviolet (UV) light and the semiconductor, electrons are excited and then, they can be injected into the metal via the Schottky transition, causing the increase of the electron lifetime [6]. Meanwhile, localized surface plasmon resonance (LSPR) of the metal plays a central role in the generation of hot electrons when

interacting with a visible or infrared light, followed by injection of the hot electrons into the semiconductor [1, 3, 5]. As a result, a large number of active electrons were created, leading to the improvements in the efficiency of various applications such as sensing devices [4], photocatalysis [2], solar cells [3], photovoltaics [1], and photothermal therapies [5].

For several decades, many reports on ET process in MS structures, including both experimental and computational ones, have been published to clarify the importance of ET in the enhancement mechanisms of various technological applications [7–10]. For instance, Furube et al. utilized femtosecond transient absorption spectroscopy on Au/TiO<sub>2</sub> to observe plasmon-induced ET from Au nanodots to TiO<sub>2</sub> nanoparticles (NPs) [8]. Iida et al. proposed a directly transferred pathway of electrons from Ag nanoclusters to TiO<sub>2</sub> layers without passing through the conduction band of the Ag nanoclusters, using a computational approach [9]. Filipin et al. reported on another approach, in which they employed surface-enhanced Raman scattering (SERS) platform as an experimental model to investigate the enhanced Raman signals of R6G using TiO<sub>2</sub> nanotubes decorated with Ag NPs, resulting in  $9 \times 10^7$  of Raman enhancement factor (EF) [7]. Yazid et al. investigated the enhanced catalytic reduction of 4-nitrophenol (4-NP) using AuNPs immobilized on the TiO<sub>2</sub> support; Au/TiO<sub>2</sub> exhibited superior catalytic activity in reduction of 4-NP, compared to AuNPs only [10]. Those reports have clarified the ET process in MS interfaces. However, each of those reports only focused on one kind of material for one specific application while ET process in MS materials may have led to the enhancement of the performance of various applications. Therefore, using different experimental models to investigate the enhancement of the performance efficiency of different applications with one material structure may answer the question if ET process in MS structures would exhibit the same effects on those distinct applications. Furthermore, it would provide more convincing evidence for the ET process in internal MS structures.

However, one of the main drawbacks of MS structures is their low adsorption capacity due to the poor adsorption capacity of their components (i.e., metals and semiconductors) [11]. Unfortunately, many popular applications including SERS sensors [12], photodegradation [13], and catalytic reaction [14] require an intimate interaction between the target molecules and the surface of the MS structures. Because of the poor adsorption capacity, only few target molecules can be adsorbed on MS surfaces to interact with active electrons, leading to the low performance of the applications using MS materials [12, 13]. Therefore, it is necessary to improve the adsorption capacity of MS materials to enhance their performance in those applications.

In the effort to find out an effective solution to improve the adsorption capacity of the MS structures, the introduction of graphene oxide (GO) to the nanocomposite structures has been regarded as a promising approach [15, 16]. GO is a two-dimensional carbon-based nanostructure which exhibits excellent adsorption capacity due to the presence of abundant oxygen functional groups such as hydroxyl, epoxy,

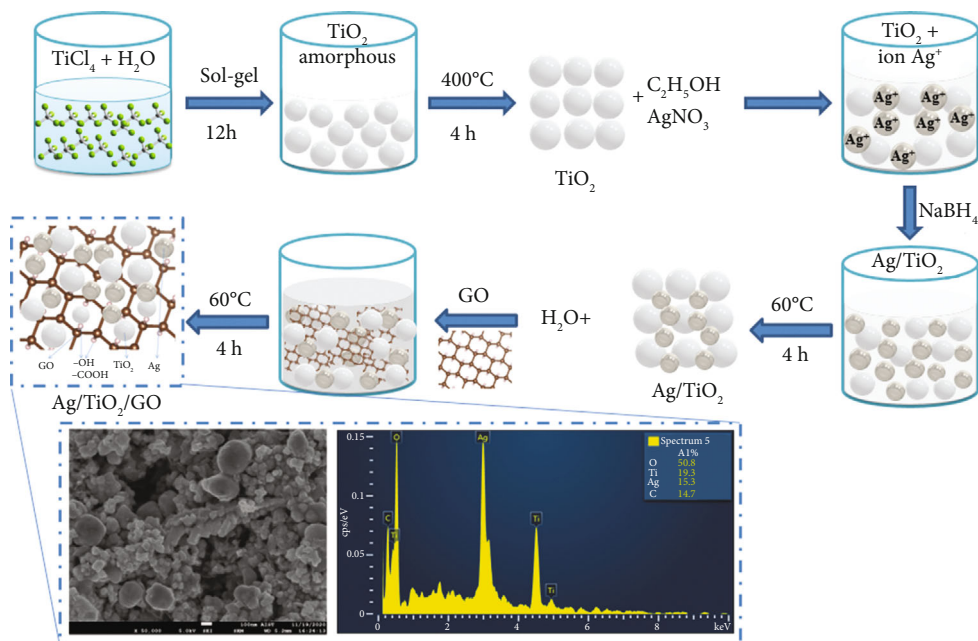
and carboxyl groups on its surface [16]. Wang et al. claimed that the photodegradation activity of TiO<sub>2</sub>/GO composites was remarkably superior to that of TiO<sub>2</sub> due to the strong absorption capacity of GO [17]. In addition, GO can serve as an electron transporter. Gillespie et al. employed hybrid density functional theory calculations to propose that reduced-GO (rGO) in TiO<sub>2</sub>/rGO had acted as a photoelectron trap (electron acceptor) via Ti-O-C bonds, leading to extended lifetimes of photoexcited charge carriers in TiO<sub>2</sub>/rGO composites and improved photocatalytic efficiency [18]. Electrons should have continued to be transferred from TiO<sub>2</sub> to the GO sheets, leading to a stronger enhancement in the performance of TiO<sub>2</sub>/rGO nanocomposites, in comparison to bare TiO<sub>2</sub> NPs. This study suggested an idea to fabricate other MS/GO nanocomposites, in which electrons can be transferred from metals to semiconductors and then GO sheets and improve the overall performance of their applications.

In this work, we prepared a set of Ag/TiO<sub>2</sub>/GO nanocomposites (as MS/GO nanocomposites) to investigate their ET process. However, instead of focusing on specific measurements, such as femtosecond transient absorption spectroscopy [8], we stressed on the enhancement of the performance of the MS/GO structures and the repeat of this phenomenon in different experimental models. Thus, we aimed to discuss in detail about the correlation between the ET process and the performance of these empirical models. In more detail, we employed two experimental models including a physical model (i.e., SERS sensor) and a chemical model (i.e., catalytic reduction). Using a set of MS nanostructures that differed in Ag ratios, we further clarified the effects of Ag content in the composite structure on the performance of Ag/TiO<sub>2</sub>/GO in each model. Moreover, the roles of TiO<sub>2</sub>, GO in the performance enhancement were also discussed. The similar optimal Ag content in two models provided a convincing evidence for the ET process in multifunctional Ag/TiO<sub>2</sub>/GO nanostructures.

## 2. Experimental Procedures

**2.1. Materials.** Silver nitrate (AgNO<sub>3</sub>, ≥99.0 wt%), sodium borohydride (NaBH<sub>4</sub>, 99 wt%), titanium tetrachloride (TiCl<sub>4</sub>, ≥99.8 wt%), ammonium hydroxide (NH<sub>4</sub>OH, 28.0–30.0% NH<sub>3</sub>), ethanol (C<sub>2</sub>H<sub>5</sub>OH, 98 v/v%), methylene blue (MB, C<sub>16</sub>H<sub>18</sub>ClN<sub>3</sub>S), and 4-nitrophenol (4-NP, C<sub>6</sub>H<sub>5</sub>NO<sub>2</sub>) were purchased from Shanghai Chemical Reagent and used directly without further purification. Graphene oxide (GO) was prepared using a modified Hummers method. Double distilled water was used throughout the experiments.

**2.2. Synthesis of Ag/TiO<sub>2</sub>/GO Nanocomposites.** Ag/TiO<sub>2</sub>/GO nanocomposites (ATG Nces) were synthesized through a facile wet chemistry approach as described in Scheme 1. First, pure TiO<sub>2</sub> NPs were fabricated via a modified sol-gel method based on TiCl<sub>4</sub> precursors [19]. Gel solution was obtained by aging for 12 h at room temperature, followed by the annealing process at 400°C for 4 h, which induced the crystallization of TiO<sub>2</sub> NPs. The crystalline TiO<sub>2</sub> (0.2 g)



SCHEME 1: Schematic illustration of the synthesis steps for Ag/TiO<sub>2</sub>/GO ternary nanocomposite.

was added into 50 ml of C<sub>2</sub>H<sub>5</sub>OH. Subsequently, to arrive at different Ag contents in the nanocomposites, 10 ml of AgNO<sub>3</sub> solution at different concentrations (62 mM, 91 mM, 185 mM, and 555 mM) was added to the solutions. The mixture was subjected to vigorous stirring at room temperature for 1 h, allowing the adsorption of Ag<sup>+</sup> ions onto the TiO<sub>2</sub> NP's surface. A required 10 ml volume of NaBH<sub>4</sub> (62 mM, 91 mM, 185 mM, and 555 mM) was added to reduce ions Ag<sup>+</sup> to Ag<sup>0</sup> metals in each solution. After 2 hours of reduction, the as-synthesized Ag/TiO<sub>2</sub> NPs were purified by three washing cycles (1000 rpm) using deionized water and were dried at 60°C for 4 h. Then, GO nanosheets were synthesized using the modified Hummers' method reported by Paulchamy in 2015 [20]. A simple self-assembly approach was employed to decorate GO nanosheets with functional Ag/TiO<sub>2</sub> NPs. A homogeneous solution containing Ag/TiO<sub>2</sub> NPs was prepared by an ultrasonic homogenizer for 20 min. Then, the self-assembly of Ag/TiO<sub>2</sub> on the GO (3 ml, 2 mg/ml) surface occurred under constant stirring at 200 rpm for 2 h. Finally, we obtained a set of ATG Nces with varied ratios of Ag including 25, 33, 50, and 75 wt%, named as A1TG, A2TG, A3TG, and A4TG, respectively. GO content is fixed to be 6 wt% in every kind of ATG Nces investigated in this study.

**2.3. Characterizations.** The crystal phase and composition of Ag/TiO<sub>2</sub>/GO were investigated by X-ray diffraction (Bruker D5005 X-ray diffractometer, Cu K<sub>α</sub>, λ = 1.5406 Å) under a voltage of 40 kV and a current of 30 mA. The morphologies of Ag/TiO<sub>2</sub>/GO were analyzed using scanning electron microscopy (SEM Hitachi S-4800) operating under an acceleration voltage of 5 kV and transmission electron microscopy (TEM JEOL JEM-1010) at an accelerating voltage of 80 kV. Chemical analyses of the nanocomposite were performed by Fourier-transform infrared spectroscopy (FTIR

HL ReactIR 45P), Raman spectroscopy (Horiba Macro-RAM™) with 785 nm laser excitation, and Energy Dispersive X-ray Spectroscopy (EDS). Optical analyses were carried out using a UV-Vis spectrophotometer (JENWAY 6850), and 10 mm path length quartz cuvettes were used for the measurements of absorption ranges.

**2.4. Investigated Experimental Models: SERS Sensor, Catalytic Reduction.** To investigate the enhanced electron transfer in ATG Nces, two experimental models with different electronic excitation/providing sources were undertaken. The first model was a SERS sensor based on the electronic excitation of a high-energy laser beam on Ag nanoparticles. To evaluate the SERS activity of ATG Nces, methylene blue (MB) was selected as a reporter molecule. Solutions at various concentrations of MB (10<sup>-4</sup> to 10<sup>-9</sup> M) were prepared in water. The substrates were fabricated through a few facile steps, in which square aluminum (Al) substrates were prepared with the dimension of 1 × 1 cm<sup>2</sup> and surface-active circular area with a diameter of 0.2 cm. ATG Nces with different contents of Ag was dispersed in water, then coated on the surface-active of Al substrate by a drop-casting method, and dried naturally at room temperature. MB reporter with various concentrations was dropped directly onto the ATG Nces-Al substrate, followed by the natural evaporation of water. SERS measurements were acquired via Raman spectroscopy under an excitation wavelength of 785 nm by means of a 100x objective lens with a 0.90 numerical aperture. The laser power was set to be 45 mW at 45° of contacting angle, with a diffraction-limited laser spot diameter of 1.1 μm (1.22 λ/NA, where λ is the wavelength of the laser, and NA is the numerical aperture of the microscope objective) and focal length of 115 nm. The expose time for each measurement was 10 seconds with 2 accumulations. A baseline calibration was conducted to obtain the final spectrum.

The second experimental model was based on the catalytic reduction property of ATG Nces with  $\text{BH}_4^-$  ions as an electron donor. The reduction of 4-nitrophenol (4-NP) to 4-aminophenol (4-AP) by  $\text{NaBH}_4$  was selected as a model reaction for evaluating the catalytic reduction performance of our ATG Nces. First, 5 ml of 4-NP ( $2 \times 10^{-4}$  M in water) was mixed with 5 ml  $\text{NaBH}_4$  (0.01 M in water); the solution turned from light yellow to bright yellow rapidly. Subsequently, 0.8 mg of ATG Nces with different contents of Ag was added to the solution. Time-dependent absorption spectra were recorded by UV-Vis spectroscopy. The degradation rate catalytic reduction model was calculated by using the following equation:

$$\text{Percentage of degradation (\%)} = \frac{C_0 - C_t}{C_0} \times 100, \quad (1)$$

where  $C_0$  and  $C_t$  represent, respectively, the initial 4-NP concentration and that at time  $t$  of degradation.

### 3. Results and Discussion

**3.1. Characterizations of Ag/TiO<sub>2</sub>/GO.** Scheme 1 demonstrates the formation of ATG nanostructures. Firstly, the Ag/TiO<sub>2</sub> NPs were fabricated due to the reduction of  $\text{Ag}^+$  ions adsorbed onto TiO<sub>2</sub> crystal matrix. Then, the as-synthesized Ag/TiO<sub>2</sub> NPs were self-assembled onto the surface of the GO sheets via electrostatic interactions. The morphology of ATG has been revealed in TEM and SEM images (Figure 1). Figure 1(a) shows the TEM image of ATG Nces with the presence of three types of materials with distinct shapes and sizes marked as Type 1, Type 2, and Type 3. Both Type 1 and Type 2 are spherical nanostructures but differed in size. The distribution histograms of SEM result shown in Figure 1(c) reveals the average diameters of Type 1 and Type 2 nanoparticles to be 50 nm and 100 nm with frequencies of 35% and 65%, respectively. Besides, Figure 1(b) shows the presence of Type 1 on the surface of Type 2. Thus, it can be assumed that Type 1 nanostructures represent Ag nanoparticles while Type 2 ones represent TiO<sub>2</sub> nanoparticles. In addition, Figure 1(c) and its magnified image (Figure 1(e)) also exhibit a sheet-like structure which reminds of the two-dimensional structure of GO-pristine (Figure 1(d)). The presence of Ag and TiO<sub>2</sub> nanoparticles on the surface of this sheet-like structure reveals the structure of Ag/TiO<sub>2</sub>/GO, in which the Ag/TiO<sub>2</sub> nanostructures have been situated on the surface of GO sheets. The presence of GO in the nanocomposite can be also observed in the TEM image (Figure 1(a)) as large and plane nanostructures (Type 3).

The XRD pattern of ATG Nces is shown in Figure 2(a), in comparison with the reference patterns of TiO<sub>2</sub>, Ag, and Ag/TiO<sub>2</sub>. The position of the diffraction peaks at  $2\theta = 38.010$ ,  $44.09^\circ$ , and  $64.03^\circ$  can be assigned to the (111), (200), and (220) planes of Ag NPs (ICDD file No. 01-087-0597), respectively. In addition, the XRD pattern also shows the diffractions of the crystal planes (101), (200), (211), (105), and (022) at  $2\theta = 25.410$ ,  $47.830$ ,  $54.990$ ,  $53.800$ , and  $62.660$ , which correspond to anatase TiO<sub>2</sub> (ICDD file No.

01-086-1175). These results suggest successful formation of both Ag NPs and TiO<sub>2</sub> NPs in our as-synthesized composite nanomaterials. Furthermore, the diffraction peaks of ATG Nces are well-matched with those of Ag/TiO<sub>2</sub> (ICDD file No. 98-005-8369), which provides an evidence for the presence of Ag NPs in the TiO<sub>2</sub> crystal matrix. Besides, the Scherrer formula was employed to calculate the average crystal grain size of Ag NPs and TiO<sub>2</sub> NPs via their diffraction peaks [21]. The obtained results of 43 nm for Ag NPs and 125 nm for TiO<sub>2</sub> NPs have confirmed the assumptions about their sizes that we have provided from TEM and SEM analysis.

FTIR, Raman, and EDX spectra were recorded to analyze the chemical properties of ATG Nces. In the FTIR spectrum of ATG Nces (Figure 2(b)), the characteristic peaks of O–H stretching vibrations ( $3651 \text{ cm}^{-1}$ ,  $3078 \text{ cm}^{-1}$ ) and C=O stretching vibrations ( $1715 \text{ cm}^{-1}$ ) are in agreement with the peaks observed in the FTIR of GO, including a broad band appeared at  $3580 \text{ cm}^{-1}$  and a sharp peak at  $1640 \text{ cm}^{-1}$ , respectively [22]. It can be ascribed to GO-containing ATG Nces. In addition, the characteristic peaks at  $800 \text{ cm}^{-1}$  and  $467 \text{ cm}^{-1}$  indicate to Ti–O–C bonding, which demonstrates the direct binding of TiO<sub>2</sub> onto the surface of GO sheets [23, 24]. Figure 2(d) shows Raman spectrum of ATG Nces, in comparison to those of GO and TiO<sub>2</sub>. The Raman spectrum of the nanocomposite reveals two prominent peaks corresponding to D-band ( $1300 \text{ cm}^{-1}$ ) and G-band ( $1600 \text{ cm}^{-1}$ ) of GO, between which D-band is broad and higher in intensity compared to G-band. The ratio of intensities between D-band and G-band ( $I_D/I_G$ ) of ATG Nces (1.6) is larger than that of GO-pristine (1.4). It has been reported that a broad D-band with higher relative intensity compared to that of G-band can be the result of high disorder in graphite [25]. The disorder of graphite in our materials may be due to the deposition of Ag/TiO<sub>2</sub> on the surface of GO sheets [25]. In addition, the two bands at  $156 \text{ cm}^{-1}$  and  $635 \text{ cm}^{-1}$  are also observed in the spectrum of TiO<sub>2</sub>, which are assigned to the  $E_g$  modes of TiO<sub>2</sub> anatase phase. These Raman spectra have reconfirmed the presence of TiO<sub>2</sub> in the nanocomposite materials [26]. The chemical composition of the ATG Nces surface was studied by EDX spectroscopy. The EDX spectrum (Scheme 1) indicates the presence of Ag, Ti, O, and C and proves the high level of purity of ATG Nces. To analyze the optical properties of ATG Nces, UV-Vis absorption spectra were recorded (Figure 2(c)). The spectra of both TiO<sub>2</sub> and ATG Nces exhibit a significant absorption band in the UV region. However, the absorption spectrum of ATG Nces shows higher band intensity and a red-shift in the absorption edge. To clarify this difference in absorption edge, the optical bandgap of TiO<sub>2</sub> and ATG Nces were determined via Tauc plot (Figure 2(c), inset) using Kubelka-Munk function [27]. Tauc plot results indicate that the absorption edges in the spectra of TiO<sub>2</sub> and ATG Nces correspond to optical bandgaps of 3.15 eV and 2.83 eV, respectively. The difference in optical bandgap values between ATG Nces and TiO<sub>2</sub> can be explained by the interactions of TiO<sub>2</sub> and Ag (via attachment) and GO (via Ti–O–C bonding), which has been

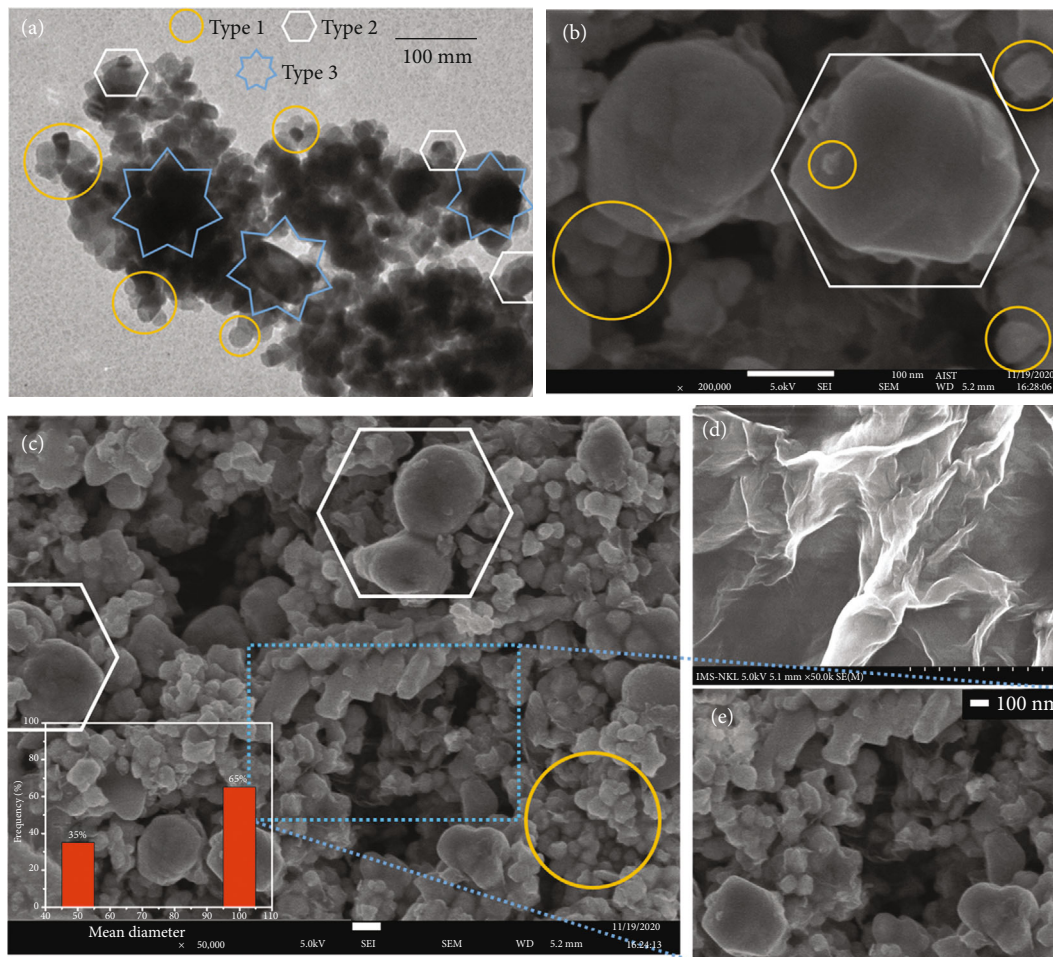


FIGURE 1: TEM image of (a) Ag/TiO<sub>2</sub>/GO, (b, c, e) SEM images with different magnification and particle size distribution histograms of Ag/TiO<sub>2</sub>/GO, and (d) GO-pristine.

confirmed by XRD and FTIR spectra, respectively. The formation of Ag/TiO<sub>2</sub> and Ti-O-C bonds has fulfilled all the requirements for the nanocomposite materials to be employed to study the electronic transfer process in their internal structures.

**3.2. SERS Sensor Model.** SERS sensor was the first model that we employed to investigate the enhanced electron transfer in ATG Nces, taking advantages of the unique plasmonic properties of Ag and enhanced Raman scattering caused by chemical enhancement of the nanocomposite materials [4, 12, 28]. As the plasmonic properties of Ag are the key to fabricate SERS sensors based on ATG Nces, a set of samples with distinct contents of Ag has been employed for SERS measurements as mentioned in Section 2, including A1TG, A2TG, A3TG, and A4TG. Figure 3(a) exhibits the SERS signals of MB in the presence of 4 kinds of nanomaterials as active substrates. On the substrate with 25 wt% of Ag (A1TG), the SERS spectrum reveals two characteristic peaks of GO (1300 cm<sup>-1</sup> and 1600 cm<sup>-1</sup>) at high intensity. In contrast, the intensity of the characteristic peak of MB at 450 cm<sup>-1</sup> is much lower. In the increase of Ag contents, the SERS spectra of MB on A2TG and A3TG do not show such

significant peaks of GO but the characteristic peaks of MB at 450, 505, 1396, and 1620 cm<sup>-1</sup>, which corresponds to vibrations of C-N-C skeletal deformation, C-S-C skeletal deformation, C-H in-plane ring deformation, and C-C stretching ring, respectively [29]. Unexpectedly, when the Ag content increases up to 75 wt%, the intensity of the characteristic peaks of MB suffered a great loss, compared to A3TG. It has to be stressed that the concentration of MB solution for every measurement was the same; thus, it is undeniable that the Ag content has a great effect on SERS activity of the nanocomposite material. In this case, the highest intensity of the MB characteristic bands allows A3TG to be the most SERS-effective substrate, compared to A1TG, A2TG, and A4TG.

Enhancement factor (EF) of ATG Nces with varied contents of Ag was calculated to further testify the SERS performance (Figure 3(a)). The SERS EF was observed in agreement with the previous report following the equation below [30]:

$$EF = \frac{I_{SERS}}{I_{Raman}} \times \frac{N_{bulk}}{N_{surface}}, \quad (2)$$

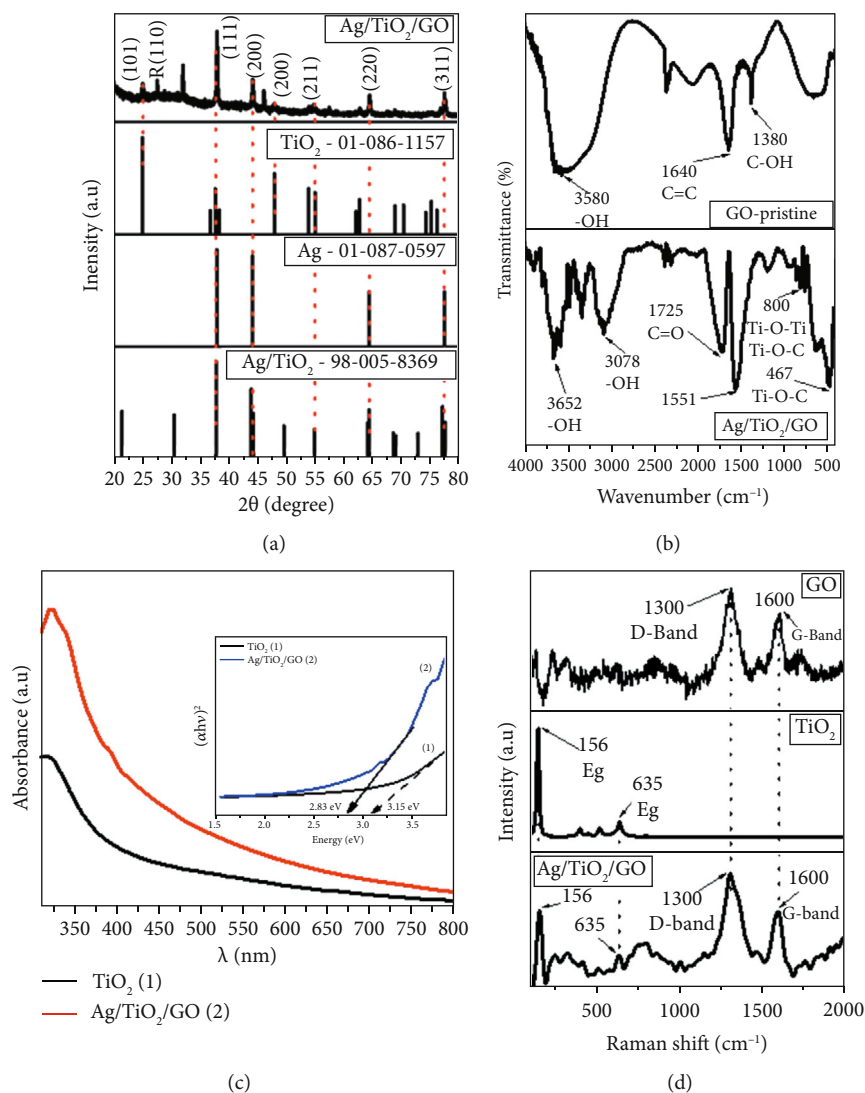


FIGURE 2: XRD pattern of Ag/TiO<sub>2</sub>/GO (a), FTIR spectra of GO-pristine and Ag/TiO<sub>2</sub>/GO (b), UV-Vis spectra and Tauc plot of TiO<sub>2</sub> and Ag/TiO<sub>2</sub>/GO (c), Raman spectra of GO, TiO<sub>2</sub>, and Ag/TiO<sub>2</sub>/GO (d).

where  $I_{\text{SERS}}$  and  $I_{\text{Raman}}$  are Raman signal intensities of MB reporter with and without SERS from ATG Nces, respectively, and  $N_{\text{bulk}}$  is the average number of MB molecules in the scattering volume for the non-SERS measurement;  $N_{\text{surface}}$  is the number of the average number of MB molecules in the surface-active area for the SERS experiments (see Supporting information).

The EF values of A1TG, A2TG, A3TG, and A4TG were calculated to be  $9.7 \times 10^4$ ,  $2.1 \times 10^5$ ,  $3.6 \times 10^5$ , and  $1.3 \times 10^5$ , respectively. This calculation reconfirms that A3TG Nces is the highest SERS-effective substrate. In addition to the impressive enhancement factor of A3TG, the limit of detection for MB deposited on this SERS substrate was down to 0.93 nM with a linear range from  $10^{-9}$  M to  $10^{-4}$  M (Figure 3(b)). It is obvious that Ag content has a great effect on the performance of SERS sensor using ATG Nc substrates. In this case, the optimal Ag content is 50 wt%. Similar results have been reported in previous studies on other composites such as ternary Au@Cu<sub>2</sub>O-Ag nanocomposite

and Ag-TiO<sub>2</sub> composite [31, 32]. In Section 3.1, we have pointed out that the formation of Ag/TiO<sub>2</sub> structures and Ti-O-C bonds, which might be convenient charge-separation pathways to increase the hot-electron age. Due to the local surface plasmon resonance (LSPRs) phenomenon, in which coherent electrons oscillate around the Ag NP surface formed hot electrons, it is reasonable that higher Raman intensity of MB was achieved when Ag content in ATG Nces increased (A1TG, A2TG, and A3TG). However, the unexpected decrease in the Raman signal of MB in the presence of A4TG might be explained by the surplus of Ag, which led to the decrease of TiO<sub>2</sub> and GO contents, as well as the formation of Ag/TiO<sub>2</sub> structures and Ti-O-C bonds. As a result, the electron transfer rate in the charge-separation pathway in the internal structure of ATG Nces might have been reduced. In addition, the EF value of A3TG is no more than 5 times higher than that of A1TG, A2TG, and A4TG. These small differences cannot be due to electromagnetic mechanism as it is usually related to large

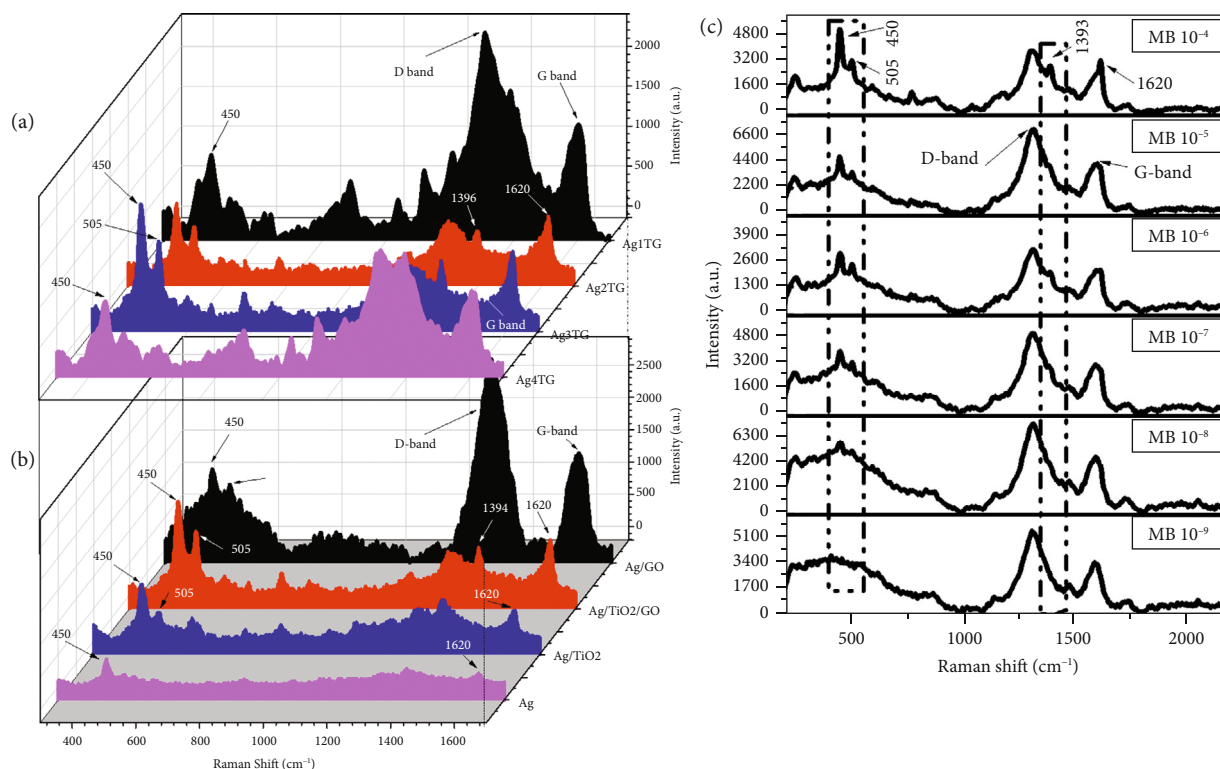


FIGURE 3: SERS spectra of MB ( $10^{-6}$  M) in the presence of ATG Nces with different Ag contents (A1TG, A2TG, A3TG, and A4TG) (a), and Ag-containing materials including Ag NPs, Ag/TiO<sub>2</sub>, Ag/TiO<sub>2</sub>/GO, and Ag/GO (b). SERS spectra of different concentrations of MB ( $10^{-4}$ – $10^{-9}$  M) in the presence of A3TG (c).

enhancement ( $10^6$ – $10^{10}$  or even more) [30]. Instead, it can be explained by chemical mechanism, of which EFs are in the range of  $10^1$ – $10^3$  [33]. It is worth mentioning that CM is directly related to electron transfer. Thus, in addition to the presence of Ag, the electron transfer through Ag/TiO<sub>2</sub> contacts and Ti-O-C bonds may be another factor causing the differences in the enhancement of Raman signal of MB on the ATG Nces containing varied Ag content.

The important role of TiO<sub>2</sub> and GO in the improvement of the SERS sensitivity of ATG Nces was confirmed by a comparison among the SERS spectra of MB ( $10^{-6}$  M) in the presence of only Ag NPs, Ag/TiO<sub>2</sub>, Ag/GO, and Ag/TiO<sub>2</sub>/GO (A3TG) (Figure 3(b)). Instead of 4 characteristic bands as mentioned previously, MB only exhibits 2 weak peaks at 450 cm<sup>-1</sup> and 1620 cm<sup>-1</sup> in the presence of only Ag NPs. The use of Ag/TiO<sub>2</sub> (50:50 wt%) obviously improves the sensitivity of the SERS sensing due to the presence of all characteristics. However, the intensity and the sharpness of the peaks are relatively lower than those using Ag/TiO<sub>2</sub>/GO as SERS substrate. The utilization of Ag/GO also results in high intensity of SERS signal. However, D-band and G-band of GO overlap the peaks at 1393 cm<sup>-1</sup> and 1620 cm<sup>-1</sup> of MB while two other ones at 450 cm<sup>-1</sup> and 505 cm<sup>-1</sup> are not as clear as those in the use Ag/TiO<sub>2</sub>/GO. This comparison has emphasized the role of TiO<sub>2</sub> and GO to enhance the SERS performance in the nanocomposite materials. Moreover, the materials achieved the highest efficiency in the presence of both TiO<sub>2</sub> and GO. It would confirm the hypothesis above about the impacts of the

electron transfer through Ag/TiO<sub>2</sub> contacts and Ti-O-C bonds of ATG Nces in their SERS performance improvement.

**3.3. Catalytic Reduction Model.** In addition to the physical model, we also generated a chemical one to answer the question of whether the electron transfer in the ATG Nces has any influences on other applications and how it affects their performance. A model of catalytic reduction was selected as its performance is directly related to electron transfer phenomena. The catalytic reduction model was studied through the reduction of 4-NP to 4-AP using NaBH<sub>4</sub> as an electronic providing source from BH<sub>4</sub><sup>-</sup> to investigate the catalytic reduction properties of ATG Nces [34]. To clarify the role of TiO<sub>2</sub> and GO on the catalytic reduction performance of ATG Nces, we prepared two sets of samples. One set included Ag, Ag/TiO<sub>2</sub>, Ag/GO, and Ag/TiO<sub>2</sub>/GO. The other one consisted of ATG Nces containing varied Ag contents. The materials from each set were employed as catalysts for the reduction of 4-NP to 4-AP in the same experimental conditions as mentioned in Section 2.4. For each comparison, we used the same experimental conditions as the mass of catalyst material (0.8 mg), the concentration of 4-NP ( $2 \times 10^{-4}$  M), NaBH<sub>4</sub> (0.01 M), and catalytic reduction reaction time (30 s). The absorption spectra of the reaction solutions in the presence of different catalysts were then recorded using UV-Vis spectroscopy. The peak at 400 nm in UV-Vis spectra, which is ascribed to 4-nitrophenolate ions, would be decreased gradually with time in the presence

of catalytic materials, signifying the degradation of 4-NP. Contemporaneously, the appearance of a new band at 300 nm represents the formation of 4-AP [34]. Figure 4 demonstrates the absorption spectra of the reaction samples using different catalytic materials in the two experimental sets.

Concerning the first set including Ag, Ag/TiO<sub>2</sub>, Ag/GO, and Ag/TiO<sub>2</sub>/GO, the 4-NP degradation efficiency of these four materials can be calculated based on the intensity of the absorption band at 400 nm (Figure 4(a)). Using Ag as the catalysts, the obtained absorption spectrum only exhibits a small decrease in the band at 400 nm, which represents the degradation efficiency of about 10% which is much lower than those of Ag/GO (~28%) and Ag/TiO<sub>2</sub> (~80%). Meanwhile, under the same reaction conditions, in the presence of Ag/TiO<sub>2</sub>/GO, 4-NP was nearly completely degraded with the disappearance of the 400 nm band. The reduction of 4-NP to 4-AM is also confirmed by the increase in intensity of the 300 nm band. As expected, the absorption spectrum of reaction solution in the presence of Ag/TiO<sub>2</sub>/GO shows the highest intensity at 300 nm, in comparison to the others. The differences in catalytic degradation efficiencies of the reaction using four distinct catalytic materials demonstrate the great effect of TiO<sub>2</sub> and GO on catalytic reduction performance of ATG Nces. In addition, Ag content also influences the performance of this application (Figure 4(b)). Thanks to the presence of Ag, TiO<sub>2</sub>, and GO in the composite structures, it is not surprising that the 4-NP degradation efficiencies of A1TG, A2TG, A3TG, and A4TG are relatively high. However, the differences appear in the 300 nm band as the reaction solution using A3TG results in the highest intensity compared to the other one. Therefore, in the catalytic reduction model, 50% wt is still the optimal content of Ag in ATG Nces.

As negatively charged 4-nitrophenolate and BH<sub>4</sub><sup>-</sup> preferably interact with the metallic catalyst and facilitate the hydrogenation process on the 4-nitrophenolate, it is obvious that Ag is the key component in ATG Nces, which has the highest effect on catalytic performance. However, the presence of TiO<sub>2</sub> in Ag/TiO<sub>2</sub> has also enhanced catalytic performance. Moreover, the addition of GO has continued improving this performance. When discussing about the characterization of ATG Nces and the SERS sensor model, we have demonstrated the formation of Ag/TiO<sub>2</sub> nanostructures and Ti-O-C bonds as well as their effects on SERS sensing efficiency. Once again, TiO<sub>2</sub> and GO have exhibited their importance in the performance of another application using the ATG Nces. Furthermore, the same optimal Ag content in ATG Nces in both SERS and catalytic reduction models suggests a similarity in the mechanism of performance enhancement in both models. As mentioned in the previous section, this mechanism is based on the separation pathway in the internal structure of ATG Nces through Ag/TiO<sub>2</sub> nanostructures and Ti-O-C bonds. It has been claimed in previous studies that when a metal oxide contacted with a metal intimately, a Schottky junction would be formed and Fermi level alignment would lead to charge redistribution, which was also known as the electron transfer process [2, 34]. Besides, other reports stated that an additional band edge and a

bandgap tuning were created due to the formation of Ti-O-C bonds and provided a conductive pathway for electron transfer from TiO<sub>2</sub> to GO [18, 35].

*3.4. Relationship of SERS Sensor Model and Catalytic Reduction Model: Effects of Electron Transfer on Their Performance.* The interesting similarity in optimal Ag content in both models has triggered us to further analyze the relationship between their performances and clarify the effect of electron transfer process on their performance. The comparisons of EFs in the SERS model and degradation efficiencies in the catalytic reduction model using ATG Nces with varied Ag contents are shown in Figures 5(a) and 5(b), respectively. A similar trend can be observed in the two graphs as EFs and degradation efficiencies both increase in the increase of Ag content and reach the highest peak at the content of 50 wt% (A3TG). Then, both of them decrease dramatically when the content of Ag rises to 75% (A4TG). Moreover, the similarity in impacts of TiO<sub>2</sub> and GO in the improvement of ATG Nces performance in both models is also worth mentioning. It may be an evidence for the ET pathway that will be further discussed in this section.

Concerning the SERS sensor model, according to quantum theory, when an incident laser light interacts with Ag NPs surface, Ag NPs serve as a light absorber, where hot electrons are generated due to by LSPR phenomenon [2]. Previous reports have stated that the specific interaction of the adsorbed MB molecule and the surface of Ag might lead to electron transfer from Ag to MB molecule, named metal to molecular transfer [12]. The superposition of energy levels should have been formed between Ag and adsorbed MB molecule [36]. The Fermi level of Ag was reported to be -4.26 eV [37], while the absolute energy of the lowest unoccupied molecular orbital (LUMO) of MB is -3.328 eV [38]. Thus, the plasmon-induced hot electrons can be transferred from Ag into the LUMO level of MB, then decay with the SERS signal of MB. However, the adsorbed surface area of Ag is relatively small and MB ions are positively charged, so the absorption of MB on the Ag surface can be prevented. Therefore, that ET process should not have been completely responsible for the obtained SERS signal enhancement of our materials. This hypothesis has been confirmed by a significant loss of SERS signal when using the ATG Nces with surplus Ag content. Another ET pathway in the internal structure of ATG Nces, the metal-semiconductor transition, might have taken the lead in this case. Wu et al. proposed the ET pathway in a study about a system of CdSe-Au hetero-nanostructures and named this hot-electron transfer pathway a plasmon-induced interfacial charge-transfer transition (PICTT) to discriminate against the common plasmon-induced hot-electron transfer (PHET) or direct metal-to-semiconductor interfacial charge-transfer transition (DICTT) [39]. In PICTT, the metal serves as a light absorber, but strong interdomain coupling and mixing of the metal and semiconductor levels lead to a new plasmon decay pathway. Besides, PICTT also exhibits the quantum efficiency to be higher than 24%. In addition, Iida and Noda reported on the photoinduced silver-TiO<sub>2</sub> electronic interaction that allowed the excited electrons to be directly

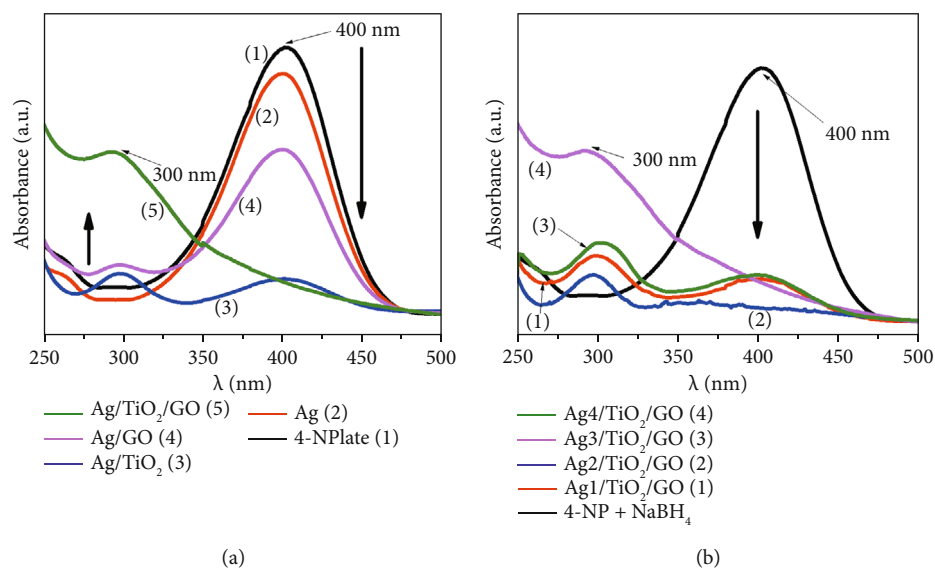


FIGURE 4: UV-Vis spectra of the catalytic reduction of 4-nitrophenolate (400 nm) to 4-aminophenol (300 nm) in the water and comparison of catalytic efficiency of Ag, Ag/TiO<sub>2</sub>, Ag/GO, and Ag/TiO<sub>2</sub>/GO (a); comparison of catalytic efficiency of varied contents of Ag in ATG Nces (b).

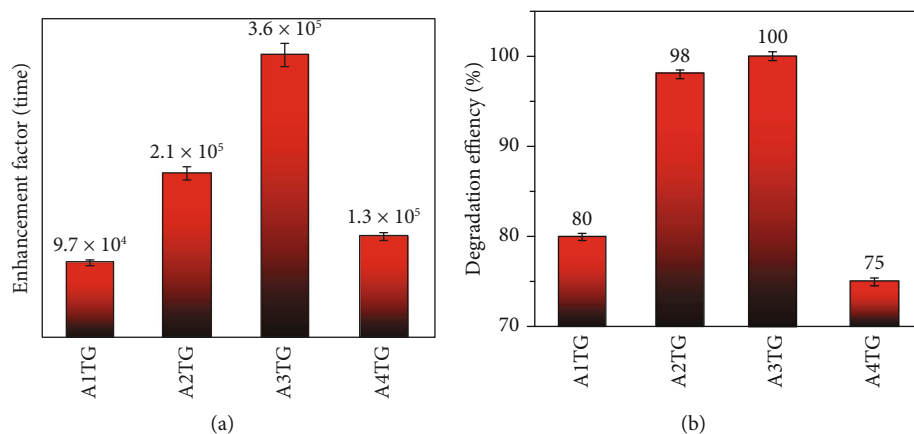


FIGURE 5: Comparison of enhancement factor (at 10<sup>-6</sup> M) (a) and degradation efficiency (b) of Ag/TiO<sub>2</sub>/GO with different Ag contents.

transferred from the silver nanocluster to the TiO<sub>2</sub> layer without passing through the conduction band of the silver nanocluster. Nevertheless, it might potentially occur due to the formation of Ag-O bonds between the silver-TiO<sub>2</sub> layers [9] while in our nanocomposites, Ag and TiO<sub>2</sub> only form a weak interaction due to natural deposition. Thus, the PHET pathway might be the more suitable mechanism that has occurred in our materials. In PHET, the metal decays into a hot electron-hole pair through Landau damping, followed by injection of the hot electrons into the conduction band (CB) of the semiconductor [40]. Here, electrons might have been transferred through Ag/TiO<sub>2</sub> interaction (Schottky junction). Moreover, TiO<sub>2</sub> is an excellent electron acceptor via d-orbital [41]. In addition, plasmon-induced hot electrons can inject into CB of TiO<sub>2</sub> with conduction band minimum energy of -4.0 eV [42]. Therefore, the transferred electrons have more opportunities to interact with MB molecule. Nevertheless, electron transfer process in CB of TiO<sub>2</sub>

competes with electron relaxation through rapid electron-electron scattering. Then again, Ti-O-C might have been allowed electrons to be transferred from TiO<sub>2</sub> to GO sheets, whose Fermi level is -5.02 eV [25]. Since GO is an excellent adsorber [16], the GO sheets might have increased the direct interaction between hot electrons to MB molecular. As a result, many active electrons have interacted with MB reporters via the charge-separation pathways in ATG Nces; thus, the Raman signal of MB has been enhanced by the chemical mechanism.

Concerning the catalytic reduction model, the potential charge-separation pathway in ATG Nces should have been an important factor to lead to the enhancement of 4-NP degradation efficiency. Due to the adsorption of negatively charged BH<sub>4</sub><sup>-</sup> on the surface of Ag NPs, BH<sub>4</sub><sup>-</sup> ions acted as electron donors that provided active electrons to Ag. In the same electron transfer pathway as in the SERS sensor model, electrons would have escaped from Ag and

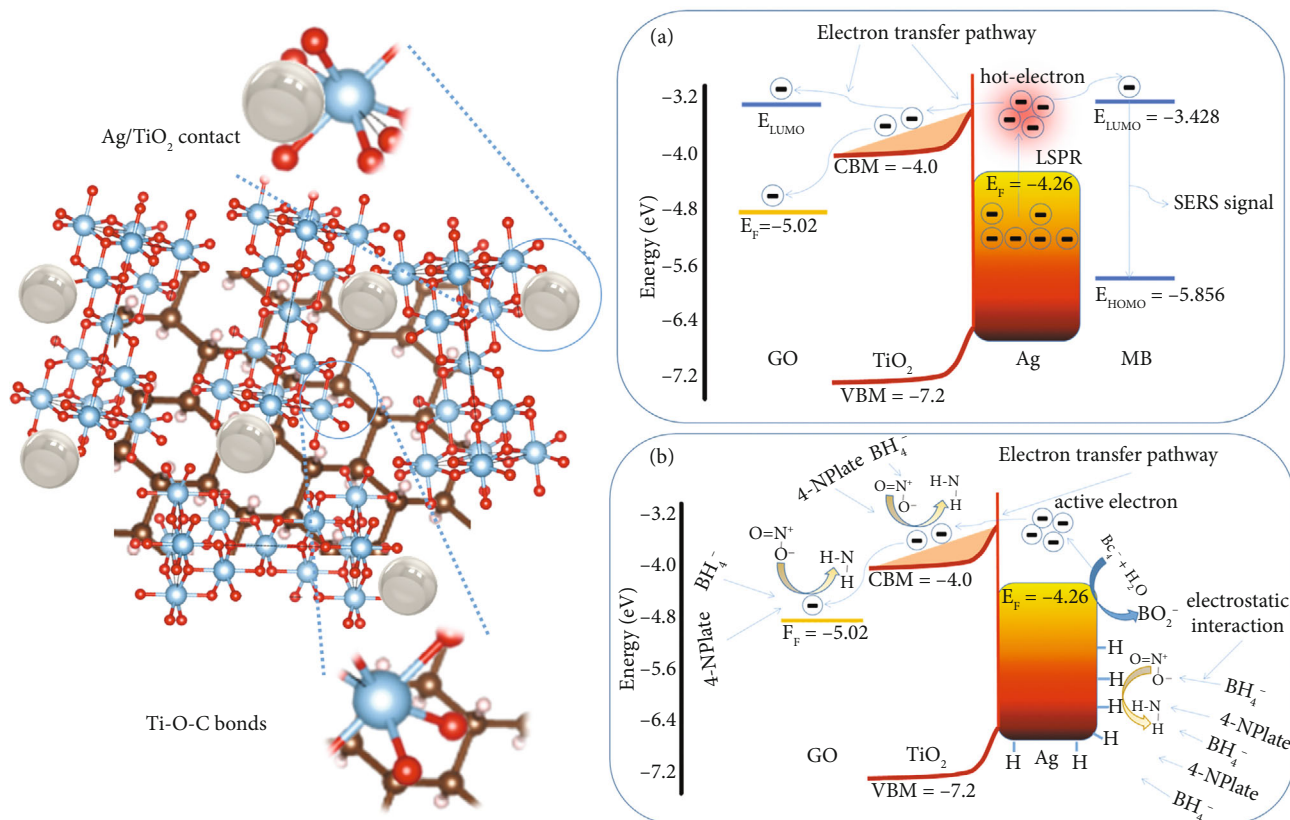


FIGURE 6: Potential electron transfer process in ATG Nces for both SERS sensor model (a) and catalytic reduction model (b) through Ag/TiO<sub>2</sub> contact and Ti-O-C bonds.

TABLE 1: Several reported AgNP-based SERS sensors to determine MB and their sensing performance (LOD, EF; nanoparticles (NPs); graphene foam (GF); nanotube array (NTA); 4-mercaptobenzoic acid (4-MBA).

Materials	Analyte	Substrate	LOD	EF	References
AgNPs/GF	MB	Si	10 <sup>-9</sup> (M)	5 × 10 <sup>4</sup>	[43]
Au@Cu <sub>2</sub> O-Ag	4-MBA	—	10 <sup>-9</sup> (M)	7.19 × 10 <sup>5</sup>	[31]
GO/Ag/TiO <sub>2</sub> NTA	MB	—	10 <sup>-9</sup> (M)	2.1 × 10 <sup>7</sup>	[44]
Ag/TiO <sub>2</sub> /GO	MB	Al	3.32 × 10 <sup>-10</sup> (M)	7.3 × 10 <sup>4</sup>	This work

TABLE 2: Comparison catalytic performance of several reported AgNP-based nanomaterials to remove 4-NP (concentration, reaction time, and removal performance); poly(acrylic acid) (PPA); reduced-GO (rGO); cellulose nanocrystals (CNC).

Catalyst	4-NP (M)	NaBH <sub>4</sub> (M)	Reaction time	Removal efficiency (%)	References
Ag@PPA	10 <sup>-4</sup>	0.1	300 s	100	[45]
Ag-rGO	5 × 10 <sup>-5</sup>	0.1	360 s	98	[46]
CuFe <sub>2</sub> O <sub>4</sub> /CNC@Ag	5 × 10 <sup>-3</sup>	0.1	360 s	100	[34]
Ag/TiO <sub>2</sub> /GO	2 × 10 <sup>-4</sup>	0.01	20 s	100	This work

transferred into TiO<sub>2</sub> and GO sheets. Zhang et al. suggested that electron transfer between Ag and CuFe<sub>2</sub>O<sub>4</sub> led to the surplus electrons on CuFe<sub>2</sub>O<sub>4</sub>, which facilitated the capture of electrons by 4-NP molecules [34]. Herein, the transferred electrons in the GO sheets and TiO<sub>2</sub> might have provided a

large active-surface area to capture more BH<sub>4</sub><sup>-</sup> and 4-nitrophenolate ions, thus, increased the rate of the catalytic reduction reaction.

In summary, the Ag content has a great effect on the electron transfer process in the internal nanostructure of

ATG Nces; therefore, it also influences the performance of SERS and catalytic reduction of ATG Nces. The same optimal Ag content, as well as the similar trend of performance changing observed in the presence of ATG Nces containing varied Ag content in those two models, has demonstrated the important role of electron transfer in the enhancement of their performance. Through the SERS sensor model and the catalytic reduction model, we propose a potential electron transfer pathway in ATG Nces via Ag/TiO<sub>2</sub> interaction and Ti-O-C bonds, which is exhibited in Figure 6.

Thanks to the ET process, the performance of ATG Nces materials in different applications has been enhanced. With a low LOD of 0.93 nM, our ATG Nces-based SERS sensor for MB detection is capable to determine MB at extremely low levels. Table 1 presents the comparison in SERS sensibility among ATG Nces and several reported materials, in which ATG Nces-based sensor results in the lowest LOD. It suggests the development of high-performance SERS sensors using this nanocomposite material as the substrate for detection of other contaminants. Moreover, ATG Nces also exhibit excellent 4-NP removal efficiency via catalytic reduction reaction with 100% of 4-NP degraded after 20 s, which is competitive in comparison to several reported catalytic materials (Table 2). Similarly, the performance of other applications related to the electron transfer pathway, such as photocatalysis, electrocatalysts, and solar cells, might be also enhanced with the utilization of ATG Nces. Thus, with a few facile steps of preparation as mentioned in Section 2, we can fabricate a multifunctional material that consists of nontoxic components (i.e., Ag, TiO<sub>2</sub>, and GO). Furthermore, the synthesis can be scaled up to increase the mass production and reduce the cost of the fabrication. It suggests a direction to fabricate multifunctional, high-performance, cost-effective, facile-preparation, and nontoxic materials for detecting and removing contaminants.

## 4. Conclusions

In this work, Ag/TiO<sub>2</sub>/GO Nces were successfully synthesized. The SEM, TEM, XRD, FTIR, Raman, UV-Vis, and EDX results confirmed the formation of Ag/TiO<sub>2</sub> structure and the deposition of Ag/TiO<sub>2</sub> on GO nanosheets via Ti-O-C bonds. We investigated the electron transfer process in Ag/TiO<sub>2</sub>/GO Nces using two experimental models including SERS sensor and catalytic reduction, in which the Ag/TiO<sub>2</sub>/GO Nces acted as SERS substrates and catalysts. The optimal Ag content of 50 wt% was appropriate in both models. From these results, we proposed a charge-separation pathway in the internal structure of ATG Nces that is suitable for both models. This study provides a clear explanation for the electron transfer process in composite nanostructures which leads to the enhancement of application efficiencies.

## Data Availability

Data are available on request.

## Conflicts of Interest

The authors declare that they have no known competing financial interests or personal relationships that could have appeared to influence the work reported in this paper.

## Authors' Contributions

M. Q. Doan and N. H. Anh contributed equally to this work.

## Acknowledgments

This research was supported by the Vietnam National Foundation for Science and Technology Development (NAFOSTED) through a fundamental research project (103.02-2018.50). The authors would like to acknowledge the supports with Raman, UV-Vis measurements from NEB Lab at the Phenikaa University.

## Supplementary Materials

Figure S1: regression equation expressing the linear relationship between concentration of 4-nitrophenolate and absorption intensity of the reaction solution. Calculation of limit of detection (LOD-SERS sensor model). Figure S2: plot of Log of SERS intensity against Log of analyte concentration at 450 cm<sup>-1</sup>, 505 cm<sup>-1</sup>, 1393 cm<sup>-1</sup>, and 1620 cm<sup>-1</sup>. Calculation of enhancement factor (EF-SERS sensor model). (*Supplementary Materials*)

## References

- [1] H. Atwater and A. Polman, "Plasmonics for improved photovoltaic devices," *Nature Mater.*, vol. 9, pp. 205–213, 2010.
- [2] C. Clavero, "Plasmon-induced hot-electron generation at nanoparticle/metal-oxide interfaces for photovoltaic and photocatalytic devices," *Nature Photonics*, vol. 8, no. 2, pp. 95–103, 2014.
- [3] J. Li, S. K. Cushing, F. Meng, T. R. Senty, A. D. Bristow, and N. Wu, "Plasmon-induced resonance energy transfer for solar energy conversion," *Nature Photonics*, vol. 9, no. 9, pp. 601–607, 2015.
- [4] H. Zhang, J. Wei, X.-G. Zhang et al., "Plasmon-induced interfacial hot-electron transfer directly probed by Raman spectroscopy," *Chem*, vol. 6, no. 3, pp. 689–702, 2020.
- [5] T. Zheng, T. Zhou, X. Feng, J. Shen, M. Zhang, and Y. Sun, "Enhanced plasmon-induced resonance energy transfer (PIRET)-mediated photothermal and photodynamic therapy guided by photoacoustic and magnetic resonance imaging," *ACS Applied Materials & Interfaces*, vol. 11, no. 35, pp. 31615–31626, 2019.
- [6] A. Bumajdad and M. J. P. C. C. P. Madkour, "Understanding the superior photocatalytic activity of noble metals modified titania under UV and visible light irradiation," *Physical Chemistry Chemical Physics*, vol. 16, no. 16, p. 7146, 2014.
- [7] N. Filippin, J. Castillo-Seoane, M. C. López-Santos et al., "Plasma-enabled amorphous TiO<sub>2</sub> Nanotubes as hydrophobic support for molecular sensing by SERS," *ACS Applied Materials & Interfaces*, vol. 12, no. 45, pp. 50721–50733, 2020.
- [8] A. Furube, L. du, K. Hara, R. Katoh, and M. Tachiya, "Ultrafast plasmon-induced electron transfer from gold nanodots into

- TiO<sub>2</sub>Nanoparticles,” *Journal of the American Chemical Society*, vol. 129, no. 48, pp. 14852–14853, 2007.
- [9] K. Iida and M. Noda, “Electron transfer governed by light-matter interaction at metal- semiconductor interface,” *npj Computational Materials*, vol. 6, no. 1, 2020.
- [10] H. Yazid, N. A. A. Rahman, and A. M. M. Jani, “Catalytic reduction of p-nitrophenol on Au/TiO<sub>2</sub> powder and Au/TiO<sub>2</sub> membrane,” *AIP Conference Proceedings*, vol. 2332, p. 070004, 2021.
- [11] M. Manyangadze, N. Chikuruwo, T. B. Narsaiah, C. S. Chakra, M. Radhakumari, and G. Danha, “Enhancing adsorption capacity of nano-adsorbents via surface modification: a review,” *South African Journal of Chemical Engineering*, vol. 31, pp. 25–32, 2020.
- [12] A. M. Michaels, M. Nirmal, and L. E. Brus, “Surface enhanced Raman spectroscopy of individual rhodamine 6G molecules on large Ag nanocrystals,” *Journal of the American Chemical Society*, vol. 121, no. 43, pp. 9932–9939, 1999.
- [13] F. Azeez, E. al-Hetlani, M. Arafa et al., “The effect of surface charge on photocatalytic degradation of methylene blue dye using chargeable titania nanoparticles,” *Scientific Reports*, vol. 8, no. 1, 2018.
- [14] J. Sun, J. Zhang, H. Fu et al., “Enhanced catalytic hydrogenation reduction of bromate on Pd catalyst supported on CeO<sub>2</sub> modified SBA-15 prepared by strong electrostatic adsorption,” *Applied Catalysis B: Environmental*, vol. 229, pp. 32–40, 2018.
- [15] H. Lai, F. Xu, Y. Zhang, and L. Wang, “Recent progress on graphene-based substrates for surface-enhanced Raman scattering applications,” *Journal of Materials Chemistry B*, vol. 6, no. 24, pp. 4008–4028, 2018.
- [16] S. Thangavel and G. J. P. Venugopal, “Understanding the adsorption property of graphene-oxide with different degrees of oxidation levels,” *Powder Technology*, vol. 257, pp. 141–148, 2014.
- [17] R. Wang, K. Shi, D. Huang, J. Zhang, and S. An, “Synthesis and degradation kinetics of TiO<sub>2</sub>/GO composites with highly efficient activity for adsorption and photocatalytic degradation of MB,” vol. 9, no. 1, 2019.
- [18] P. N. Gillespie and N. Martsinovich, “Origin of charge trapping in TiO<sub>2</sub>/reduced graphene oxide photocatalytic composites: insights from theory,” *ACS Applied Materials & Interface*, vol. 11, no. 35, pp. 31909–31922, 2019.
- [19] M. E. Simonsen and E. G. Sjøgaard, “Sol-gel reactions of titanium alkoxides and water: influence of pH and alkoxy group on cluster formation and properties of the resulting products,” *Journal of Sol-Gel Science and Technology*, vol. 53, no. 3, pp. 485–497, 2010.
- [20] B. Paulchamy, G. Arthi, and B. D. Lignesh, “A simple approach to stepwise synthesis of graphene oxide nanomaterial,” *Journal of Nanomedicine & Nanotechnology*, vol. 6, no. 1, 2015.
- [21] U. Holzwarth and N. Gibson, “The Scherrer equation versus the ‘Debye-Scherrer equation,’” *Nature Nanotechnology*, vol. 6, no. 9, pp. 534–534, 2011.
- [22] D. Khalili, “Graphene oxide: a promising carbocatalyst for the regioselective thiocyanation of aromatic amines, phenols, anisols and enolizable ketones by hydrogen peroxide/KSCN in water,” *New Journal of Chemistry*, vol. 40, no. 3, pp. 2547–2553, 2016.
- [23] L. C. Sim, K. H. Leong, S. Ibrahim, and P. Saravanan, “Graphene oxide and Ag engulfed TiO<sub>2</sub>nanotube arrays for enhanced electron mobility and visible-light-driven photocatalytic performance,” *Journal of Materials Chemistry A*, vol. 2, no. 15, pp. 5315–5322, 2014.
- [24] H. Zhang, X. Wang, N. Li et al., “Synthesis and characterization of TiO<sub>2</sub>/graphene oxide nanocomposites for photoreduction of heavy metal ions in reverse osmosis concentrate,” *RSC Advances*, vol. 8, no. 60, pp. 34241–34251, 2018.
- [25] W. Su, N. Kumar, A. Krayev, and M. Chaigneau, “In situ topographical chemical and electrical imaging of carboxyl graphene oxide at the nanoscale,” *Nature Communications*, vol. 9, pp. 1–7, 2018.
- [26] M. Ceballos-Chuc, C. Ramos-Castillo, J. Alvarado-Gil, G. Oskam, and G. Rodríguez-Gattorno, “Influence of brookite impurities on the Raman spectrum of TiO<sub>2</sub>Anatase nanocrystals,” *The Journal of Physical Chemistry C*, vol. 122, no. 34, pp. 19921–19930, 2018.
- [27] P. Makuła, M. Pacia, and W. Macyk, *How to Correctly Determine the Band Gap Energy of Modified Semiconductor Photocatalysts based on UV-Vis Spectra*, ACS Publications, 2018.
- [28] Y. Liu, H. Ma, X. X. Han, and B. Zhao, “Metal-semiconductor heterostructures for surface-enhanced Raman scattering: synergistic contribution of plasmons and charge transfer,” *Materials Horizons*, vol. 8, pp. 370–382, 2021.
- [29] X. Guo, Z. Guo, Y. Jin, Z. Liu, W. Zhang, and D. Huang, “Silver-gold core-shell nanoparticles containing methylene blue as SERS labels for probing and imaging of live cells,” *Microchimica Acta*, vol. 178, no. 1-2, pp. 229–236, 2012.
- [30] E. C. le Ru, E. Blackie, M. Meyer, and P. G. Etchegoin, “Surface enhanced Raman scattering enhancement factors: a comprehensive study,” *The Journal of Physical Chemistry C*, vol. 111, no. 37, pp. 13794–13803, 2007.
- [31] T. Wu, H. Zheng, Y. Kou et al., “Self-sustainable and recyclable ternary Au@Cu<sub>2</sub>O-Ag nanocomposites: application in ultrasensitive SERS detection and highly efficient photocatalysis of organic dyes under visible light,” *Microsystems & Nanoengineering*, vol. 7, no. 1, p. 23, 2021.
- [32] Y. Zhang, F. Fu, Y. Li, D. Zhang, and Y. Chen, “One-step synthesis of Ag@TiO<sub>2</sub> nanoparticles for enhanced photocatalytic performance,” *Nanomaterials*, vol. 8, no. 12, p. 1032, 2018.
- [33] V. Shvalya, G. Filipič, J. Zavašnik, I. Abdulhalim, and U. Cvelbar, “Surface-enhanced Raman spectroscopy for chemical and biological sensing using nanoplasmonics: the relevance of interparticle spacing and surface morphology,” *Applied Physics Reviews*, vol. 7, no. 3, article 031307, 2020.
- [34] S. Zhang, Y. Xu, D. Zhao, W. Chen, H. Li, and C. Hou, “Preparation of magnetic CuFe<sub>2</sub>O<sub>4</sub>@Ag@ZIF-8 nanocomposites with highly catalytic activity based on cellulose nanocrystals,” *Molecules*, vol. 25, no. 1, p. 124, 2020.
- [35] Q. Zhang, N. Bao, X. Wang et al., “Advanced fabrication of chemically bonded graphene/TiO<sub>2</sub> continuous fibers with enhanced broadband photocatalytic properties and involved mechanisms exploration,” *Scientific Reports*, vol. 6, no. 1, article 38066, 2016.
- [36] L. Jensen, C. M. Aikens, and G. C. Schatz, “Electronic structure methods for studying surface-enhanced Raman scattering,” *Chemical Society Reviews*, vol. 37, no. 5, pp. 1061–1073, 2008.
- [37] H. B. Michaelson, “The work function of the elements and its periodicity,” *Journal of Applied Physics*, vol. 48, no. 11, pp. 4729–4733, 1977.
- [38] M. Alshabib, M. A. Oluwadamilare, A. Tanimu, I. Abdulazeez, K. Alhooshani, and S. A. Ganiyu, “Experimental and DFT investigation of ceria-nanocomposite decorated AC derived

- from groundnut shell for efficient removal of methylene-blue from wastewater effluent,” *Applied Surface Science*, vol. 536, p. 147749, 2021.
- [39] K. Wu, J. Chen, J. R. McBride, and T. Lian, “Efficient hot-electron transfer by a plasmon-induced interfacial charge-transfer transition,” *Science*, vol. 349, no. 6248, pp. 632–635, 2015.
- [40] A. O. Govorov, H. Zhang, and Y. K. Gun’ko, “Theory of photo-injection of hot plasmonic carriers from metal nanostructures into semiconductors and surface molecules,” *The Journal of Physical Chemistry C*, vol. 117, no. 32, pp. 16616–16631, 2013.
- [41] R. Katoh, A. Furube, T. Yoshihara et al., “Efficiencies of electron injection from excited N3 dye into nanocrystalline semiconductor ( $ZrO_2$ ,  $TiO_2$ ,  $ZnO$ ,  $Nb_2O_5$ ,  $SnO_2$ ,  $In_2O_3$ ) films,” *The Journal of Physical Chemistry B*, vol. 108, no. 15, pp. 4818–4822, 2004.
- [42] M. Parashar, V. K. Shukla, and R. Singh, “Metal oxides nanoparticles via sol–gel method: a review on synthesis, characterization and applications,” *Journal of Materials Science: Materials in Electronics*, vol. 31, pp. 3729–3749, 2020.
- [43] C. Srichan, M. Ekpanyapong, M. Horprathum et al., “Highly-sensitive surface-enhanced Raman spectroscopy (SERS)-based chemical sensor using 3D graphene foam decorated with silver nanoparticles as SERS substrate,” *Scientific Reports*, vol. 6, no. 1, article 23733, 2016.
- [44] Y. Xie and Y. Meng, “SERS performance of graphene oxide decorated silver nanoparticle/titania nanotube array,” *RSC Advances*, vol. 4, no. 79, pp. 41734–41743, 2014.
- [45] C. Kästner and A. F. Thünemann, “Catalytic reduction of 4-nitrophenol using silver nanoparticles with adjustable activity,” *Langmuir*, vol. 32, no. 29, pp. 7383–7391, 2016.
- [46] Y. Y. Liu, Y. H. Zhao, Y. Zhou et al., “High-efficient catalytic reduction of 4-nitrophenol based on reusable Ag nanoparticles/graphene-loading loofah sponge hybrid,” *Nanotechnology*, vol. 29, no. 31, p. 315702, 2018.

## Research Article

# Electrochemical Determination of Diclofenac by Using ZIF-67/g-C<sub>3</sub>N<sub>4</sub> Modified Electrode

Dang Thi Ngoc Hoa,<sup>1,2</sup> Nguyen Thi Thanh Tu ,<sup>3</sup> Le Van Thanh Son,<sup>4</sup> Le Vu Truong Son,<sup>4</sup> Tran Thanh Tam Toan,<sup>1</sup> Pham Le Minh Thong,<sup>5</sup> Dao Ngoc Nhiem,<sup>6</sup> Pham Khac Lieu,<sup>7</sup> and Dinh Quang Khieu <sup>1</sup>

<sup>1</sup>University of Sciences, Hue University, 53000, Vietnam

<sup>2</sup>University of Medicine and Pharmacy, Hue University, 55000, Vietnam

<sup>3</sup>Faculty of Technology, Van Lang University, 70000, Vietnam

<sup>4</sup>University of Education and Science, The University of Danang, 55000, Vietnam

<sup>5</sup>Institute of Research and Development, Duy Tan University, 55000, Vietnam

<sup>6</sup>Institute of Materials Science, Vietnam Academy of Science and Technology, 100000, Vietnam

<sup>7</sup>Hue University, 53000, Vietnam

Correspondence should be addressed to Dinh Quang Khieu; [dqkhieu@hueuni.edu.vn](mailto:dqkhieu@hueuni.edu.vn)

Received 30 May 2021; Accepted 19 August 2021; Published 3 September 2021

Academic Editor: Thanh Son Le

Copyright © 2021 Dang Thi Ngoc Hoa et al. This is an open access article distributed under the Creative Commons Attribution License, which permits unrestricted use, distribution, and reproduction in any medium, provided the original work is properly cited.

A facial differential pulse voltammetric procedure using a glassy carbon electrode modified with zeolite imidazolate framework-67/graphitic carbon nitride (ZIF-67/g-C<sub>3</sub>N<sub>4</sub>) for the diclofenac (DCF) determination is demonstrated. ZIF-67/g-C<sub>3</sub>N<sub>4</sub> with different mass ratios of the components was synthesized in a self-assembly process. The obtained materials were characterized by using X-ray diffraction, scanning electron microscopy (SEM), EDX-mapping, and nitrogen adsorption/desorption isotherms. The peak current varies linearly with the DCF concentration in the range of 0.2–2.2 μmol·L<sup>-1</sup> and has a detection limit of 0.071 μmol·L<sup>-1</sup>. The modified electrode exhibits acceptable repeatability, reproducibility, and selectivity towards DCF. The proposed electrode allows determining DCF in human urine without pretreatment, and the results are comparable with those determined with HPLC.

## 1. Introduction

Diclofenac, 2-(2',6'-dichloroanilino) phenylacetic acid (denoted as DCF), is used for the treatment of several diseases, such as ankylosing spondylitis, rheumatoid arthritis, and osteoarthritis [1]. However, diclofenac causes acute hepatotoxicity, and this chemical-driven liver damage leads to the change in the kidney function and gills in rainbow trout (*O. mykiss*). Diclofenac also presents acute toxicity to phytoplankton and zooplankton. Moreover, the possible synergetic effects with other pharmaceuticals or chemicals in the aquatic environment increase the environmental risk [2]. Various techniques have been developed to determine

diclofenac because of the prominence of DCF in the environment and pharmaceutical and clinical applications. The techniques include capillary zone electrophoresis with electrochemical detection [3], high-performance liquid chromatography (HPLC) [4], HPLC combined with solid-phase extraction [5], and spectrofluorimetry [6]. Besides these techniques, electrochemical methods possess several advantages, such as high sensitivity, selectivity, and quick, cheap analysis for actual samples. These techniques use various types of porous materials to modify the working, such as ionic liquid/carbon nanotube-paste electrode [7], carboxyl/multiwalled carbon nanotubes/screen-printed carbon electrode [8], and gold/multiwalled carbon nanotube/glassy carbon electrode [9].

Zeolite imidazolate framework-67 (ZIF-67) is a subclass of metal-organic frameworks (MOFs). It is an organic-inorganic hybrid solid with infinite and uniform crystalline coordination networks consisting of cobalt ions (II) and imidazolate ligands [10]. ZIF-67 exhibits various unique properties, such as thermal and chemical stability, high surface area, large pores, accessible coordinative unsaturated sites, and excellent chemical and solvent stability [10]. At present, ZIF-67 attracts increasing attention from researchers in various fields, such as adsorption and separation [11], catalysis [12], and gas separation [13]. However, its poor electroconductivity leads to limited applications in electrochemistry [14]. Graphitic carbon nitride ( $g\text{-C}_3\text{N}_4$ ) with graphitic-like structure possesses a unique ability to be simply prepared by thermally condensation of cheap nitrogen-rich compounds such as urea, melamine, and cyanamide [15, 16], and this is unlike graphene, reduced graphene oxide, and graphitic oxide that require the more complex synthesis processes. It has gradually attracted attention in multidisciplinary areas due to its characteristic physicochemical properties, such as ability to resist attacks from strong acid/alkaline solution [17], moderate bandgap ( $\sim 2.7$  eV), and superior electronic properties [18]. Therefore, the combination of highly electroconductive  $g\text{-C}_3\text{N}_4$  with large surface area ZIF-67 might lead to versatile materials with properties of both components.

To the best of our knowledge, only a few papers have been reported on the voltammetric or amperometric detection of DCF on a ZIF-67/ $g\text{-C}_3\text{N}_4$  modified electrode. Therefore, to fabricate new electrodes, we expand our research on modifying glassy carbon electrodes (GCE). In the present work, we describe the determination of DCF by using a GCE electrode modified with ZIF-67/ $g\text{-C}_3\text{N}_4$ . This modified electrode exhibits sound electrocatalytic and accumulative effects on DCF and enables us to determine the DCF content in human urine with satisfactory results.

## 2. Experimental

**2.1. Materials.** Melamine ( $\text{C}_3\text{N}_3(\text{NH}_2)_3$ ), absolute ethanol ( $\text{C}_2\text{H}_5\text{OH}$ ), methanol ( $\text{CH}_3\text{OH}$ ), cobalt nitrate hexahydrate ( $\text{Co}(\text{NO}_3)_2 \cdot 6\text{H}_2\text{O}$ ), and 2-methylimidazole ( $\text{CH}_3\text{C}_3\text{H}_2\text{N}_2\text{H}$ ) were purchased from Merck company. Diclofenac sodium salt ( $\text{C}_{14}\text{H}_{10}\text{Cl}_2\text{NNaNO}_2$ ) was procured from Sigma-Aldrich. Acetic acid ( $\text{CH}_3\text{COOH}$ ), phosphoric acid ( $\text{H}_3\text{PO}_4$ ), boric acid ( $\text{H}_3\text{BO}_3$ ), and potassium hydroxide (KOH) were purchased from Daejung (Korea).

The phosphate buffer solution (PBS) with pH 7 was prepared from 0.5 M  $\text{Na}_2\text{HPO}_4$ , 0.5 M  $\text{KH}_2\text{PO}_4$ , 0.5 M NaCl, and 0.5 M KCl solutions. The Britton–Robinson buffer solution (B–RBS) with pH 3–9 was prepared from 1 M  $\text{H}_3\text{BO}_3$ , 1 M  $\text{H}_3\text{PO}_4$ , and 1 M  $\text{CH}_3\text{COOH}$  solutions and adjusted with a 1 M KOH solution. The stock solution was prepared by dissolving 29.6 mg of diclofenac in a 10 mL volumetric flask containing a pH 6 buffer solution. The flask was subjected to ultrasonication in a cold water bath and stored in a refrigerator at 5°C. The stock sample was prepared 30 min before analysis.

**2.2. Material Synthesis.** ZIF-67 was synthesized according to Qian et al. [10]. Briefly, 1.16 g of  $\text{Co}(\text{NO}_3)_2 \cdot 6\text{H}_2\text{O}$  and 1.31 g of 2-methylimidazole (Hmim) were dissolved in 100 mL of methanol separately. These two solutions were mixed so that the resulting mixture has the following molar composition:  $\text{Co}^{2+}/\text{Hmim}/\text{CH}_3\text{OH} = 1 : 4 : 1.2$  and stirred for 24 h at ambient temperature. Then, the purple solid (ZIF-67) was collected by centrifuging, washed with ethanol five times, and dried at 80°C for 24 h.

The  $g\text{-C}_3\text{N}_4$  was synthesized according to Yan et al. [19]. In brief, 10 g of melamine powder was put into an alumina crucible with a cover and heated at 500°C in a muffle furnace for 2 h.

The ZIF-67/ $g\text{-C}_3\text{N}_4$  was synthesized as follows: 0.5 g of the  $g\text{-C}_3\text{N}_4$  and ZIF-67 mixture was distributed in 100 mL of ethanol under ultrasonication for 6 h. The ZIF-67/ $g\text{-C}_3\text{N}_4$  mass ratio is as follows: 0:10, 3:7, 4:6, 5:5, 6:4, and 10:0. The samples are denoted as (0/10)ZIF-67/ $g\text{-C}_3\text{N}_4$ , (3/7)ZIF-67/ $g\text{-C}_3\text{N}_4$ , (4/6)ZIF-67/ $g\text{-C}_3\text{N}_4$ , (5/5)ZIF-67/ $g\text{-C}_3\text{N}_4$ , (6/4)ZIF-67/ $g\text{-C}_3\text{N}_4$ , and (10/0)ZIF-67/ $g\text{-C}_3\text{N}_4$ .

**2.3. Instruments.** The material was characterized by using X-ray diffraction (XRD) with a D8-Advance device (Bruker, USA; Cu  $K\alpha$  radiation,  $\lambda = 1.5406$  Å), scanning electron microscopy (SEM) with JMS-5300LV (USA), Raman spectroscopy with Xplora Plus (Horiba with 785 nm laser excitation), transmission electron microscopy (TEM) with JEM-2100, and nitrogen adsorption/desorption isotherms with a Micromeritics 2020 volumetric adsorption analyzer system (the sample was degassed at 150°C for 12 h). The specific surface area was calculated according to the Brunauer–Emmett–Teller (BET) model. The meso/micro-surface area was calculated with the  $t$ -plot method. Electrochemical measurements were conducted with a CPA-HH5 computerized polarography analyzer (Vietnam). A three-electrode system consisting of a working electrode (GCE,  $0.28$  cm<sup>2</sup>), a reference electrode (Ag/AgCl in saturated KCl), and a counter electrode (platinum wire) was used for the measurements. The high-performance liquid chromatography (HPLC) was performed to measure DLF for the sake of comparison. The HPLC measurements were conducted on an HPLC Shimadzu with LC 20 AD pump, PDA SPD–M20A detector (Japan), C18 column ( $250 \times 4.6$  mm; particle size  $5$  μm). The mobile phase is a mixture of methanol/5 mM  $\text{NaH}_2\text{PO}_4$  (pH 2.3) (66:34 v/v). The flow rate was  $1$  mL·min<sup>-1</sup> with an injection volume of  $20$  μL. For HPLC analysis, DCF detection was performed at a wavelength of 274 nm.

### 2.4. Preparation of Electrode and Actual Sample

**2.4.1. Electrode Preparation.** Prior to modification, the GCE was first polished with alumina slurry ( $0.05$  μm) on a polishing pad, followed by successive ultrasonication in ethanol and distilled water. Then, the electrode was washed with double distilled water and dried at ambient temperature. The suspension of ZIF-67/ $g\text{-C}_3\text{N}_4$  was prepared by mixing 10 mg of ZIF-67/ $g\text{-C}_3\text{N}_4$  with 10 mL of ethanol under ultrasonication for 24 h. Five microliters of suspension was cast dropwise on the GCE surface and dried in an oven for a

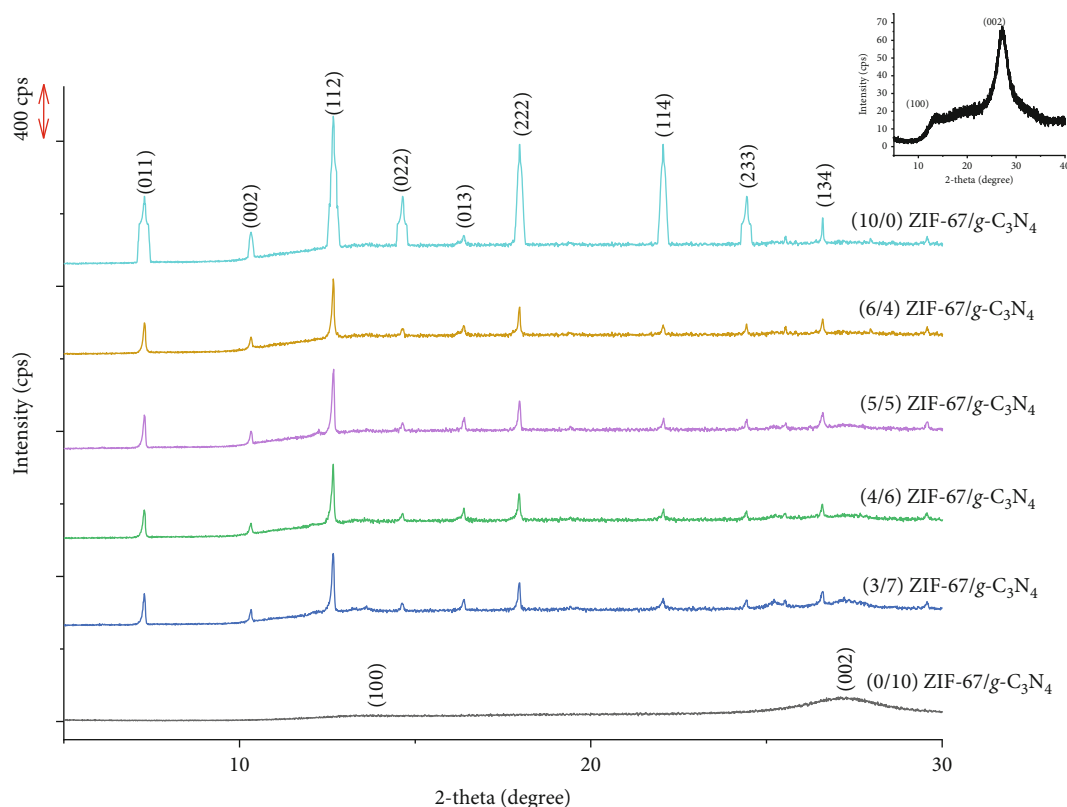


FIGURE 1: XRD patterns of ZIF-67,  $g\text{-C}_3\text{N}_4$ , and ZIF-67/ $g\text{-C}_3\text{N}_4$  (the inset presents the XRD pattern of (0/10)ZIF-67/ $g\text{-C}_3\text{N}_4$ ).

few minutes. The *as*-prepared electrode was denoted as ZIF-67/ $g\text{-C}_3\text{N}_4$ -GCE.

**2.4.2. Real Samples.** Human urine samples were received from five healthy persons aged 25–30 and stored in a refrigerator at 5°C. About 5 mL of the sample was filtered through a 0.2  $\mu\text{m}$  membrane. One milliliter of the supernatant was collected and diluted with 2 mL of pH 6.5 BRS to avoid complex interference. The resulting solution was transferred to a 100 mL electrochemical cell for analysis.

### 3. Results and Discussion

**3.1. Characterization of Materials.** The XRD patterns of  $g\text{-C}_3\text{N}_4$ , ZIF-67, and ZIF-67/ $g\text{-C}_3\text{N}_4$  are shown in Figure 1. Two peaks at around 13.7 and 27.1° are found in  $g\text{-C}_3\text{N}_4$  ((0/10)ZIF-67/ $g\text{-C}_3\text{N}_4$ ). It is well known that  $g\text{-C}_3\text{N}_4$  consists of tri-s-triazine building blocks [20]. The higher peak at 27.1° is assigned to the characteristic interlayer of aromatic systems, indexed for graphitic materials as (002), while the peak at 13.7°, indexed as (100), is attributed to the periodic arrangement of the condensed tri-s-triazine units in the sheets [21] (the inset of Figure 1). For the XRD pattern of (10/0)ZIF-67/ $g\text{-C}_3\text{N}_4$ , the characteristic peaks for ZIF-67 at 18.20, 30.22, 35.68, 43.28, 53.68, 57.18, and 62.76°, indexed as (111), (220), (311), (400), (422), (511), and (440) according to CCDC 671073, are clearly observed indicating that the (10/0)ZIF-67/ $g\text{-C}_3\text{N}_4$  is ZIF-67. The intensity of these peaks in ZIF-67/ $g\text{-C}_3\text{N}_4$  increases with an increase in the ZIF-

67/ $g\text{-C}_3\text{N}_4$  fraction. This increase manifests the coexistence of  $g\text{-C}_3\text{N}_4$  and ZIF-67 phases in the composite. Clear characteristic peaks of ZIF-67 witness that the hybrid of ZIF-67 with  $g\text{-C}_3\text{N}_4$  has no significant effects on the crystal structure of ZIF-67.

Nitrogen adsorption/desorption isotherms are employed to evaluate the samples' specific surface area and porosity (Figure 2). The isotherm curves of ZIF-67 have a type I isotherm, indicating the presence of a microporous material. The  $g\text{-C}_3\text{N}_4$  has a type IV isotherm with an H3 hysteresis loop at high relative pressure between 0.46 and 1.0, confirming the existence of a mesoporous structure. The BET surface area ( $S_{\text{BET}}$ ) and total pore volume ( $V_{\text{pore}}$ ) are listed in Table 1.

Compared with pure ZIF-67, the ZIF-67/ $g\text{-C}_3\text{N}_4$  has the  $S_{\text{BET}}$  declining from 1217.1 to 335.6  $\text{m}^2\cdot\text{g}^{-1}$  as the amount of  $g\text{-C}_3\text{N}_4$  increases. This decline might result from the low surface area of  $g\text{-C}_3\text{N}_4$  and blockage of micropores of the increasing  $g\text{-C}_3\text{N}_4$  amount in the composite. The primary test reveals that the (5/5)ZIF-67/ $g\text{-C}_3\text{N}_4$  sample has the highest electrocatalytic activity for DCF oxidation. Therefore, (5/5)ZIF-67/ $g\text{-C}_3\text{N}_4$  is selected for further experiments.

As shown in Figure 3(a), smooth rhombic dodecahedral-shaped crystals with 1.5  $\mu\text{m}$  in width are observed for ZIF-67. The surface of  $g\text{-C}_3\text{N}_4$  exhibits a layered and platelet-like morphology (Figure 3(b)). Although several inclusions of  $g\text{-C}_3\text{N}_4$  appear on the ZIF-67 surface, the rhombic dodecahedral structure of ZIF-67 remains (Figure 3(c)). The TEM image illustrates a sheet-like structure of  $g\text{-C}_3\text{N}_4$  embroiled with dark-colored ZIF-67 crystals

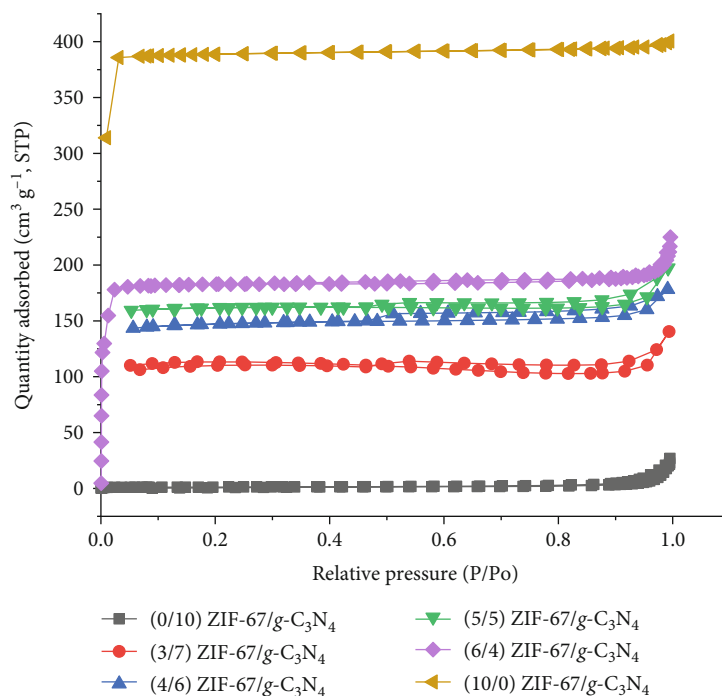


FIGURE 2: Nitrogen adsorption/desorption isotherms of ZIF-67,  $g\text{-C}_3\text{N}_4$ , and ZIF-67/ $g\text{-C}_3\text{N}_4$ .

TABLE 1: Textural properties of ZIF-67/ $g\text{-C}_3\text{N}_4$ .

Notation	$S_{\text{BET}}$ ( $\text{m}^2\cdot\text{g}^{-1}$ )	$S_{\text{meso}}$ ( $\text{m}^2\cdot\text{g}^{-1}$ )	$S_{\text{micro}}$ ( $\text{m}^2\cdot\text{g}^{-1}$ )	$V_{\text{total}}$ ( $\text{cm}^3\cdot\text{g}^{-1}$ )
(0/10)ZIF-67/ $g\text{-C}_3\text{N}_4$	4.2	2.7	1.5	26.9
(3/7)ZIF-67/ $g\text{-C}_3\text{N}_4$	335.6	25.1	310.5	140.4
(4/6)ZIF-67/ $g\text{-C}_3\text{N}_4$	449.0	9.8	439.2	197.3
(5/5)ZIF-67/ $g\text{-C}_3\text{N}_4$	492.0	10.5	481.5	178.2
(6/4)ZIF-67/ $g\text{-C}_3\text{N}_4$	731.9	10.6	721.3	225.0
(10/0)ZIF-67/ $g\text{-C}_3\text{N}_4$	1217.1	6.9	1210.1	400.6

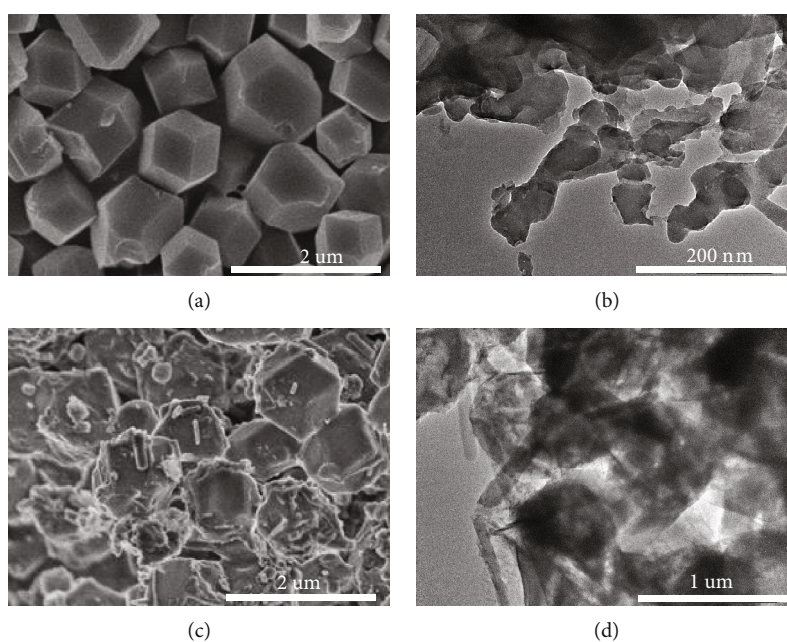
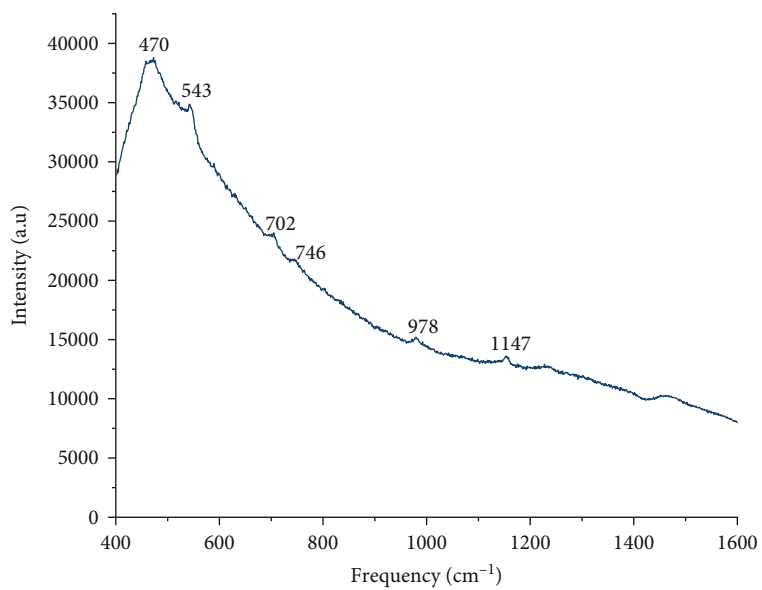
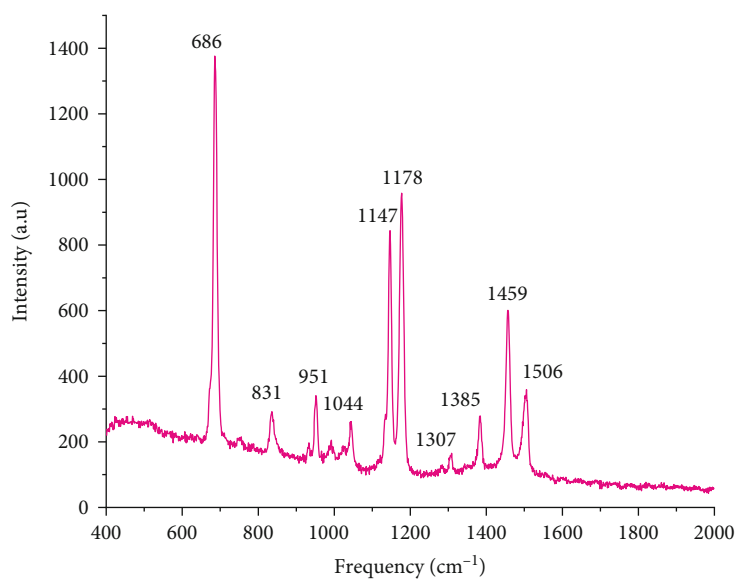


FIGURE 3: (a) SEM image of ZIF-67, (b) TEM image of  $g\text{-C}_3\text{N}_4$ , (c) SEM image of ZIF-67/ $g\text{-C}_3\text{N}_4$ , and (d) TEM image of (5/5)ZIF-67/ $g\text{-C}_3\text{N}_4$ .



(a)



(b)

FIGURE 4: Continued.

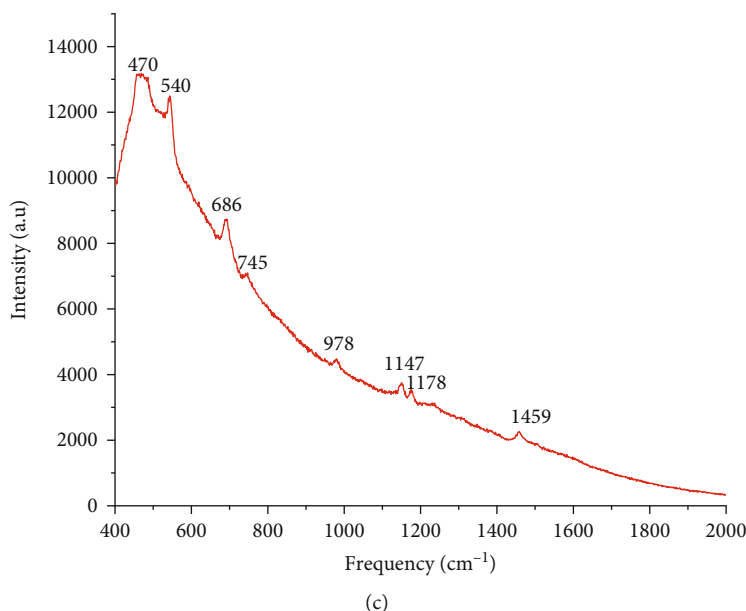


FIGURE 4: Raman spectra of (a)  $g\text{-C}_3\text{N}_4$ , (b) ZIF-67, and (c) ZIF-67/ $g\text{-C}_3\text{N}_4$ .

(Figure 3(d)). These results indicate the coexistence of ZIF-67 and  $g\text{-C}_3\text{N}_4$  via self-assembly.

The ZIF-67/ $g\text{-C}_3\text{N}_4$  structure is characterized by using Raman spectra (Figure 4). Typical characteristic peaks of  $g\text{-C}_3\text{N}_4$  at 470, 543, 702, 746, 978, and 1147  $\text{cm}^{-1}$  are observed, and they are consistent with those in a previously published report [22]. The peaks at 702 and 978  $\text{cm}^{-1}$  indicate the existence of the heptazine ring structure [23]. The peak at 702  $\text{cm}^{-1}$  is ascribed to the inplane bending vibrations of the heptazine linkages, whereas the 978  $\text{cm}^{-1}$  peak is assigned to the symmetric N-breathing mode of the heptazine units [24]. For ZIF-67, characteristic peaks at 686, 831, 951, 1044, 1147, 1178, 1307, 1385, 1459, and 1506  $\text{cm}^{-1}$  are attributed to the cobalt ion [25], imidazolium ring puckering,  $\delta$  H (out of plane), bending C-H (out of plane) (C4-C5), bending C-H (out of plane) (C2-H), stretching C-N, N-H wag, bending of  $\text{CH}_3$ , stretching of C2-N1, and stretching of C-H (methyl), respectively [26]. The characteristic vibrations of ZIF-67 and  $g\text{-C}_3\text{N}_4$  in the Raman spectrum of ZIF-67/ $g\text{-C}_3\text{N}_4$  confirm the coexistence of ZIF-67 and  $g\text{-C}_3\text{N}_4$  again.

The elemental composition of ZIF-67/ $g\text{-C}_3\text{N}_4$ , derived from the EDX spectrum, is presented in Figure 5. As expected, the elements in (5/5)ZIF-67/ $g\text{-C}_3\text{N}_4$  are only carbon (at 0.3 keV), nitrogen (0.4 keV), oxygen (0.6 keV), and cobalt (0.8; 7.0; 7.7 keV), indicating that the obtained material has high purity (Figures 5(a) and 5(b)). The EDX mapping of carbon (Figure 5(c)), cobalt (Figure 5(d)), nitrogen (Figure 5(e)), and oxygen (Figure 5(f)) on the ZIF-67/ $g\text{-C}_3\text{N}_4$  surface shows that all these elements are not confined to a single site. Instead, they are distributed in the matrix.

Although Figure 6 shows that ZIF-67 could attach to the surface of  $g\text{-C}_3\text{N}_4$ , such self-assembly can be further confirmed by studying the surface charges of ZIF-67,  $g\text{-C}_3\text{N}_4$ , and their composite (Figure 6). These values are determined with the drift pH method [27]. As seen from the figure, the

material's surface is positively charged when  $\text{pH} < 9.2$  for ZIF-67 and  $\text{pH} < 3.8$  for  $g\text{-C}_3\text{N}_4$ . Therefore, the electrostatic attraction between ZIF-67 and  $g\text{-C}_3\text{N}_4$  could form ZIF-67/ $g\text{-C}_3\text{N}_4$  with a positively charged surface at pH below 8.4.

The stability of (5/5)ZIF-67/ $g\text{-C}_3\text{N}_4$  in the solutions with different pHs is essential for the electrochemical application. Figure 7 presents the XRD patterns of (5/5)ZIF-67/ $g\text{-C}_3\text{N}_4$  immersed in water with different pHs for 5 hours. At pH less than 4, the characteristic diffractions of ZIF-67 are absent, revealing that the material is destroyed at these pHs. The peaks of ZIF-67 remain in the solutions with pH 5–10, indicating that ZIF-67 is stable in this pH range.

### 3.2. Electrochemical Determination of Diclofenac by Using (5/5)ZIF-67/ $g\text{-C}_3\text{N}_4$

**3.2.1. The Cyclic Voltammetry of DCF on (5/5)ZIF-67/ $g\text{-C}_3\text{N}_4$  Modified Electrode (ZC-GCE).** The cyclic voltammograms (CVs) (Figure 8) are obtained in the presence of 5 mM DCF on GCE, ZIF-67-GCE,  $g\text{-C}_3\text{N}_4$ -GCE, and ZIF-67/ $g\text{-C}_3\text{N}_4$ -GCE in 0.2 M BRS pH 6. The bare GCE does not exhibit any electrochemical signals, indicating that this electrode cannot detect DCF. The modified electrodes (with ZIF-67,  $g\text{-C}_3\text{N}_4$ , or ZIF-67/ $g\text{-C}_3\text{N}_4$ ) exhibit an oxidation peak of DCF at around 0.68 V. In particular, the ZIF-67/ $g\text{-C}_3\text{N}_4$  modified electrode significantly enhances the electrochemical response, and the intensity of peak current depends on the ZIF-67 and  $g\text{-C}_3\text{N}_4$  mass ratio. The (5/5)ZIF-67/ $g\text{-C}_3\text{N}_4$ -GCE (henceforth denoted as ZC-GCE) provides the highest intensity with a peak potential of 0.671 V. The peak current is 2.1-fold and 2.12-fold higher than that of  $g\text{-C}_3\text{N}_4$ /GCE and ZIF-67-GCE, respectively. The substantial enhancement in the anodic peak current clearly shows the catalytic effect of ZIF-67/ $g\text{-C}_3\text{N}_4$ . No reduction peaks are observed on the reverse scan, indicating that the electron transfer on the ZC modified electrode is

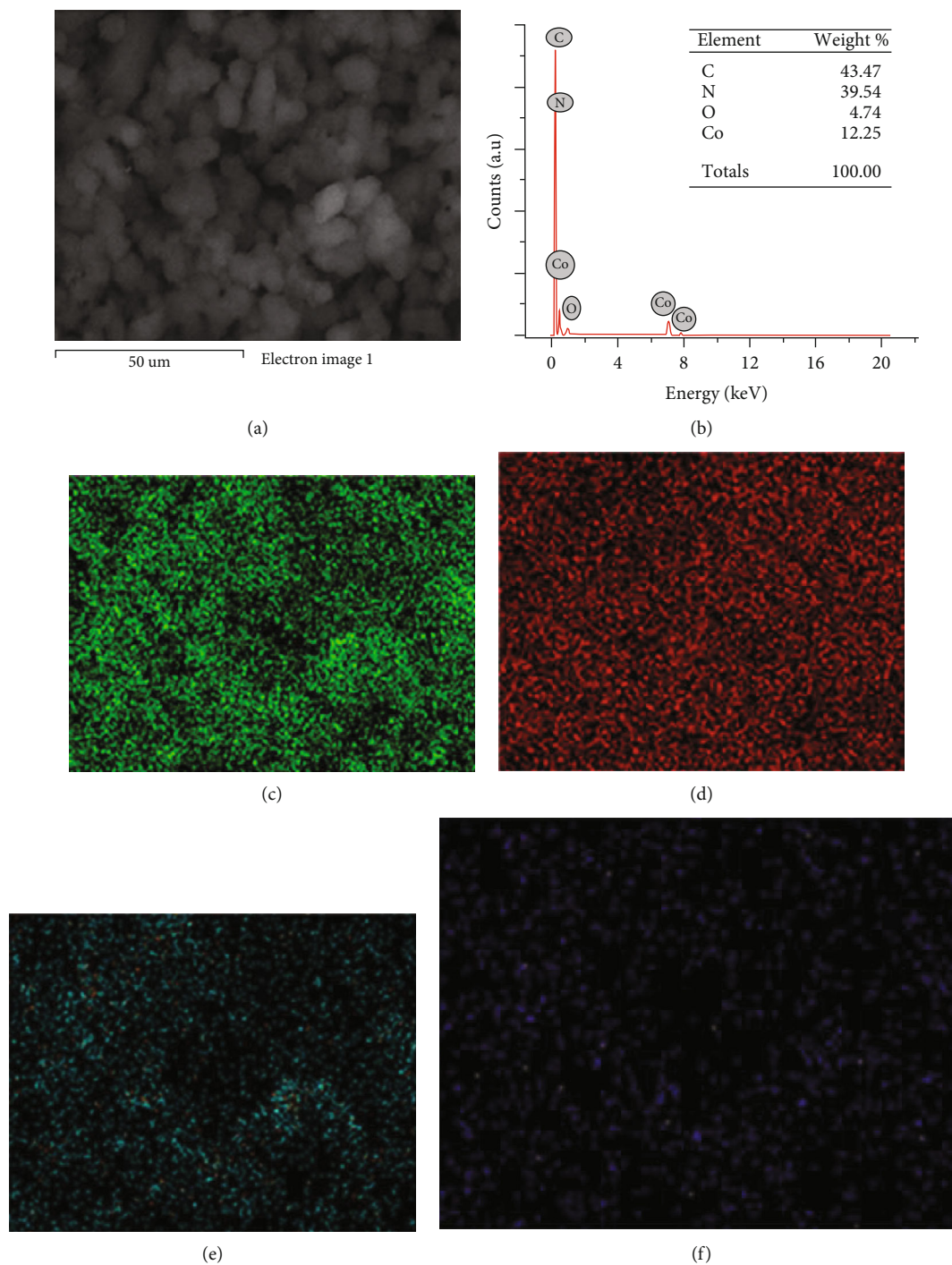


FIGURE 5: EDX-mapping of electron image for ZIF-67/ $g\text{-C}_3\text{N}_4$  (a, b), carbon element (c), cobalt element (d), nitrogen element (e), and oxygen element (f).

irreversible. In addition, the ZC-GCE does not exhibit an oxidation/reduction peak on the voltammogram in the solution without DCF, indicating the ZC-GCE is inactive in the studied potential range.

(1) *Effect of pH.* The influence of pH on the oxidation peak current of the  $5.0 \times 10^{-3}$  M DCF solution is studied by using CV in the BR buffer. At pH 3–5, DCF oxidation at the elec-

trode is not observed. It is possibly due to the unstable structure of ZIF-67 in ZIF-67/ $g\text{-C}_3\text{N}_4$  in this pH range (Figure 7). The peak current increases with pH and has the highest value at pH 6.5. Higher pHs witness a decrease of the peak current up to pH 8, and then the current increases again (Figure 9(c)). Therefore, pH 6.5 is selected for further experiments. The point of zero charge of ZIF-67/ $g\text{-C}_3\text{N}_4$  is 8.4, and the  $pK_a$  of DCF is around 4 [28]. The pH dependence

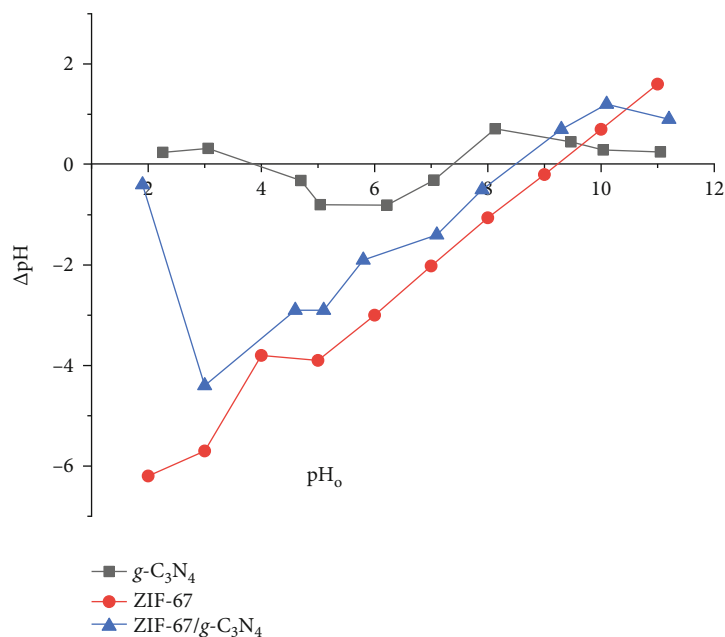


FIGURE 6: Point of zero charge ( $\text{pH}_{\text{PZC}}$ ) of (5/5)ZIF-67/ $g\text{-C}_3\text{N}_4$ , ZIF-67, and  $g\text{-C}_3\text{N}_4$ .

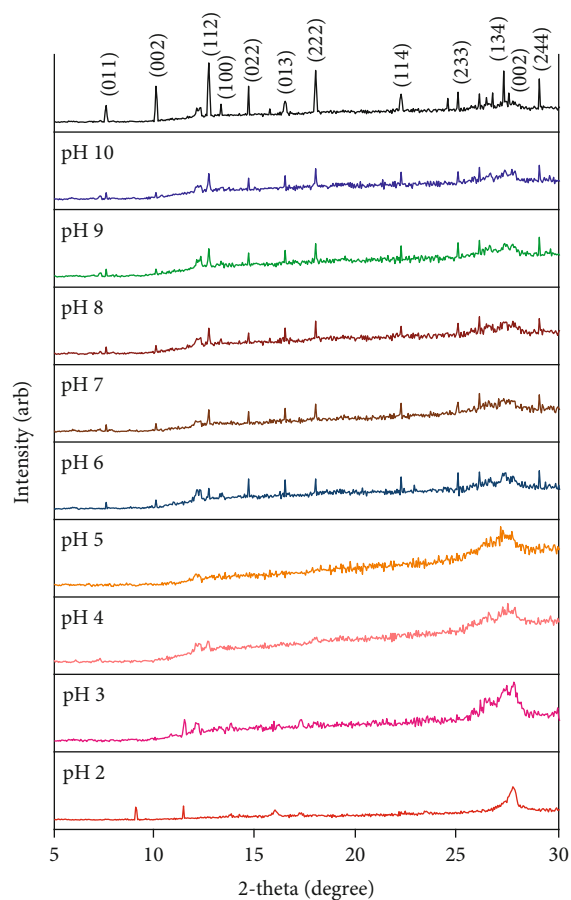


FIGURE 7: XRD patterns of (5/5)ZIF-67/ $g\text{-C}_3\text{N}_4$  at pH 2–10.

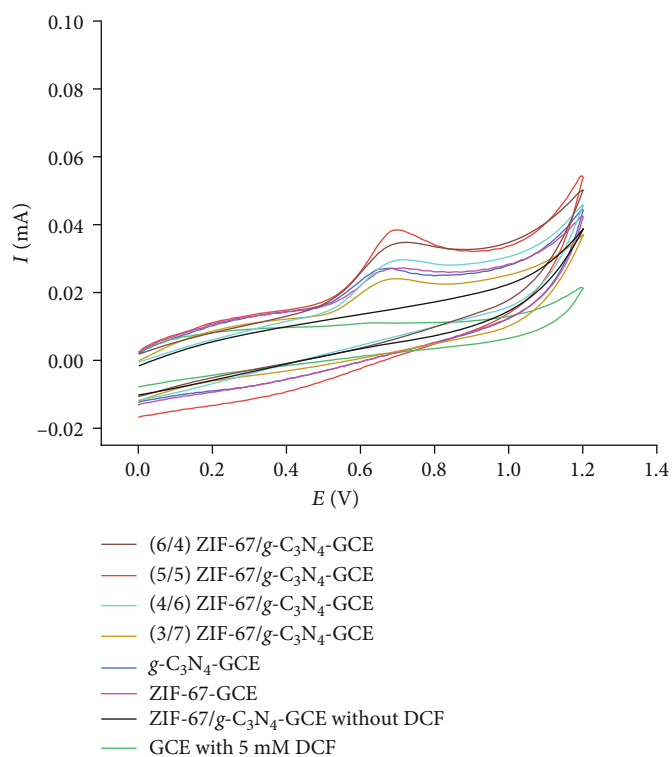


FIGURE 8: Cyclic voltammograms of 5 mM DCF in 0.2 M BRB pH 6 on GCE, ZIF-67-GCE,  $g\text{-C}_3\text{N}_4$ -GCE, and ZIF-67/ $g\text{-C}_3\text{N}_4$ -GCE.

of peak currents of DCF oxidation could not be explained by the electrostatic interaction between charged species on the opposite sites. This process may follow a mechanism different from electrostatic interaction.

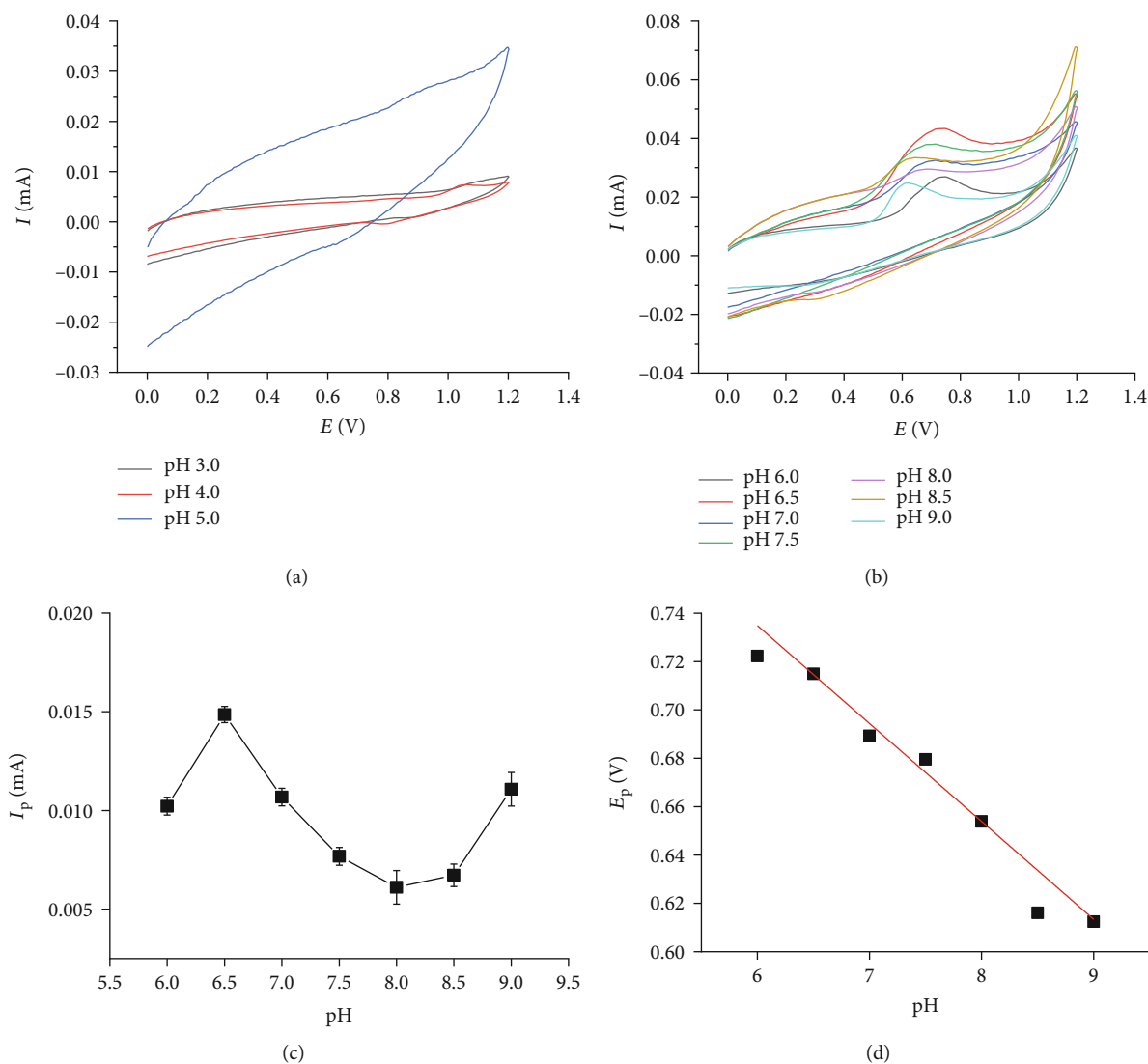


FIGURE 9: CVs of 5 mM DCF with (a) pH 3–5, (b) pH 6–9 in 0.2 M BRB, (c)  $I_p$  vs. pH, and (d)  $E_p$  vs. pH.

When pH is greater than 5, the peak potential decreases, suggesting the involvement of protons in the oxidation reaction (Figure 9(d)). The peak potential in the DCF oxidation on the ZC-GCE decreases linearly with the pH of the buffer solution according to the following equation:  $E_{pa} \text{ (V)} = -0.0514 \times \text{pH} + 0.9409$  ( $r^2 = 0.9988$ ). The slope of the equation is close to the Nernstian value ( $-0.0592 \text{ mV}$ ) for the electrochemical processes involving an equal number of protons and electrons.

(2) *Effect of Scan Rate.* The scan rate of CVs is chosen from 0.1 to  $0.5 \text{ mV} \cdot \text{s}^{-1}$ . In this range, the anodic peak current increases (Figure 10(a)). The highly linear relationship between  $I_p$  and the scan rate manifests that the electrode process is predominantly controlled by adsorption [29] (Figure 10(b)). The scan rate effect is also examined from the function  $I_p = f(v^{1/2})$  plot. A straight line passing the origin suggests an adsorption-controlled electrode process [30]. This relationship in our study is  $I_p = (0.003 \pm 0.011) + (0.028 \pm 0.006) \times v^{1/2}$ ;  $r =$

0.927. With the 95% confident interval, the intercept passes 0 (between  $-0.008$  and  $0.014$ ) and confirms an adsorption-controlled process again.

The relationship between the peak potential and the natural logarithm of the scan rate can provide the number of electrons transferred ( $n$ ) on the electrode surface. For an irreversible system, this relationship is described by Laviron's equation [31]:

$$E_p = E^0 - \frac{R \times T}{(1 - \alpha) \times n \times F} \times \ln \frac{R \times T \times K_s}{(1 - \alpha) \times n \times F} + \frac{R \times T}{(1 - \alpha) \times n \times F} \times \ln v, \quad (1)$$

where  $\alpha$  is the electron-transfer coefficient,  $K_s$  is the apparent charge-transfer rate constant,  $n$  is the number of electrons transferred,  $v$  is the scan rate ( $\text{V} \cdot \text{s}^{-1}$ ),  $R = 8.314 \text{ J} \cdot \text{mol}^{-1} \cdot \text{K}^{-1}$ , and  $F = 96500 \text{ C} \cdot \text{mol}^{-1}$  at 298 K. The linear regression of  $E_p$  versus  $\ln(v)$  is as follows:

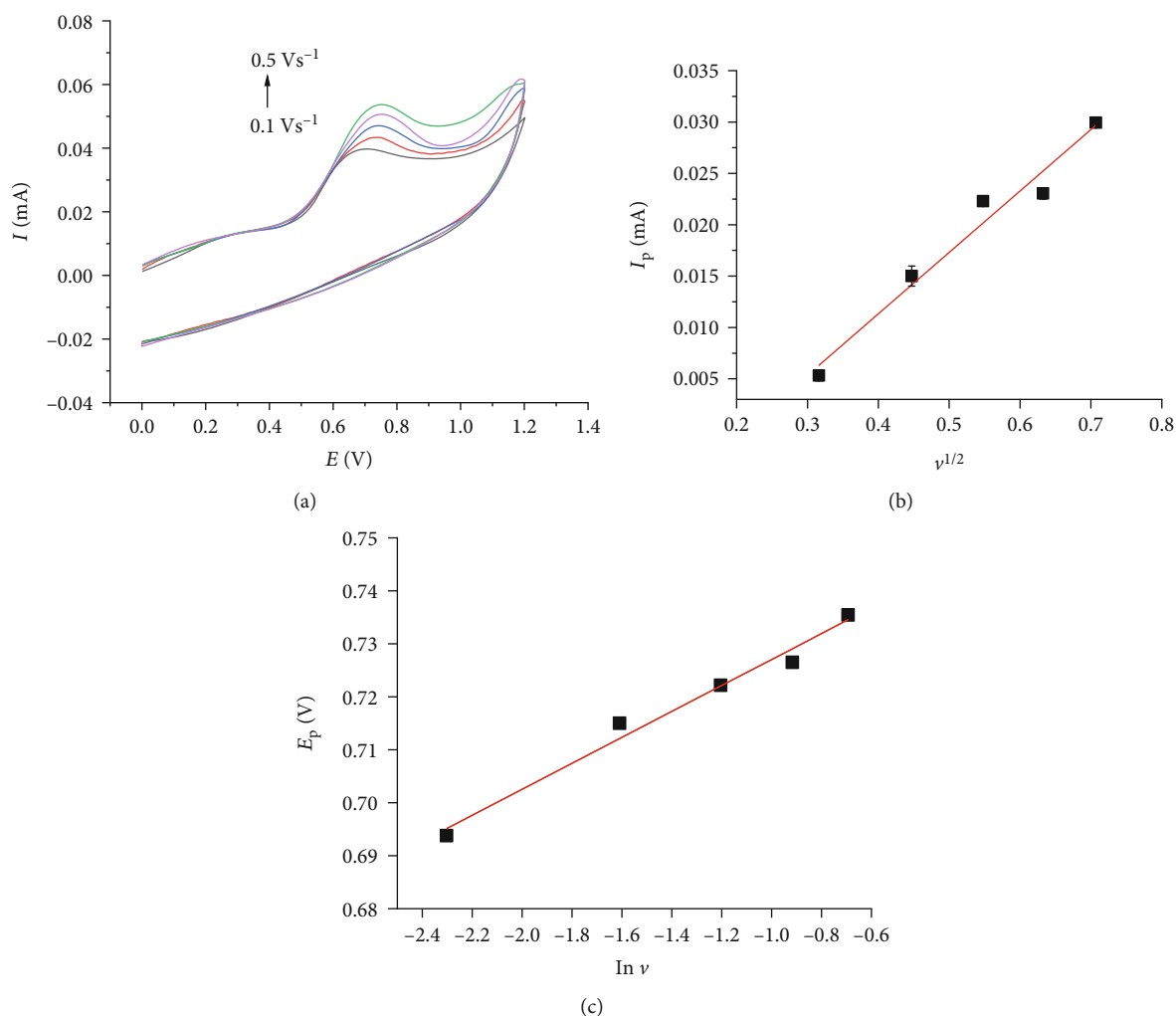
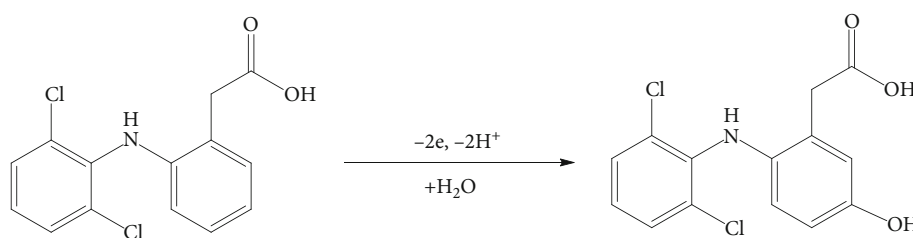


FIGURE 10: CVs of 5 mM DCF at various scan rates in 0.2 M BRS pH 6.5 on ZIF-67/ $g\text{-C}_3\text{N}_4$  (a), the plot of  $I_p$  vs.  $v^{1/2}$  (b), and  $E_p$  vs.  $\ln v$  (c).



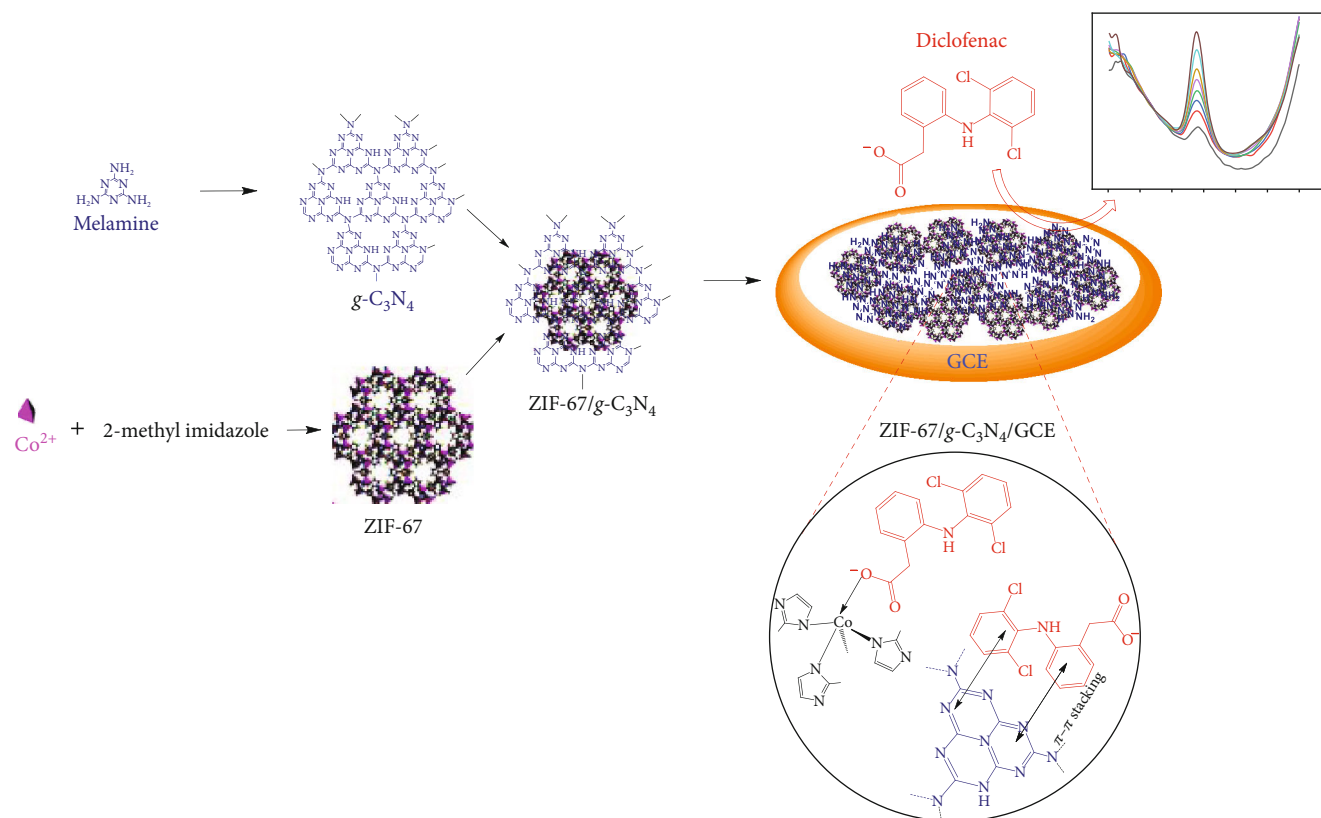
SCHEME 1: Oxidation mechanism of DCF on ZC-GCE.

$$E_p = (0.751 \pm 0.002) + (0.025 \pm 0.001) \times \ln v; r = 0.991. \quad (2)$$

The value of  $(1 - \alpha) \times n$  calculated from the slope of this straight line is 0.95. For an irreversible system,  $\alpha$  is considered as 0.5 [32]; therefore, the value of  $n$  is equal to 1.9 ( $\approx 2$ ). Considering the pH effect on the anodic peak current, we can conclude that the redox reaction on the modified electrode involves the transfer of two electrons and two protons.

These results are consistent with those reported by Madsen et al. [33] and Goyal et al. [34], in which DCF is oxidized to 5-hydrodiclofenac via losing two electrons and two protons, as shown in Scheme 1.

The enhancement of electrochemical signals could result from the synergic effect of ZIF-67 and  $g\text{-C}_3\text{N}_4$ . The open Co(II) sites, as a Lewis acid [35], could attract the carboxyl group in DCF, and as a Lewis base via acid-base interaction, the graphitic rings in  $g\text{-C}_3\text{N}_4$  could attract the benzene rings in DCF via  $\pi\text{-}\pi$  interaction. These arguments are schematically illustrated in Scheme 2.



SCHEME 2: Schematic illustration of the formation of ZIF-67/ $g\text{-C}_3\text{N}_4$  modified GCE and its oxidation of DCF.

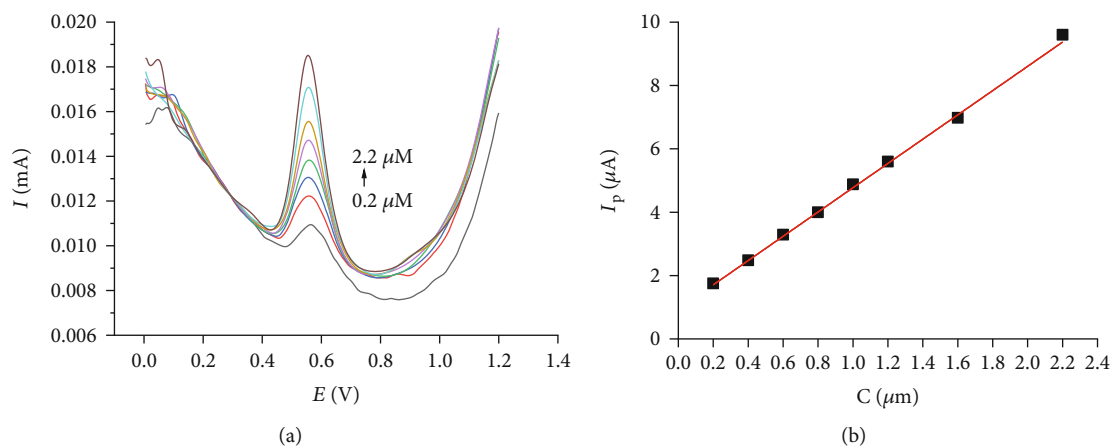


FIGURE 11: DPV curves of DCF with different concentrations (0.2–2.2  $\mu\text{M}$ ) in 0.2 M BRS pH 6.5 at the modified electrode (a). The plot of  $I_p$  vs. concentration (b).

### 3.2.2. Linear Range, Detection Limit, Repeatability, and Interference

(1) *Linear Range and Detection Limit.* The relationship between the peak current and DCF concentration is studied by using differential pulse voltammetry (DPV). In this case, the peak current increases linearly with the concentration of DCF, from 0.2 to 2.2  $\mu\text{M}$  (Figure 11). The regression equation is  $I_p = (0.941 \pm 0.02) + (3.889 \pm 0.03) \times C$ ;  $r = 0.999$ . The LOD ( $3S/n$ ) is 0.071  $\mu\text{M}$ . The detection limit, the linear range, and the sensitivity of the proposed DPV method are

compared with previously reported values for the determination of DCF (Table 2). Although the proposed electrode has a relatively narrow linear range, it has high sensitivity and a lower detection limit. This method can be used to determine DCF in pharmaceuticals and water samples in the micromole range.

(2) *Reproducibility and Repeatability.* The reproducibility is studied from four replicates measurements of DCF determination. To investigate the repeatability of this modified electrode, we conduct the measurements ten times with the

TABLE 2: Comparison of the analytical performance of the different modified electrodes for the determination of DCF.

Electrodes	Technique	Linear range ( $\mu\text{M}$ )	LOD ( $\mu\text{M}$ )	References
Gold nanoparticle/multiwalled carbon nanotube modified glassy carbon electrode	SWV	0.03–200	0.02	[9]
Cu-doped zeolite-expanded graphite-epoxy electrode	DPV	0.3–20	0.05	[36]
APTES-amino-AT-silica/GCE	SWV	0.3–20	0.053	[37]
Gold nanoparticles decorated multiwalled carbon nanotubes/graphene oxide/AuE	DPV	0.4–80	0.09	[38]
Ionic liquid modified carbon nanotube paste electrode	DPV	0.5–300	0.2	[7]
Amino-AT/GCE	SWV	0.3–20	0.204	[37]
Au-Pt bimetallic nanoparticles decorated multiwalled carbon nanotubes/gold electrode	DPV	0.5–1000	0.3	[39]
ZIF-67/g-C <sub>3</sub> N <sub>4</sub>	DPV	0.2–2.2	0.071	The present work

Square wave voltammetry: SWV.

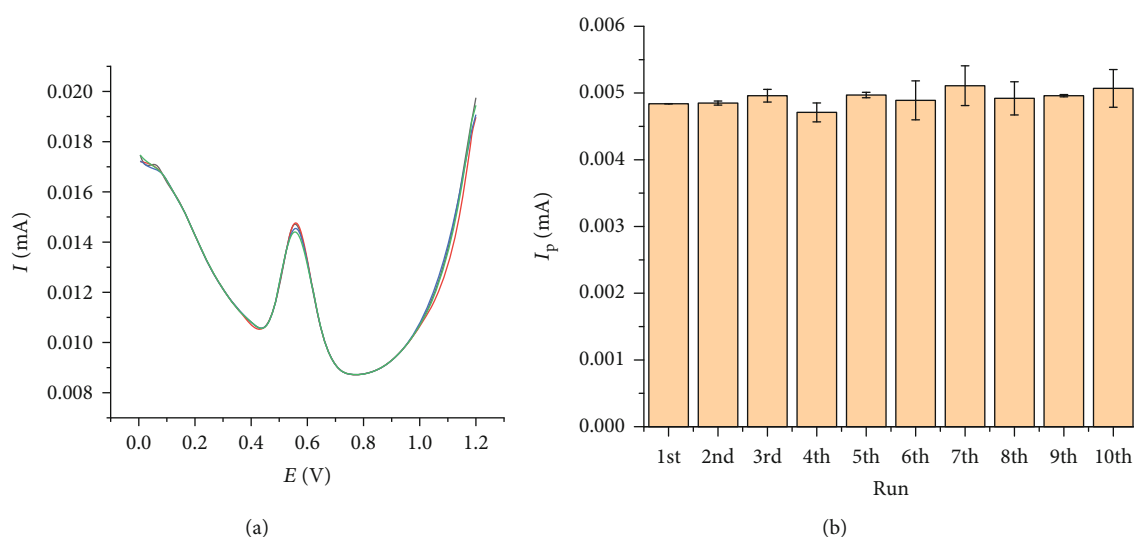


FIGURE 12: The DPV of four replicates measurement (a) and the values of peak current of DCF on ZC-GCE modified using (5  $\mu\text{L}$  ZC (1 mg/mL) for ten times on the same electrode (b).

sample electrode. Figure 12(a) shows very similar DPV curves of four scans on the same working electrode. The small RSD of 1.32% indicates good reproducibility of the proposed method. Figure 12(b) presents the values of peak currents measured on 10 distinct working electrodes under the same modified electrode procedure. The RSD varies from 0.151% to 5.315% in run 1 to run 10, manifesting excellent repeatability.

The biological sample is a very complex mixture consisting of various ions and molecules. Possible interfering electroactive species on the biological samples include inorganic salts ( $\text{KHCO}_3$ ,  $\text{Na}_2\text{SO}_4$ ,  $\text{CaCl}_2$ , and  $\text{NH}_4\text{NO}_3$ ) and organic compounds (uric acid, caffeine, paracetamol, and ascorbic acid). Table 3 reveals that inorganic salts do not significantly interfere with the measurement even at extremely high content (100–320 fold). Ascorbic acid does not seem to affect the peak current at 480-fold concentra-

TABLE 3: Effect of some foreign substances on the determination of 1  $\mu\text{M}$  DFC in 0.2 M BRBS pH 6.5.

Interferents	Tolerance level (M/M)	Rev. (%)
$\text{KHCO}_3$	320	6.80
$\text{Na}_2\text{SO}_4$	480	13.57
$\text{CaCl}_2$	320	12.86
$\text{NH}_4\text{NO}_3$	80	6.58
Uric acid	80	6.34
Caffeine	80	10.14
Paracetamol	40	5.13
Ascorbic acid	480	9.38

tion. Paracetamol, uric acid, and caffeine exert a medium effect on the peak current at a concentration of 40 to 80-fold higher than that of DCF. These results confirm the relevant selectivity of the proposed method for DCF detection.

TABLE 4: The results of DCF analysis in urine by the proposed DPV method and HPLC.

Sample	DPV analysis			Rev (%)	HPLC analysis	
	Original content ( $\mu\text{M}$ )	Spiked ( $\mu\text{M}$ )	Found ( $\mu\text{M}$ )		Original content ( $\mu\text{M}$ )	Found ( $\mu\text{M}$ )
Urine 1	—	50	51.243 $\pm$ 0.229	102.49	—	48.931 $\pm$ 0.015
Urine 2	—	50	48.102 $\pm$ 0.085	96.20	—	47.823 $\pm$ 0.204
Urine 3	—	50	49.215 $\pm$ 0.081	98.43	—	50.387 $\pm$ 0.139
Urine 4	0.257 $\pm$ 0.074	50	54.013 $\pm$ 0.167	104.96	0.261 $\pm$ 0.009	52.715 $\pm$ 0.077
Urine 5	—	50	47.692 $\pm$ 0.073	95.38	—	47.570 $\pm$ 0.008

(-): not found.

**3.2.3. Real Sample Analysis.** This DPV method is used to analyze five actual human urine samples. To determine the method's accuracy, we spike each sample with 50  $\mu\text{M}$  of DCF, and the relative recovery (Rev.) is calculated. All the values fall in the expectable range of 95.4–105% (Table 4). The content of DCF in the samples is also determined with the HPLC method for comparison. When  $\alpha = 0.05$ , the paired samples  $t$ -test proves that there is no statistically significant difference between the two methods ( $p_{\text{two-tailed}} = 0.388 (>0.05)$ ;  $t(4) = 0.968$ ). These results demonstrate a good performance of the presented method for the determination of DCF in urine samples.

## 4. Conclusion

In this research, we successfully synthesized ZIF-67/ $g\text{-C}_3\text{N}_4$  with the self-assembly method and used the material to modify a glassy carbon electrode for the electrocatalytic determination of diclofenac. The  $g\text{-C}_3\text{N}_4$  is highly dispersed in ZIF-67 through an ultrasonic assisted stir to form a composite of  $g\text{-C}_3\text{N}_4$  and ZIF-67. The enhancement of electrochemical signals is due to the synergic effect of ZIF-67 and  $g\text{-C}_3\text{N}_4$ . The oxidation of diclofenac on the modified electrode takes place with a two-electron-proton mechanism. The electrode process is controlled by adsorption. The proposed DPV method exhibits high sensitivity with a low detection limit and can be used to determine diclofenac at trace levels.

## Data Availability

The data used to support the findings of this study are available from the corresponding author upon request.

## Conflicts of Interest

The authors declare that they have no conflicts of interest.

## Acknowledgments

This work was supported by the Hue University under the Core Research Program No. NCM.DHH.2019.08.

## References

- [1] J. A. Arancibia and G. M. Escandar, "Complexation study of diclofenac with  $\beta$ -cyclodextrin and spectrofluorimetric determination," *Analyst*, vol. 124, no. 12, pp. 1833–1838, 1999.
- [2] M. Cleuvers, "Mixture toxicity of the anti-inflammatory drugs diclofenac, ibuprofen, naproxen, and acetylsalicylic acid," *Ecotoxicology and Environmental Safety*, vol. 59, no. 3, pp. 309–315, 2004.
- [3] W. Jin and J. Zhang, "Determination of diclofenac sodium by capillary zone electrophoresis with electrochemical detection," *Journal of Chromatography. A*, vol. 868, no. 1, pp. 101–107, 2000.
- [4] B. T. Alquadeib, "Development and validation of a new HPLC analytical method for the determination of diclofenac in tablets," *Saudi pharmaceutical journal*, vol. 27, no. 1, pp. 66–70, 2019.
- [5] C. Arcelloni, R. Lanzi, S. Pedercini et al., "High-performance liquid chromatographic determination of diclofenac in human plasma after solid-phase extraction," *Journal of Chromatography. B, Biomedical Sciences and Applications*, vol. 763, no. 1–2, pp. 195–200, 2001.
- [6] J. A. Arancibia, M. A. Boldrini, and G. M. Escandar, "Spectrofluorimetric determination of diclofenac in the presence of  $\alpha$ -cyclodextrin," *Talanta*, vol. 52, no. 2, pp. 261–268, 2000.
- [7] A. A. Ensafi, M. Izadi, and H. Karimi-Maleh, "Sensitive voltammetric determination of diclofenac using room-temperature ionic liquid-modified carbon nanotubes paste electrode," *Ionics*, vol. 19, no. 1, pp. 137–144, 2013.
- [8] A. Sasal, K. Tyszczyk-Rotko, M. Wójciak, and I. Sowa, "First electrochemical sensor (screen-printed carbon electrode modified with carboxyl functionalized multiwalled carbon nanotubes) for ultratrace determination of diclofenac," *Materials*, vol. 13, no. 3, p. 781, 2020.
- [9] A. Afkhami, A. Bahiraei, and T. Madrakian, "Gold nanoparticle/multi-walled carbon nanotube modified glassy carbon electrode as a sensitive voltammetric sensor for the determination of diclofenac sodium," *Materials Science and Engineering: C*, vol. 59, pp. 168–176, 2016.
- [10] J. Qian, F. Sun, and L. Qin, "Hydrothermal synthesis of zeolitic imidazolate framework-67 (ZIF-67) nanocrystals," *Materials Letters*, vol. 82, no. 2012, pp. 220–223, 2012.
- [11] Q. Yang, S. S. Ren, Q. Zhao et al., "Selective separation of methyl orange from water using magnetic ZIF-67 composites," *Chemical Engineering Journal*, vol. 333, pp. 49–57, 2018.
- [12] Y. Li, Z. Jin, and T. Zhao, "Performance of ZIF-67 - Derived fold polyhedrons for enhanced photocatalytic hydrogen evolution," *Chemical Engineering Journal*, vol. 382, p. 123051, 2020.

- [13] X. Wu, W. Liu, H. Wu et al., "Nanoporous ZIF-67 embedded polymers of intrinsic microporosity membranes with enhanced gas separation performance," *Journal of Membrane Science*, vol. 548, pp. 309–318, 2018.
- [14] E. Sohoulı, M. S. Karimi, E. M. Khosrowshahi, M. Rahimi-Nasrabadi, and F. Ahmadi, "Fabrication of an electrochemical mesalazine sensor based on ZIF-67," *Measurement*, vol. 165, p. 108140, 2020.
- [15] X. Wang, K. Maeda, A. Thomas et al., "A metal-free polymeric photocatalyst for hydrogen production from water under visible light," *Nature Materials*, vol. 8, no. 1, pp. 76–80, 2009.
- [16] J. Li, B. Shen, Z. Hong, B. Lin, B. Gao, and Y. Chen, "A facile approach to synthesize novel oxygen-doped g-C<sub>3</sub>N<sub>4</sub> with superior visible-light photoreactivity," *Chemical Communications*, vol. 48, no. 98, pp. 12017–12019, 2012.
- [17] Y. Zhang, A. Thomas, M. Antonietti, and X. Wang, "Activation of carbon nitride solids by protonation: morphology changes, enhanced ionic conductivity, and photoconduction experiments," *Journal of the American Chemical Society*, vol. 131, no. 1, pp. 50–51, 2009.
- [18] Z. Chen, S. Zhang, Y. Liu et al., "Synthesis and fabrication of g-C<sub>3</sub>N<sub>4</sub>-based materials and their application in elimination of pollutants," *Science of The Total Environment*, vol. 731, article 139054, 2020.
- [19] S. C. Yan, Z. S. Li, and Z. G. Zou, "Photodegradation performance of g-C<sub>3</sub>N<sub>4</sub> fabricated by directly heating melamine," *Langmuir*, vol. 25, no. 17, pp. 10397–10401, 2009.
- [20] A. Thomas, A. Fischer, F. Goettmann et al., "Graphitic carbon nitride materials: variation of structure and morphology and their use as metal-free catalysts," *Journal of Materials Chemistry*, vol. 18, no. 41, pp. 4893–4908, 2008.
- [21] M. J. Bojdy, J. Müller, M. Antonietti, and A. Thomas, "Ionothermal synthesis of crystalline, condensed, graphitic carbon nitride," *Chemistry - A European Journal*, vol. 14, no. 27, pp. 8177–8182, 2008.
- [22] X. Bai, L. Wang, Y. Wang, W. Yao, and Y. Zhu, "Enhanced oxidation ability of g-C<sub>3</sub>N<sub>4</sub> photocatalyst via C60 modification," *Applied Catalysis B: Environmental*, vol. 152, pp. 262–270, 2014.
- [23] S. Tonda, S. Kumar, S. Kandula, and V. Shanker, "Fe-doped and -mediated graphitic carbon nitride nanosheets for enhanced photocatalytic performance under natural sunlight," *Journal of Materials Chemistry A*, vol. 2, no. 19, pp. 6772–6780, 2014.
- [24] B. Long, J. Lin, and X. Wang, "Thermally-induced desulfurization and conversion of guanidine thiocyanate into graphitic carbon nitride catalysts for hydrogen photosynthesis," *Journal of Materials Chemistry A*, vol. 2, no. 9, pp. 2942–2951, 2014.
- [25] K.-Y. A. Lin and W.-D. Lee, "Self-assembled magnetic graphene supported ZIF-67 as a recoverable and efficient adsorbent for benzotriazole," *Chemical Engineering Journal*, vol. 284, pp. 1017–1027, 2016.
- [26] A. Awadallah-F, F. Hillman, S. A. Al-Muhtaseb, and H.-K. Jeong, "On the nanogate-opening pressures of copper-doped zeolitic imidazolate framework ZIF-8 for the adsorption of propane, propylene, isobutane, and n-butane," *Journal of Materials Science*, vol. 54, no. 7, pp. 5513–5527, 2019.
- [27] Y. Jiao, D. Han, Y. Lu et al., "Characterization of pine-sawdust pyrolytic char activated by phosphoric acid through microwave irradiation and adsorption property toward CDNB in batch mode," *Desalination and Water Treatment*, vol. 77, pp. 247–255, 2017.
- [28] C. M. Adeyeye and P.-K. Li, "Diclofenac sodium," in *Analytical profiles of drug substances*, vol. 19, pp. 123–144, Elsevier, 1990.
- [29] A. J. Bard and L. R. Faulkner, "Fundamentals and applications," *Electrochemical methods*, vol. 2, no. 482, pp. 580–632, 2001.
- [30] J. Soleymani, M. Hasanzadeh, N. Shadjou et al., "A new kinetic-mechanistic approach to elucidate electrooxidation of doxorubicin hydrochloride in unprocessed human fluids using magnetic graphene based nanocomposite modified glassy carbon electrode," *Materials Science and Engineering: C*, vol. 61, pp. 638–650, 2016.
- [31] E. Laviron, "General expression of the linear potential sweep voltammogram in the case of diffusionless electrochemical systems," *Journal of Electroanalytical Chemistry and Interfacial Electrochemistry*, vol. 101, no. 1, pp. 19–28, 1979.
- [32] C. Li, "Electrochemical determination of dipyrindamole at a carbon paste electrode using cetyltrimethyl ammonium bromide as enhancing element," *Colloids Surfaces B Biointerfaces*, vol. 55, no. 1, pp. 77–83, 2007.
- [33] K. G. Madsen, C. Skonberg, U. Jurva et al., "Bioactivation of diclofenac in vitro and in vivo: correlation to electrochemical studies," *Chemical Research in Toxicology*, vol. 21, no. 5, pp. 1107–1119, 2008.
- [34] R. N. Goyal, S. Chatterjee, and B. Agrawal, "Electrochemical investigations of diclofenac at edge plane pyrolytic graphite electrode and its determination in human urine," *Sensors and Actuators B: Chemical*, vol. 145, no. 2, pp. 743–748, 2010.
- [35] X. D. du, C. C. Wang, J. G. Liu et al., "Extensive and selective adsorption of ZIF-67 towards organic dyes: performance and mechanism," *Journal of Colloid and Interface Science*, vol. 506, pp. 437–441, 2017.
- [36] F. Manea, M. Ihos, A. Remes, G. Burtica, and J. Schoonman, "Electrochemical determination of diclofenac sodium in aqueous solution on Cu-doped zeolite-expanded graphite-epoxy electrode," *Electroanalysis*, vol. 22, no. 17–18, pp. 2058–2063, 2010.
- [37] S. L. Z. Joikeng, I. K. Tonle, and A. Walcarius, "Amino-attapulgite/mesoporous silica composite films generated by electro-assisted self-assembly for the voltammetric determination of diclofenac," *Sensors and Actuators B: Chemical*, vol. 287, pp. 296–305, 2019.
- [38] F. Nasiri, G. H. Rounaghi, N. Ashraf, and B. Deiminiat, "A new electrochemical sensing platform for quantitative determination of diclofenac based on gold nanoparticles decorated multi-walled carbon nanotubes/graphene oxide nanocomposite film," *International Journal of Environmental Analytical Chemistry*, vol. 101, no. 2, pp. 153–166, 2021.
- [39] M. M. Eteya, G. H. Rounaghi, and B. Deiminiat, "Fabrication of a new electrochemical sensor based on AuPt bimetallic nanoparticles decorated multi-walled carbon nanotubes for determination of diclofenac," *Microchemical Journal*, vol. 144, pp. 254–260, 2019.